In compliance with the
Canadian Privacy Legislation
some supporting forms
may have been removed from
this dissertation.

While these forms may be included
in the document page count,
their removal does not represent
any loss of content from the dissertation.

University of Alberta

Three-Dimensional Mapping of Oxygen Distribution in Wastewater Biofilms Using Microelectrodes.

By

Carlos de la Rosa Romero

A thesis submitted to the Faculty of Graduate Studies and Research in partial fulfillment of the requirements for the degree of Master of Science

In

Environmental Science

Department of Civil and Environmental Engineering.

Edmonton, Alberta

Fall, 2003

National Library
of Canada

Acquisitions and
Bibliographic Services

395 Wellington Street
Ottawa ON K1A 0N4
Canada

Bibliothèque nationale
du Canada

Acquisisitons et
services bibliographiques

395, rue Wellington
Ottawa ON K1A 0N4
Canada

Your file Votre référence
ISBN: 0-612-87925-9
Our file Notre référence
ISBN: 0-612-87925-9

The author has granted a non-exclusive licence allowing the National Library of Canada to reproduce, loan, distribute or sell copies of this thesis in microform, paper or electronic formats.

The author retains ownership of the copyright in this thesis. Neither the thesis nor substantial extracts from it may be printed or otherwise reproduced without the author's permission.

L'auteur a accordé une licence non exclusive permettant à la Bibliothèque nationale du Canada de reproduire, prêter, distribuer ou vendre des copies de cette thèse sous la forme de microfiche/film, de reproduction sur papier ou sur format électronique.

L'auteur conserve la propriété du droit d'auteur qui protège cette thèse. Ni la thèse ni des extraits substantiels de celle-ci ne doivent être imprimés ou aturement reproduits sans son autorisation.

Canada

University of Alberta

Library Release Form

Name of Author: Carlos de la Rosa Romero

Title of thesis: Three-Dimensional Mapping of Oxygen Distribution in Wastewater Biofilms Using Microelectrodes.

Degree: Master of Science.

Year this Degree Granted: 2003.

Permission is hereby granted to the University of Alberta Library to reproduce single copies of this thesis and to lend or sell such copies for private, scholarly or scientific research purposes only.

The author reserves all other publication and other rights in association with the copyright in the thesis, and except as herein before provided, neither the thesis nor any substantial portion thereof may be printed or otherwise reproduced in any material form whatever without the author's prior written permission.

Date: July 25, 2003

University of Alberta

Faculty of Graduate Studies and Research

The undersigned certify that they have read, and recommend to the Faculty of Graduate Studies and Research for acceptance, a thesis entitled *Three-Dimensional Mapping of Oxygen Distribution in Wastewater Biofilms Using Microelectrodes* submitted by *Carlos de la Rosa Romero* in partial fulfillment of the requirements for the degree of *Master of Science* in *Environmental Science*.

Dr. Howard Ceri

Date: July 23, 2003

ABSTRACT

The three-dimensional oxygen distribution in wastewater biofilms was evaluated using combined oxygen microelectrodes and an automation system. The biofilm samples studied were mature biofilms with thickness from 630 μm to 1600 μm, sampled from the rotating biological contactors of a well-operated municipal wastewater treatment plant. The concentration and the level of heterogeneity of dissolved oxygen inside the biofilms decreased with depth, forming stratification. A high heterogeneity of dissolved oxygen was found in the top portions of the biofilms. The high variability of dissolved oxygen suggested the presence of water with oxygen in the top portions of biofilms. The three-dimensional oxygen distribution maps revealed the existence of "pockets" with dissolved oxygen in deep sections of biofilms. The dissolved oxygen concentrations of these pockets in the biofilms were from 0.4 mg/L to 1.1 mg/L at 600 μm and 760 μm depths. It was demonstrated that the biofilm surface is physically heterogeneous.

ACKNOWLEDGMENTS

This project would not have been successful without the aid and advice of many people to whom I owe my thanks and appreciation.

Foremostly I would like to acknowledge Dr. Tong Yu, my supervisor and teacher at the University of Alberta. His guidance throughout this project was invaluable to the development of my academic skills, and his enthusiasm for research has strengthened my own dedication to scientific discovery.

My special thanks to Mr. Andy Bebbington, Mr. Jim Hepler and Mr. Dave Barabash from the Water and Wastewater Treatment Plant in the Town of Devon. Their cooperation in growing the biofilm samples made this experiment a reality. I am indebted to Debra Long for her willing assistance throughout the course of the experiment. My thanks to Richard Lu for his teaching and advice about the oxygen microelectrode construction, and for his help in the laboratory. I also appreciated the help of Sincy Modayil.

I thank members of the thesis examining committee, Dr. Ian Buchanan and Dr. Howard Ceri, for their suggestions on the revision of this thesis.

I thank all teachers and classmates of the department of Civil and Environmental Engineering who always supported me throughout the course of my studies. My special thanks to my classmates Omar Lopez and Carlos Ibiza for their invaluable support while overcoming our challenges.

Finally, I want to thank my girlfriend Dee, and my parents and brothers in Mexico, for their love and support.

This project was partially funded by the Natural Sciences and Engineering Research Council (NSERC) of Canada and a scholarship from the National Council of Science and Technology (CONACyT) of Mexico.

TABLE OF CONTENST

1.0 INTRODUCTION 1

1.1 ENVIRONMENTAL BIOFILMS. 1

1.2 MAPPING OXYGEN IN WASTEWATER BIOFILMS. 2

1.3 AUTOMATION SYSTEM. 4

1.4 OBJECTIVES. 7

2.0 LITERATURE REVIEW 9

3.0 MATERIALS AND METHODS 20

3.1 AUTOMATION SYSTEM DEVELOPMENT. 20

3.1.1 THE DATA ACQUISITION SYSTEM. 21

3.1.2 THE MOTION CONTROL SYSTEM. 23

3.1.3 THE SOFTWARE. 24

3.2 OXYGEN MICROELECTRODE CONSTRUCTION. 26

3.2.1 PREPARATION OF GLASS TUBING FOR THE WORKING CATHODE SHAFT. 29

3.2.2 ETCHING OF THE WORKING CATHODE WIRE. 29

3.2.3 ASSEMBLY OF THE WORKING CATHODE. 30

3.2.4 TAPERING OF THE WORKING CATHODE TIP. 31

3.2.5 GOLD PLATING OF THE CATHODE TIP. 31

3.2.6 THE OUTER CASING. 32

3.2.7 GUARD CATHODE. 33

3.2.8 Ag/AgCl REFERENCE ELECTRODE. 34

3.2.9 ASSEMBLY OF THE OXYGEN MICROELECTRODE. 34

3.2.10 POLARIZATION AND CALIBRATION OF THE OXYGEN MICROELECTRODE. 36
3.3 EXPERIMENTS. 38
4.0 EXPERIMENTAL RESULTS AND DISCUSSIONS 48
4.1 AUTOMATION SYSTEM. 48
4.2 THE OXYGEN MICROELECTRODES. 49
4.3 THE DISSOLVED OXYGEN DISTRIBUTION 51
4.3.1 THE INDIVIDUAL PROFILES. 52
4.3.2 DISSOLVED OXYGEN DISTRIBUTION FROM THE ARTIFICIAL PLANE. 55
4.3.3 BIOFILM SURFACE DESCRIPTION. 69
4.3.4 THE DISSOLVED OXYGEN DISTRIBUTION INSIDE THE BIOFILMS. 79
4.3.5 THE DISSOLVED OXYGEN DISTRIBUTION ABOVE THE BIOFILM SURFACE. 94
5.0 CONCLUSIONS AND RECOMMENDATIONS 107
6.0 REFERENCES 110
7.0 APPENDICES 115
APPENDIX A. COMPUTER PROGRAM DEVELOPMENT. 116
APPENDIX B. OXYGEN DISTRIBUTION FROM THE ARTIFICIAL PLANE. 141
APPENDIX C. OXYGEN DISTRIBUTION FROM THE BIOFILM SURFACE. 185

APPENDIX D. OXYGEN DISTRIBUTION ABOVE THE BIOFILM SURFACE..... 208

List of Figures

Figure 1. Components and connections of the automation system..... 21

Figure 2. General diagram of the data acquisition system used to measure dissolved oxygen concentration in wastewater biofilms..... 23

Figure 3. Schematic diagram of the combined oxygen microelectrode..... 28

Figure 4. The RBC system in the wastewater treatment plant at Devon in Alberta, Canada..... 39

Figure 5. Coupons on a RBC disk for growing biofilm samples..... 41

Figure 6. The measuring chamber: (a) first compartment, (b) second compartment, (c) third compartment, (d) fixed wall dividing the first and second compartments, (e) fixed wall dividing the second and third compartments, (f) inlet tubing connected to the first compartment, (g) removable base used to place the biofilm sample, (h) outlet tubing from the second compartment, (i) outlet tubing from the third compartment, and (j1, j2, j3) clamps to control the flowrate..... 42

Figure 7. Calibration curve of the oxygen microelectrode used for the measurement of biofilm sample 1..... 50

Figure 8. Calibration curve of the oxygen microelectrode used for the measurement of biofilm sample 2..... 50

Figure 9. Calibration curve of the oxygen microelectrode used for the measurement of biofilm sample 3. 51

Figure 10. Calibration curve of the oxygen microelectrode used for the measurement of biofilm sample 4. 51

Figure 11. The dissolved oxygen profile of biofilm sample 1. 54

Figure 12. The dissolved oxygen profile of biofilm sample 2. 54

Figure 13. The dissolved oxygen profile of biofilm sample 3. 55

Figure 14. The dissolved oxygen profile of biofilm sample 4. 55

Figure 15. Dissolved oxygen concentration at the artificial plane in biofilm sample 1, about 920 μm above the biofilm surface. 57

Figure 16. Dissolved oxygen concentration 320 μm below the artificial plane in biofilm sample 1 58

Figure 17. Dissolved oxygen concentration 720 μm below the artificial plane in biofilm sample 1. 58

Figure 18. Dissolved oxygen concentration 1120 μm below the artificial plane in biofilm sample 1. 59

Figure 19. Dissolved oxygen concentration at the artificial plane in biofilm sample 2, about 920 μm above the biofilm surface. 60

Figure 20. Dissolved oxygen concentration 320 μm below the artificial plane in biofilm sample 2. 60

Figure 21. Dissolved oxygen concentration 720 μm below the artificial plane in biofilm sample 2. 61

Figure 22. Dissolved oxygen concentration 1120 μm below the artificial plane in biofilm sample 2. 61

Figure 23. Dissolved oxygen concentration at the artificial plane in biofilm sample 3, about 920 μm above the biofilm surface. 62

Figure 24. Dissolved oxygen concentration 320 μm below the artificial plane in biofilm sample 3. 63

Figure 25. Dissolved oxygen concentration 720 μm below the artificial plane in biofilm sample 3. 63

Figure 26. Dissolved oxygen concentration 1120 μm below the artificial plane in biofilm sample 3. 64

Figure 27. Dissolved oxygen concentration at the artificial plane in biofilm sample 4, about 920 μm above the biofilm surface. 65

Figure 28. Dissolved oxygen concentration 320 μm below the artificial plane in biofilm sample 4. 65

Figure 29. Dissolved oxygen concentration 720 μm below the artificial plane in biofilm sample 4. 66

Figure 30. Dissolved oxygen concentration 1120 μm below the artificial plane in biofilm sample 4. 66

Figure 31. The physical structure of the biofilm surface and the thickness of the biofilm for biofilm sample 1. 71

Figure 32. The physical structure of the biofilm surface and the thickness of the biofilm for biofilm sample 2. 71

Figure 33. The physical structure of the biofilm surface and the thickness of the biofilm for biofilm sample 3. 72

Figure 34. The physical structure of the biofilm surface and the thickness of the biofilm for biofilm sample 4. 72

Figure 35. Changes of biofilm thickness over time at one point of a biofilm sample. 74

Figure 36. Changes of biofilm thickness over time at one point of a biofilm sample. 75

Figure 37. The dissolved oxygen concentration presented at the biofilm surface of biofilm sample 1 76

Figure 38. The dissolved oxygen concentration presented at the biofilm surface of biofilm sample 2. 77

Figure 39. The dissolved oxygen concentration presented at the biofilm surface of biofilm sample 3. 77

Figure 40. The dissolved oxygen concentration presented at the biofilm surface of biofilm sample 4. 78

Figure 41. The dissolved oxygen concentrations 40 μm below the biofilm surface in biofilm sample 1..... 81

Figure 42. The dissolved oxygen concentrations 280 μm below the biofilm surface in biofilm sample 1..... 81

Figure 43. The dissolved oxygen concentrations 440 μm below the biofilm surface in biofilm sample 1..... 82

Figure 44. The dissolved oxygen concentrations 600 μm below the biofilm surface in biofilm sample 1..... 82

Figure 45. The dissolved oxygen concentrations 40 μm below the biofilm surface in biofilm sample 2..... 84

Figure 46. The dissolved oxygen concentrations 280 μm below the biofilm surface in biofilm sample 2..... 84

Figure 47. The dissolved oxygen concentrations 520 μm below the biofilm surface in biofilm sample 2..... 85

Figure 48. The dissolved oxygen concentrations 760 μm below the biofilm surface in biofilm sample 2..... 85

Figure 49. The dissolved oxygen concentrations 40 μm below the biofilm surface in biofilm sample 3..... 87

Figure 50. The dissolved oxygen concentrations 280 μm below the biofilm surface in biofilm sample 3. 87

Figure 51. The dissolved oxygen concentrations 520 μm below the biofilm surface in biofilm sample 3. 88

Figure 52. The dissolved oxygen concentrations 760 μm below the biofilm surface in biofilm sample 3. 88

Figure 53. The dissolved oxygen concentrations 40 μm below the biofilm surface in biofilm sample 4. 89

Figure 54. The dissolved oxygen concentrations 280 μm below the biofilm surface in biofilm sample 4. 90

Figure 55, The dissolved oxygen concentrations 520 μm below the biofilm surface in biofilm sample 4. 90

Figure 56. The dissolved oxygen concentrations 760 μm below the biofilm surface in biofilm sample 4. 91

Figure 57. Dissolved oxygen concentration 760 μm above the biofilm surface in biofilm sample 1. 96

Figure 58. Dissolved oxygen concentration 520 μm above the biofilm surface in biofilm sample 1. 96

Figure 59. Dissolved oxygen concentration 280 μm above the biofilm surface in biofilm sample 1. 97

Figure 60. Dissolved oxygen concentration 40 μm above the biofilm surface in biofilm sample 1. 97

Figure 61. Dissolved oxygen concentration 760 μm above the biofilm surface in biofilm sample 2. 98

Figure 62. Dissolved oxygen concentration 520 μm above the biofilm surface in biofilm sample 2. 99

Figure 63. Dissolved oxygen concentration 280 μm above the biofilm surface in biofilm sample 2. 99

Figure 64. Dissolved oxygen concentration 40 μm above the biofilm surface in biofilm sample 2. 100

Figure 65. Dissolved oxygen concentration 760 μm above the biofilm surface in biofilm sample 3. 101

Figure 66. Dissolved oxygen concentration 520 μm above the biofilm surface in biofilm sample 3. 101

Figure 67. Dissolved oxygen concentration 280 μm above the biofilm surface in biofilm sample 3. 102

Figure 68. Dissolved oxygen concentration 40 μm above the biofilm surface in biofilm sample 3. 102

Figure 69. Dissolved oxygen concentration 760 μm above the biofilm surface in biofilm sample 4. 103

Figure 70. Dissolved oxygen concentration 520 µm above the biofilm surface in biofilm sample 4. 104

Figure 71. Dissolved oxygen concentration 280 µm above the biofilm surface in biofilm sample 4. 104

Figure 72. Dissolved oxygen concentration 40 µm above the biofilm surface in biofilm sample 4. 105

1.0 INTRODUCTION

1.1 ENVIRONMENTAL BIOFILMS.

Biofilms are widely used in the treatment of industrial and municipal wastewater. A biofilm can be defined as a group of living cells, dead cells and cell debris in a matrix of extracellular polymeric substances (EPS) attached to a surface (Bishop *et al.*, 1995). The EPS and the microorganisms themselves form a protective barrier that helps some specific species of microorganisms to survive. This type of configuration provides an advantage because these species, which could degrade specific pollutants, would not survive in a regular suspended growth system. Biofilm's physical, chemical and biological properties change continuously due to growth, hydraulic conditions and sloughing.

Initially, the biofilm structure models assumed that biofilms were structurally homogeneous (Rittmann and McCarty, 1980a; Rittmann and McCarty, 1980b). It was thought that biofilm characteristics such as porosity, density and microbial population were constant in terms of depth. Development of mass transport models were based on these assumptions. However, in the past decade several investigations have suggested that biofilms are characterized by gradients of cell types and physical/chemical parameters, which means that they are heterogeneous (Bishop, 1997; Bishop and Yu, 1999; de Beer and Schramm, 1999; Noguera *et al.*, 1999a; Santegoeds *et al.*, 1998).

Several techniques have been applied to analyze biofilm structure and develop new models that can explain the transport of substrates through the films. One of the

techniques applied to biofilm research is the microelectrodes. Different microelectrodes have been used as powerful tools to measure different parameters such as oxygen, pH, redox potential, ammonium, and sulfide (Bishop and Yu, 1999; de Beer and Schramm, 1999; Fu *et al.*, 1994; Nishidome *et al.*, 1994; Rasmussen and Lewandowski, 1998b; Santegoeds *et al.*, 1998). The use of microelectrodes has proven that the structure and processes occurring in biofilms are heterogeneous and complex.

1.2 MAPPING OXYGEN IN WASTEWATER BIOFILMS.

Understanding the complex operation of biofilms is essential for the optimization of biofilm reactor design and operation. This includes an understanding of the structure of a biofilm, the biodegradation kinetics that take place within the biofilm and the impact of biofilm structure on degradation kinetics (Bishop, 1997). These characteristics are usually considered in biofilm model development.

Due to the heterogeneity of biofilms it is clear that biofilm modeling should take into account many parameters. However, it is not necessary and practical to consider all the possible parameters interacting with biofilms but to define and contemplate only the most important parameters affecting biofilm processes functionality. Oxygen is an important parameter because it is the substance that microorganisms use as final electron acceptor in aerobic degradation. It is the substance used to oxidize biodegradable organic matter; therefore, it is important to comprehend its dynamic within the biofilm.

In order to study the dissolved oxygen distribution into biofilms, it is indispensable to carry out direct measurements in biofilm samples. A very reliable

analytical tool available to do these measurements is the combined oxygen microelectrode. The combined oxygen microelectrode is a transducer that converts a chemical reaction signal into an electrical signal that can be measured. The device consists of a sensing electrode (the working cathode) made of platinum or gold; a reference electrode (the anode) made of silver/silver chloride (Ag/AgCl); a guard cathode made of silver; an oxygen permeable membrane; and an electrolyte solution (Lu, 2001; Lu and Yu, 2002a; Overgaard, 1993; Revsbech, 1989). The main advantage of this type of electrode is its small tip diameter (15-30 μm), which allows direct measurement without altering the biofilm structure.

One-dimensional dissolved oxygen penetration profiles carried out with oxygen microelectrodes have always shown that oxygen is depleted at about 200 – 800 μm depth in the biofilms (Bishop and Yu, 1999; Fu *et al.*, 1994; Santegoeds *et al.*, 1998). In order to verify if oxygen depletion is a common phenomenon in biofilm systems and to evaluate the biofilm heterogeneity in terms of oxygen, it is necessary to map the three-dimensional dissolved oxygen distribution in biofilms. This can be achieved by carrying out various dissolved oxygen profiles in a specific biofilm section. Due to the heterogeneous nature of biofilms, the three-dimensional dissolved oxygen distribution could show functional and structural characteristics that might not be observed with the typical one-dimensional dissolved oxygen profiles.

It is also important to map the three-dimensional dissolved oxygen distribution in biofilms because the data generated can be incorporated in models that evaluate the importance of the three dimensional heterogeneity of oxygen in biofilms. One

of the goals of advanced models is to evaluate the relevance of three-dimensional heterogeneities to the predictive capability of traditional biofilm models. The new models provide sophisticated two- and three-dimensional descriptions of biofilms and incorporate not only mass transport but also hydrodynamics and population dynamics (Eberl *et al.*, 2000; Morgenroth *et al.*, 2000a; Morgenroth *et al.*, 2000b; Noguera *et al.*, 1999a).

The amount of data needed to map the three-dimensional dissolved oxygen distribution in biofilms using oxygen microelectrodes with tip diameters of 15 to 30 μm requires the development of an automation system that allow precise microelectrode positioning and the recording of large quantity of data with the least possible error. The following section presents an overview of the main components of an automation system capable to map the three-dimensional dissolved oxygen distribution in biofilms.

1.3 AUTOMATION SYSTEM.

The automation system consists of three parts. The first part is the data acquisition system, which is the group of components used to collect, compute and store the data gathered from the oxygen microelectrode. The second part is the motion control system, which is the group of components used to accurately position the microelectrode at any part of a biofilm sample. And the third part is the software, which is a computer program developed in National Instruments' LabVIEW®. This program is used to automatically synchronize the data acquisition system and the motion control system.

The first part of the automation system is the data acquisition. The main

advantage of using a computerized data acquisition system is the large quantity of data that can be collected in short periods of time and with fewer errors. Biofilm researchers gather data that needs to be stored and analyzed. However, there is always a limit in terms of the frequency and accuracy researchers can gather the information they need. The amount of data and accuracy required to map the three-dimensional dissolved oxygen distribution in biofilms is considerably high. Therefore, in order to improve the quantity and quality of data collection a data acquisition system can be used.

An important part of a data acquisition system is the analog-to-digital conversion, which is the process of converting an analog signal to a digital signal. The device that does the conversion is an Analog-to-Digital Converter (ADC). This device provides a computer with the digital codes that represent an analog input signal (Miner and Comer, 1992). Digital signals have discrete values (only certain values are allowed) and have a specified time interval between values, which is usually constant. If a digital signal is recorded for a certain time, the waveform obtained will have a "stepped" (non continuous) appearance. When the time interval is small enough, the digital waveform becomes a good approximation of the analog signal (Austerlitz, 1991).

The second part of the automation system is the motion control system. Solenoids and motors are two of the most common actuators used in motion systems. An actuator is a device that converts a signal input to a mechanical motion. In general solenoids are used to produce linear motion in response to an input signal from a controller, whereas motors are used for rotary motion (Lenk, 1984). However, with the use of gears and linkages motors can perform linear movements too.

There are two types of motors used to perform movements controlled by a computer. The "stepless" motors, which are devices that move continuously until they finish a loop (360 °); and the "stepper" motors, which are systems that turn at particular step angles. The shaft of the motor can be made to rotate a precise number of degrees, ranging from some fraction of a turn, to one or more complete turns (Clifford, 1990). With stepper motors, small linear movements can be achieved. In addition, the motor resolution can be considerably increased by electronic micro-stepping. The advantage of micro-stepping is multiplication of the numbers of steps per revolution, thereby increasing the resolution of the stepper motor system. The stepper motors characteristics, together with the micro-stepping technology can be implemented to develop an automation system used for the study in environmental biofilms using microelectrodes. These technologies can provide the accuracy needed to perform linear movements in the order of micrometers. The fine accuracy will allow a better control of the oxygen microelectrode. The accuracy will improve the quality of the experimental results and it will decrease the risk of breaking the microelectrode tip.

The third part of the automation system is the software. The computer program necessary to control both the data acquisition system and motion control system to study wastewater biofilms using microelectrodes can be programmed using the features of LabVIEW®. LabVIEW®, which stands for "Laboratory Virtual Instrument Engineering Workbench," is a program environment in which programs are created with graphics and not with text like in traditional programming languages such as C or C++. The main uses of LabVIEW® are data acquisition, data analysis, instrument control and presentation of

results.

1.4 OBJECTIVES.

Summarizing the previous sections it can be stated that a better understanding of the dissolved oxygen distribution in biofilm systems is essential for the optimization of biofilm reactor design and operation. It is important to obtain the three-dimensional dissolved oxygen distribution in biofilms because the results could show functional and structural biofilm characteristics that may not be observed with typical one-dimensional dissolved oxygen profiles. The results generated can also be incorporated in models that evaluate the importance of three-dimensional heterogeneity of oxygen in biofilms.

There are two main tools that combined can be very useful to map the three-dimensional dissolved oxygen distribution in biofilms. The oxygen microelectrode that allows direct measurement without altering the biofilm structure and the automation system that allows the precise positioning of the microelectrode and data acquisition of the experimental results.

Therefore, the general objective of the present work was to study the three-dimensional dissolved oxygen distribution in wastewater biofilms using oxygen microelectrodes.

The specific objectives were:

(1) To develop an automation system formed by a data acquisition system, a motion control system and a computer program that permit automated data collection and

precise microelectrode positioning.

(2) To construct oxygen microelectrodes with tip diameters of 15-30 μm.

(3) To map the three-dimensional dissolved oxygen distribution in biofilms sampled from a municipal wastewater treatment plant operating with a Rotating Biological Contactor (RBC) system, using the automation system and the oxygen microelectrodes.

2.0 LITERATURE REVIEW

Biofilm systems have become an important process for the treatment of industrial and municipal wastewater. Environmental engineers and scientists have found a number of advantages over conventional activated sludge process. Some of the advantages include the ability to support a variety of microbial populations at different locations within the biofilm, which may degrade different organic substrates, and the sequestering ability of the EPS surrounding the microorganisms, which protects them from toxicants (Bishop, 1997). Biofilm researchers have applied different technologies in order to understand the structure and function of biofilm systems. It is clear that the application of these technologies will produced important knowledge for the continuous optimization of biofilm reactor design and operation.

Some of the techniques applied to biofilm research that have contributed to the knowledge of biofilm systems range from measurement of total suspended solids, phospholipids and dye adsorption to more complex technologies such as Scanning Electron Microscopy (SEM) and Confocal Scanning Laser Microscopy (CSLM). The use of a particular technology depends on the type of information that the researcher wants to evaluate in the biofilm system.

The active bacteria, densities, porosities and mean pore radius were evaluated in biofilms by measuring total suspended solids, phospholipids, AR18 dye adsorption, and bacterial population distributions in laboratory cultured biofilms (Zhang and Bishop, 1994a; Zhang and Bishop, 1994c). The authors found that the densities in the bottom layers of the biofilms were 4-10 times higher that those in the top layers. The

ratio of living cells to total biomass decreased from 72-91 % in the top layers to 58-67 % in the bottom layers. The mean pore radius decreased from 1.7-2.7 μm in the top layers to 0.3-0.4 μm in the bottom layers. For thick biofilms (thickness > 500 μm) the active bacteria decreased from 82-89 % in the top layers to 5-11 % in the bottom layers. The porosities of thick biofilms changed from 83-92 % in the top layers to 56-64 % in the bottom layers. For thin biofilms (thickness < 500 μm), the porosities of biofilms changed from 72-75 % in the top layers to 35-44 % in the bottom layers. These experiments have shown that biofilm structure is stratified and heterogeneous.

The studies using CSLM have provided important information about biofilm structure. Using this technique de Beer and Stoodley, (1995) characterized aerobic biofilms. The biofilms were found to consist of microbial clusters of cells and EPS separated by interstitial voids. The cell clusters were about 300 μm and the voids were about 100 μm. Some other authors have found the same clusters and voids using CSLM (Lewandowski *et al.*, 1995; Massol-deya *et al.*, 1995). They have stated that these voids facilitate oxygen transport from the bulk liquid to the biofilm and they have actually reported water flow through some biofilms (de Beer *et al.*, 1994). All the experiments with CSLM have been carried out using young biofilms with thickness from 10 to about 200 μm. Many wastewater treatment biofilm systems operate with a biofilm thickness of 0.5 to 2.0 mm (Bishop, 1997). This means that only young biofilms have been studied with this technique. It is not known whether the cluster and voids observed in thin biofilms are present in the bottom parts of mature biofilms. There are other tools that allow the assessment of biofilm functions and components in mature biofilms. One of

these tools is the microelectrode technique. Microelectrodes allow direct measurements without altering the biofilm structure because their tip diameter is very small, usually no more than 30 μm.

Different microelectrodes have been used as powerful tools to measure *in situ* different parameters such as oxygen, pH, redox potential, ammonium and sulfide (Bishop and Yu, 1999; de Beer and Schramm, 1999; Fu *et al.*, 1994; Nishidome *et al.*, 1994; Rasmussen and Lewandowski, 1998b; Santegoeds *et al.*, 1998; Yu, 2000). Some important biofilm characteristics have been discovered using microelectrodes. One of the important microelectrodes is the oxygen microelectrode because it allows the measurement of dissolved oxygen, which is an important element in the biodegradation process.

There are several works where the application of oxygen microelectrodes has played an important role in the evaluation of important biofilm characteristics. In the following paragraphs important contributions to biofilm research using oxygen microelectrodes is presented.

Early studies of dissolved oxygen concentration in wastewater biofilms using microelectrodes were reported in 1969 (Bungay *et al.*, 1969; Whalen *et al.*, 1969). By measuring dissolved oxygen profiles in cultured biofilms, the authors demonstrated the applicability of the oxygen microelectrodes for the direct measurement of dissolved oxygen concentrations and gradients in liquids and in microbial slime films. Later, several authors continued the application of oxygen microelectrodes in biofilm research. Fu *et al.* (1994) concluded that miniaturizing the size of microelectrodes it is

possible to detect dissolved oxygen variations inside biofilms. The authors carried out direct dissolved oxygen measurements using microelectrodes inside a deactivated biofilm at intervals of 100 μm in a fixed point. They evaluated the effective diffusion coefficient at different depths in biofilms and found that the effective diffusivity of oxygen is highly related to the biofilm density, and decreases from 90 % at the surface of the biofilm to 25 % at the bottom of the biofilm.

The thickness of the dissolved oxygen boundary layer have been investigated using oxygen microelectrodes (Zhang and Bishop, 1994b). The experiments were carried out under different flow rates. The experimental results indicated that the concentration boundary layer was a function of the organic loading rate in the feed solution and the dissolved oxygen concentration in the bulk solution; the thickness of the dissolved oxygen concentration boundary layer decreased with an increase of the flow rate; and the boundary layer increased with the increase of the organic loading and the dissolved oxygen concentration in the bulk water.

The influence of biofilm structure on transport and transformation process in biofilms was investigated using a combination of physical, chemical and microbiological tests together with oxygen microelectrodes (Bishop *et al.*, 1995). The study demonstrated that the biofilm structure is highly stratified, characterized by an increase of biofilm density, a decrease of metabolically active biomass, a decrease of effective oxygen diffusivity and a decrease of porosity with biofilm depth. There are different trends for the density increase and the decrease of porosity, microbial activity and dissolved oxygen effective diffusivity with biofilm depth for different biofilm

thickness. The rate of density increase and porosity decrease with biofilm depth is greater for thin biofilms than for thick biofilms. For this reason, the porosity decrease and density increase of thin biofilms are much faster with biofilm depth than those of thick biofilms.

A study of the mass transfer phenomena in biofilm systems was conducted, with special attention in the boundary layer (Wasche *et al.*, 2000). The authors found that the thickness of the concentration layer depend on the surface structure, which depends on the substrate loading and the hydrodynamic conditions during the growth phase of the biofilm. They also found that high substrate loadings and low shearing forces produce a rough biofilm surface, while low substrate loadings and high shearing forces produce a smooth biofilm surface.

Santegoeds *et al.* (1998) studied biofilm dynamics with microelectrodes. They measured dissolved oxygen, sulfide and pH during the development of the biofilm. They detected anoxic zones after one week of incubation. They found that the dissolved oxygen was depleted in the first 200 μm of the biofilm. Sulfide was detected in the 6th week of incubation.

Bishop and Yu (1999) examined the stratification of microbial processes and the associated redox potential. The microelectrodes they used were oxygen, sulfide, ammonium, pH and redox potential. They used two types of biofilms: one carrying aerobic oxidation and sulfate reduction processes and the other carrying aerobic oxidation and nitrification. They found that the metabolic processes studied have a stratified structure with depth. The dissolved oxygen profile showed a clearly decrement

with depth: in both systems the dissolved oxygen was depleted at a depth of about 800 μm from the surface of the biofilm.

It is important to conduct experiments in biofilms that come directly from wastewater treatment plants. Most of the studies in the biofilm research area have been conducted in laboratory-cultured biofilms (de Beer and Stoodley, 1995; Nishidome *et al.*, 1994; Wasche *et al.*, 2000; Zhang and Bishop, 1994b). It is not known whether these types of biofilms are different than biofilms commonly found in wastewater treatment systems. Recently, *in situ* dissolved oxygen measurements in biofilms from municipal wastewater treatment plants operating with RBC systems have been conducted (Lu and Yu, 2002b). Using combined oxygen microelectrodes, the authors found a dissolved oxygen penetration of no more than 600 μm in the biofilms. In a study on heterotrophic biofilms in tube reactors Wasche *et al.* (2002) measured with microelectrodes the dissolved oxygen concentration profiles in the biofilms and in the boundary layer directly in the biofilm tube reactors. They found that the thickness of the concentration boundary layer depends on the surface structure of the biofilm. Therefore more studies of dissolved oxygen in biofilms that grow in wastewater treatment plants will produce important information of the structure and function of biofilm systems used in the treatment of wastewater.

As seen before, the oxygen microelectrode has been a valuable tool used to evaluate important structural and functional characteristics of biofilms. However, these types of studies have been carried out in one-dimensional dissolved oxygen profiles. Due to the heterogeneous nature of biofilms it is possible that evaluating only one-

dimensional dissolved oxygen concentration profiles could miss important information about the oxygen dynamics in biofilm systems. Therefore, it is important to map the three-dimensional dissolved oxygen distribution in biofilms. New information could be found in three-dimensional dissolved oxygen distribution maps that normally would not show up in one-dimensional dissolved oxygen concentration profiles. In addition, the experimental data generated can be of value to the calibration of three-dimensional biofilm models.

The experimental evidence that biofilm system composition is heterogeneous has lead to serious considerations for the use of three-dimensional biofilm models for the design and operation of biofilm processes. Some authors have emphasized the importance of multi-dimensional models and developed two- and three- dimensional approach for biofilm growth and structure formation (Picioreanu *et al.*, 1999). The model incorporated the flow over the irregular biofilm surface, convective and diffusive mass transfer of substrate, bacterial growth and biomass spreading. They found that heterogeneous biofilms with rough surface and high porosity occur in a slow substrate transfer regime, whereas in a fast flow and fast internal diffusion regime, biofilms develop a compact structure.

Other mathematical models have been developed to simulate the three-dimensional growth of multi-species anaerobic biofilms (Noguera *et al.*, 1999b). The simulations resulted in the formation of biofilm heterogeneous in structure and composition. The authors stressed that three-dimensional diffusion reaction models are

the only way to provide quantitative solutions that can be used to analyze substrate gradients and biomass distributions inside the biofilms.

Mathematical models developed in biofilm research need to be implemented so that full-scale plant operators can use them in their everyday work for design, control, optimization and trouble shooting of biofilm processes (Morgenroth *et al.*, 2000b). Practitioners, experimenters and modelers should work together to identify the important processes that should be included in models. The authors remarked that biofilm models would only be helpful for practical applications if guidance on model calibration is provided along with the model. To calibrate a model a large number of experimental input parameters are required. Therefore, it should be investigated which parameters in biofilm models are significant and have to be evaluated experimentally.

Horn *et al.* (2002) provided a good example of how experimental data gathered with oxygen microelectrodes, substrate conversion rates and biofilm densities can be later translated to formulate model equations for the simulation of biofilm growth under different hydrodynamic and substrate conditions. The authors found that mass transfer and biofilm density are strongly related to the substrate load and the hydraulic conditions during the cultivation of the biofilm.

As can be seen, there is a need for three-dimensional experimental data of important factors affecting biofilm systems, such as oxygen. The data generated from three-dimensional dissolved oxygen distribution maps in biofilms would be valuable for modelers interested in the evaluation of three-dimensional heterogeneity of dissolved

oxygen in biofilms.

The application of several technologies would be required in order to evaluate the three-dimensional dissolved oxygen distribution in biofilm systems. For instance, the oxygen microelectrode technology would provide the means to acquire the dissolved oxygen concentration in the biofilms without altering its structure. The experimental procedure would involve the acquisition of large quantity of data. And due to the small size of the microelectrode tip (15-30 μm) a precise microelectrode positioning is critical. The application of automation technologies can provide an accurate positioning of the oxygen microelectrode and the acquisition of large quantity of data.

There have been some studies in the field of biofilm research where some level of automation has been applied. Zhang *et al.* (1995) used a data acquisition system in order to record readings from oxygen and ion-selective microelectrodes. The signal of the microelectrodes was digitized by a data acquisition system interfaced to a computer. Later, the data was exported to a spreadsheet program for subsequent analysis. However, there has been a limited use of automated motion control systems in biofilm experimentation using microelectrodes, in part because the microelectrode positioning requirements in those experiments were not very strict and could be done manually. Some researchers have used stepper motors fixed to micromanipulator in order to achieve an accurate one-dimensional control of the microelectrode through a computer (de Beer and Stoodley, 1995). The requirements needed for the three-dimensional mapping of dissolved oxygen distribution in biofilms using microelectrodes are stricter than in one-dimensional measurement. It is necessary for the automatic acquisition of large

quantity of experimental data (in a range of thousands of measurements), the precise positioning of the oxygen microelectrode in three dimensions, and a way to control and synchronize these operations. Therefore, the development of an automation system with a data acquisition system, a motion control system and a computer program capable of controlling and synchronizing all the elements is crucial for the evaluation of dissolved oxygen in wastewater biofilms in three dimensions.

As discussed before, the oxygen microelectrode has been an important tool in biofilm research. There are two types of oxygen microelectrodes: the separate oxygen microelectrode and the combined oxygen microelectrode. The high stability of the combined oxygen microelectrode makes it suitable for dissolved oxygen measurements in wastewater biofilms. The first combined oxygen electrode was reported by (Clark *et al.*, 1953) for the measurement of oxygen tension in blood. Later, the Clark-type electrode was developed into a micro-scale electrode (Revsbech and Jorgensen, 1986). In order to obtain a more stable reading some parts of the Clark-type oxygen microelectrode were further modified (Revsbech, 1989). The most important modification was the addition of an internal auxiliary electrode as the guard cathode, which is integrated with the working and the reference electrode. The guard cathode removes the oxygen diffusing toward the sensor from the internal electrolyte. The combined oxygen microelectrode have showed a fast response time (<2 seconds), stable reading with good calibration linearity ($R^2 = 1$), low residual current (6 pA), and a stirring effect of 4 % (Lu and Yu, 2002a). The mapping of the dissolved oxygen distribution in wastewater biofilms would require accurate dissolved oxygen measurements for long periods of time. The accuracy and

high stability of the combined oxygen microelectrode makes it very suitable for this kind of experiment.

3.0 MATERIALS AND METHODS

The general approach used to achieve the objective of this study was first to set up an automation system and construct the combined oxygen microelectrodes; then, obtain biofilm samples from a wastewater treatment plant and set up all the equipment with the biofilm sample in place; and finally, run the experiments.

3.1 AUTOMATION SYSTEM DEVELOPMENT.

The automation system consisted of three parts. A data acquisition system, a motion control system, and a computer program. In Figure 1, a schematic diagram with all the components and connections is presented.

The data acquisition system is the group of components used to collect, compute and store the data gathered from the oxygen microelectrode. The components of this system are the combined oxygen microelectrode, a picoammeter, and an analog-to-digital converter.

The motion control system is the group of components used to accurately position the microelectrode at any part of a biofilm sample. The main components of this system are a two-dimensional stage and a motorized micromanipulator. The motorized micromanipulator is a micromanipulator with a stepper motor.

The software is a computer program developed in LabVIEW® and used to automatically synchronize the data acquisition system and the motion control system through a computer. A complete description of the automation system is described in the

following sections.

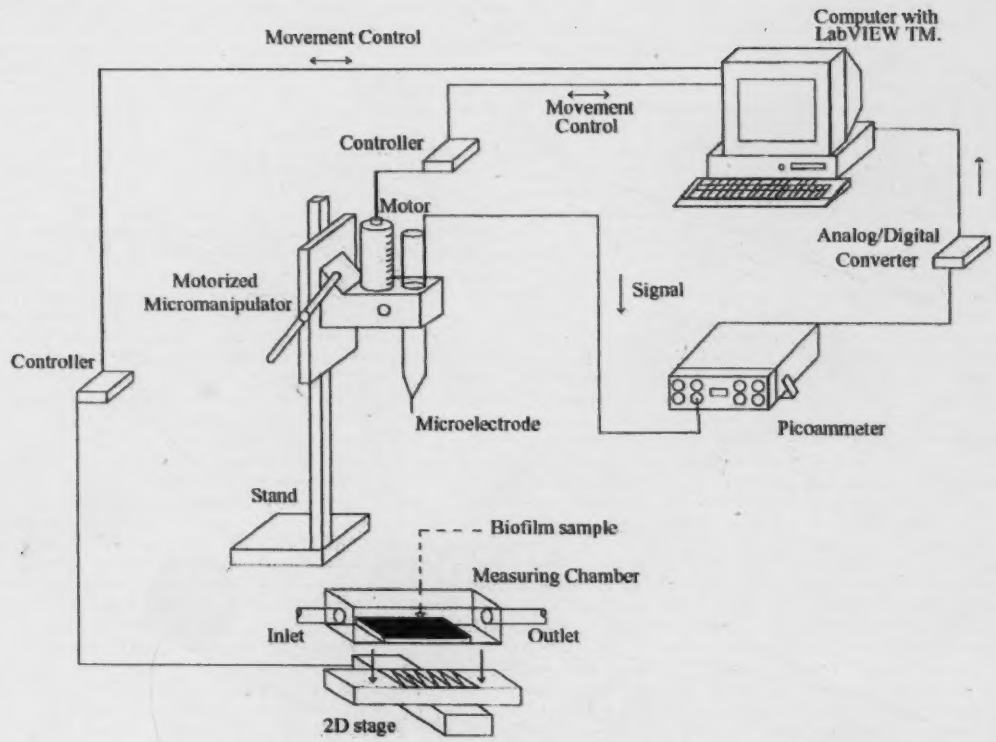

Figure 1. Components and connections of the automation system

3.1.1 THE DATA ACQUISITION SYSTEM.

As illustrated in Figure 1, the oxygen microelectrode was connected to a picoammeter (Unisense, Denmark, Model No. PA2000), the picoammeter was connected to an external analog-to-digital converter card (Pico Technology Ltd., Cambridgeshire, UK. Model ADC-101), and the analog-to-digital converter card was connected to a computer (Dell Model Inspiron 5000) using serial communication (LPT1 port).

In order to record data from the oxygen microelectrode into the computer, the analog signal produced by the oxygen microelectrode was converted to a digital signal. This signal process, which is represented in Figure 2, followed a series of steps. The oxygen microelectrode converted a chemical signal, proportional to the dissolved oxygen concentration in the biofilms, into an electrical signal (current), which is also an analog signal. That electrical signal was then transmitted to the picoammeter. Due to the small microelectrode tip, the resulting electrical signal is very small (in the order of pico-amperes) and needs to be amplified. The piccoammeter amplifies the current signal and converts it to voltage. Then, the output voltage signal from the picoammeter was sent to the analog-to-digital converter to be converted to a digital signal. The analog-to-digital converter constantly receives an input voltage signal from the picoammeter and generates a digital output code proportional to the input voltage signal. Finally, the digital signal from the analog-to-digital converter was sent to the computer where it can be recorded by the computer program developed in LabWIEW®. The analog-to-digital converter is a 12-bit converter. This means that it produces values from 0 to 4095 to represent the selected input voltage range.

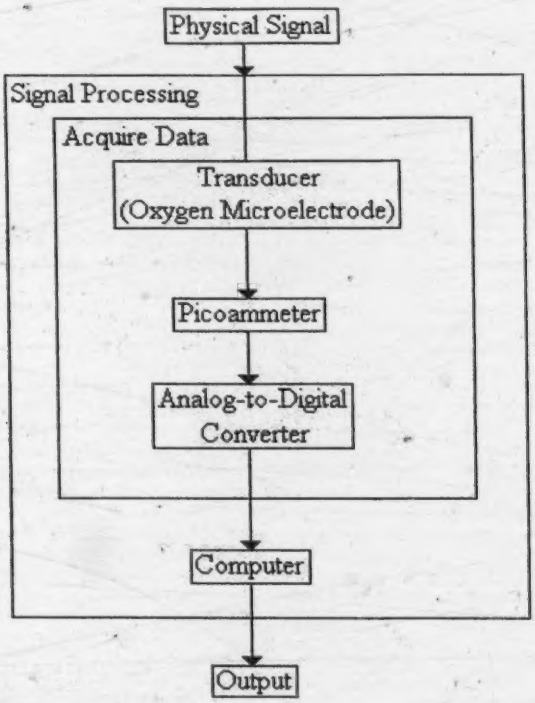

Figure 2. General diagram of the data acquisition system used to measure dissolved oxygen concentration in wastewater biofilms.

3.1.2 THE MOTION CONTROL SYSTEM.

The motion control system consisted of two basic components that allow the three-dimensional positioning of the microelectrode: a two-dimensional stage for horizontal control (Phytron Inc. Waltham, MA. USA. Model MT-65) and a motorized micromanipulator for vertical control (Unisense, Denmark, Model No. MM33M). The components and connections of the motion control system are shown in Figure 1. The two-dimensional stage consisted of two fixed one-dimensional stages with

stepper motors that allow the linear movement of two bases; the motors have the capability of moving the bases in two horizontal axes (X and Y) in a range of up to 50 mm with an accuracy of ± 8 μm, a bi-directional repeatability of ± 0.2 μm and a resolution of 0.3 μm. The motorized micromanipulator is a micromanipulator with a stepper motor. The motor can achieve vertical movements in a 100 mm range with a maximum resolution of up to 0.1 μm.

The motors of the two-dimensional stage and the motorized micromanipulator cannot be controlled directly by the computer software. There was the need for a device with digital-to-analog conversion functionality, which is a function similar to the analog-to-digital converter but in the opposite direction. The device that does this operation is called controller. The computer program sends a movement command in the form of a digital signal to the controller. The controller interprets this signal and sends an analog (electrical) signal to the motor, which finally moves. The two-dimensional stage was connected to a two-axes microstep-controller (Phytron Inc. Waltham, MA. USA. Model SMC basic 7160-9-010), which was connected to one of the serial ports (RS-232) of the computer. The motorized micromanipulator was also connected to a controller (Oriel Instruments, Stratford, CT., USA. Model 18011). This controller was also connected to one of the serial ports (RS-232) of the computer.

3.1.3 THE SOFTWARE.

The goal of the computer program was to synchronize the functionalities of the data acquisition system and the motion control system. The program has to be able to control the data acquisition system and the motion control system in a way that

three-dimensional movements and data acquisition tasks previously programmed could be completed.

LabVIEW® works under the principle of dataflow, in which functions execute only after receiving the necessary data. LabVIEW® programs are called "Virtual Instruments" (VIs), and the tasks they execute are analogous to the main programs, functions and subroutines from programming languages such as C or Basic.

A virtual instrument (VI) has three main parts:

- The "front panel". It is the interactive user interface. It simulates the front panel of a physical instrument. It contains the controls and indicators, which are used to introduce commands (inputs) and view the results (outputs) in the computer screen. Knobs, push buttons, and graphs represent the controls and indicators in the front panel.

- The "block diagram". It is the source code of the VIs. It is constructed in LabVIEW's graphical programming "G". The block diagram is formed by lower level VIs, built in functions, constants, and program execution control structures.

- The "icons" and "connectors". They are special structures that allow using a VI within another VI. When a VI is being used within another VI it is called "subVI". The icon is the pictorial representation of a VI and is used as an object in the block diagram of another VI. A connector is a mechanism used to define the inputs and outputs of a subVI (Travis, 2002f).

Virtual instruments are hierarchical and modular. Hierarchical means that the VI's can be used as top level programs or as subprograms (SubVIs), and modular means that VIs can be constructed to perform small tasks and then they can form part of a bigger VI that perform more complicated tasks.

The computer program development for this study consisted of two main parts. The first part was the construction of a front panel with a friendly user interface. This part contains all the controls and indicators needed to automatically synchronize the automation system. The front panel construction was aimed to provide the user with a logical and easy way to preset and conduct different microelectrode movement and data acquisition tasks with the automation system. The second part was the creation of the block diagram, which is the source code of the program. This part contains the algorithm used to synchronize the components of the automation system. The components of the front panel and the algorithm used are described in Appendix A.

3.2 OXYGEN MICROELECTRODE CONSTRUCTION.

An oxygen microelectrode is an electrochemical device whose normal function is based on the reduction of oxygen on the surface of its cathode (the working cathode). Connected with the negative pole of an applied external voltage, the cathode, which is made from an inert material such as platinum or gold, provides the oxygen molecule with electrons, hence makes it reduced on the surface of the cathode (Lu, 2001). The chemical reaction may be expressed by the following equation (Heineman, 1989):

$$O_2 + 2H_2O + 4e^- = 4OH^- \quad (1)$$

The above reaction may be separated into two steps:

$$O_2 + 2H_2O + 2e^- = H_2O_2 + 2OH^- \quad (2)$$

$$H_2O_2 + 2e^- = 2OH^- \quad (3)$$

The combined oxygen microelectrode, which is shown in Figure 3, consisted of a sensing electrode (the working cathode) made of platinum plated with gold; a reference electrode (the anode) made of silver/silver chloride (Ag/AgCl); a guard cathode made of silver; an oxygen permeable membrane; and an electrolyte solution.

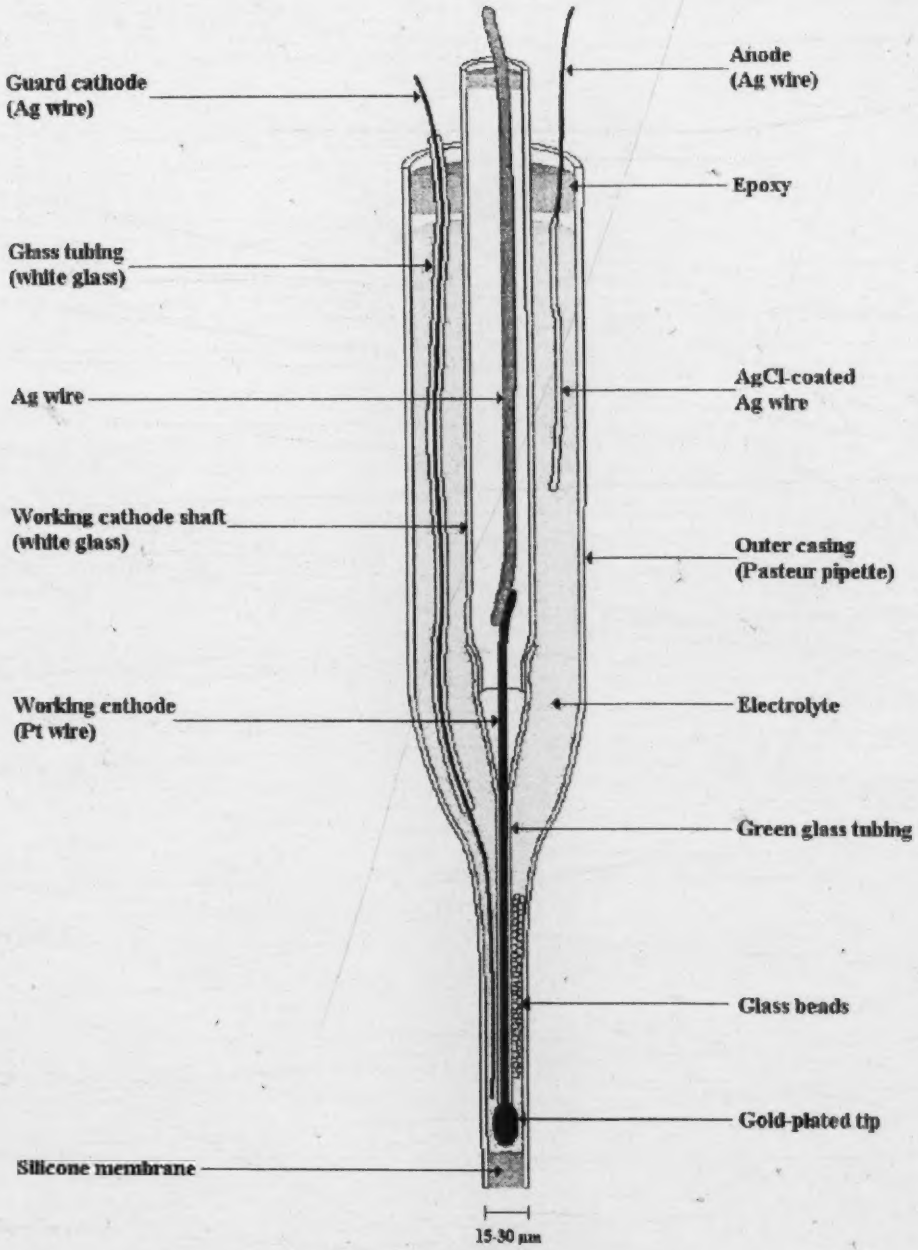

Figure 3. Schematic diagram of the combined oxygen microelectrode.

The combined oxygen microelectrodes used in this study were constructed following procedure reported by Lu and Yu (2002) which is based on the design by Revsbech (1989) with some modifications.

3.2.1 PREPARATION OF GLASS TUBING FOR THE WORKING CATHODE SHAFT.

Two types of glass tubing were used: white tubing (Schott Glass Export GmbH, Mainz, Germany; Schott 8350) and green tubing (Schott 8533). Glass tubing of 15 cm in length for both glasses types were cleaned with 0.1 M HCl, rinsed with deionized water and dried in oven at 103 °C. After being cooled down, the glass tubing of both glass types were heated, one at a time, at the middle section over a natural gas burner. When the middle section became soft, the glass tubing was taken out of the flame and simultaneously pulled by both hands until the middle section became around 2.5 mm in diameter for the white glass or a fine capillary for the green glass. These pulled glass tubes were then cut in the middle. Finally, the un-pulled end of the green glass tubing was cut off such that only about 2 cm of un-pulled tubing was left.

3.2.2 ETCHING OF THE WORKING CATHODE WIRE.

A long piece of platinum (Pt) wire (Aldrich Chem. Co., Milwaukee, WI, USA; Cat. No. 35,736-7) was cut in about 6 cm long pieces. A 60 mL transparent glass bottle with 1M alkakine KCN solution, three beakers with deionized water, and a power supply were placed in a well-ventilated fume hood. One of the electric poles of the power supply was connected to one end of a graphite rod and the other end of the

graphite rod was placed in the KCN solution. The other electric pole of the power supply was connected to one of the Pt wire pieces. Then, in the well-ventilated fume hood, the tip of the Pt wire (about 1 cm in length) was etched in the 1M KCN solution under 6-7 V voltage. The Pt wire was moved up and down slowly for several minutes. During this process, the tip of the Pt wire was checked several times under the microscope until the tip diameter was about 2 μm. Each time the tip diameter was checked under the microscope, the power supply was turned off and the Pt wire cleaned by being immersed, in each of the tree beakers of deionized water. Once the etched Pt wire tip reached a diameter of about 2 μm, the Pt wire was inserted into the green glass tube prepared before with the etched part in the capillary end and leaving about 2 mm of Pt wire outside the un-pulled end of the tube. The safety precautions contained in the Material Safety Data Sheet of KCN must be followed.

3.2.3 ASSEMBLY OF THE WORKING CATHODE.

The joint of the transparent and the green tubes were sealed together by melting both tubes using a butane burner (BernzOmatic, NY, USA; Micro Torch, Model No. ST1000TS). To do this the pulled end of the transparent glass prepared before was inserted into the un-pulled end of the green glass tube. During this process the Pt wire in the green tube has to be introduced into the transparent tube. The joint of both tubes was exposed to the fine flame of the burner until the green glass turned soft and red. Then the tubes were taken out of the flame and pulled a little to ensure the joint was sealed. The assembled working cathode shaft was fixed in a one-hole rubber cork and inserted into a test tube for storage and to avoid any damage to the cathode.

3.2.4 TAPERING OF THE WORKING CATHODE TIP.

The following set up was prepared before starting the tapering process: an adjustable stand with a micromanipulator (World Precision Instruments, Inc., Sarasota FL, USA; Model M3301R) fixed on it; an extension clamp stand which holds a porcelain socket with a W-shaped platinum wire used as a heating loop; a power supply connected to the heating loop; a (200 ml) beaker with tissue paper on the bottom and on the walls; and a horizontal microscope (Carl Zeiss, Jena, Germany; Model: Stemi SV11).

The capillary end of the cathode shaft was hung from the micromanipulator using a small clip. The capillary part of the cathode shaft was placed into the W-shaped part of the heating loop. Using the micromanipulator and the microscope the Pt wire tip was placed about 1.5-2.0 cm above the heating loop. The heating loop was heated gradually by increasing the voltage of the power supply. The glass started melting and the cathode started falling down slowly. When the Pt wire tip was about 0.5-1 cm above the heating loop, the voltage was quickly increased (doubled) in order to make the glass less viscous and have a better coating of the Pt wire. Finally, the whole cathode shaft fell into the beaker that contained tissue paper. The finished cathode shaft was placed in a one-hole rubber stopper and inserted into a test tube for storage and protection.

3.2.5 GOLD PLATING OF THE CATHODE TIP.

This step was completed using the following equipment and material: a vertical microscope (Carl Zeiss, Model: Axioskop 2 Plus); a micromanipulator; and a battery (1.5 V) connected in series to an adjustable resistor (Duncan Electronics Inc., California,

USA; Model3253, 0-200 ?), a piece of Ag wire (Aldrich Chem. Co., Milwaukee, WI, USA), and a Pasteur pipette with a piece of Pt wire inside.

The cathode shaft was fixed on the microscope and one end of the Silver wire (which was connected to the battery) was introduced into the cathode making sure that the Ag wire was touching the etched Pt wire. The tip of the Pasteur pipette was introduced into a 0.1 M $AuCl_3$ (Fisher Scientific, catalog number G54-1; $HAuCl_4 \cdot 3H_2O$) solution. Some of the solution was sucked by capillarity into the Pasteur pipette. It is important to make sure that the Pt wire that is inside the Pasteur pipette is touching the $AuCl_3$ solution. Then the Pasteur pipette was fastened in the micromanipulator and placed under the microscope in front of the cathode shaft. Under the microscope, the glass coating over the tip of the cathode was removed by breaking it using a micro-dissecting tweezers (Roboz Surgical Instrument Co., Inc., Rockville, MD, USA; Cat. No. RS-4905). The naked part of the cathode was introduced into the pipette containing the $AuCl_3$ solution and stayed there for a few seconds under a voltage of about 0.8 V. The result of the plating process was a layer of electro-plated gold on the naked cathode tip. Finally, the gold-plated cathode was stored using a one-hole rubber stopper and a test tube.

3.2.6 THE OUTER CASING.

It is necessary to prepare the same set up as the one described before in the "tapering of the working cathode tip" section. In addition, a small heating loop made of 0.1 mm Pt wire (Aldrich Chem. Co., Milwaukee, WI, USA; Cat. No. 35,736-7) connected

to a power supply was used.

First, the fine section (specific location dependent on the ultimate length of the microelectrode) of a clean Pasteur pipette was heated over the natural gas burner and then pulled by hands until a diameter of about 0.5 mm was obtained. Then, the pulled pipette was hung with its fine end clipped in the micromanipulator and its pulled part placed in the W-shaped heating loop. The pipette was heated by gradually turning up the power supplier until the glass started melting. As the pipette started dropping, it was moved upwards slowly so as to obtain a suitable length and diameter of the casing tip. The casing dropped into the beaker underneath, with tissue paper on its bottom. The ultimate diameter of the casing tip was determined according to the tip size of the gold-plated cathode at the following assembly stage. Finally the outer case was stored using a one-hole rubber stopper and a test tube.

3.2.7 GUARD CATHODE.

A piece of white glass tubing was heated over the natural gas burner and pulled until an inner diameter a little bigger than the 0.127 mm diameter of the Ag wire (Aldrich Chem. Co., Milwaukee, WI, USA; Cat. No. 26,555-1) was obtained. The capillary section of the tube was cut in small pieces of 7-8 cm long. A piece of the Ag wire with a length of about 20 cm was inserted into the capillary with its two ends extending out of the capilarlly. One end of the capillary was sealed with epoxy (Mastercraft Canada, Toronto; 5 minute Epoxy, Resin and Hardener) and then was dried in the air. Afterwards, in the fume hood, the tip (about 1 cm in length) of the sealed Ag wire was etched in 0.5 M alkaline KCN solution under 3-4 V voltage until a diameter around 1-5 μm

was obtained. The procedure and the safety precautions of the etching process were the same as the ones used for the etching of the Pt wire.

3.2.8 Ag/AgCl REFERENCE ELECTRODE.

In this step, part of an Ag wire was electrochemically treated to produce an Ag wire with an AgCl cover. A piece of Ag wire (0.25 mm in diameter) was connected to the negative pole of a 1.5 V AA battery and a 9 cm piece of Ag wire (diameter: 0.25 mm) was connected to the positive pole of the same battery. About 3-4 cm of both wires were immersed in 1N HCl solution for about 2 minutes. The Ag wire connected to the positive pole turned brown, which is the color of AgCl. The AgCl-covered Ag wire was rinsed with deionized water and stored in a container.

3.2.9 ASSEMBLY OF THE OXYGEN MICROELECTRODE.

The outer casing was fixed on the microscope stage. The cathode was cleaned with ethanol and inserted into the outer case. The cathode was pushed toward the tip of the outer case by using the micromanipulator with a fixed Pasteur pipette until the cathode tip was 30- 50 µm from the outer casing tip. If the distance was too long then the outer casing tip was cut using micro-dissecting tweezers. To have a better control when cutting the outer casing a tip-closed Pasteur pipette mounted in a micromanipulator can be used to bump and cut the outer casing tip. Once the cathode was at the desired position it was fastened on the stage of the microscope using the microscope clip. The guard cathode was inserted in the outer casing and its tip positioned just behind the cathode's tip. The reference electrode was inserted into the outer casing so that its brown

part was kept within the outer casing. A small amount of Epoxy was applied to the three components just enough to fix them together and making sure that an open space was left for the future addition of the electrolyte and glass beads. The closed tip of a Pasteur pipette was covered with silicon (Dow Corning Co., MI, USA; Silastic Medical Adhensive, Type A, Content sterile) and the pipette was mounted in a micromanipulator. The micromanipulator was placed under the microscope so that the pipette tip containing silicon was facing the outer casing tip. The outer casing tip and the Pasteur pipette tip were placed in a way that both of them were being observed under the microscope. Then the outer casing tip was moved towards the pipette and dipped it in the silicon to obtain a 10-20 μm length of membrane within the outer casing tip. After 45 minutes pre-dry, the half finished microelectrode was fixed in a one-hole rubber stopper and stored in a test tube overnight to dry the Epoxy and the silicone membrane in the air. A piece of Ag wire was inserted into the working cathode shaft and the end of the working cathode shaft was sealed with Epoxy. Afterwards, a little electrolyte was injected into the assembled outer casing, using 1 mL syringe (Becton Dicson & Co., Franklin Lakes, NJ, USA; Catalog No. 309597). The electrolyte is a mixture of 0.2 M $KHCO_3$ (50 ml); 0.3 M K_2CO_3 (50 ml); 1 M KCl (100 ml) and some thymol crystals. The outer casing was checked under the microscope to see if there were any bubbles. If there was any bubble the tip was immersed in degassed water to eliminate the bubbles. The degassed water can be obtained by boiling water for ten minutes and cooling it fast before the tip is immersed. After the bubbles were eliminated, a very small amount of glass beads (3M Empore, St. Paul, MN, USA; Filter Aid 400; Diameter: 20-40 μm) was added into the outer casing and more electrolyte solution was injected until the outer casing was full.

Finally, Epoxy was applied to completely seal the outer casing and then was dried in the air.

3.2.10 POLARIZATION AND CALIBRATION OF THE OXYGEN MICROELECTRODE.

The proportionality between current signal and oxygen partial pressure in a sample is valid only when oxygen reduction rate on the working electrode surface is oxygen-diffusion-limited from outside of the membrane. Therefore, pre-existing dissolved oxygen in the electrolyte should be consumed first and a limiting current should be obtained through the polarization. During polarization, an external voltage of – 0.8 V is applied to the cathode. This will provide the gold tip of the microelectrode with the voltage necessary to reach a limiting current. When a limiting current is obtained, the reaction rate of the oxygen reduction occurs fast and there is little or not oxygen accumulation on the cathode surface. This will ensure that the oxygen reduction rate on the working electrode surface is oxygen-diffusion-limited from outside of the membrane.

A calibration factor for a specific oxygen microelectrode is unique. This is because some characteristics of the oxygen microelctrode such as the cathode tip surface area and the membrane thickness vary from one microelectrode to another. Consequently, to establish the linear relationship between the current signal and oxygen partial pressure, the calibration factor was determined for each of the oxygen microelectrodes used in this study.

In the laboratory, the polarization and calibration of the oxygen microelectrode

were conducted with a picoammeter (Unisense, Denmark, Model No. PA2000). Before starting the polarization, the polarization voltage was adjusted to –0.8 V on the picoammeter. This is the potential that is needed between the working cathode and the Ag/AgCl anode. The oxygen microelectrode was connected to the picoammeter and secured in a calibration chamber, with its tip immersed in deionized water. The calibration chamber was made of plexiglass with a volume of 500 ml. When the polarization is initiated, the current signal can be very high (e.g. 2.5 nA) and then it drops very quickly in the first few minutes. The whole polarization process lasted overnight and a stable current readout was then achieved.

After the polarization, the next step was the calibration process. The calibration factor was determined by measuring the current signals for two standard waters with known oxygen partial pressure or concentrations. One of the standard waters was oxygen-free (0 % oxygen) and the other air-saturated (21 % oxygen).

In the laboratory, the calibration chamber was filled with the same filtered wastewater used for the experiments. The oxygen microelectrode was secured in the calibration chamber with its tip immersed in the wastewater. The picoammeter was connected to the analog-to-digital converter and the analog-to-digital converter was connected to the computer. In the computer, the software of the automation system was loaded and the "CALIBRATION CURVE" window, which is shown in Figure A5, was opened. The program was set to take one reading from the analog-to-digital converter output signal every 10 seconds and then the program was started. First, compressed air (21 % oxygen) was flushed vigorously into the wastewater through a gas

dispersion tube. Afterwards, nitrogen gas (0 % oxygen) was flushed vigorously into the wastewater. As a result, a two-point calibration curve was constructed, and then, the real measurements were interpolated based on this calibration curve. The calibration factor is the slope of the calibration curve. The oxygen microelectrodes were calibrated at the beginning and at the end of each experiment.

3.3 EXPERIMENTS.

The biofilm samples for this study were taken from a municipal wastewater treatment plant situated in the Town of Devon in Alberta, Canada. The treatment plant uses an RBC system with four stages. The treatment plant uses the RBC system as a secondary treatment to remove carbonaceous BOD. During the months from September to October 2002, when the experiments were conducted, the plant received a municipal wastewater influent with an average of 230 mg/L of BOD, and produced an effluent with an average of 4.8 mg/L of BOD. The average removal percentage during these months was 97.7 %. There is a picture of this RBC system in Figure 4. The wastewater flows from the first stage, showed in the background on the right side of the picture, to the fourth stage, showed in the foreground on the left side of the picture. The RBC system is made of a series of closely spaced disks partially immersed in a tank through which wastewater flows. Its biological principle is based on the development of thick and complex biofilms on the disk surfaces (Martin-Cereceda *et al.*, 2002). The main characteristics of the RBC system are described in Table 1.

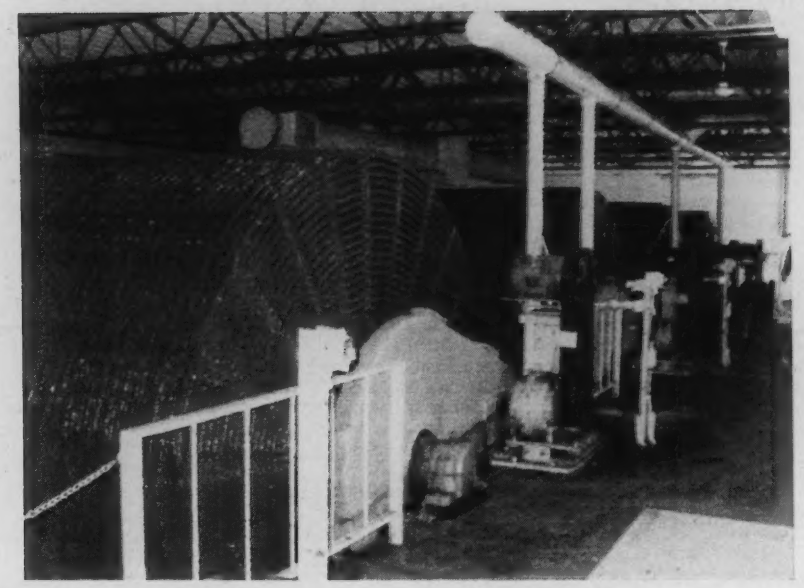

Figure 4. The RBC system in the wastewater treatment plant at Devon in Alberta, Canada.

Table 1. Major characteristics of the RBC system in the wastewater treatment plant at Devon (Lu and Yu, 2002b).

Characteristics	Stage 1	Stage 2	Stage 3	Stage 4
Disc Diameter (m)	3.7	3.7	3.7	3.7
Length of Trough (m)	7.9	7.9	7.9	7.9
Width of trough (m)	4.3	4.3	4.3	4.3
Water depth in trough (m)	1.5	1.5	1.5	1.5
Disc submertion ratio (%)	40	40	40	40
Disc effective area (m2/stg)	9290	9290	9290	9290
Effective trough volume (m3/stg)	50.9	50.9	50.9	50.9
Disc material	HDPE*	HDPE*	HDPE*	HDPE*
Rotational speed (r/min)	1.7	1.7	1.5	1.5

*HDPE: High Density Polyethylene

One biofilm sample from each stage of the RBC system was collected to obtain the three-dimensional dissolved oxygen distribution. The biofilm sample collected from the first stage was called biofilm sample 1, the biofilm sample collected from the second stage was called biofilm sample 2, and so on. The data was processed using Ecxel® and the maps were plotted using LabVIEW®.

Due to the highly heterogeneous nature of biofilms, the biofilm samples in this experiment are considered replicate samples. They were not measured to show differences between the four biofilm samples but to show the dissolved oxygen distribution in samples taken from each of the four RBC disks of the wastewater treatment plant. Previous studies have indicated that there are as much variation between dissolved oxygen measurements carried out on the same RBC disk than in dissolved oxygen measurements carried out on different RBC disks (Lu, 2001).

The biofilm samples were grown on coupons that were fixed on the RBC disks in the wastewater treatment plant. The coupons were made of HDPE, which is the same material the RBC disks are made of. Seven coupons of 2 cm × 5 cm were screwed to a 6 cm × 40 cm acrylic stripe using stainless steel screws. The acrylic stripe was then fixed in the RBC disk as shown in Figure 5. Two stripes, each with seven coupons, were fixed on each of the four stages for 6 weeks until there were biofilms of about 1.5 mm in thickness.

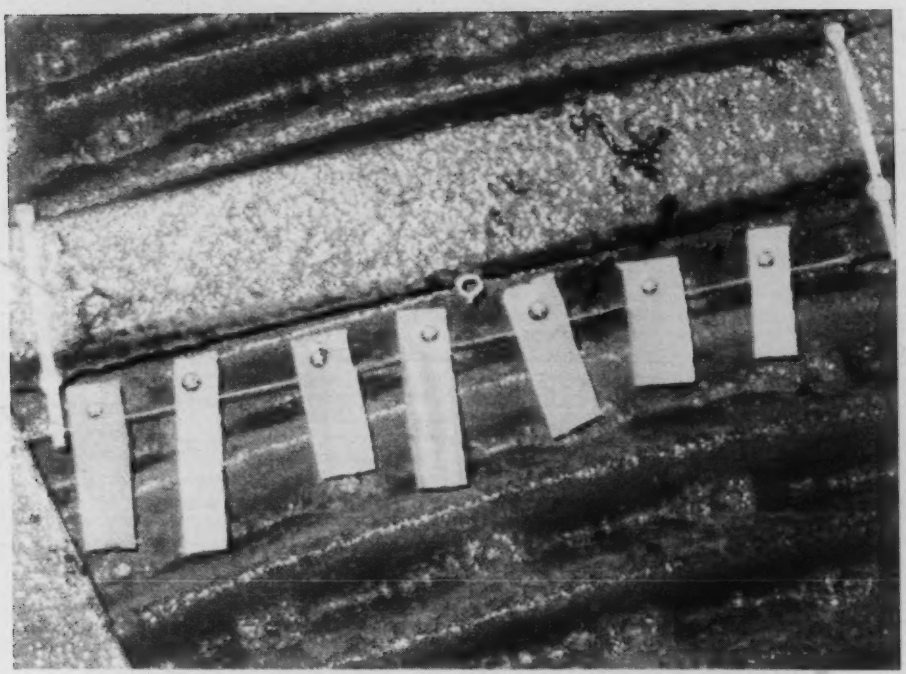

Figure 5. Coupons on a RBC disk for growing biofilm samples.

A measuring chamber was constructed using acrylic materials. The main purpose of the measuring chamber was the placement of the biofilm sample and the alternate exposure of the biofilm to wastewater during the measurement period. The measuring chamber is divided into three compartments and can be filled with wastewater from the inlet and drained from the outlets. It can also be fixed to the two-dimensional stage of the automation system. Figure 6 shows a picture of the measuring chamber. It has a length of 5.5 cm, a width of 3.5 cm, and a height of 4.0 cm. The three compartments are labeled as a, b and c in the picture. The first and the second compartments (a and b) were divided by a wall (d), which has a height of 2.5 cm. The second and the third compartments (b and c) were also divided by a wall (e), which has a height of 2.0 cm. The first

compartment (a) has an inlet tube (f) with an internal diameter of 3.0 mm and is connected to the wall of the measuring chamber as shown in the figure. The second compartment (b) of the measuring chamber has a removable base made of Plexiglas (g) upon which the biofilm sample is placed, and an outlet tube (h) with an internal diameter of 6.0 mm that is connected on the lateral wall of the measuring chamber as shown in the figure. The third compartment (c) has an outlet tube (i) with an internal diameter of 6.0 mm and is connected to the wall of the measuring chamber as shown in the figure. All the tubing has clamps (j1, j2 and j3) (Fisher Scientific, Canada, Edmonton. Catalog number 05-869) to control the flowrate.

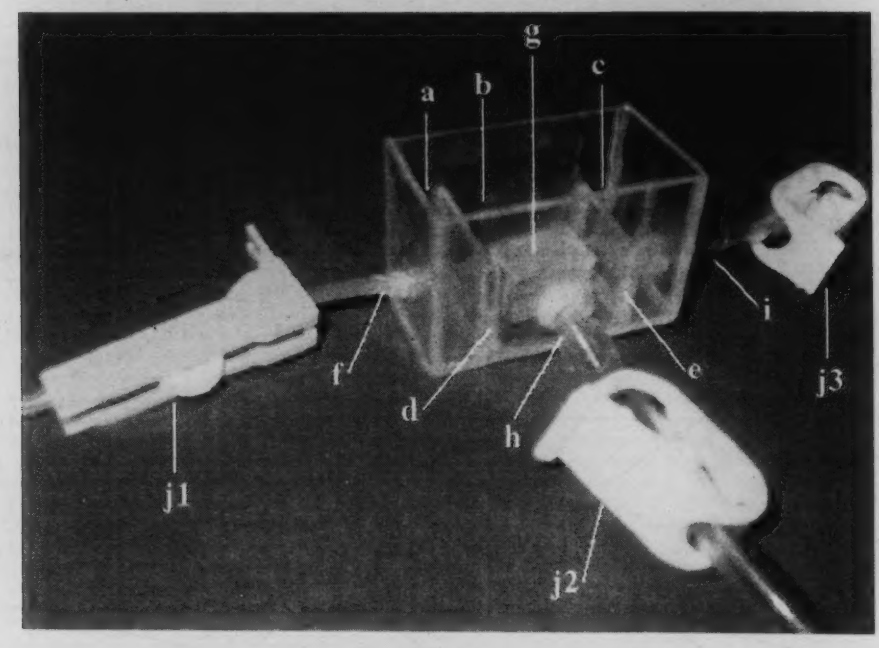

Figure 6. The measuring chamber: (a) first compartment, (b) second compartment, (c) third compartment, (d) fixed wall dividing the first and second compartments, (e) fixed wall dividing the second and third compartments, (f)

inlet tubing connected to the first compartment, (g) removable base used to place the biofilm sample, (h) outlet tubing from the second compartment, (i) outlet tubing from the third compartment, and (j1, j2, j3) clamps to control the flowrate.

Before each experiment was started all the necessary equipment was set up preperly. The components of the automation system were connected as shown in Figure 1. The measuring chamber was fixed on the two-dimensional stage and all its clamps were closed. A horizontal microscope (Carl Zeiss, Jena, Germany; Model: Stemi SV11) was placed close to the measuring chamber. A container filled with two liters of filtered wastewater was placed in a stand above the level of the measuring chamber. The container was connected to the inlet tube of the measuring chamber. The purpose of the container was to supply the measuring chamber with wastewater during the experiment. The container was placed above the level of the measuring chamber in order to generate a water flow from the container through the measuring chamber driven by gravity.

To run one experiment, one or two coupons were taken off fom the acrylic strip. Six liters of wastewater from the wastewater treatment plant were collected and taken to the laboratory together with the sample. The samples were transported in a cooler with wet sponges to keep the humidity high and the temperature constant. This measure kept the biofilm samples from desiccation during transportation. Once in the laboratory the biofilm sample was measured immediately.

In the laboratory, the wastewater was filtered with a paper filter (Whatman model 1002185). A portion of the filtered wastewater was transferred to the two-liter container connected to the flow chamber and 500 mL of the filtered wastewater were transferred to the calibration chamber. The wastewater in the two-liter container was aerated using compressed air. Then, the microelectrode was calibrated following the calibration

procedure described in the polarization and calibration section.

One of the coupons was taken out of the cooler using a small dissecting tweezers. The surface of the coupon that was in touch with the sponges was cleaned with an absorbent paper. The coupon with the biofilm was cut in a piece of 1 × 1 cm and the piece was placed on the removable base of the measuring chamber using a double-sided tape. The removable base with the sample was placed in the second compartment of the measuring chamber using the tweezers. The removable base and the biofilm sample were fixed to the measuring chamber using specially designed clips. The first and second compartments of the measuring chamber were filled with wastewater from the two-liter container. The oxygen microelectrode was fastened on the motorized micromanipulator and its tip was set manually at about 1000 μm above the biofilm surface. The area formed by the 10 × 10 array 80 μm below this position, which is about 920 μm above the biofilm surface, was named the artificial plane in this study.

The computer program of the automation system was preset to measure 100 profiles in a 10 × 10 array. The distance required between each profile was 100 μm. In order to execute each profile measurement, the motorized micromanipulator had to move down a total of 1600 μm, stopping every 80 μm to collect two readings from the analog-to-digital converter output. This means that the motorized micromanipulator had to move twenty "steps" down (80 μm each step) to cover the 1600 μm required (in this computer program a "step" is a movement of a preset distance). When the twenty steps down were completed, then the micromanipulator had to move up 1600 μm to its original position in

one single step. Then, the two-dimensional stage had to move 100 μm to the next position, where the new profile measurement had to be executed.

The program was run and the automation system started the profile measurements in series of rows until the preset array of profile measurements (10 × 10) was completed. During the experiment, the biofilm sample was alternately exposed to air and wastewater. The profile measurements were taken by the automation system when the biofilm sample was exposed to wastewater. The reason for the alternate exposure of the biofilm sample to wastewater and air was to simulate the real conditions present in an RBC system. A RBC system rotates continuously under normal operation. The rotation alternately exposes the biofilm to air and water constantly.

In order to accomplish the alternate exposure of the biofilm sample to wastewater and air, a procedure involving draining and filling the different compartments of the measuring chamber with wastewater was carried out before the automation system started each profile. The procedure can be explained using Figure 6 as a model. The wastewater was drained from the second compartment (b) of the measuring chamber by opening the clamp (j2) on that section. When the wastewater was drained the clamp (j2) was closed again. This operation exposed the biofilm to air. The inlet clamp (j1) was opened and the wastewater entered the chamber until the three compartments of the measuring chamber (a, b and c) were filled. Once the three compartments of the measuring chamber were filled with wastewater, the clamp (f) of the first compartment was closed again. Using the microscope and the manual gauge on the motorized micromanipulator the microelectrode was moved down to measure the distance between the artificial

plane and the biofilm surface, then the microelectrode was moved back to its original position 80 μm above the artificial plane. The wastewater was then drained from the third compartment (c) of the measuring chamber by opening the clamp (j3) in that compartment. This operation drained the wastewater from the third compartment but it kept the water in the second compartment (b) of the chamber always at the same level during each profile measurement. Then the software executed the corresponding profile measurement. This operation was repeated before every new profile measurement was started.

4.0 EXPERIMENTAL RESULTS AND DISCUSSIONS

The experimental results will be described and analyzed in this section. First, the components and performance of the tools used for the three-dimensional mapping of the dissolved oxygen distribution in wastewater biofilms will be analyzed. These tools are the automation system and the combined oxygen microelectrodes. Then, the experimental results of the dissolved oxygen distribution in the biofilm samples studied will be analyzed.

4.1 AUTOMATION SYSTEM.

The automation system developed made it possible to map the three-dimensional dissolved oxygen distribution in wastewater biofilms using combined oxygen microelectrodes. The data acquisition system allowed the acquisition and storage of a total of 4000 measurements from the combined oxygen microelectrode for each biofilm sample. The motion control system allowed the precise positioning of the combined oxygen microelectrode in order to measure 100 dissolved oxygen profiles in a 1000 μm $\times$ 1000 μm biofilm area.

The computer program used to automate the data acquisition system and the motion control system functioned properly during the experiments, controlling the tasks that the data acquisition and the motion control systems had to execute. This means that the algorithm used to develop the program was adequate. The computer program was easy to use. The controls and indicators of the program were well organized in a logic way, so that the user can easily program the automation system to execute complicated

tasks involving data collection and positioning of the oxygen microelectrode in three dimensions.

4.2 THE OXYGEN MICROELECTRODES.

The calibration curves of the oxygen microelectrodes used to interpolate the dissolved oxygen readings obtained from the biofilm samples are shown in Figure 7, Figure 8, Figure 9 and Figure 10. The two-point (0 % and 21 % oxygen) calibration curves indicate that the fabrication procedure of the combined oxygen microelectrode was effective. Three-point calibration curves (0 %, 10.5 % and 21 % of oxygen) have been constructed for this type of microelectrodes. Linear regression in these curves produce $R^2 = 1$. In previous studies involving the fabrication of separate and combined oxygen microelectrodes, the authors have stated that excellent calibration curves are relatively easy to obtain for most oxygen microelectrodes and the two-point calibration curve is sufficient for normal sample measurements (Lu, 2001; Yu, 2000).

The tip diameters of the microelectrodes constructed were between 15 and 30 μm. As mentioned before, each microelectrode completed 100 profile measurements, and a total of 4000 dissolved oxygen measurements were taken from each of the biofilm samples. Each microelectrode worked properly during the whole experiment. This showed that the combined oxygen microelectrode is an affective tool for studies where large numbers of dissolved oxygen measurements are needed, such as determining the three-dimensional dissolved oxygen distribution in wastewater biofilms.

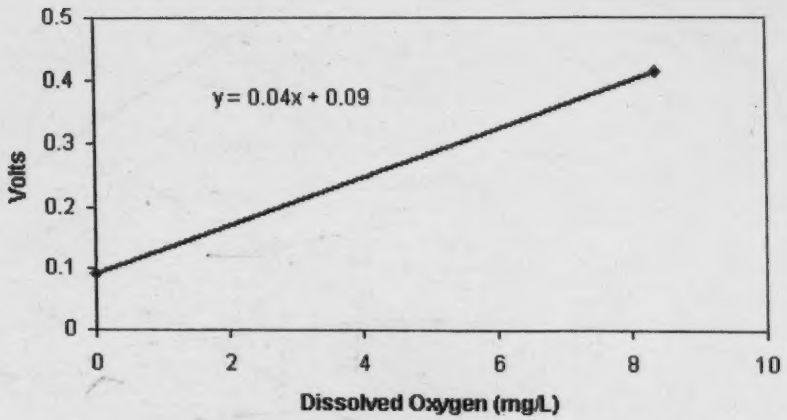

Figure 7. Calibration curve of the oxygen microelectrode used for the measurement of biofilm sample 1.

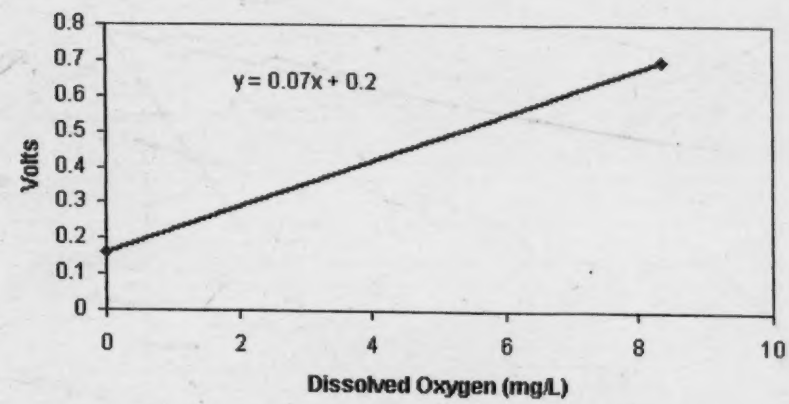

Figure 8. Calibration curve of the oxygen microelectrode used for the measurement of biofilm sample 2.

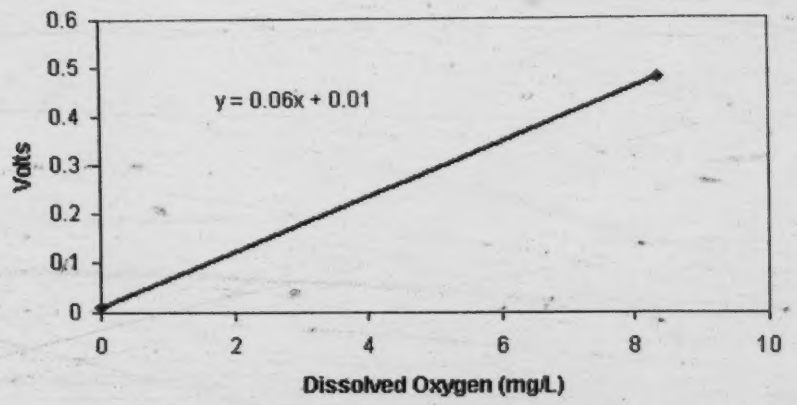

Figure 9. Calibration curve of the oxygen microelectrode used for the measurement of biofilm sample 3.

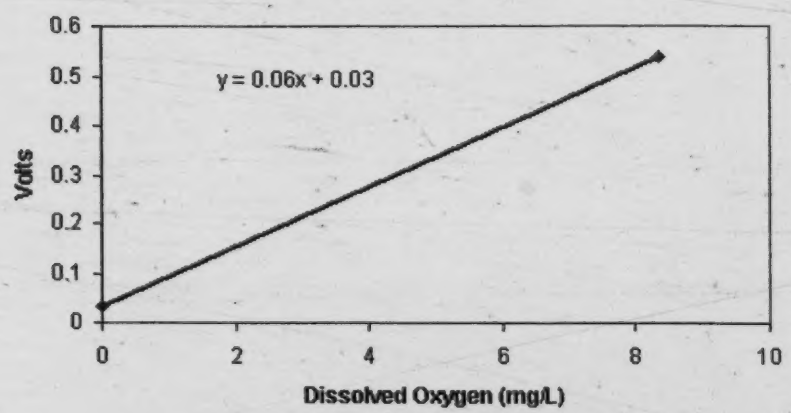

Figure 10. Calibration curve of the oxygen microelectrode used for the measurement of biofilm sample 4.

4.3 THE DISSOLVED OXYGEN DISTRIBUTION.

The experimental results yielded three-dimensional maps of the dissolved oxygen distribution in the biofilm samples studied. In order to facilitate their presentation, the experimental results will be described first in the form of individual profiles. Then, the

individual profiles will be arranged to describe the three-dimensional profiles of dissolved oxygen concentration from the artificial plane down to the biofilm. The biofilm surface is not a flat structure; therefore, setting the artificial plane as reference is not enough to determine the dissolved oxygen concentration at exact locations inside or above the biofilm surface. In order to solve this problem the physical structure of the biofilm surface will be constructed. Once the physical biofilm surface is identified it will be possible to determine the dissolved oxygen distribution at the biofilm surface, inside the biofilm, and above the biofilm in the water layer. All these characteristics will be described in the following sections.

As mentioned in the materials and methods section, one sample was taken from each of the four stages of the RBC system for measurement. The sample collected from the first stage, where the wastewater first entered the RBC system, was called biofilm sample 1. The sample collected from the second stage, third stage, and fourth stage was called biofilm sample 2, biofilm sample 3, and biofilm sample 4, respectively. Due to the highly heterogeneous nature of biofilms, the biofilm samples in this experiment are considered replicate samples. They were not measured to show differences between the four biofilm samples but to show the dissolved oxygen distribution in samples taken from each of the four RBC disks of the wastewater treatment plant.

4.3.1 THE INDIVIDUAL PROFILES.

The number of dissolved oxygen profiles measured in an area of 1000 μm $\times$ 1000 μm was 100. One of these profiles, from each RBC stage, was chosen as an example to

describe how each profile measurement that forms part of the three-dimensional maps was constructed.

The dissolved oxygen of the profile measurement from biofilm sample 1, which is shown in Figure 11, started with a concentration of 7.4 mg/L, and decreased gradually until it reached zero at about 40 μm below the biofilm surface. The thickness of the biofilm sample 1 at this specific location was 754 μm. The profile measurement from biofilm sample 2, which is shown in Figure 12, started with a dissolved oxygen concentration of 7.4 mg/L that decreased to total depletion at 320 μm below the biofilm surface. The thickness of the biofilm sample 2 at this point was 1472 μm. The dissolved oxygen concentration of the profile measurements from biofilm sample 3 and biofilm sample 4, which are shown in Figure 13 and Figure 14, respectively, presented similar trends. They are clear examples of how the typical one-dimensional dissolved oxygen profile measurements, reported by several authors, are constructed (Bishop and Yu, 1999; Bishop *et al.*, 1995; Fu *et al.*, 1994; Rasmussen and Lewandowski, 1998a; Wasche *et al.*, 2000; Zhang and Bishop, 1994b; Zhang *et al.*, 1995).

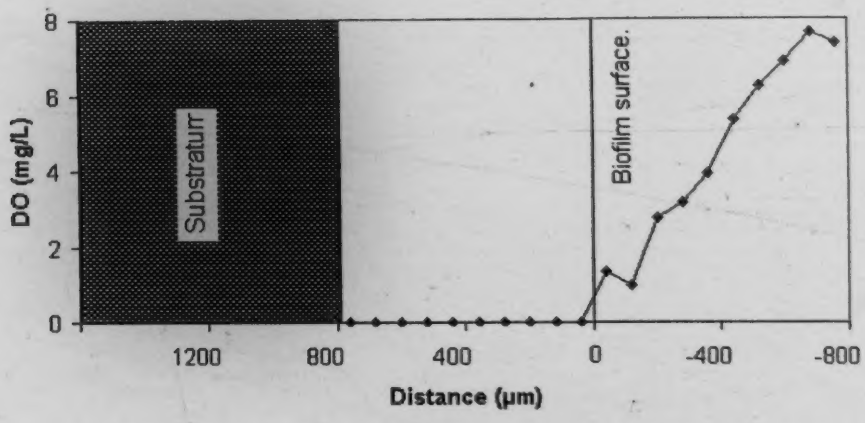

Figure 11. The dissolved oxygen profile of biofilm sample 1.

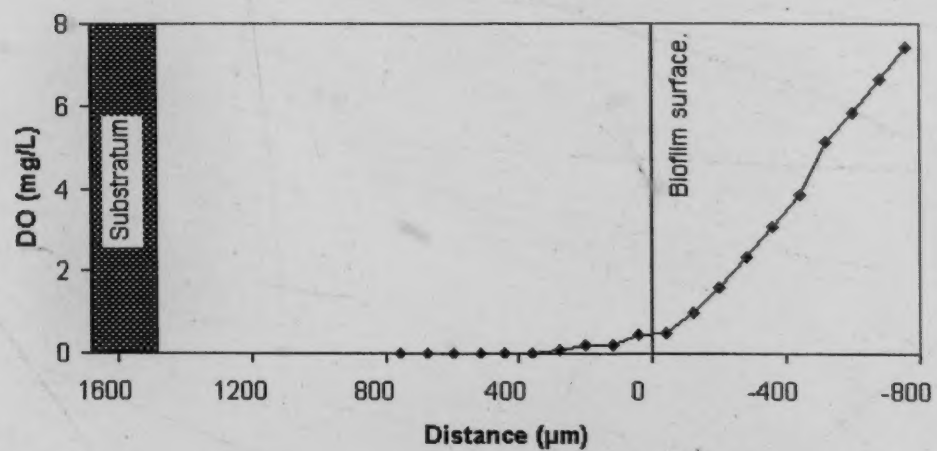

Figure 12. The dissolved oxygen profile of biofilm sample 2.

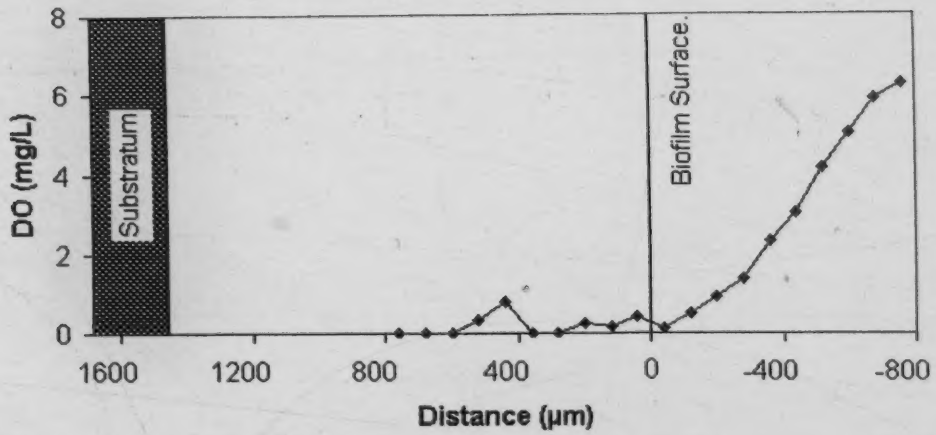

Figure 13. The dissolved oxygen profile of biofilm sample 3.

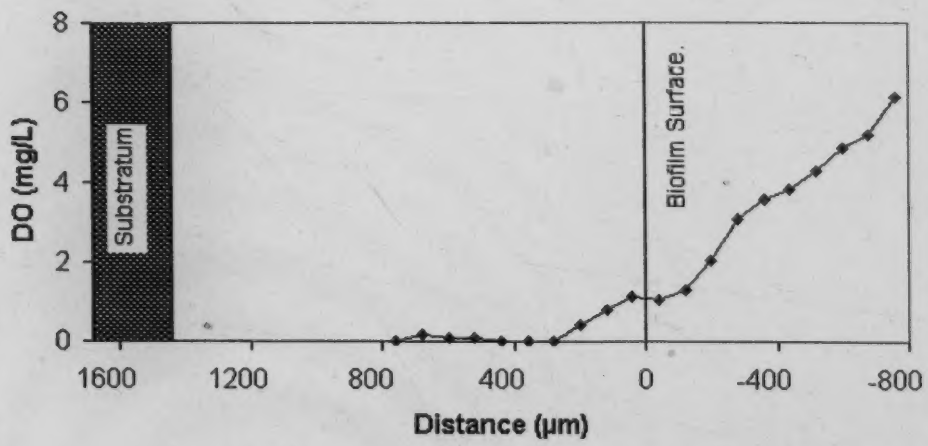

Figure 14. The dissolved oxygen profile of biofilm sample 4.

4.3.2 DISSOLVED OXYGEN DISTRIBUTION FROM THE ARTIFICIAL PLANE.

In this section, all the one-dimensional dissolved oxygen profiles are plotted together to show the dissolved oxygen distribution in three dimensions, and

form new "three-dimensional profiles". In order to do this, all the first measurements of each profile measurement were aligned in one single plane. This plane, named the artificial plane, is about 920 μm above the biofilm surface. The other measurements were aligned in subsequent planes parallel to the artificial plane according to the respective depth at which they were taken. This means that the three-dimensional profiles presented in this section show the dissolved oxygen distribution in two horizontal axes (X and Y) at different depths. Each depth is parallel to the artificial plane, not to the biofilm surface. The three-dimensional profiles give information of the dissolved oxygen distribution above the biofilms and inside the biofilms. To simplify the presentation of the results, only four depths of each biofilm sample are shown in this section. These depths are 0 μm (or the artificial plane), 320 μm, 720 μm, and 1120 μm below the artificial plane. These depths represent the general trend of the dissolved oxygen distribution in the samples. The entire three-dimensional profiles, which include 20 different depths, can be found in Appendix B.

The plots of the three-dimensional dissolved oxygen distribution measured from biofilm sample 1 can be seen in Figure 15, Figure 16, Figure 17, and Figure 18. In Figure 15, it can be seen that 72 % of the dissolved oxygen concentration measured at the artificial plane was in a range from 6.5 to 8.2 mg/L. Figure 16 shows that 320 μm below the artificial plane 74 % of the measured dissolved oxygen concentration decreased to a range from 4.4 to 6.1 mg/L. At 720 μm below the artificial plane, as shown in Figure 17, 81 % of the measured dissolved oxygen concentration decreased to a range from 0.1 to 1.6 mg/L and 1120 μm below the artificial plane, 84 % of the measured dissolved oxygen

concentration decreased to a range from 0 to 0.1 mg/L. This can be observed in Figure 18.

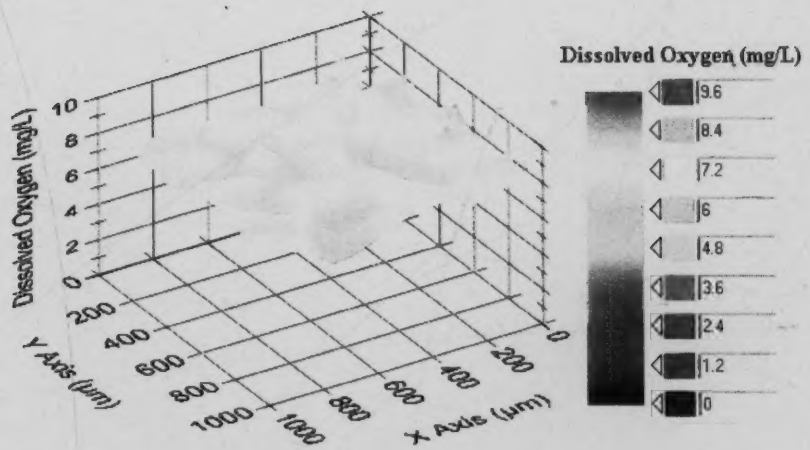

Figure 15. Dissolved oxygen concentration at the artificial plane in biofilm sample 1, about 920 µm above the biofilm surface.

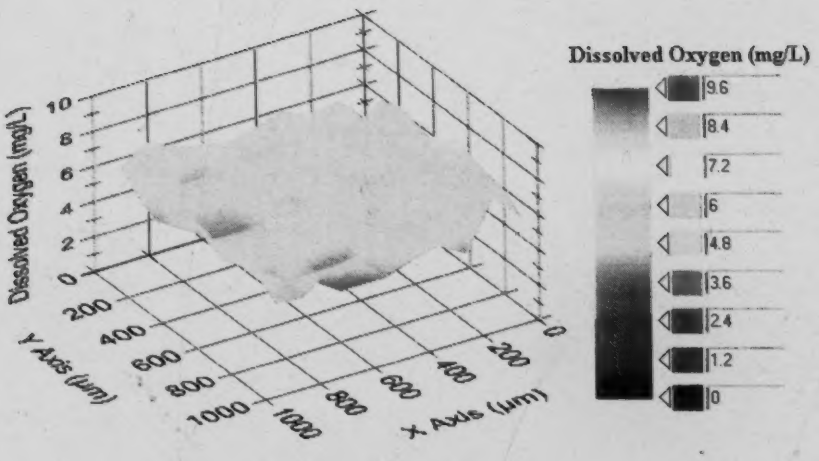

Figure 16. Dissolved oxygen concentration 320 µm below the artificial plane in biofilm sample 1

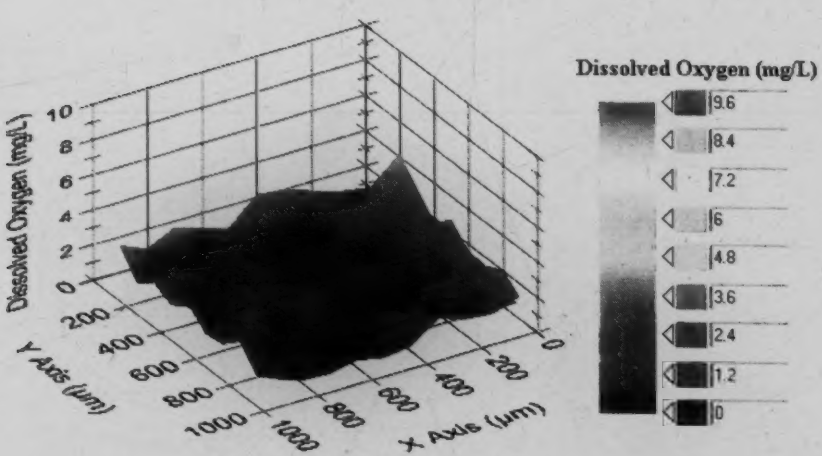

Figure 17. Dissolved oxygen concentration 720 µm below the artificial plane in biofilm sample 1.

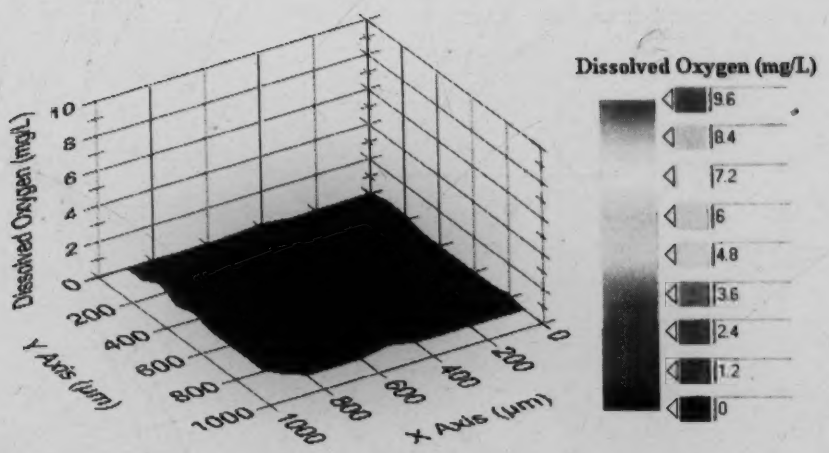

Figure 18. Dissolved oxygen concentration 1120 µm below the artificial plane in biofilm sample 1.

Figure 19, Figure 20, Figure 21, and Figure 22 represent the three-dimensional dissolved oxygen distribution measured in biofilm sample 2. As shown in the figures, there is also a reduction of the dissolved oxygen concentration at the different depths. As can be seen in Figure 19, 70 % of the dissolved oxygen concentration measured at the artificial plane was in a range from 5.8 to 8.3 mg/L. And 1120 µm below the artificial plane, 82 % of the measured dissolved oxygen concentration decreased to a range from 0 to 0.6 mg/L. This can be observed in Figure 22.

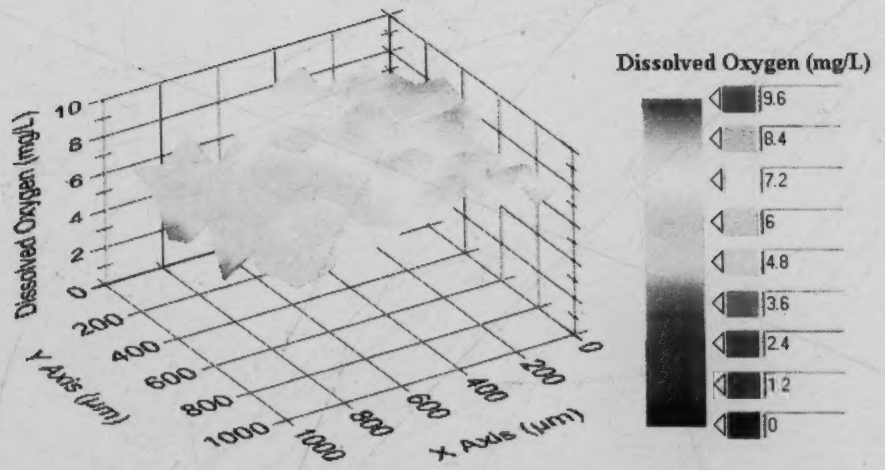

Figure 19. Dissolved oxygen concentration at the artificial plane in biofilm sample 2, about 920 µm above the biofilm surface.

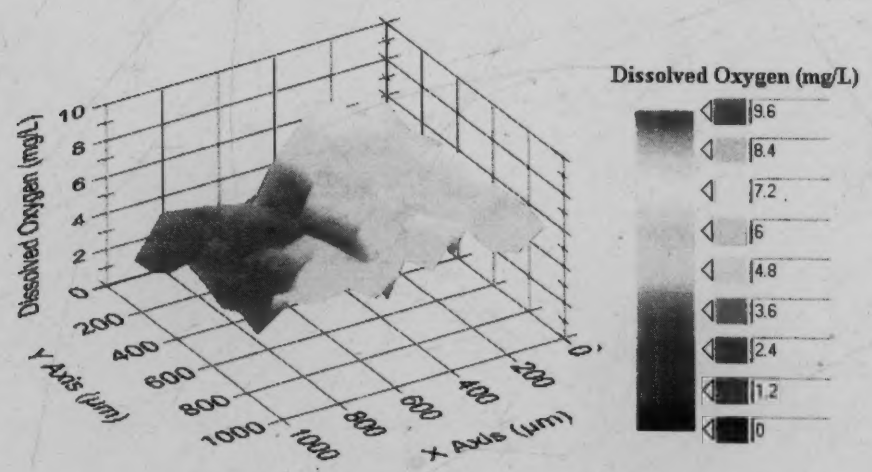

Figure 20. Dissolved oxygen concentration 320 µm below the artificial plane in biofilm sample 2.

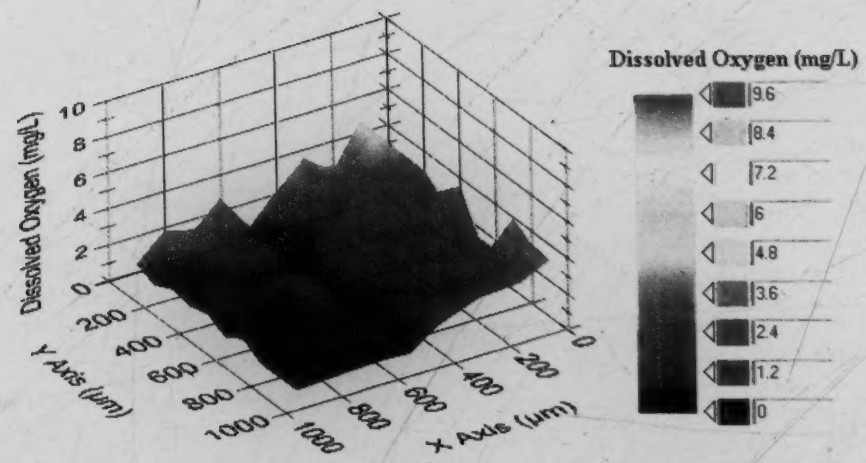

Figure 21. Dissolved oxygen concentration 720 µm below the artificial plane in biofilm sample 2.

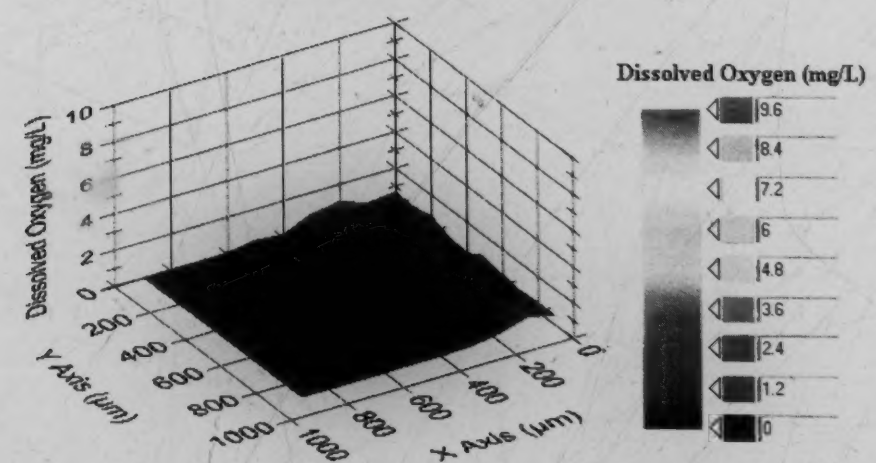

Figure 22. Dissolved oxygen concentration 1120 µm below the artificial plane in biofilm sample 2.

Figure 23, Figure 24 Figure 25, and Figure 26 represent the three-dimensional dissolved oxygen distribution in biofilm sample 3. Figure 23 shows that 70 %

of the dissolved oxygen concentration measured at the artificial plane started at a range from 6.2 to 8.2 mg/L and then, Figure 26 shows that 79 % of the dissolved oxygen concentration measured at 1120 μm below the artificial plane dropped to a range from 0 to 0.4 mg/L.

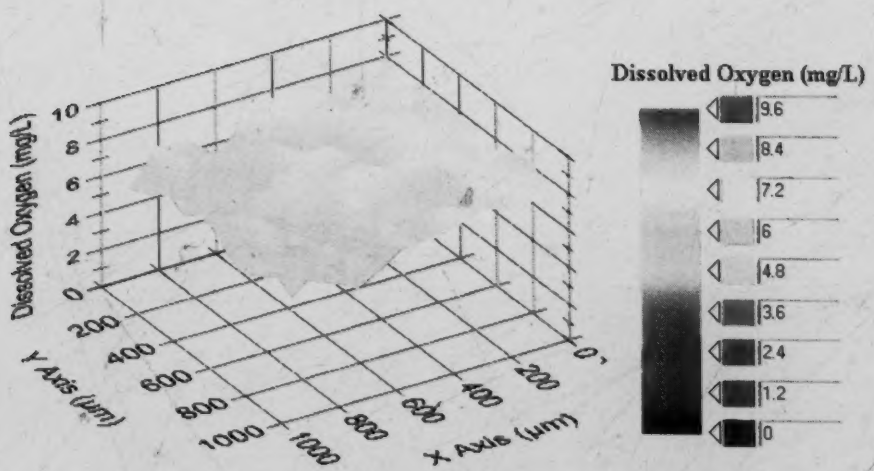

Figure 23. Dissolved oxygen concentration at the artificial plane in biofilm sample 3, about 920 μm above the biofilm surface.

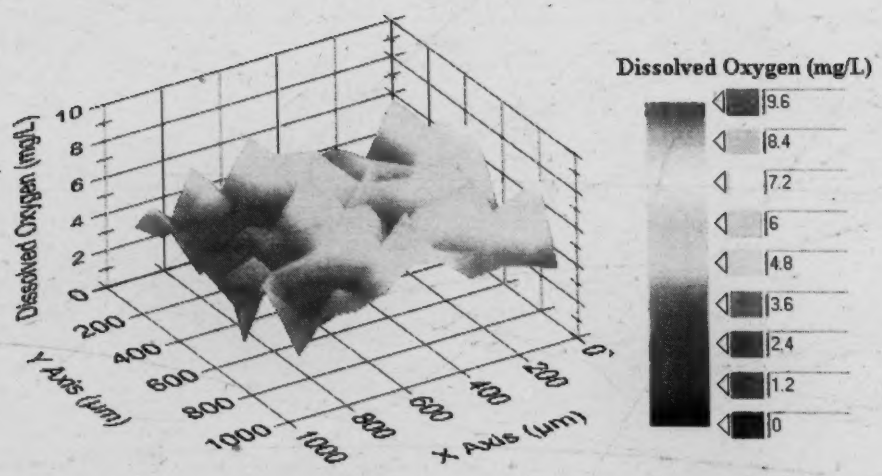

Figure 24. Dissolved oxygen concentration 320 µm below the artificial plane in biofilm sample 3.

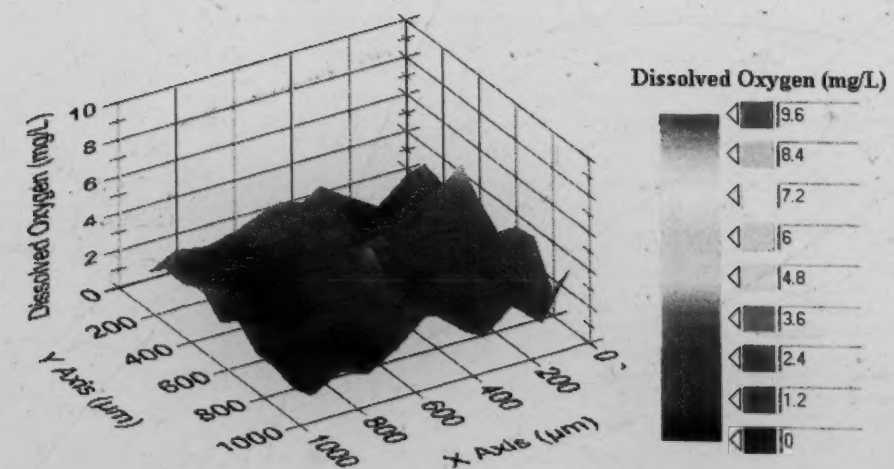

Figure 25. Dissolved oxygen concentration 720 µm below the artificial plane in biofilm sample 3.

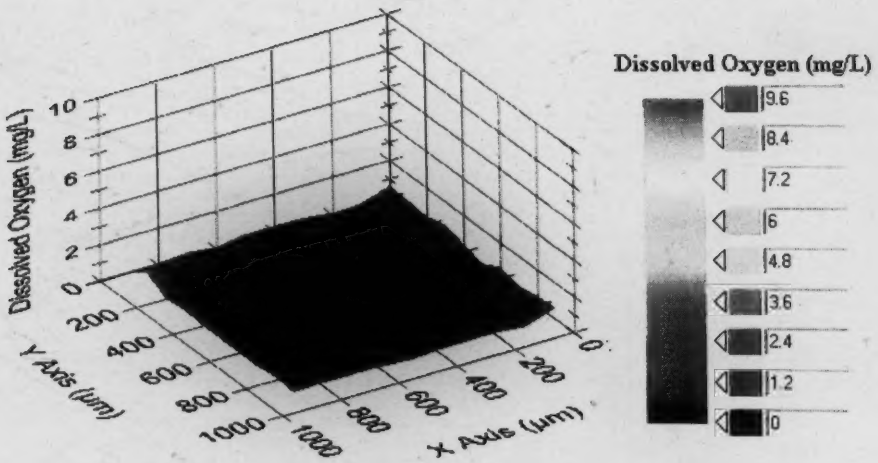

Figure 26. Dissolved oxygen concentration 1120 µm below the artificial plane in biofilm sample 3.

Figure 27, Figure 28, Figure 29, and Figure 30 represent the three-dimensional dissolved oxygen distribution in biofilm sample 4. As in the previous biofilm samples, this sample showed the same trend, a decrease of dissolved oxygen concentration with depth. 72 % of the dissolved oxygen concentration measured at the artificial plane was in a range from 6.1 to 8.0 mg/L and 1120 µm below the artificial plane, 75 % of the measured dissolved oxygen concentration was in a range from 0 to 0.4 mg/L

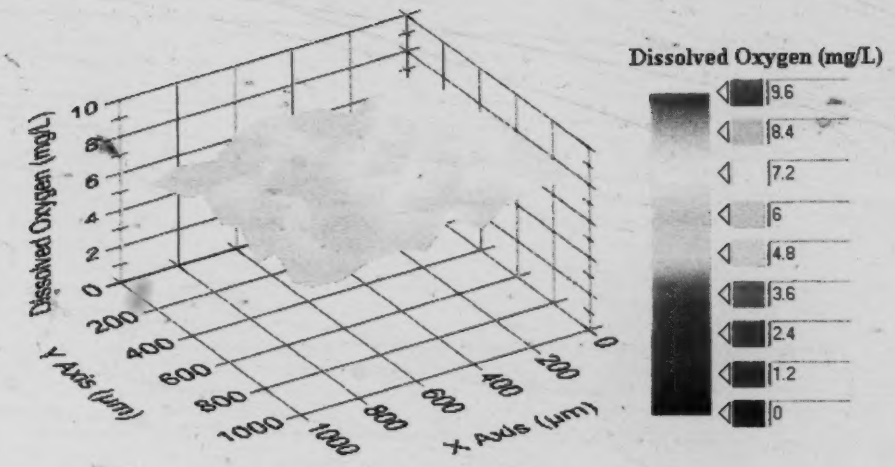

Figure 27. Dissolved oxygen concentration at the artificial plane in biofilm sample 4, about 920 µm above the biofilm surface.

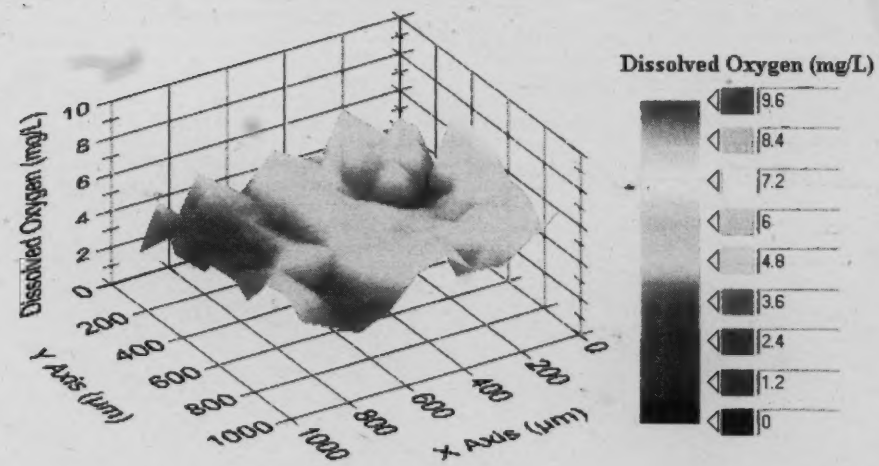

Figure 28. Dissolved oxygen concentration 320 µm below the artificial plane in biofilm sample 4.

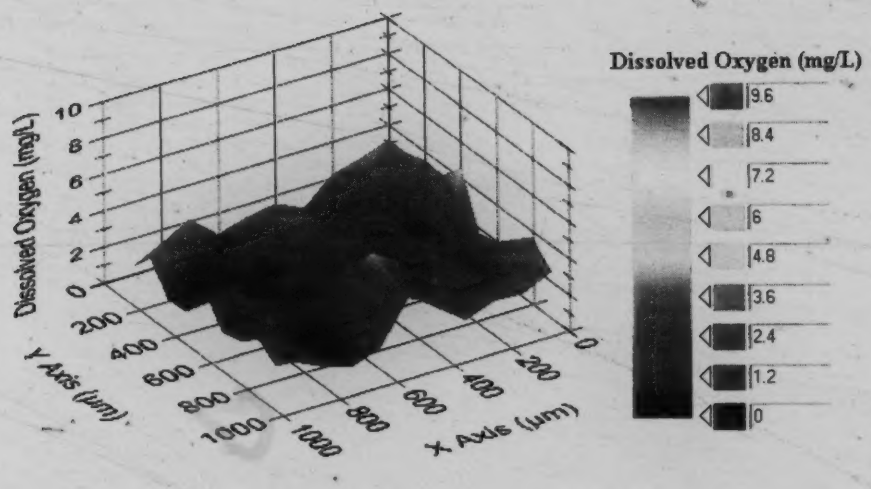

Figure 29. Dissolved oxygen concentration 720 µm below the artificial plane in biofilm sample 4.

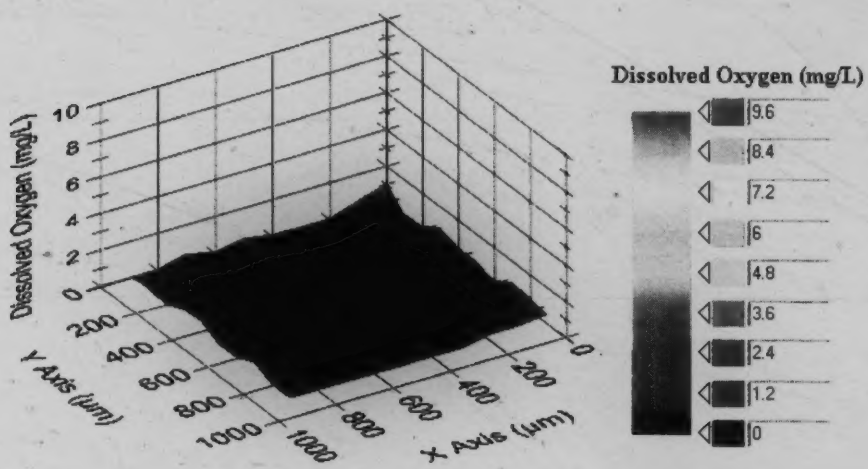

Figure 30. Dissolved oxygen concentration 1120 µm below the artificial plane in biofilm sample 4.

The experimental results of the three-dimensional dissolved oxygen distribution represented as planes parallel to a defined artificial plane produced significant information about biofilms.

The physical three-dimensional distribution of dissolved oxygen in biofilms obtained from a municipal wastewater treatment plant was presented. This presentation includes the dissolved oxygen distribution in the water above the biofilm and inside the biofilm in a relative position with reference to the artificial plane. The artificial plane was situated about 920 μm above the surface of the biofilm samples, and the profile measurements carried out by the automation system were 1520 μm depth. This means that the three-dimensional profiles constructed by using the artificial plane as a reference represent the dissolved oxygen distribution in the water above the biofilm samples and approximately 600 μm inside the biofilm samples.

The three-dimensional dissolved oxygen distribution provided a better view of the way dissolved oxygen penetrates into biofilms. It provided not only information that is in agreement with what has been previously reported, but also information that might not be observed with the typical one-dimensional profile measurements. For example, the reduction of the dissolved oxygen concentration inside the biofilms, which is a normal phenomenon that has been observed with one-dimensional profile measurements by several authors (Bishop and Yu, 1999; Bishop *et al.*, 1995; Fu *et al.*, 1994; Rasmussen and Lewandowski, 1998a; Wasche *et al.*, 2000; Zhang and Bishop, 1994b; Zhang *et al.*, 1995), was also observed in all the samples of this study. Besides, this study showed that the three-dimensional dissolved oxygen penetration in biofilms is not constant

but heterogeneous. As described before, in the four biofilm samples the decrease of dissolved oxygen with depth can be categorized in different ranges. This means that the three-dimensional profiles allow evaluating these characteristics in two planes (horizontal and vertical) instead of only the typical vertical axis perpendicular to the substratum where the biofilm is attached. For the dissolved oxygen distribution of biofilm sample 1, which is shown in Figure 15 to Figure 18, 72 % of the dissolved oxygen concentration measured at the artificial plane was in a range from 6.5 to 8.2 mg/L, and 1120 μm below the artificial plane, 84 % of the measured dissolved oxygen concentration was in a range from 0 to 0.1 mg/L. For the dissolved oxygen distribution of biofilm sample 2, which is shown in Figure 19 to Figure 22, 70 % of the dissolved oxygen concentration measured at the artificial plane was in a range from 5.8 to 8.3 mg/L, and 1120 μm below the artificial plane, 82 % of the measured dissolved oxygen concentration was in a range from 0 to 0.6 mg/L. For the dissolved oxygen distribution of biofilm sample 3, which is shown in Figure 23 to Figure 26, 70 % of the dissolved oxygen concentration measured at the artificial plane was in a range from 6.2 to 8.2 mg/L, and 1120 μm below the artificial plane, 79 % of the measured dissolved oxygen concentration was in a range from 0 to 0.4 mg/L. And for the dissolved oxygen distribution of biofilm sample 4, which is shown in Figure 27 to Figure 30, 72 % of the dissolved oxygen concentration measured at the artificial plane was in a range from 6.1 to 8.0 mg/L, and 1120 μm below the artificial plane, 75 % of the measured dissolved oxygen concentration was in a range from 0 to 0.4 mg/L.

4.3.3 BIOFILM SURFACE DESCRIPTION.

The previous three-dimensional profiles presented a general idea about how dissolved oxygen was distributed in the water layer above the biofilm and inside the biofilm in relationship with the artificial plane. They also provided a three-dimensional description of how the dissolved oxygen concentration decreased as the measured depth in the biofilm sample increased. However, those profiles do not provide the information of dissolved oxygen concentration at exact locations at the biofilm surface, inside the biofilm, or above the biofilm. This is because the physical reference used to plot the three-dimensional profiles was the artificial plane. This means that the biofilm surface was not considered when the three-dimensional profiles were constructed. The following sections will describe and analyze the physical biofilm surface; the dissolved oxygen concentration at the biofilm surface; and then, the dissolved oxygen concentration inside the biofilm and above the biofilm in the water layer using the physical biofilm surface as the reference instead of the artificial plane.

The surface structure of the biofilm samples was determined by measuring the distance between the artificial plane and the biofilm surface at every location where the profile was measured. Using the microscope and the manual gauge on the motorized micromanipulator, this measurement was carried out before each profile measurement was started. The biofilm thickness was measured after the experiment, also by using the microscope and the manual gauge on the motorized micromanipulator.

The physical structure of the biofilm surface of the biofilm samples studied is shown in Figure 31, Figure 32, Figure 33, and Figure 34. In all the biofilm

samples it can be seen that the surface of the biofilm was not a flat surface but a heterogeneous surface. The heterogeneity of the biofilms surface structure is an important characteristic of biofilms because the thickness and roughness of biofilms can affect significantly the distribution of dissolved oxygen inside the biofilms. It has been reported that an increase in surface roughness appeared to decrease the thickness of the boundary layer, therefore, the rougher the biofilm the less external mass transfer resistance (Zhang and Bishop, 1994b). For biofilm sample 1, as shown in Figure 31, the biofilm thickness was from 670 μm in the right part of the graph to 834 μm in some areas in the left part of the graph. In biofilm sample 2, as shown in Figure 32, the biofilm thickness was from 1302 μm in the right part of the graph to 1592 μm in some areas in the left part of the graph. In biofilms sample 3, as shown in Figure 33, the biofilm thickness was from 1252 μm in the right part of the graph to 1552 μm in some areas in the left part of the graph. Finally, the biofilm sample 4, as shown in Figure 34, the biofilm thickness was from 1123 μm in some areas in the right part of the graph to 1673 μm in some areas in the left part of the graph. Based on these results, it can be stated that the biofilm samples studied were mature biofilms. Many wastewater biofilm systems operate with a biofilm thickness of 500 μm to 2000 μm (Bishop, 1997).

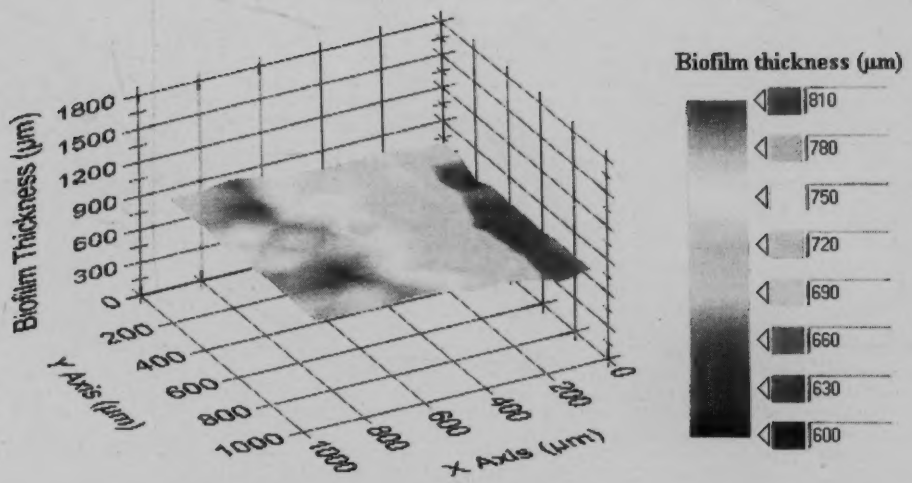

Figure 31. The physical structure of the biofilm surface and the thickness of the biofilm for biofilm sample 1.

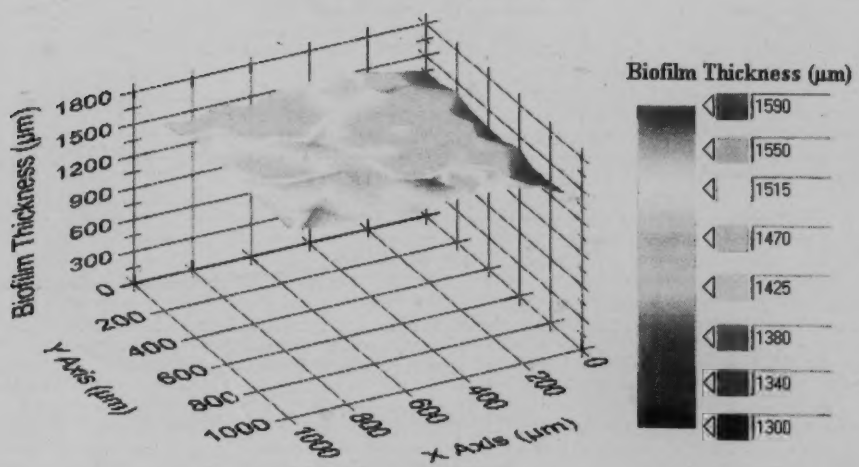

Figure 32. The physical structure of the biofilm surface and the thickness of the biofilm for biofilm sample 2.

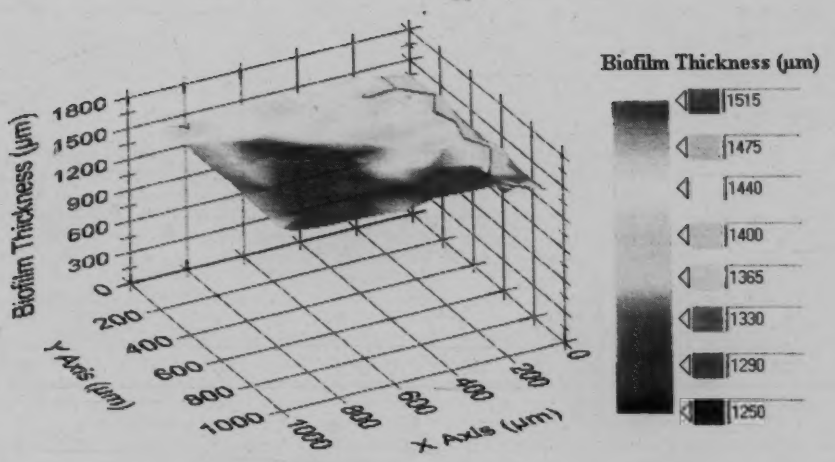

Figure 33. The physical structure of the biofilm surface and the thickness of the biofilm for biofilm sample 3.

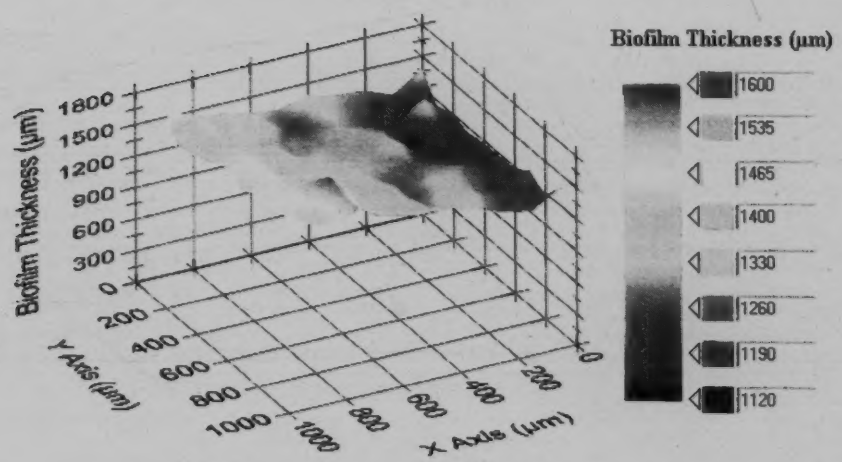

Figure 34. The physical structure of the biofilm surface and the thickness of the biofilm for biofilm sample 4.

The measurements conducted to determine the biofilm surface were started in the right part of the graph and finished in the left part of the graph. A variation of

the physical surface in all the biofilm samples was noticed. In the four samples, the biofilms were thinner at their right side (blue and purple areas in the graphs) and thicker at their left side (red and orange areas in the graphs). The distances between the lowest parts and the highest parts of the biofilms were 180 μm, 250 μm, 185 μm, and 480 μm for the biofilm sample 1, biofilm sample 2, biofilm sample 3, and biofilm sample 4, respectively. The surface variation was mainly due to the heterogeneous nature of biofilms.

However, it was not known if an experimental factor could have influenced the identification of the biofilm surface structure. As stated in the Materials and Methods section, the experiments were run from the right side of the graphs to the left side of the graphs. Therefore, there was a period of time about 10 hours from the first measurement at the right side of the graph to the last measurement at the left side of the graph. During this time the biofilm samples could have expanded because they were exposed to water. In order to evaluate the biofilm expansion and decide if it was an important factor affecting the determination of the biofilm surface structure, an experiment was conducted. The experimental conditions of this experiment were the same as the ones described for the determination of the biofilm surface structure. However, this time, the distance between the artificial plane and the biofilm surface was measured at the same place in the biofilm sample every hour for nine hours in order to detect any change of the biofilm thickness with time. The same experiment was run in two different samples.

The biofilm samples tested to identify any thickness change over time yielded the results presented in Figure 35 and Figure 36. Figure 35 shows that the biofilm

thickness increased 80 μm from 1370 μm to 1450 μm during the first two hours, and then it stayed stable during the next seven hours. Figure 36 shows that the biofilm thickness of that sample increased 130 μm from 1310 μm to 1440 μm during the first three hours and then the thickness stayed stable for the next six hours.

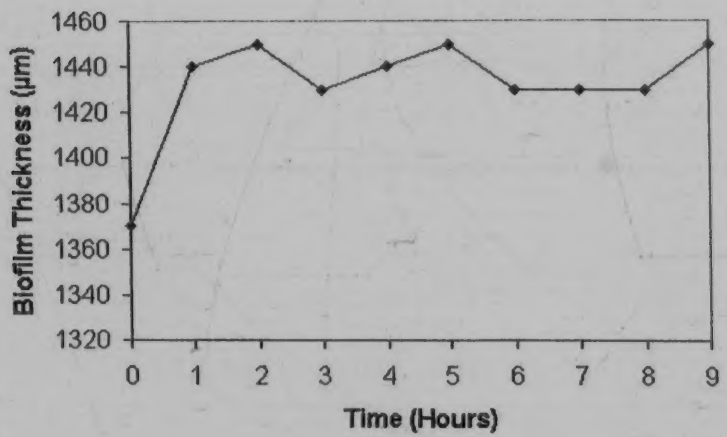

Figure 35. Changes of biofilm thickness over time at one point of a biofilm sample.

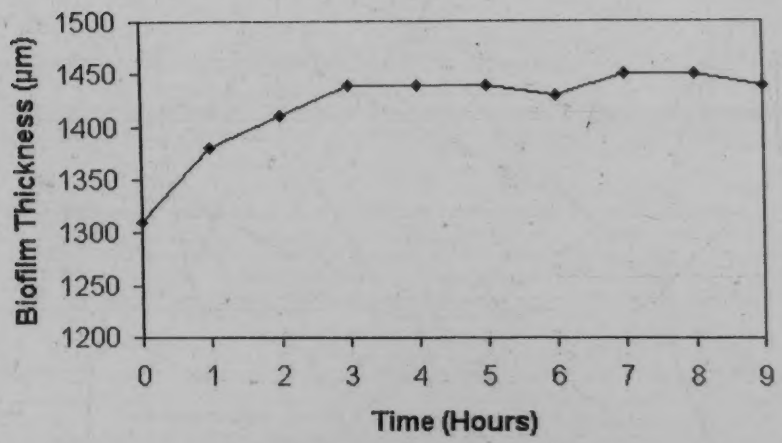

Figure 36. Changes of biofilm thickness over time at one point of a biofilm sample.

Based in these experiments, it was found that the expansion of the biofilm did not have a significant effect on the determination of the biofilm surface structure, and the biofilm surface roughness evaluated was due mainly to the heterogeneous nature of biofilms. The experiments conducted to determine the three-dimensional dissolved oxygen distribution in the biofilm samples from the four RBC stages lasted about ten hours. Consequently, the biofilm expansion could have been only about 100 µm and affected the experiment only during the first 2-3 hours. This phenomenon probably corresponded to the right part of the biofilm thickness graphs of the four stages because the right part of these graphs, where the measurements started (blue and purple area in the graphs) presented the lowest biofilm thickness. This can be observed in Figure 31, Figure 32, Figure 33, and Figure 34.

The dissolved oxygen concentrations at the surface of the biofilm sample 1,

biofilm sample 2, biofilm sample 3 and biofilm sample 4 are shown in Figure 37, Figure 38, Figure 39, and Figure 40, respectively. Figure 37 shows that the dissolved oxygen concentration at the biofilm surface of biofilm sample 1 was in a range from 0 to 0.8 mg/L. In most of the right area of biofilm sample 1, dissolved oxygen was already depleted. Figure 38 shows that the dissolved oxygen concentration at the surface of biofilm sample 2 was in a range from 0 to 3.8 mg/L. Figure 39 shows that the dissolved oxygen concentration at the surface of biofilm sample 3 was in a range from 0.3 to 3.5 mg/L. And finally, Figure 40 shows that the dissolved oxygen concentration at the surface of biofilm sample 4 was in a range from 0 to 2.5 mg/L.

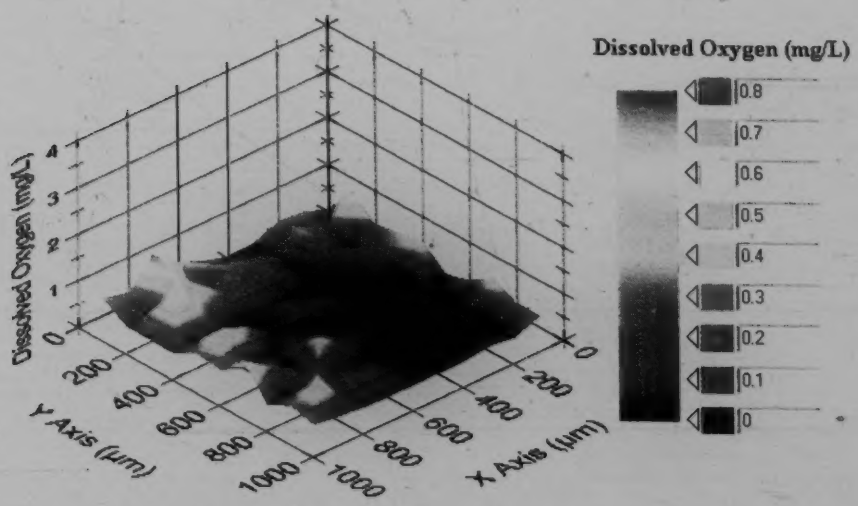

Figure 37. The dissolved oxygen concentration presented at the biofilm surface of biofilm sample 1

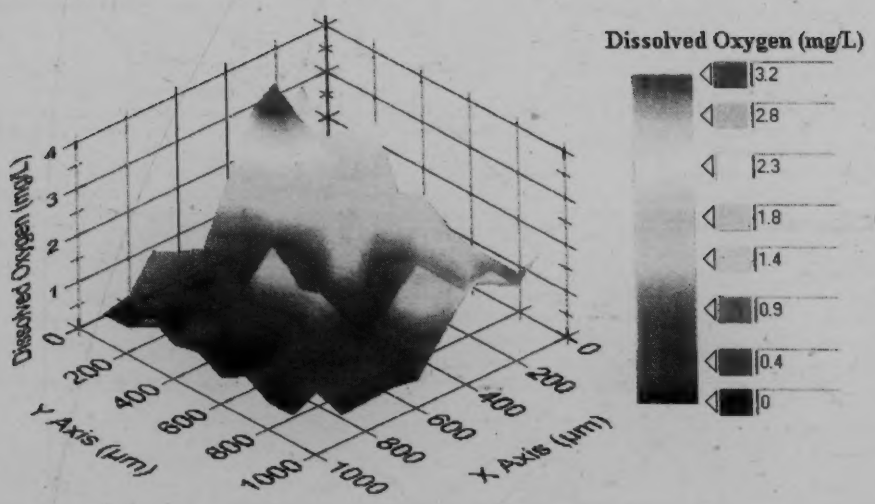

Figure 38. The dissolved oxygen concentration presented at the biofilm surface of biofilm sample 2.

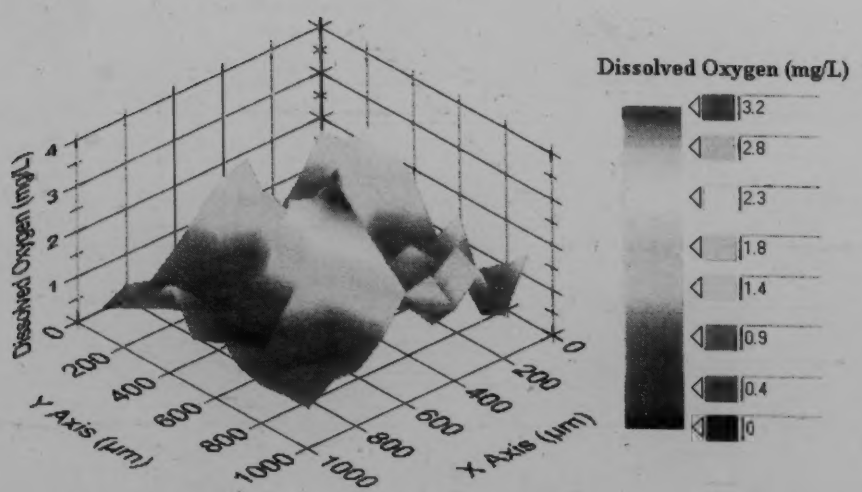

Figure 39. The dissolved oxygen concentration presented at the biofilm surface of biofilm sample 3.

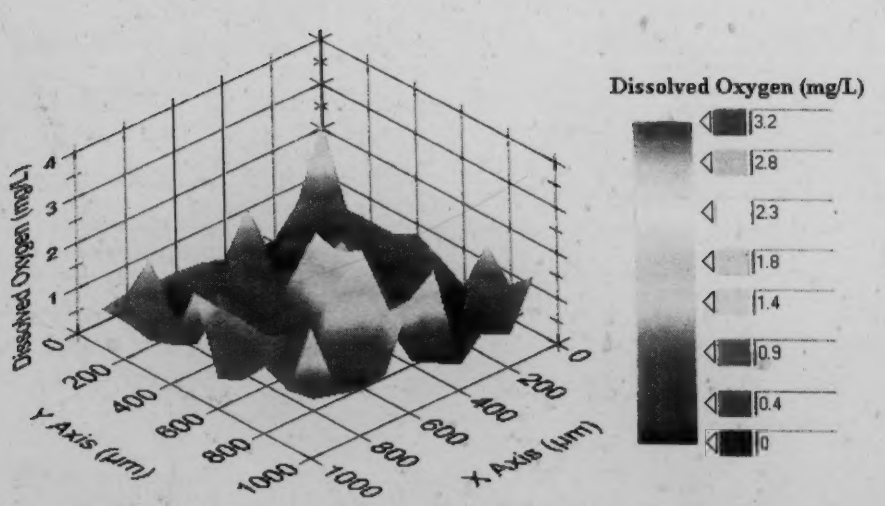

Figure 40. The dissolved oxygen concentration presented at the biofilm surface of biofilm sample 4.

Based on the above experimental results, it has been found that the dissolved oxygen concentration can reach depletion on the biofilm surface. The dissolved oxygen depletion at the biofilm surface could be due to the metabolic activity inside biofilms. Oxygen diffuses from the boundary layer through the biofilm and reaches certain depth. If the metabolic activity of microorganisms inside biofilms is high, the microorganisms will consume the oxygen available and, therefore, oxygen will have less penetration into the biofilms. In this study, there was not dissolved oxygen present in some parts of the biofilm surface of the samples. It means that there was probably a high metabolic activity inside the biofilms, consuming the dissolved oxygen available in the water layer above the biofilm samples.

4.3.4 THE DISSOLVED OXYGEN DISTRIBUTION INSIDE THE BIOFILMS.

Once the biofilm surface was identified, it is possible to know the dissolved oxygen distribution below and above the biofilm surface. In this section, the dissolved oxygen distribution below the biofilm surface of the four biofilm samples will be described.

The three-dimensional profiles where the artificial plane was used as physical reference did not consider the biofilm surface. As explained before, the biofilm surface structure of the biofilm samples were physically irregular. The surfaces of the biofilm samples were not flat like the form of the artificial plane. Therefore, those profiles do not provide the information of dissolved oxygen concentration at exact locations above the biofilms, or inside the biofilms. In order to know the dissolved oxygen distribution at exact locations in the biofilm samples, the following sections will describe the dissolved oxygen distribution inside and above the biofilm samples taking their actual biofilm surface as the reference plane. This means that the three-dimensional profiles inside and above the biofilm samples will show the dissolved oxygen distribution in two horizontal axes (X and Y) at different depths. This time, each depth is parallel to the actual biofilm surface, not to the artificial plane.

To simplify the presentation of the experimental results, only four depths of each biofilm sample are presented in this section. These depths are: 40 μm, 280 μm, 440 μm, and 600 μm below the biofilm surface for the biofilm sample 1; and 40 μm, 280 μm, 520 μm, and 760 μm below the biofilm surface for the biofilm sample 2, biofilm sample 3 and biofilm sample 4. These depths represent the general trend of the dissolved

oxygen distribution inside the biofilm samples. The entire three-dimensional profiles can be found in Appendix C.

Figure 41, Figure 42, Figure 43, and Figure 44 show the dissolved oxygen concentration at 40 μm, 280 μm, 440 μm, and 600 μm below the biofilm surface of biofilm sample 1. The general trend of the three-dimensional profile was the reduction of dissolved oxygen with depth. Figure 41 shows that the dissolved oxygen concentration was very low 40 μm below the biofilm surface. Dissolved oxygen was depleted in most of the biofilm area at this depth. As seen in Figure 41, 86 % of the dissolved oxygen concentration measured at 40 μm below the biofilm surface was in a range from 0 to 0.3 mg/L; however, some locations had a dissolved oxygen concentration of 0.5 mg/L. Figure 42 and Figure 43 show that 280 μm and 440 μm below the biofilm surface the dissolved oxygen concentration kept decreasing, but some locations with dissolved oxygen concentration of 0.5 mg/L were still present. Finally, Figure 44 shows that most of dissolved oxygen had been depleted at 600 μm below the biofilm surface. As seen in this figure, 95 % of the dissolved oxygen concentration measured at 600 μm below the biofilm surface was in a range from 0 to 0.3 mg/L. However, some "pockets" with dissolved oxygen of 0.5 mg/L and 0.6 mg/L were found at this depth.

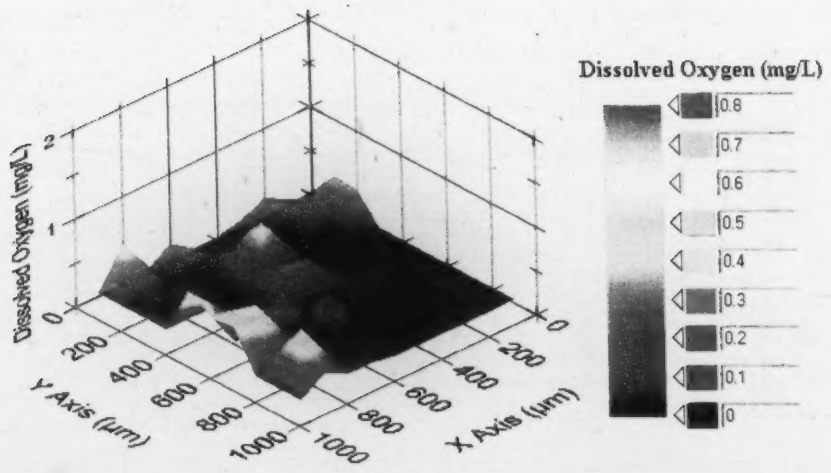

Figure 41. The dissolved oxygen concentrations 40 µm below the biofilm surface in biofilm sample 1.

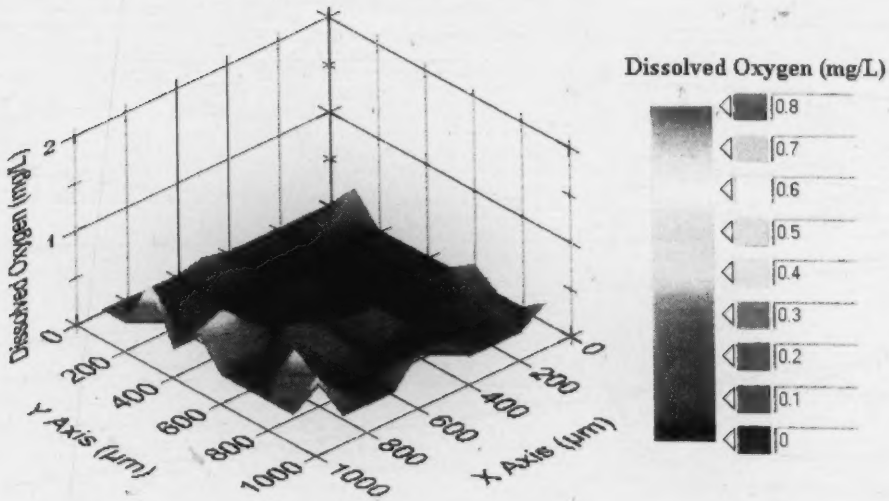

Figure 42. The dissolved oxygen concentrations 280 µm below the biofilm surface in biofilm sample 1.

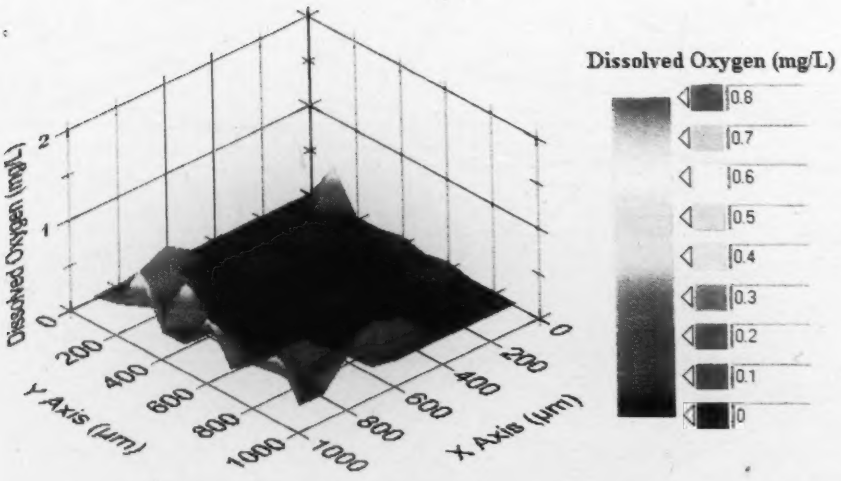

Figure 43. The dissolved oxygen concentrations 440 µm below the biofilm surface in biofilm sample 1.

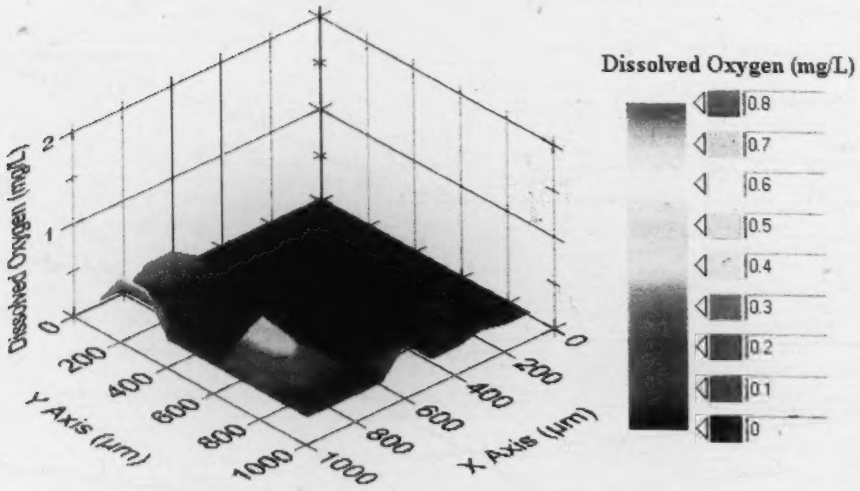

Figure 44. The dissolved oxygen concentrations 600 µm below the biofilm surface in biofilm sample 1.

Figure 45, Figure 46, Figure 47, and Figure 48 show the dissolved oxygen concentration at 40 μm, 280 μm, 520 μm, and 760 μm below the biofilm surface of biofilm sample 2. The general trend of the three-dimensional profile was the reduction of dissolved oxygen with depth, forming stratification. A high heterogeneity was found 40 μm below the biofilm surface. As Figure 45 shows, a dissolved oxygen concentration from 0 to 2.3 mg/L was found 40 μm below the biofilm surface. The dissolved oxygen concentration and the heterogeneity kept decreasing as the depth increased. This can be seen 280 μm and 520 μm below the biofilm surface in Figure 46 and Figure 47. At 760 μm depth, as shown in Figure 48, most of dissolved oxygen had been depleted. As seen in this figure, 83 % of the dissolved oxygen concentration measured at 760 μm below the biofilm surface was in a range from 0 to 0.1 mg/L. However, some "pockets" with 1.1 mg/L of dissolved oxygen were found in some locations of the biofilm sample at this depth.

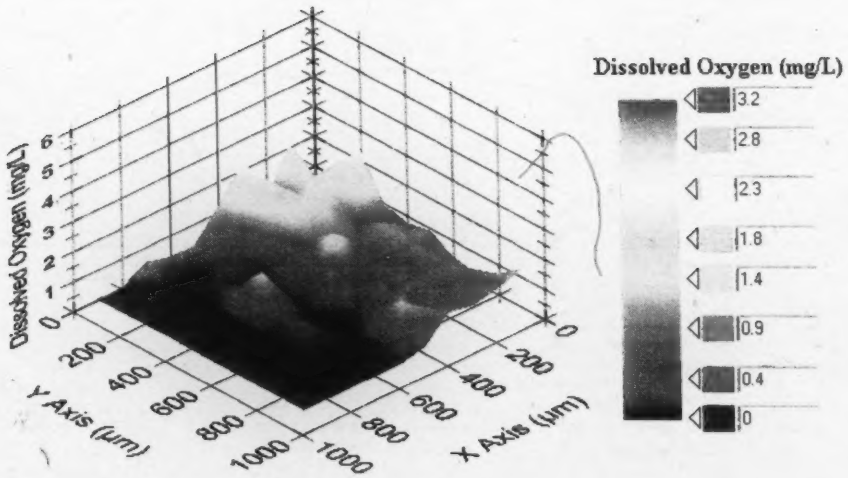

Figure 45. The dissolved oxygen concentrations 40 µm below the biofilm surface in biofilm sample 2.

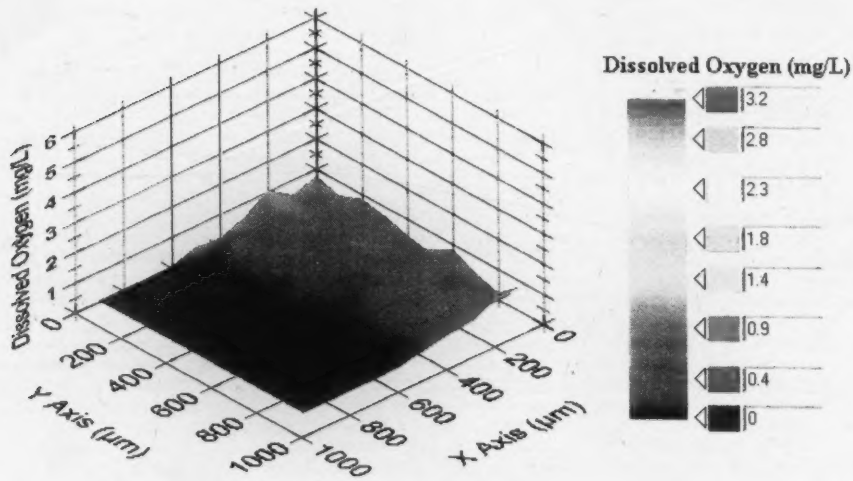

Figure 46. The dissolved oxygen concentrations 280 µm below the biofilm surface in biofilm sample 2.

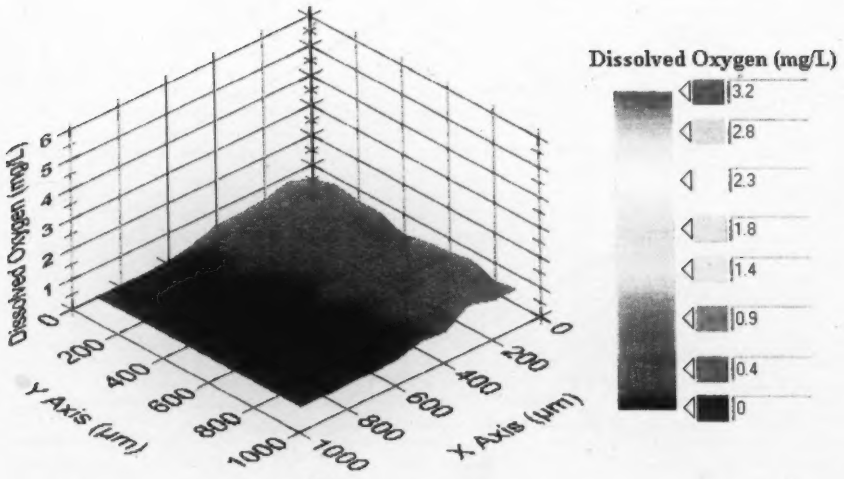

Figure 47. The dissolved oxygen concentrations 520 µm below the biofilm surface in biofilm sample 2.

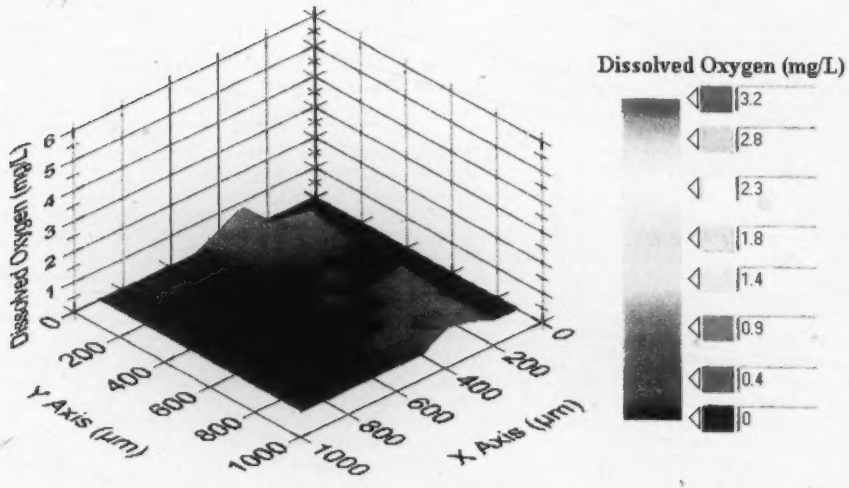

Figure 48. The dissolved oxygen concentrations 760 µm below the biofilm surface in biofilm sample 2.

Figure 49, Figure 50, Figure 51, and Figure 52 show the dissolved oxygen concentration at 40 μm, 280 μm, 520 μm, and 760 μm below the biofilm surface of biofilm sample 3. The general trend of the three-dimensional profile was the reduction of dissolved oxygen with depth, forming stratification. A high heterogeneity was found 40 μm below the biofilm surface. Figure 49 shows a dissolved oxygen concentration from 0 to 2.7 mg/L. In the next depth, 280 μm below the biofilm surface, the dissolved oxygen concentration range went only from 0 to 0.8 mg/L in 94 % of the area, only a few locations had some "peaks" with a dissolved oxygen concentration of 1.4 mg/L. This can be seen in Figure 50. This indicates that the high dissolved oxygen heterogeneity found 40 μm below the biofilm surface decreased considerably at the depth of 280 μm below the biofilm surface. In the next depth, 520 μm below the biofilm surface, the dissolved oxygen concentration actually increased to 1.0 mg/L. This can be observed in Figure 51. Finally, Figure 52 shows that at 760 μm depth most of dissolved oxygen had been depleted. As seen in this figure, 81 % of the dissolved oxygen concentration measured at 760 μm below the biofilm surface was in a range from 0 to 0.2 mg/L. However, some "pockets" of 1.0 mg/L of dissolved oxygen were still present in the sample.

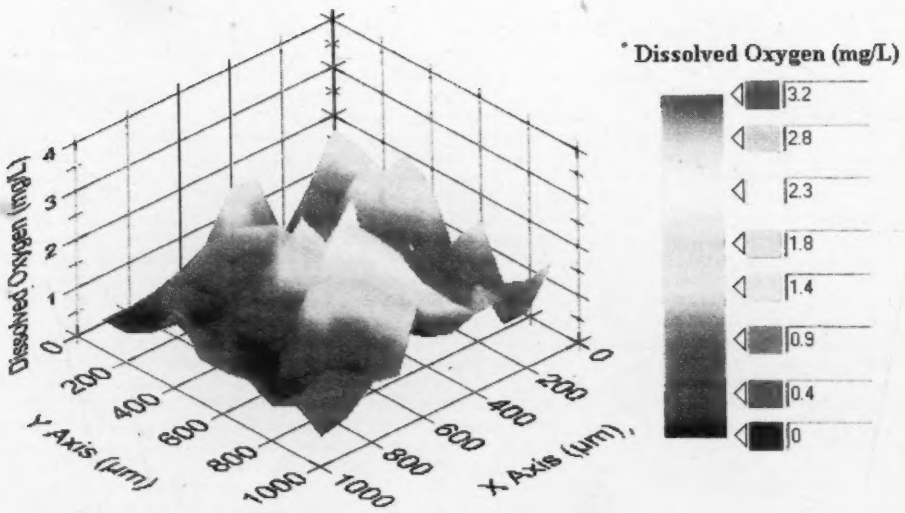

Figure 49. The dissolved oxygen concentrations 40 µm below the biofilm surface in biofilm sample 3.

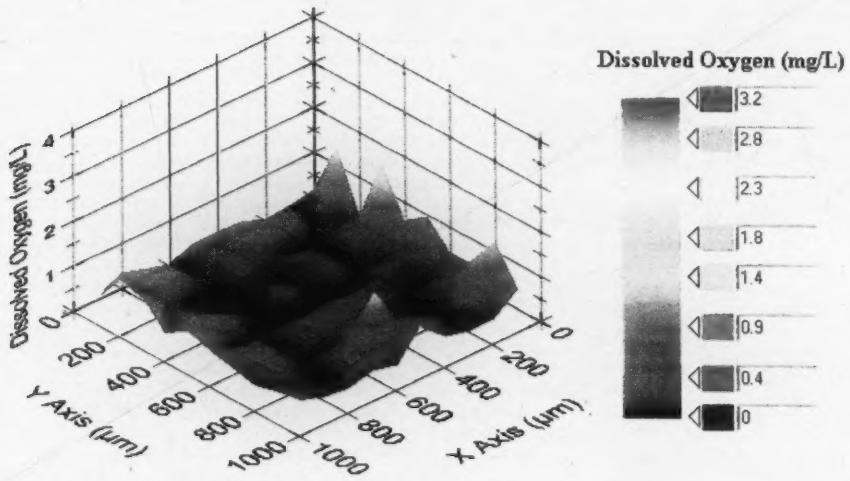

Figure 50. The dissolved oxygen concentrations 280 µm below the biofilm surface in biofilm sample 3.

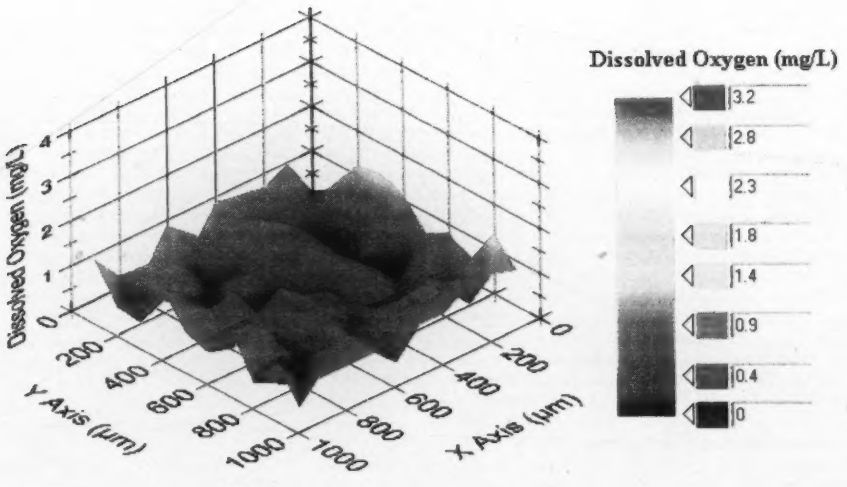

Figure 51. The dissolved oxygen concentrations 520 µm below the biofilm surface in biofilm sample 3.

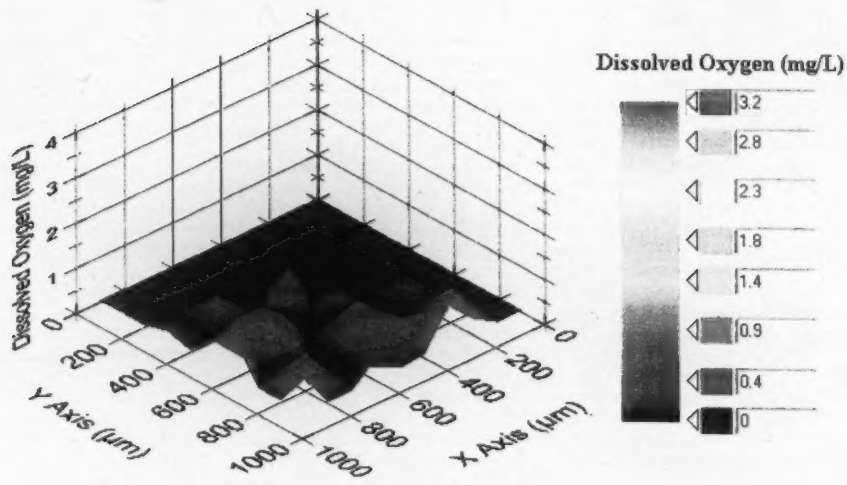

Figure 52. The dissolved oxygen concentrations 760 µm below the biofilm surface in biofilm sample 3.

Figure 53, Figure 54, Figure 55, and Figure 56 show the DO concentration at 40 μm, 280 μm, 520 μm, and 760 μm below the biofilm surface of biofilm sample 4. The general trend of reduction of dissolved oxygen with depth and the high dissolved oxygen heterogeneity 40 μm below the biofilm surface were also found in this sample. Figure 53 shows a dissolved oxygen concentration from 0 mg/L to 2.3 mg/L 40 μm below the biofilm surface. However, 280 μm below the biofilm surface, as shown in Figure 54 the heterogeneity decreased to a range from 0 to 0.7 mg/L in 93 % of the area. The dissolved oxygen concentration kept decreasing as the depth increased. This can be seen in Figure 54 and Figure 55. Figure 56 shows that at 760 μm depth most of dissolved oxygen had been depleted. As seen in this figure, 96% of the dissolved oxygen concentration measured at 760 μm below the biofilm surface was in a range from 0 to 0.1 mg/L. A few "pockets" of dissolved oxygen with 0.4 mg/L were found at this depth.

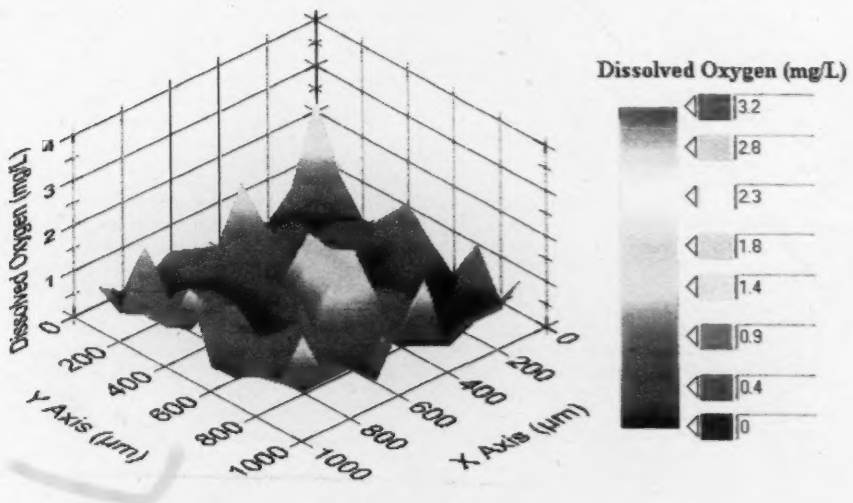

Figure 53. The dissolved oxygen concentrations 40 μm below the biofilm surface in biofilm sample 4.

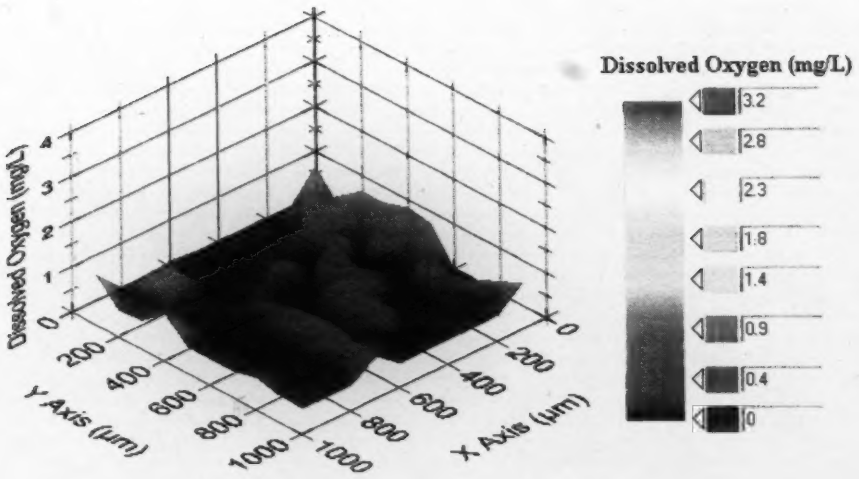

Figure 54. The dissolved oxygen concentrations 280 µm below the biofilm surface in biofilm sample 4.

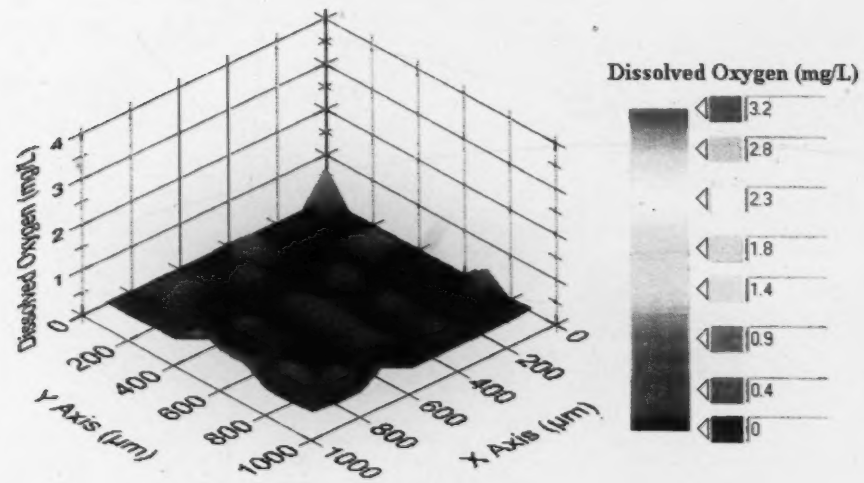

Figure 55. The dissolved oxygen concentrations 520 µm below the biofilm surface in biofilm sample 4.

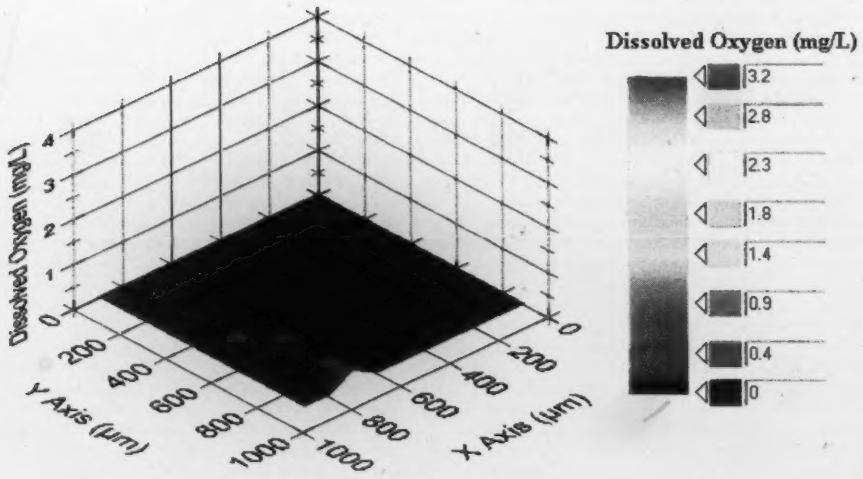

Figure 56. The dissolved oxygen concentrations 760 µm below the biofilm surface in biofilm sample 4.

The three-dimensional mapping of dissolved oxygen distribution in wastewater biofilms revealed structural and functional characteristics of biofilms, which may not be possible to observe with typical one-dimensional profiles.

The three-dimensional maps of the dissolved oxygen distribution showed that the level of heterogeneity and the concentration of dissolved oxygen inside the biofilms decreased with depth, forming stratification. This phenomenon can be clearly observed in the three-dimensional profiles of the biofilm sample 2, biofilm sample 3 and biofilm sample 4, which are shown in Figure 45 to Figure 56. The resulting stratification is in agreement with studies reported previously, which have found that the constant competition for substrate inside biofilms contributes to the stratification of different

characteristics of biofilms such as density, porosity and oxygen diffusivity (Zhang *et al.*, 1995).

It was noticed that this stratification could not be clearly observed in biofilm sample 1 because a great amount of dissolved oxygen had already been depleted, as shown in Figure 37, at its surface or as shown in Figure 41, 40 μm below its surface. The low dissolved oxygen penetration in most locations of biofilm sample 1 could be due to a high metabolic activity inside the biofilm. Therefore, the lack of a clear stratification of the dissolved oxygen concentration in this sample does not necessarily mean that there was not stratification, but that the stratification occurred faster in this sample. Figure 31 shows that the biofilm sample 1 was the thinnest of all the samples with a thickness of 630 μm to 810 μm, while the other biofilm samples presented a thickness of more than 1100 μm. It has been reported that there are different trends for the decrease of oxygen effective diffusivity with biofilm depth for different biofilm thickness (Bishop *et al.*, 1995). The authors found that the rate of dissolved oxygen effective diffusivity reduction with biofilm depth is greater for thin biofilms than for thick biofilms. For this reason, the reduction of dissolved oxygen concentration with depth in biofilm sample 1, the thinnest sample, happened within a shorter distance than in the rest of the biofilm samples and, therefore, the stratification in this sample could not be fully appreciated in the three-dimensional profile.

The heterogeneity was found higher in the top portions of the biofilm samples, 40 μm below the biofilm surface. This can be seen clearly when the figures at 40 μm depth of the biofilm sample 2, biofilm sample 3 and biofilm sample 4, which are

shown in Figure 45, Figure 49 and Figure 53, are compared with the figures at 280 μm of their respective biofilm sample, which are shown in Figure 45, Figure 50 and Figure 54. The dissolved oxygen concentration in the biofilm sample 2, biofilm sample 3 and biofilm sample 4 at 40 μm depth was of 0 to 2.7 mg/L. And the dissolved oxygen concentration in the same biofilm samples 280 μm below the biofilm surface was only of 0 to 0.2 mg/L.

The high variability of dissolved oxygen inside the top portions of the biofilm samples measured in this experiment is an indication that there might be water with dissolved oxygen in these portions of the biofilms. Several authors have reported voids or channels in biofilms that facilitate oxygen transport from the bulk liquid to the biofilm (de Beer and Stoodley, 1995; de Beer et al., 1994; Lewandowski et al., 1995; Massol-deya et al., 1995). In this study, the high variability of dissolved oxygen, which suggests the presence of water with dissolved oxygen in the top portions of the biofilm samples, were found in mature biofilm samples from the municipal wastewater treatment plant.

Although the general trend of the dissolved oxygen distribution in the biofilm samples, as shown in Figure 41 to Figure 56, was a decrease of dissolved oxygen concentration with depth until total depletion, some "pockets" of dissolved oxygen were found in deep sections of the biofilm samples measured in this experiment. In biofilm sample 1, as shown in Figure 44, the dissolved oxygen pockets at 600 μm depth were 0.2 mg/L and 0.5 mg/L. In biofilm sample 2 biofilm sample and biofilm sample 3, as shown in Figure 48 and Figure 52, the dissolved oxygen "pockets" at 760 μm were of 1.0 mg/L and 1.1 mg/L. And in biofilm sample 4, as shown in Figure 56, the dissolved

oxygen "pockets" at 760 μm were of 0.4 mg/L. As can be seen in these figures, in all the samples measured, there were some dissolved oxygen "pockets" in the deep sections of the biofilms. Although it was once observed in biofilms in a gas phase trickle-bed biofilter (Zhu *et al.*, 2001), this phenomenon has not been reported in studies on wastewater biofilms with typical single dissolved oxygen profile measurements. Using single dissolved oxygen profile measurements in biofilms, other studies have found dissolved oxygen penetrations from 200 to 800 μm (Bishop and Yu, 1999; de Beer and Stoodley, 1995; Lu and Yu, 2002b; Wasche *et al.*, 2000; Zhang and Bishop, 1994b). Although some of these studies have measured the dissolved oxygen concentration in deep section of biofilms, the dissolved oxygen "pockets" were not observed. In this study, the three-dimensional mapping of the dissolved oxygen distribution in wastewater biofilms showed pockets with dissolved oxygen in deep sections of biofilms. This is an interesting phenomenon in biofilms because the presence of dissolved oxygen in deeper sections of biofilms can have important impacts on the metabolic activities inside biofilms.

4.3.5 THE DISSOLVED OXYGEN DISTRIBUTION ABOVE THE BIOFILM SURFACE.

Once the biofilm surface was identified, it is possible to know the dissolved oxygen concentration above the biofilm surface. In this section, the dissolved oxygen distribution above the biofilm surface of the four biofilm samples will be described.

This section will describe the dissolved oxygen distribution above the biofilm samples taking the actual biofilm surface as the reference plane. This means

that the three-dimensional profiles above the biofilm samples will show the dissolved oxygen distribution in two horizontal axes (X and Y) at different planes. Each plane is parallel to the actual biofilm surface, not to the artificial plane.

To simplify the presentation of the experimental results, only four planes above the biofilm surface of each biofilm sample are presented in this section. These planes are 760 μm, 520 μm, 280 μm, and 40 μm above the biofilm surface. These depths represent the general trend of the dissolved oxygen distribution above the biofilm samples. The entire three-dimensional profiles can be found in Appendix D.

Figure 57, Figure 58, Figure 59, and Figure 60 show the dissolved oxygen distribution at 760 μm, 520 μm, 280 μm, and 40 μm above the biofilm surface of biofilm sample 1. The general trend of the dissolved oxygen distribution was the reduction of heterogeneity as the measurements were closer to the biofilm surface. Figure 57 shows that 73 % of the dissolved oxygen concentration measured at 760 μm above the biofilm surface was from 5.9 to 7.2 mg/L. At 520 μm above the biofilm surface, as shown in Figure 58, 68% of the measured dissolved oxygen concentration was in a range from 4.2 to 5.7 mg/L with a few peaks with 7.4 mg/L. Figure 59 shows that 70 % of the dissolved oxygen concentration measured at 280 μm above the biofilm surface was in a range from 1.7 to 3.1 mg/L. And just 40 μm above the biofilm surface, as shown in Figure 60, 84 % of the measured dissolved oxygen concentration was from 0 to 0.6 mg/L.

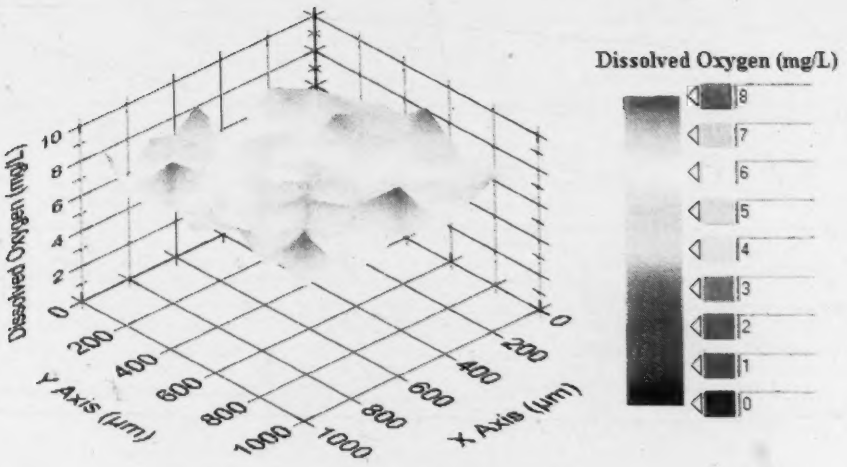

Figure 57. Dissolved oxygen concentration 760 µm above the biofilm surface in biofilm sample 1.

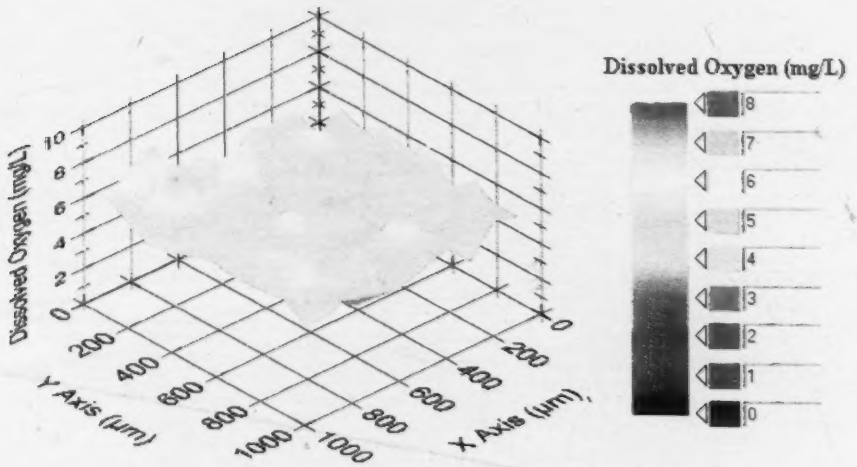

Figure 58. Dissolved oxygen concentration 520 µm above the biofilm surface in biofilm sample 1.

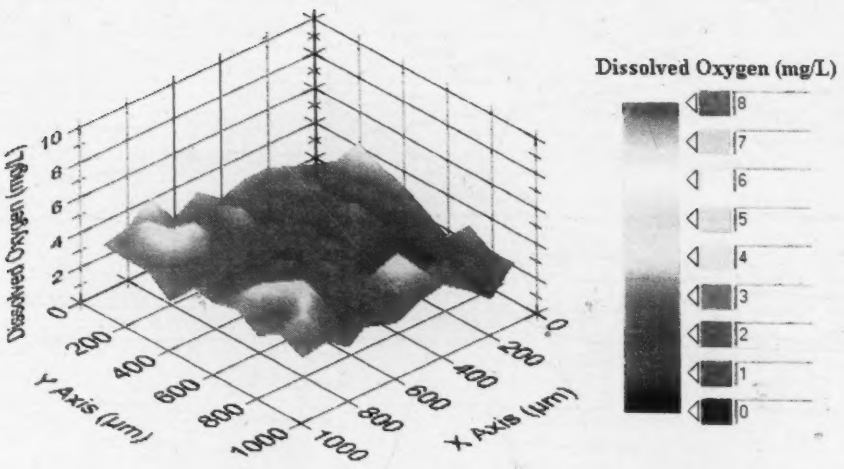

Figure 59. Dissolved oxygen concentration 280 µm above the biofilm surface in biofilm sample 1.

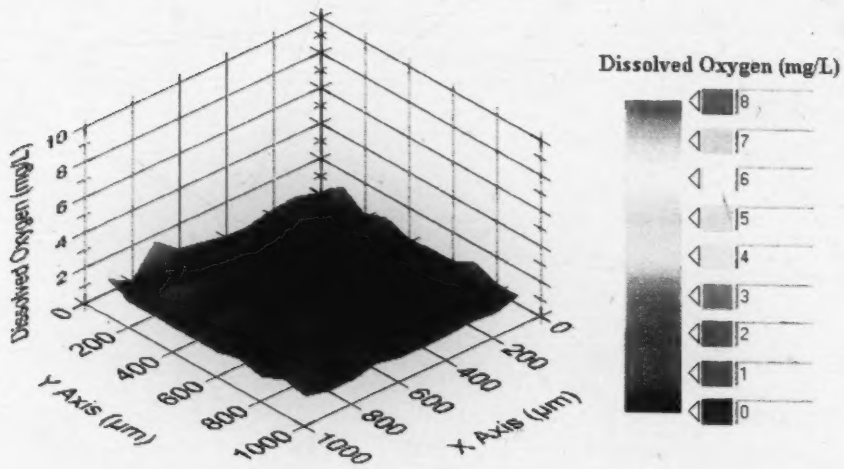

Figure 60. Dissolved oxygen concentration 40 µm above the biofilm surface in biofilm sample 1.

Figure 61, Figure 62, Figure 63, and Figure 64 show the dissolved oxygen distribution at 760 µm, 520 µm, 280 µm, and 40 µm above the biofilm surface

of biofilm sample 2. The general trend of the dissolved oxygen distribution was the reduction of heterogeneity as the measurements were closer to the biofilm surface. Figure 61 shows that 80 % of the dissolved oxygen concentration measured at 760 μm above the biofilm surface was from 6.0 to 8.6 mg/L. At 520 μm above the biofilm surface, as shown in Figure 62, 65 % of the measured dissolved oxygen concentration was from 3.2 to 5.6 mg/L. Figure 63 shows that 63 % of the dissolved oxygen concentration measured at 280 μm above the biofilm surface was from 1.0 to 3.9 mg/L. And 40 μm above the biofilm surface, as shown in Figure 64 67 % of the measured dissolved oxygen concentration was from 0 to 1.5 mg/L.

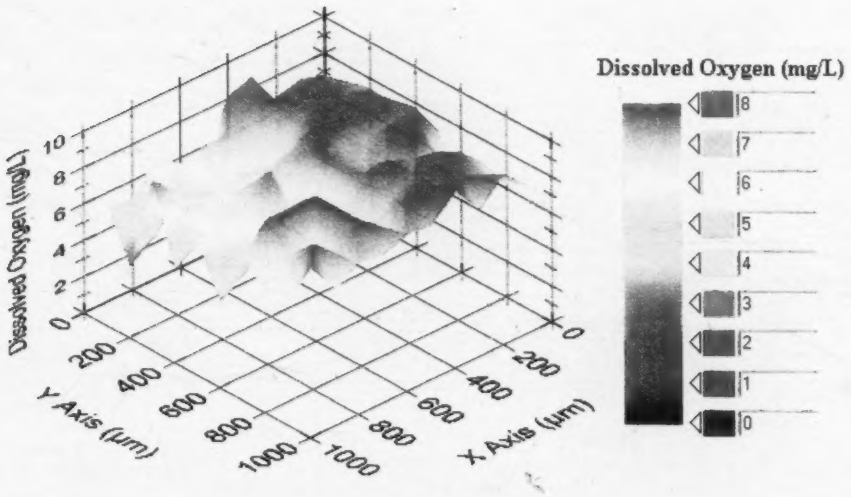

Figure 61. Dissolved oxygen concentration 760 μm above the biofilm surface in biofilm sample 2.

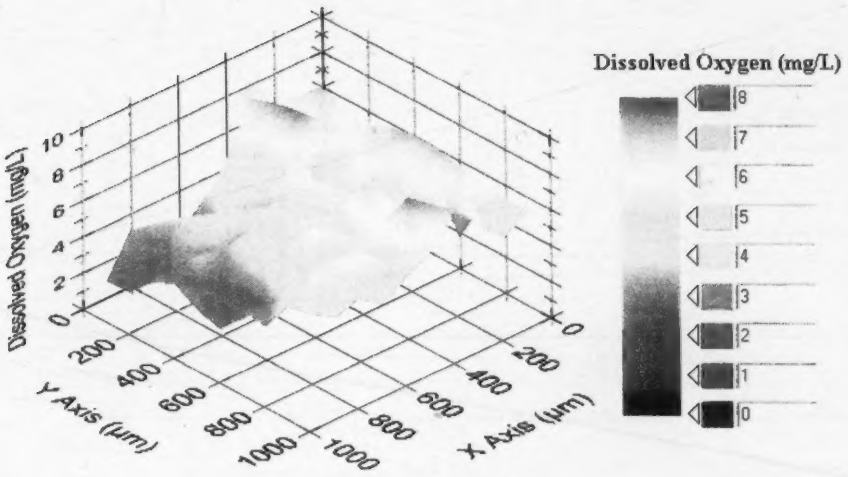

Figure 62. Dissolved oxygen concentration 520 µm above the biofilm surface in biofilm sample 2.

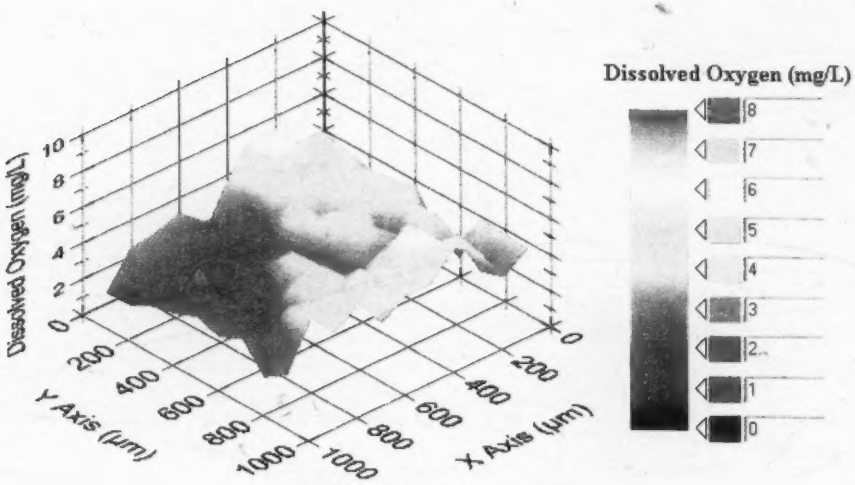

Figure 63. Dissolved oxygen concentration 280 µm above the biofilm surface in biofilm sample 2.

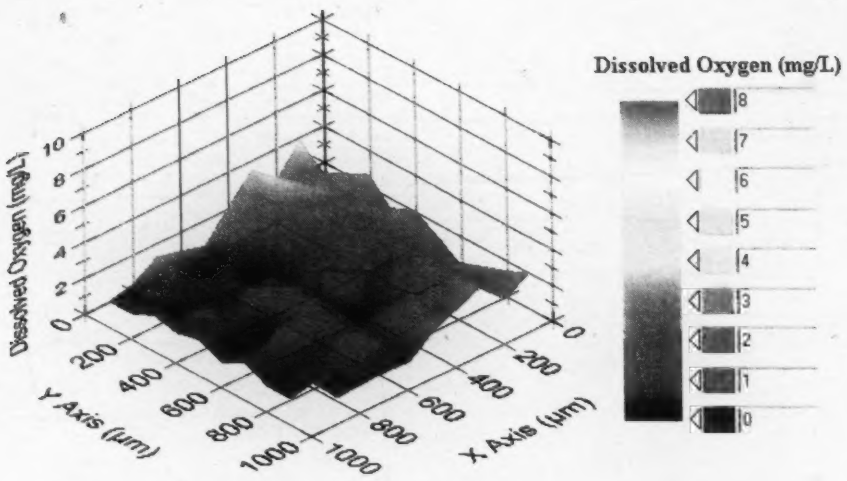

Figure 64. Dissolved oxygen concentration 40 µm above the biofilm surface in biofilm sample 2.

Figure 65, Figure 66, Figure 67, and Figure 68 show the dissolved oxygen distribution at 760 µm, 520 µm, 280 µm, and 40 µm above the biofilm surface of biofilm sample 3. The general trend of the dissolved oxygen distribution was the reduction of heterogeneity as the measurements were closer to the biofilm surface. Figure 65 shows that 61 % of the dissolved oxygen concentration measured at 760 µm above the biofilm surface was from 6.1 mg/L to 8.0 mg/L. At 520 µm above the biofilm surface, as shown in Figure 66 67 % of the measured dissolved concentrations were from 3.6 to 6.0 mg/L. Figure 67 shows that 64 % of the measured dissolved oxygen concentrations were from 1.2 to 3.9 mg/L at 280 µm above the biofilm surface. And 40 µm above the biofilm surface, as shown in Figure 68 64 % of the measured dissolved oxygen concentrations were from 0.2 to 1.7 mg/L.

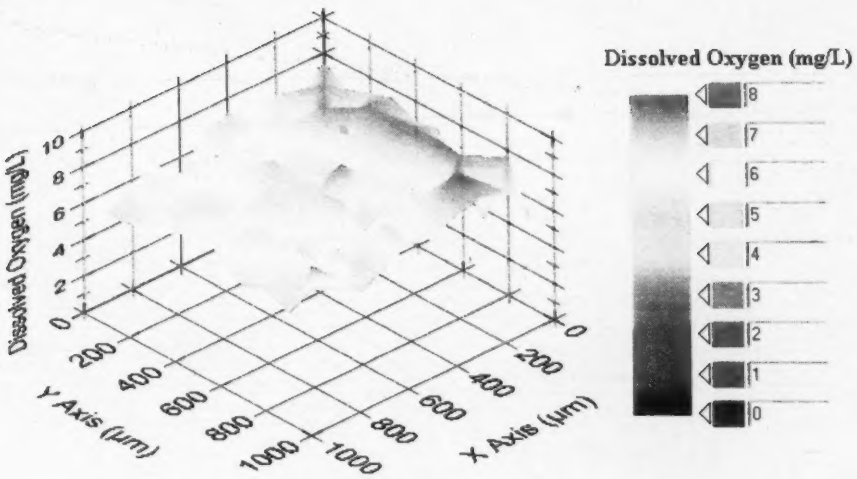

Figure 65. Dissolved oxygen concentration 760 µm above the biofilm surface in biofilm sample 3.

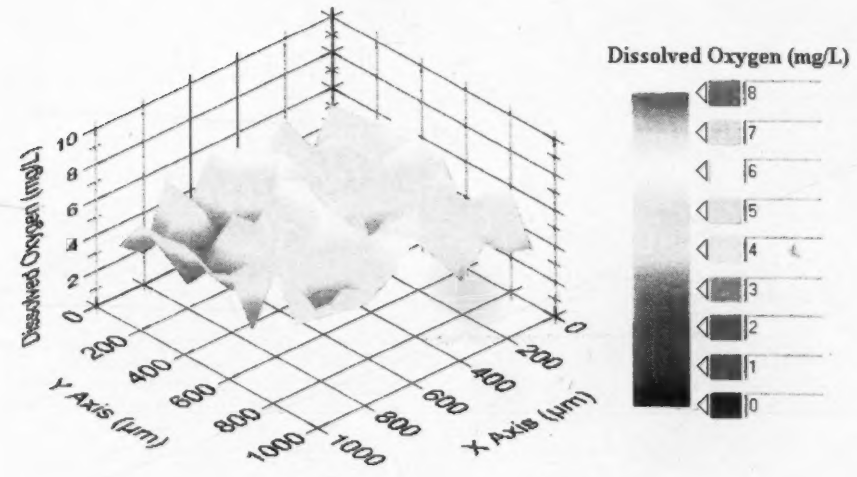

Figure 66. Dissolved oxygen concentration 520 µm above the biofilm surface in biofilm sample 3.

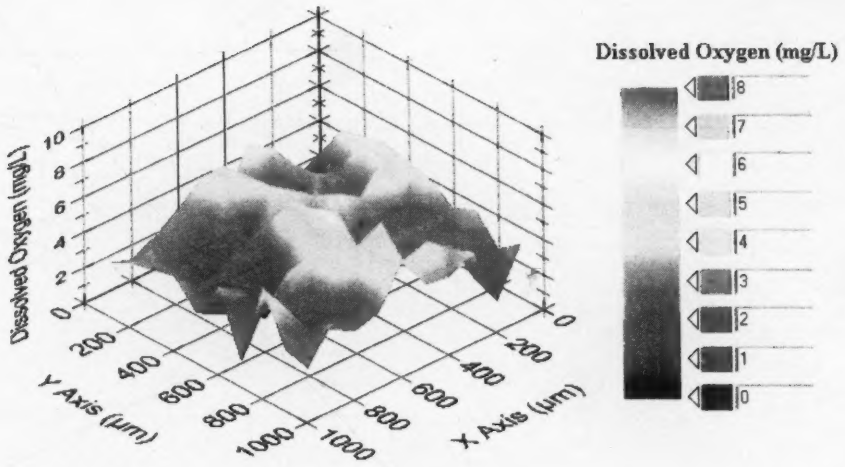

Figure 67. Dissolved oxygen concentration 280 µm above the biofilm surface in biofilm sample 3.

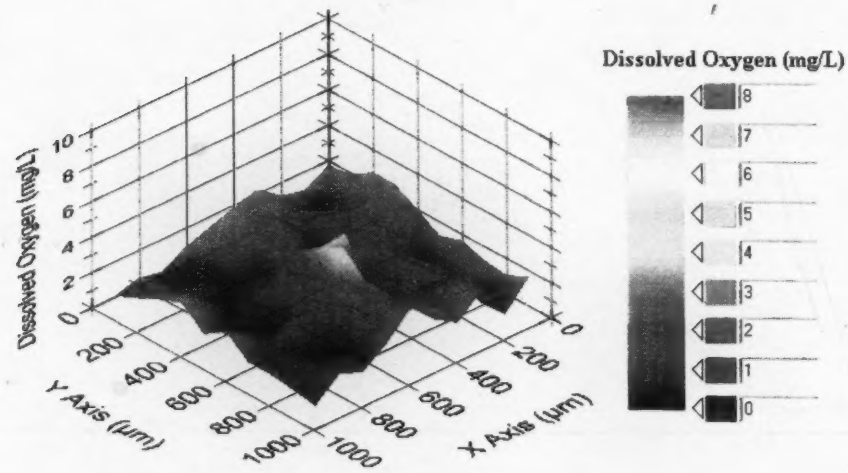

Figure 68. Dissolved oxygen concentration 40 µm above the biofilm surface in biofilm sample 3.

Figure 69, Figure 70, Figure 71, and Figure 72 show the dissolved oxygen distribution at 760 µm, 520 µm, 280 µm, and 40 µm above the biofilm surface

of biofilm sample 4. The general trend of the dissolved oxygen distribution was also the reduction of heterogeneity as the measurements were closer to the biofilm surface. Figure 69 shows that 73 % of the dissolved oxygen concentration measured at 760 μm above the biofilm surface was from 4.4 to 6.8 mg/L. At 520 μm above the biofilm surface, as shown in Figure 70, 61 % of the measured dissolved oxygen concentration was from 3.1 to 5.0 mg/L. Figure 71 shows that 66 % of the dissolved oxygen concentration measured at 280 μm above the biofilm surface was in a range from 1.1 to 3.3 mg/L. And 40 μm above the biofilm surface, as shown in Figure 72, 66 % of the measured dissolved oxygen concentration was from 0 to 1.0 mg/L, and few locations had 2.9 mg/L of dissolved oxygen.

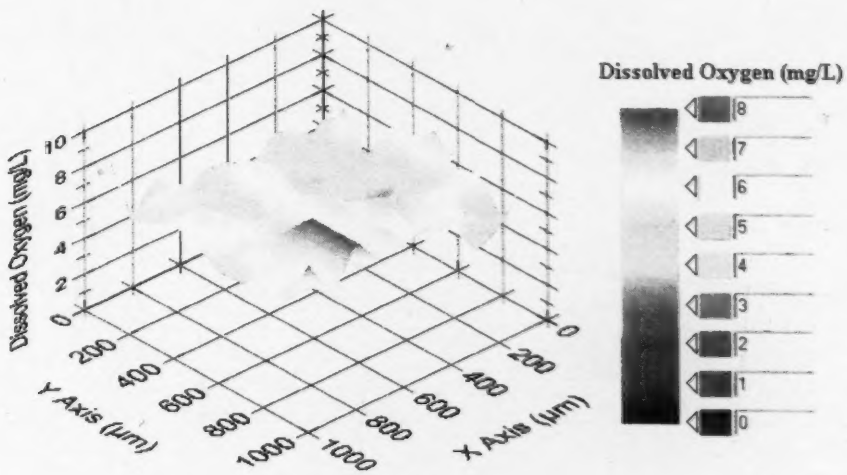

Figure 69. Dissolved oxygen concentration 760 μm above the biofilm surface in biofilm sample 4.

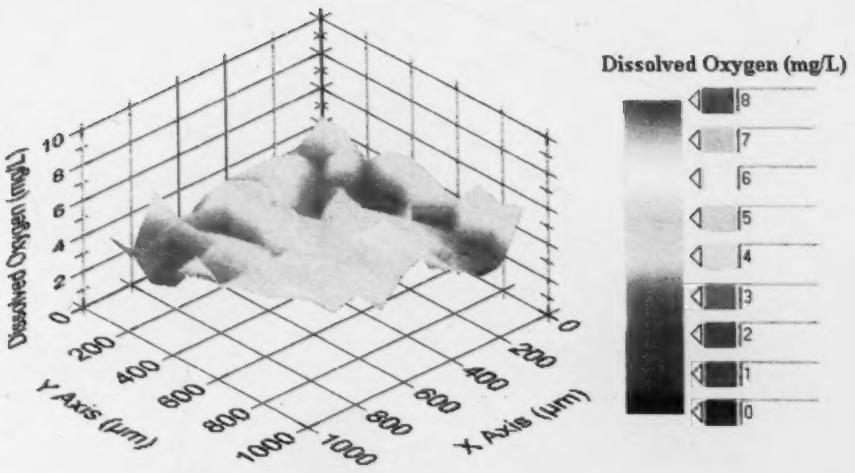

Figure 70. Dissolved oxygen concentration 520 µm above the biofilm surface in biofilm sample 4.

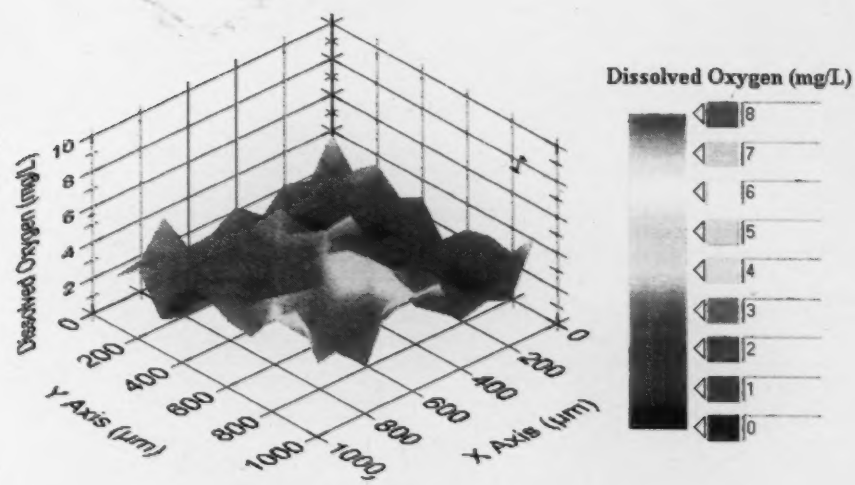

Figure 71. Dissolved oxygen concentration 280 µm above the biofilm surface in biofilm sample 4.

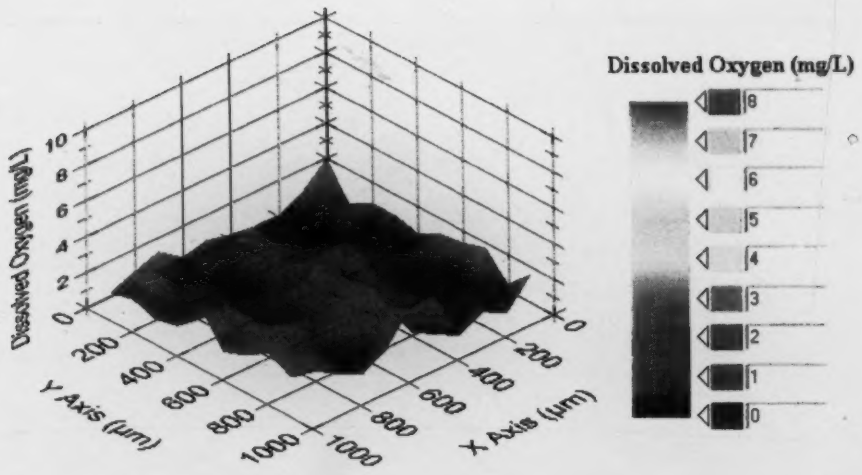

Figure 72. Dissolved oxygen concentration 40 µm above the biofilm surface in biofilm sample 4.

The experimental results of the dissolved oxygen concentration above the biofilms showed that the heterogeneity of the dissolved oxygen distribution is higher in sections that are further away from the biofilm surface than in sections closer to the biofilm surface. This phenomenon could be observed in all the samples studied, as shown in Figure 57 to Figure 72. The heterogeneity of the dissolved oxygen concentration above the biofilm surface could be due to the surface structure of the biofilm and hydraulic conditions. As explained before, the biofilm surface structure can affect significantly the distribution of dissolved oxygen inside and above biofilms. In previous studies by several authors, the thickness of the concentration boundary layer, where the oxygen diffuses from the bulk liquid to the biofilm, has been found in a range from 200 µm to 800 µm, depending on surface roughness and fluid velocity above the biofilm (Wasche *et al.*, 2002; Zhang and Bishop, 1994b). Low flow velocities above the

biofilms increase the thickness of the concentration boundary layer. Therefore, it is possible that the biofilm samples in this experiment presented thick boundary layers because the experiments were carried out in stagnant wastewater.

5.0 CONCLUSIONS AND RECOMMENDATIONS

This study has mapped the three-dimensional dissolved oxygen distribution in wastewater biofilms using an automation system and combined oxygen microelectrodes. The three-dimensional dissolved oxygen distribution in biofilm samples from a municipal wastewater treatment plant was measured. The three-dimensional profiles of the dissolved oxygen distribution in wastewater biofilms provided a better view of the dissolved oxygen distribution in biofilms and revealed structural and functional characteristics of wastewater biofilms that might not be observed with the typical one-dimensional profile measurements. Based on the experimental results, the following conclusions and recommendations can be drawn.

(1) This study demonstrated that the biofilm surface is physically heterogeneous and the dissolved oxygen concentration could be depleted at the biofilm surface. These are important characteristics in biofilms because metabolic activities together with thickness and roughness of biofilms can affect significantly the distribution of dissolved oxygen in biofilms. The dissolved oxygen concentration above the biofilms showed that the heterogeneity of the dissolved oxygen distribution was higher in sections that are further away from the biofilm surface than in sections close to the biofilm surface. This phenomenon was attributed to the surface structure of the biofilm and the hydraulic conditions.

(2) The study showed that the concentration and the level of heterogeneity of dissolved oxygen inside the biofilms decreased with depth, forming stratification. The heterogeneity of the dissolved oxygen was higher in the top

portions of the biofilm samples, close to the biofilm surface. The high variability of dissolved oxygen in these parts of the biofilms indicated the presence of water with dissolved oxygen.

(3) The three-dimensional mapping of the dissolved oxygen distribution in wastewater biofilms showed "pockets" of high dissolved oxygen concentrations in deep sections of biofilms. This is an interesting phenomenon in biofilms because oxygen has important impacts on the metabolic activities inside biofilms.

(4) The combined oxygen microelectrodes and the automation system were proven to be tools that improve the quantity and quality of experimental results needed to understand the structure and function of biofilms used in wastewater treatment. The fabrication procedure of the combined oxygen microelectrodes was successful. This type of oxygen microelctrodes can be used in biofilm studies where large numbers of continuous dissolved oxygen readings are needed.

The following recommendations for future work can be considered:

(1) A high variability of dissolved oxygen was found in small sections in the top portions of the biofilm samples. Therefore, it is recommendable to conduct a very detailed study of the dissolved oxygen distribution in this specific area of biofilms using the automation system, which provides a very accurate positioning of the oxygen microelectrode.

(2) Other types of microelectrodes could be used with the automation system in order

to know more about the three-dimensional distribution of other chemicals affecting metabolic processes inside biofilms.

(3) The amount of data generated in this study could be incorporated in new or existing models, where a comprehensive statistical analysis can be accomplished.

6.0 REFERENCES

Austerlitz, H. 1991. *Data acquisition techniques using personal computers*. Academic Press Inc., San Diego, CAL.

Bishop, P. L. 1997. Biofilm structure and kinetics. *Water Science and Technology*, 36(1), 287-294.

Bishop, P. L., and Yu, T. 1999. A microelectrode study of redox potential change in biofilms. *Water Science and Technology*, 39(7), 179-185.

Bishop, P. L., Zhang, T. C., and Fu, Y. C. 1995. Effects of biofilm structure, microbial distributions and mass transport on biodegradation processes. *Water Science and Technology*, 31(1), 143-152.

Bungay, H. R., Whalen, W. J., and Sanders, W. M. 1969. Microprobe techniques for determining diffusivities and respiration rates in microbial slime systems. *Biotechnology and Bioengineering*, 11, 765-722.

Clark, L. C., Wolf, R., Granger, D., and Taylor, A. 1953. Continuous Recording of Blood Oxygen Tension by Polarography. *Journal of Applied Physiology.*, 6, 189-193.

Clifford, M. 1990. *Electric/electronic motor data handbook*. Prentice-Hall Inc., Englewood Cliffs, NJ.

de Beer, D., and Schramm, A. 1999. Micro-environments and mass transfer phenomena in biofilms studied with microsensors. *Water Science and Technology*, 39(7), 173-178.

de Beer, D., and Stoodley, P. 1995. Relation between the structure of an aerobic biofilm and transport phenomena. *Water Science and Technology*, 32(8), 11-18.

de Beer, D., Stoodley, P., and Lewandowski, Z. 1994. Liquid flow in heterogeneous biofilms. *Biotechnology and Bioengineering*, 44(5), 636-641.

Eberl, H. J., Picioreanu, C., Heijnen, J. J., and van Loosdrecht, M. C. M. 2000. Three-dimensional numerical study on the correlation of spatial structure, hydrodynamic conditions, and mass transfer and conversion in biofilms. *Chemical Engineering Science*, 55(24), 6209-6222.

Fu, Y. C., Zhang, T. C., and Bishop, P. L. 1994. Determination of effective oxygen diffusivity in biofilms grown in a completely mixed biodrum reactor. *Water Science and Technology*, 455-462.

Heineman, W. R. 1989. Voltammetry: basic concepts and hydrodynamic techniques. Capter 29, in: *Chemical instrumentation: A systematic aproach.*, H. A. S. a. W. R. Heineman., ed., John Wiley & Sons Inc., NY.

Horn, H., Wasche, S., and Hempel, D. C. 2002. Simulation of biofilm growth, substrate conversion and mass transfer under different hydrodynamic conditions. *Water Science and Technology*, 46(1-2), 249-252.

Lenk, J. D. 1984. *Handbook of microcomputer-based instrumentation and controls.* Prentice-Hall Inc., Englewood Cliffs, NJ.

Lewandowski, Z., Stoodley, P., and Altobelli, S. 1995. Experimental and conceptual studies on mass transport in biofilms. *Water Science and Technology*, 31(1), 153-162.

Lu, R. 2001. A Field Study On Oxygen Penetration Into Wastewater Biofilms., M.Sc. Thesis, University of Alberta., Edmonton, Alberta, Canada.

Lu, R., and Yu, T. 2002a. Fabrication and evaluation of an oxygen microelectrode applicable to environmental engineering and science. *Journal of Environmental Engineering and Science*, 1(1), 225-235.

Lu, R., and Yu, T. 2002b. A field study on oxygen penetration in wastewater biofilms. *Proceedings of the 75th Annual Water Environment Federation Conference*, Chicago, Illinois, September 31 - October 2.

Martin-Cereceda, M., Perez, U. B., Serrano, S., and Guinea, A. 2002. An integrated approach to analyse biofilms of a full scale wastewater treatment plant. *Water Science and Technology*, 46(1), 199-206.

Massol-deya, A. A., Whallon, J., Hickey, R. F., and Tiedje, J. M. 1995. Channel structures in Aerobic biofilms of fixed-film reactors treating contaminated groundwater. *Applied and Environmental Microbiology*, 61(2), 769-777.

Miner, G. F., and Comer, D. J. 1992. *Physical data acquisition for digital processing.* Prentice-Hall Inc., Englewood Cliffs, NJ.

Morgenroth, E., Eberl, H., and van Loosdrecht, M. C. M. 2000a. Evaluating 3-D and 1-D mathematical models for mass transport in heterogeneous biofilms. *Water Science and Technology*, 41(4), 347-356.

Morgenroth, E., van Loosdrecht, M. C. M., and Wanner, O. 2000b. Biofilm models for the practitioner. *Water Science and Technology*, 41(4), 509-512.

Nishidome, K., Kusuda, T., Watanabe, Y., Yamauchi, M., and Mihara, M. 1994. Determination of oxygen transfer rate to a rotating biological contractor by microelectrode measurement. *Water Science and Technology*, 471-477.

Noguera, D. R., Okabe, S., and Picioreanu, C. 1999a. Biofilm modeling: presents status and future directions. *Water Science and Technology*, 39(7), 273-278.

Noguera, D. R., Pizarro, G., Stahl David, A., and Rittmann Bruce, E. 1999b. Simulation of multispecies biofilm development in three dimensions. *Water Science and Technology*, 39(7), 123-130.

Overgaard, A. B. 1993. *The oxygen microelectrode, a construction manual.* Technical University of Denmark., Lyngby, Denmark.

Picioreanu, C., van Loosdrecht, M. C. M., and Heijnen, J. J. 1999. Discrete-differential modelling of biofilm structure. *Water Science and Technology*, 39(7), 115-122.

Rasmussen, K., and Lewandowski, Z. 1998a. The accuracy of oxygen flux measurements using microelectrodes. *Water Research*, 32(12), 3747-3755.

Rasmussen, K., and Lewandowski, Z. 1998b. Microelectrode measurements of local mass transport rates in heterogeneous biofilms. *Biotechnology and Bioengineering*, 59(3), 302-309.

Revsbech, N. P. 1989. An Oxygen Microsensor with a Guard Cathode. *Limnology and Oceanography*, 34(2), 474-478.

Revsbech, N. P., and Jorgensen, B. B. 1986. Microelectrodes: their use in microbial ecology. *Advanced Microbiology and Ecology*, 9, 293-352.

Rittmann, B. E., and McCarty, P. L. 1980a. Design of Fixed-Film Processes with Steady-State-Biofilm Model. *Progress in Water and Technology*, 12, 23-27.

Rittmann, B. E., and McCarty, P. L. 1980b. Model of steady-state-biofilm kinetics. *Biotechnology Bioengineering.*, 22, 2343-2357.

Santegoeds, C. M., Muyzer, G., and de Beer, D. 1998. Biofilm dynamics studied with microsensors and molecular techniques. *Water Science and Technology*, 37(4-5), 125-129.

Travis, J. 2002a. Advanced File I/O, Printing, and Reports. Chapter 15, in: *LabVIEW for Everyone.*, Prentice-Hall., Upper Saddle River, NJ.

Travis, J. 2002b. Advanced LabVIEW Functions and Structures. Chapter 12, in: *LabVIEW for Everyone.*, Prentice-Hall, Upper Saddle River, NJ.

Travis, J. 2002c. Controlling Program Execution with Structures. Chapter 6, in: *LabVIEW for Everyone.*, Prentice-Hall, Upper Saddle River, NJ.

Travis, J. 2002d. DAQ and Instrument Control in LabVIEW. Chapter 11, in: *LabVIEW for Everyone.*, Prentice-Hall, Upper Saddle River, NJ.

Travis, J. 2002e. The LabVIEW Environment: Building your own workbench. Chapter 3, in: *LabVIEW for Everyone*, Prentice-Hall., Upper Saddle River, NJ.

Travis, J. 2002f. *LabVIEW for everyone.*, Second edition. Prentice-Hall., Upper Saddle River, NJ.

Travis, J. 2002g. LabVIEW Fundations. Chapter 4, in: *LabVIEW for Everyone.*, Prentice-Hall, Upper Saddle River, NJ.

Travis, J. 2002h. LabVIEW's Composite Data: Arrays and Clusters. Chapter 7, in: *LabVIEW for Everyone.*, Prentice Hall, Upper Saddle River, NJ.

Travis, J. 2002i. Yet More Fundations. Chapter 5, in: *LabVIEW for Everyone*, Prentice-Hall, Upper Saddle River, NJ.

Wasche, S., Horn, H., and Hempel, D. C. 2000. Mass transfer phenomena in biofilm systems. *Water Science and Technology.*, 41(4-5), 357-360.

Wasche, S., Horn, H., and Hempel Dietmar, C. 2002. Influence of growth conditions on biofilm development and mass transfer at the bulk/biofilm interface. *Water Research.*, 36(19), 4775-4784.

Whalen, W. J., Bungay, H. R., and Sabders, W. M. 1969. Microelectrode determination of oxygen profiles in microbial slime systems. *Environmental Science and Technology*, 3(12), 1297-1298.

Yu, T. 2000. Stratification Of microbial Processes And Redox Potential Changes In Biofilms., PhD Dissertation., University of Cincinnati, Cincinnati, Ohio, USA.

Zhang, T. C., and Bishop, P. L. 1994a. Density, porosity, and pore structure of biofilms. *Water Research*, 28(11), 2267-2277.

Zhang, T. C., and Bishop, P. L. 1994b. Experimental determination of the dissolved oxygen boundary layer and mass transfer resistance near the fluid-biofilm interface. *Water Science and Technology*, 30(11), 47-58.

Zhang, T. C., and Bishop, P. L. 1994c. Structure, activity and composition of biofilms. *Water Science and Technology*, 29(7), 335-344.

Zhang, T. C., Fu, Y. C., and Bishop, P. L. 1995. Competition for substrate and space in biofilms. *Water Environment Research*, 67(6), 992-1003.

Zhu, X., Suidan, M. T., Alonso, C., Yu, T., Kim, B. J., and Kim, B. R. 2001. Biofilm structure and mass transfer in a gas phase trickle-bed biofilter. *Water Science and Technology.*, 43(1), 285-293.

7.0 APPENDICES

APPENDIX A. COMPUTER PROGRAM DEVELOPMENT.

The first part of the computer program development was the construction of the front panel. The front panel of the software was designed with a friendly user interface divided in dialog tab controls to facilitate the control of each component. The program was divided in the following tab sections:

- Set Controls: used to specify the number and characteristics of the profiles required.
- Micromanipulator: used to control the parameters of the motorized micromanipulator.
- 2-D stage: used to control the two-dimensional stage parameters.
- Data Acquisition: used to control the data acquisition parameters and show the collected data in plots.
- Calibration Curve: used as a data acquisition utility, to facilitate the microelectrode calibration process.
- Help: provided directions of how to use this program.

The components and the use of the front panel will be explained in the form of a real application. The real settings used in the experiments of this study will be used as an

example to describe the functionality of the front panel.

Before the profile measurements started, the automation system was preset to measure 100 profiles in a 10 × 10 array. The distance required between each profile was 100 μm. In order to execute each profile measurement, the motorized micromanipulator had to move down a total of 1600 μm, stopping every 80 μm to collect two readings from the analog-to-digital converter output. This means that the motorized micromanipulator had to move twenty "steps" down (80 μm each step) to cover the 1600 μm required (in this computer program a "step" is a movement of a preset distance). When the twenty steps down were completed, then the micromanipulator had to move up 1600 μm to its original position in one single step. Then, the two-dimensional stage had to move 100 μm to the next position, where a new profile measurement had to be executed.

In order to set the computer program so that the automation system can achieve the automated control described previously, the following procedure needs to be conducted in the front panel of the computer program:

1. The "SET CONTROLS" window.

Open the "SET CONTROLS" window in the front panel. This window is shown in Figure A1. First, set the "profile controls" menu (number 1 in the figure). In this menu, set the "number of steps in each profile" to 20 and the "number of samples in each step" to 2. This will set the system to perform twenty steps of the desired distance (i.e. 80 μm) during each profile measurement and take two readings from the analog-to-digital converter in each step. Then, set the "X-Y axis controls" menu (2). In this

menu, set the "number of profiles in X axis" control to 10 and the "number of profiles in Y axis" control to 10. This will set the system to carry out 100 profile measurements in a 10 × 10 array. The "profile indicators" menu (3) and the "current X-Y position" menu (4) will display information about the status of the profile being taken (depth and sample taken) and the X-Y position of the microelectrode, respectively. To obtain the right status of the profile in the "profile indicators" menu (3), it is necessary to enter the distance of each step required (in this case 80 μm) in the "specify step" control.

Figure A1. The "SET CONTROLS" window in the front panel of the computer program.

2. The "MICROMANIPULATOR" window.

Open the "MICROMANIPULATOR" window. This window is shown in Figure A2. In this window, there are two main menus: the "setup step down" menu and the "setup step up" menu.

Set the "profile controls" in the "setup step down" menu (1). Set the "VISA resource name" control to port ASRL1, which means that the communication between the computer and the controller is through that specific serial port. Set the "set velocity" control to 50 μm/s. The "stand by" control, which is a specific feature of the program not used in this application, needs to be set to zero. Set the "start" control to zero. This means that each step will start at a relative position of zero. Set the "step" control to 80 μm. This will move the motor of the micromanipulator 80 μm down to complete each step. Set the "end" control to 80 μm. This will stop the motor when the micromanipulator reaches 80 μm in every step. Set the "resting time after reaching depth" control to zero. This means that the motor of the micromanipulator will wait zero seconds between each step.

Set the "profile controls" in the "setup step up" menu (2). Once again, set the "VISA resource name" to port ASRL1, the "set velocity" control to 50 μm/s and the "stand by" control to zero. Set the "start" control to –1600 μm. This will return the motor to the original position, where it was prior to the twenty steps of 80 μm were executed. Set the "step" control to 1600 μm. This will move the motor the required 1600 μm to return the motor to its original position. Set the "end" control to –1600 μm. This

will stop the motor at its original position. Set the "resting time after reaching depth" control to zero.

Set the two "time control between profiles" controls (3) to 60 seconds. This will hold the motor at its original position for one minute before the next profile starts.

The "status of the motor" menus (4 and 5) will display information about the motor-computer communication and the motor position while the program is running, executing the programmed movements and measurements.

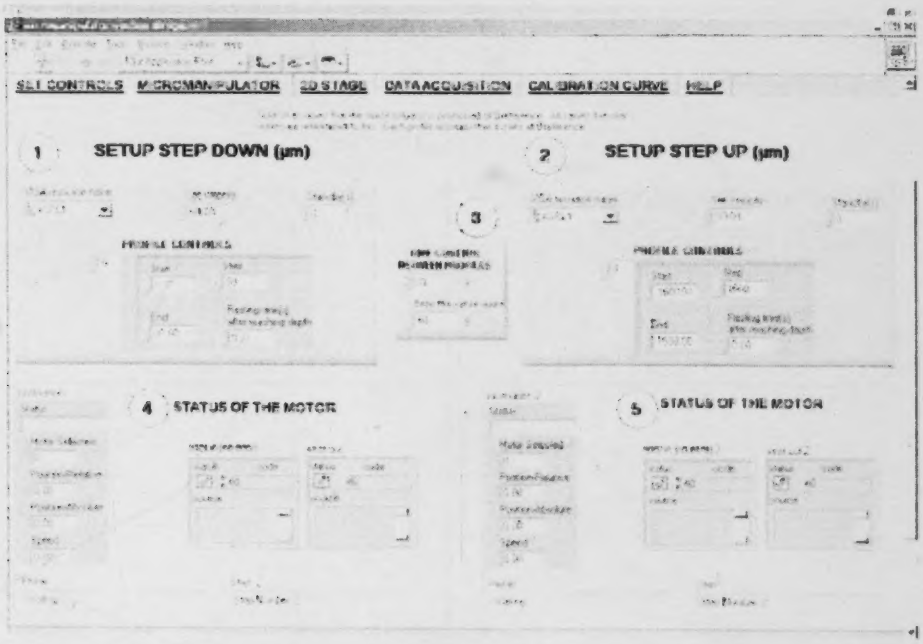

Figure A2. The "MICROMANIPULATOR" window in the front panel of the computer program.

3. The "2D STAGE" window.

Open the "2D STAGE" window. This window is shown in Fibure A3. There are three main menus in this window. The "set X axis movement", the "set Y axis movement" and the "2D stage indicators".

First the "set X axis movement" menu (1) needs to be set. This menu will control the movements of the X-axis. Through this menu, the computer program will read two files carrying the relative distance that the two-dimensional stage will move in the X-axis and Y-axis. In this part of the program only the X-axis will be controlled, however, a Y-axis movement of zero micrometer still needs to be specified. To do this, specify the source file to be read for the X-axis and Y-axis movement in the "set X axis movement" menu (1). The file for each axis must be a text file, tab delimited with only one number on it. The number specifies the relative movement in X-axis and Y-axis. In the "specify source file (X axis)" control a text file with the number 0.1 needs to be specified. This will move the two-dimensional stage 100 μm (0.1 mm) in the X-axis. In the "specify source file (Y axis)" control a text file with the number 0 needs to be specified. This means that the two-dimensional stage will not move in the Y-axis with this control. However, as stated before, a file still needs to be specified. Also in this menu, the velocity needs to be set to 10 mm/s and the acceleration to 10 mm/sec^2.

The next step is to set the "set Y axis movement" menu (2). This menu is used to control the Y-axis movements of the two-dimensional stage. In this menu, there is a one-dimensional array with ten elements. Each element represents a relative movement command. The command is a string in the format: number-number-move.

The first number represents a relative movement (in mm) in the X-axis, the second number represents a relative movement (in mm) in the Y-axis, and the word "move" is the actual command. With this menu of the window only the Y-axis will be controlled, nevertheless, the X-axis movement still needs to be specified to zero micrometer. The first element of the array needs to be the string "0 0 move". This means that the two-dimensional stage will stay at the starting position (0,0) of the 10 × 10 array when the profile measurements start. In the following commands of the one-dimensional array of the menu enter the string "0 0.1 move". The first part of the string needs to be zero, because the X-axis is not being controlled by this control. The second part of the string needs to be 0.1, which means 0.1 mm (100 μm). There are ten elements in the one-dimensional array because there will be 10 relative movements in the Y-axis to complete the profile measurements of the 10 × 10 array. If a larger array of profile measurements is needed more elements can be added to the one-dimensional array of this menu. The small window at the left of the array can be used to view the additional elements by scrolling the arrows up and down.

Finally, the "2D stage indicators" menu (3) will provide information about the status, position and dynamic parameters of the two-dimensional stage while the program is running, executing the programmed movements and measurements.

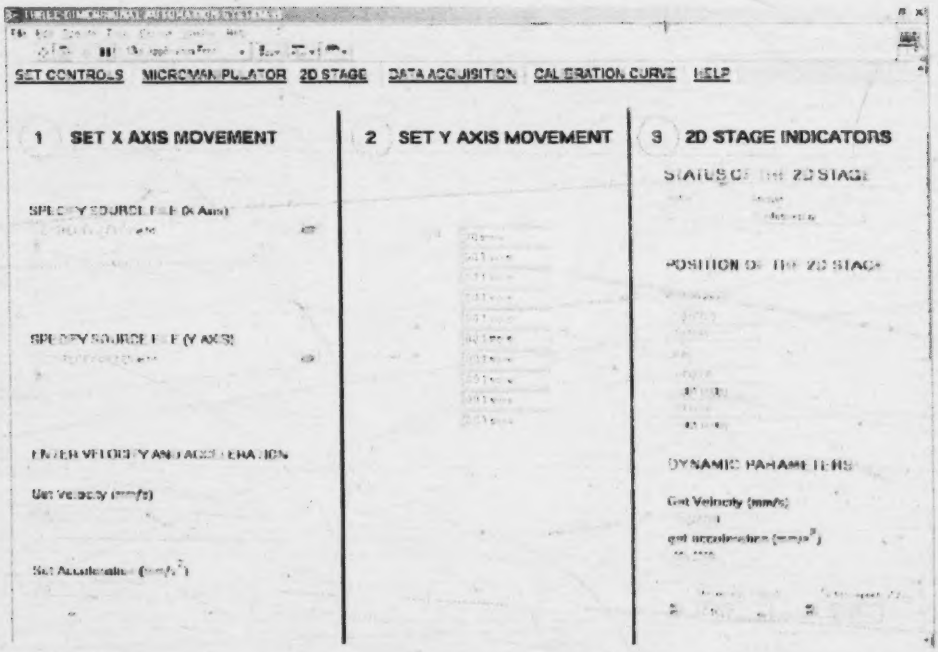

Figure A3. The "2D STAGE" window in the front panel of the computer program.

4. The "DATA ACQUISITION" window.

Open the "DATA ACQUISITION" window. This window is presented in Figure A4. The program can receive two signals (channel A and channel B) from the analog-to-digital converter. There are two graphs (1) where the signal can be plotted in real time, while the experiments are being conducted. The signal is stored in a text file. The text file has to be specified in the "save readings to" control that is placed below each graph prior to run the program.

In the "set DAS control" menu (2), enter the channel (A or B) that is been used to collect data from the picoammeter. Set the "wait to sample" control (2) to 1

second. This will make the system wait for 1 second between each reading taken from the analog-to-digital converter. Set the "port" control in the "open port" menu (3) to LPT1. This will establish communication between the program and the analog-to-digital converter through the printer port of the computer (LPT1). The indicator called "opened" that is below the "port" control (3) will report the status of the communication between the program and the analog-to-digital converter. If the number 1 is in the "opened" indicator it means that the communication between the computer and the analog-to-digital converter has been established successfully. If the number 0 is in this indicator, that means that there is an error in the communication, and the connections of the data acquisition system should be verified. The controls of the "set interval" menu (4) are fixed values. The number of samples to be taken has already been specified in the "SET CONTROLS" window previously described. Therefore, the "no of samples" control in the "set interval" menu (4) is set to 1. The "times per scan" control in the "set interval" menu (4) is an oscilloscope functionality of the program that was not used for this experiment. Therefore it should be fixed at the default value of 5000. Set the controls of the "set range" menu (5) to 20 Volts. This is the input voltage range that will be represented in digital values from 0 to 4092. It is recommendable to set the input voltage range to 20 Volts if only one channel is being used. This prevents noise from the unconnected channel interfering with the channel in use. There are indicators (6) that display the position of the microelectrode and the readings taken while the experiment is running. Once all the settings are specified, open the "SET CONTROLS" window, which is shown in Figure A1, press the "run" button, which is the white arrow located on LabVIEW's toolbar at the top part of the screen and then press the "start

profiles" button (number 5 in Figure A1). The automation system will start automatically and stop when all the profiles are completed. If for some reason, the program needs to be stopped before the completion of all the profiles, then press the "abort execution" button that is also on the LabVIEW's toolbar an the top part of the screen. The above is the procedure needed to achieve the commands described previously using the automation system. All these parts of the computer program work synchronized in order to complete preprogrammed movement and data acquisition tasks. However, there are still two more parts of the front panel that need to be described. They are the "CALIBRATION CURVE" and the "HELP" windows.

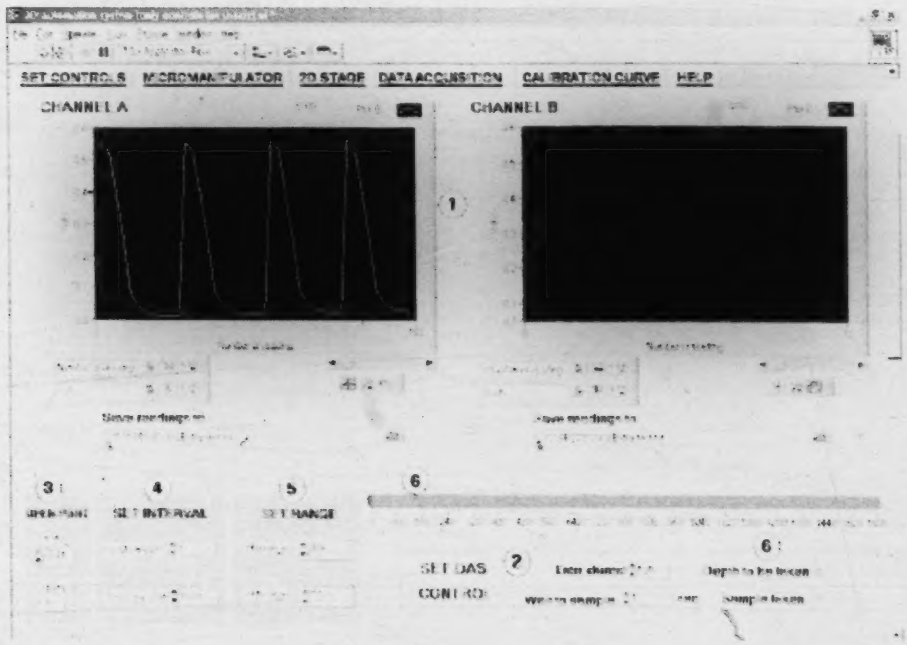

Figure A4. The "DATA ACQUISITION" window in the front panel of the computer program.

5. The "CALIBRATION CURVE" and the "HELP" windows.

The "CALIBRATION CURVE" window is very similar to the "DATA ACQUISITION" window previously described, except for the indicators of depth and samples taken, which are not present in the "CALIBRATION CURVE" window. This window is presented in Figure A5. The components of this window work independently from the other parts of the program. Its main function is to collect and store the data generated from the oxygen microelectrode calibration process. Once the readings from the experiment and the readings from the calibration process are in their respective files, the data is copied manually to MS Excel in order to plot the calibration curve. Then the experimental data is interpolated in the calibration curve in order to obtain the values of dissolved oxygen concentration. Finally, the "HELP" window, which is shown in Figure A6 contains the directions of how to use this program.

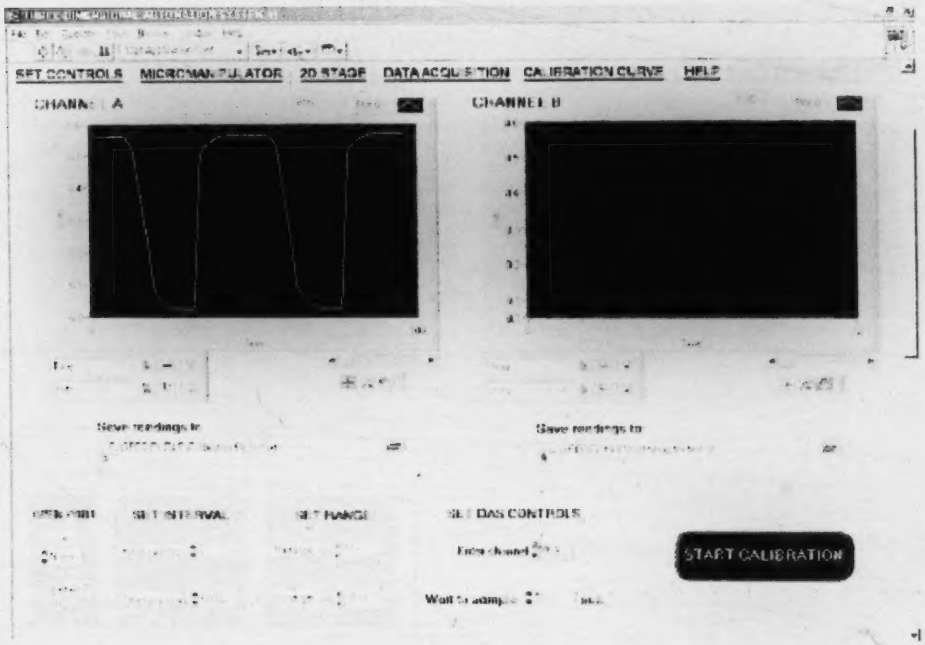

Figure A5. The "CALIBRATION CURVE" window in the front panel of the computer program.

Figure A6. The "HELP" window in the front panel of the computer program.

The second part of the computer program development was the creation of the block diagram, which contains the algorithm needed to synchronize the components of the automation system. The general approach to construct the block diagram was to construct relatively simple VIs capable of controlling each component of the automation system separately and then construct a more complex top-level program that contains the simple VIs in form of subVIs. Therefore, three single VIs were created in order to control separately the two-dimensional stage, the motor of the motorized micromanipulator and the data acquisition system.

The single VIs constructed for the control of the two-dimensional stage, the motorized micromanipulator and the data acquisition system had the same basic

principle. The principle was based on a three-steps path where the first step was to establish communication between the computer and the equipment, the second step was to read and interpret the instructions that the user enters in the front panel, and finally, the third step was to execute the commands.

The VIs constructed for the two-dimensional stage and the motorized micromanipulator establish communication with their respective controllers through two different serial ports (RS232) in the computer. The program reads the instructions entered by the user. Finally, the program interprets the commands and executes the movements.

The VI created to control the data acquisition system establishes communication with the analog-to-digital converter through the printer port (LPT1). Then the program reads the data acquisition conditions such as number of samples, time between sampling, voltage range, etc. Finally, the program collects the signal from the analog-to-digital converter output according to the preset setting interpreted previously by the program.

Once the three VIs were created, they were included in a top-level program, and then an algorithm was programmed in this top-level program to synchronize the functionality of the three VIs. For the algorithm to work, the user needs to specify the parameters of the profile measurements (step distance, number of samples, etc). The user also specifies the number of profile measurements that the automation system is going to accomplish in a form of a two-dimensional array. The algorithm executes the profile measurements in series of rows until the preset array (in this experiment the array was 10

× 10) is completed. In this way, the user can program the software and hence, the whole automation system to execute complicated tasks involving data collection and positioning of the oxygen microelectrode in three dimensions.

In the following paragraphs, the algorithm used to control the data acquisition system and the motion control system will be explained, using the source code written in the block diagram of LabVIEW®. The figures used to explain the algorithm are snapshots of the source code written in the block diagram of LabVIEW®. The elements in the figures are specific for LabVIEW® graphical programming. Therefore, the explanation of the algorithm will refer to the chapters of a LabVIEW® book by Travis, (2002f), where specific information of how to program the sections of the source code can be found. (The references that are cited in Appendix A are listed in the References section.)

The algorithm will be explained by using an example of the execution of one profile measurement. A series of seven commands are necessary to execute one profile measurement. These command series are repeated for the number of profile measurements pre-set in the front panel. The numeric values in the source code are either set by default by the computer or pre-set for the user in the front panel, therefore, they should remain unchanged in the source code of the program. These are the seven commands:

1. Calibrate the two-dimensional stage to the position zero (0,0).

The two-dimensional stage moves to the position (0,0) of the 10 × 10 array. Figure A7 shows the source code that executes this movement. The number four in the figure specifies the serial port of the computer at which the two-dimensional stage is connected; the number two specifies that the two-dimensional stage is using the two axes. The three boxes are subVIs that establish communication between the computer and the two-dimensional stage, and execute the movement (Travis, 2002e; Travis, 2002g; Travis, 2002i).

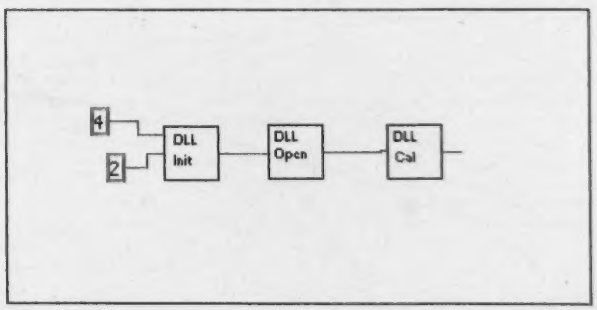

Figure A7. Source code used to calibrate the two-dimensional stage to the position (0,0) of the 10 × 10 array.

2. Set Y-axis position.

The two-dimensional stage moves to the specified Y-axis position. The first Y-axis position in the 10 × 10 array is the position (0,0). Figure A8 shows the source code that executes this movement. In the figure, the box with the letters [abc] represents the "SET Y AXIS MOVEMENT" control in the front panel of the program, and the boxes

are the subVIs used to execute the movement (Travis, 2002e; Travis, 2002g; Travis, 2002h; Travis, 2002i).

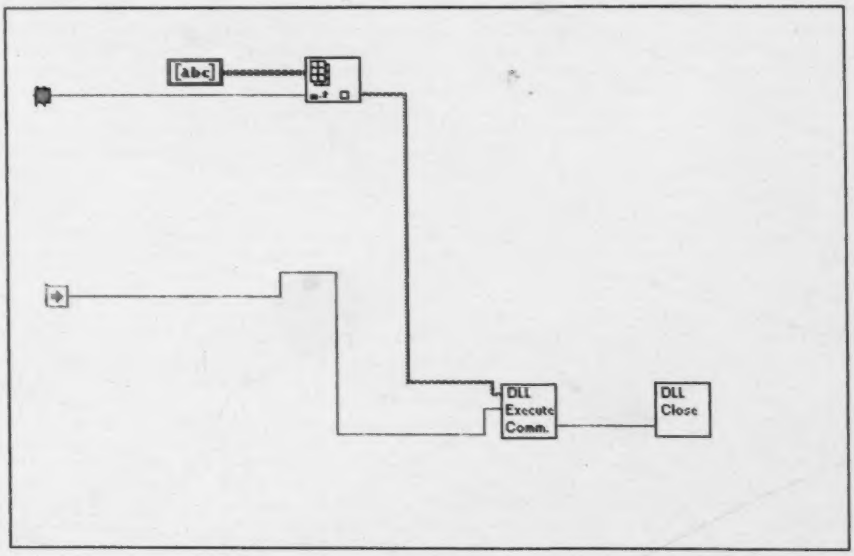

Figure A8. Source code used to control the Y-axis movement of the two-dimensional stage.

3. Set X-axis position.

The two-dimensional stage moves to the specified X-axis position. The first X-axis position in the 10 × 10 array is the position (0,0). Figure A9, Fifure A10 and Figure A11 show the source code that executes this movement. The subVIs used to establish communication between the computer and the two-dimensional stage are shown in Fifure A9 (Travis, 2002e; Travis, 2002g; Travis, 2002i). This figure also shows the subVIs used to set velocity and acceleration in the two-dimensional stage. The source code that represents the "SET X AXIS MOVEMENT" control in the front panel is shown in Figure

A10 (Travis, 2002a; Travis, 2002e; Travis, 2002g; Travis, 2002h; Travis, 2002i). The source code specifies the files to be read by the computer. As seen in the previous section, the movement in the X-axis is specified by two text files. Finally, Figure A11 shows the subVIs used to execute the X-axis movement (Travis, 2002c; Travis, 2002e; Travis, 2002g; Travis, 2002h; Travis, 2002i).

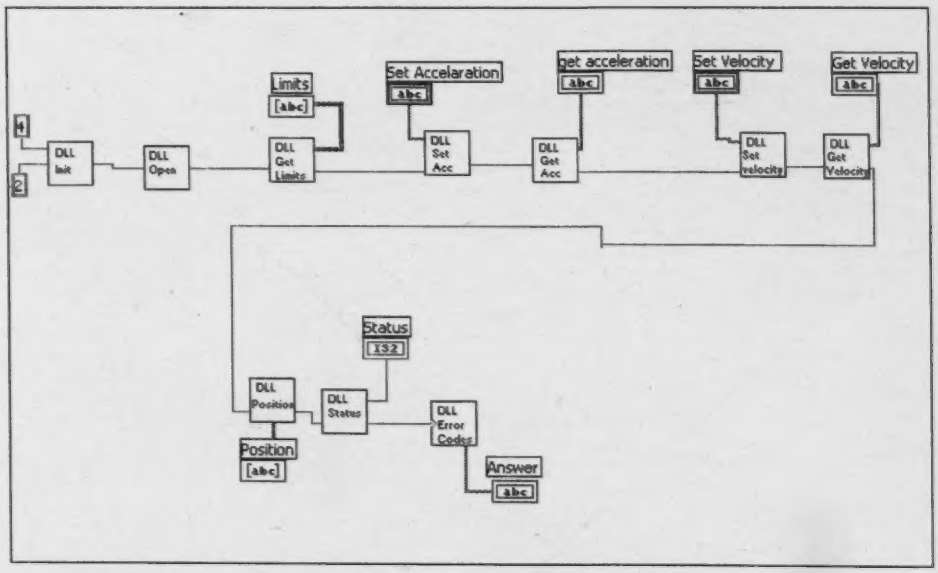

Figure A9. Source code used to establish communication between the computer and the two-dimensional stage.

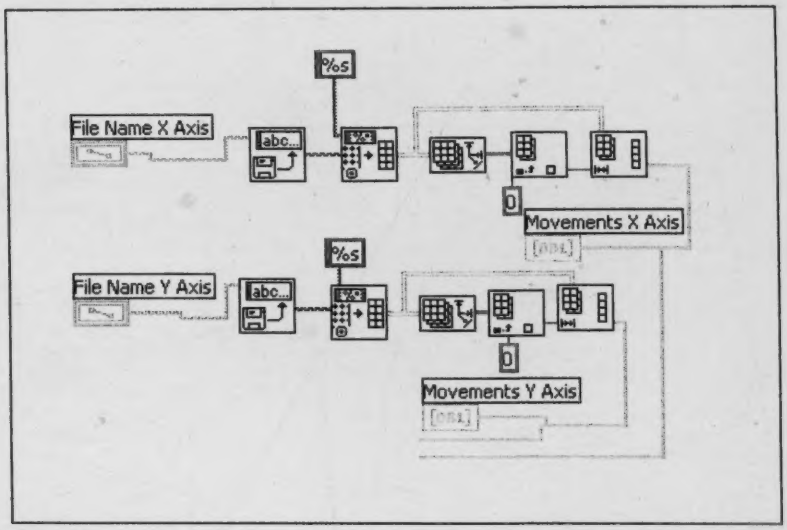

Figure A10. Source code used to read the files that set the X-axis movement of the two-dimensional stage.

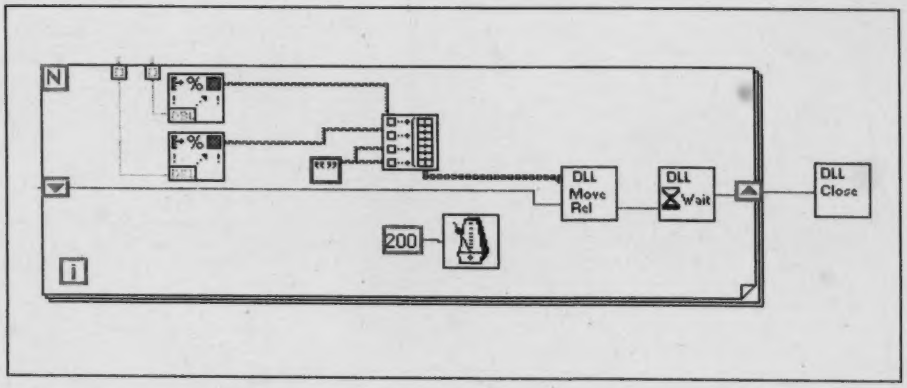

Figure A11. Source code used to control the X-axis movement of the two-dimensional stage.

4. Move motorized micromanipulator one step down.

Once the two-dimensional stage reached the specified X and Y position, the motorized micromanipulator is activated to execute the respective profile measurement. The oxygen microelectrode is moved downward by the motorized micromanipulator to the first depth, which in this experiment was 80 µm. Figure A12 and Figure A13 show the source code that executes this movement. Figure A12 shows the source code that establishes the communication between the computer and the motorized micromanipulator (Travis, 2002b; Travis, 2002d; Travis, 2002e; Travis, 2002g; Travis, 2002i). The numeric values shown in this figure are default values and, therefore, they should not be changed. Figure A13 shows the source code used to execute the 80 µm downward movement of the motorized micromanipulator (Travis, 2002c; Travis, 2002e; Travis, 2002g; Travis, 2002i).

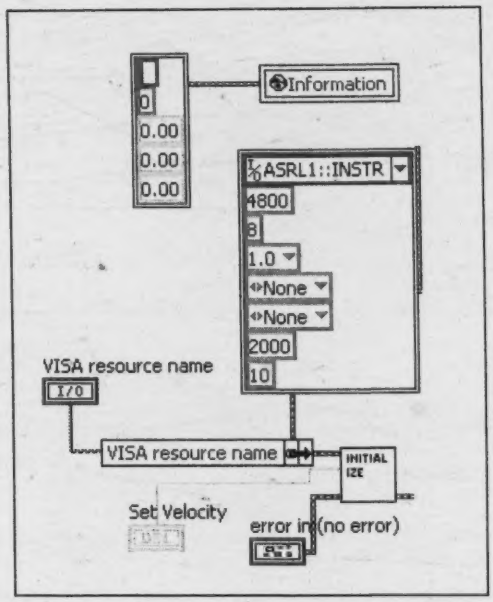

Figure A12. Source code used to establish communication between the computer and the motorized micromanipulator.

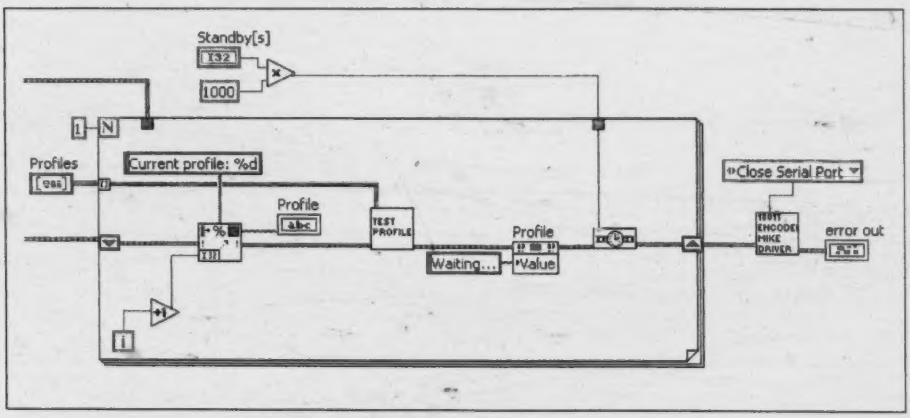

Figure A13. Source code used to control the downward movement of the motorized micromanipulator.

5. Take two readings.

Once the first downward movement of the motorized micromanipulator is executed, the data acquisition system takes two readings from the analog-to-digital converter. Figure A14 and Figure A15 show the source code that collects the readings from the analog-to-digital converter. Figure A14 shows the source code that establishes the communication between the computer and the analog-to-digital converter (Travis, 2002e; Travis, 2002g; Travis, 2002i). Figure A15 shows the source code that collects the digital data from the analog-to-digital converter. In this figure, it can be seen how the digital signal received from the analog-to-digital converter is converted to voltage values. The analog-to-digital converter is a 12-bit converter. This means that they produce values in the range from 0 to 4095 to represent the selected input voltage. Figure A15 shows how the source code converts the digital values to voltage values. First, 2048 are subtracted from the digital signal. The result is then multiplied by 20, which is the selected input voltage. Finally, this result is divided by 2048. The resulting voltage value is displayed in the plot of the front panel, which is represented in Figure A15 by the box with the words [DBL]. Figure A15 also shows the source code used to save the data to a file. This source code is shown in the right part of this figure (Travis, 2002a; Travis, 2002e; Travis, 2002g; Travis, 2002i).

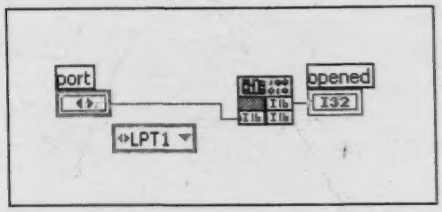

Figure A14. Source code used to establish communication between the computer and the data acquisition system.

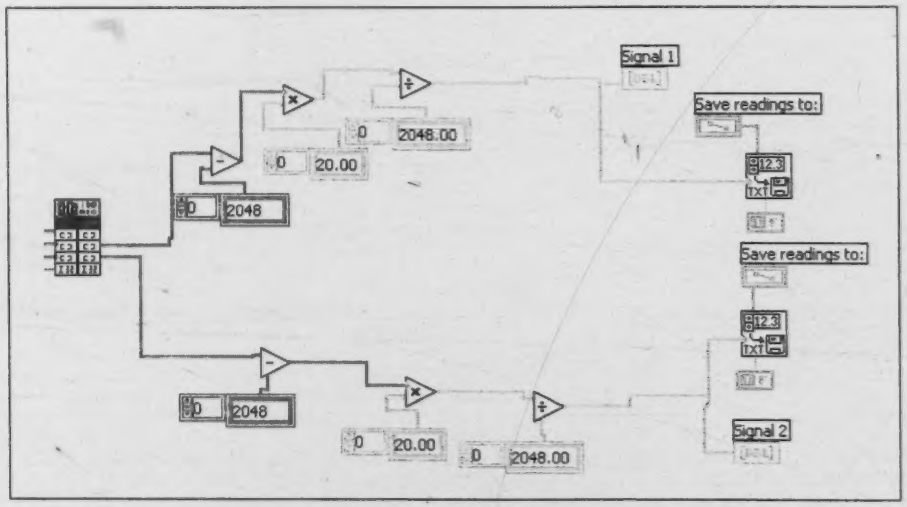

Figure A15. Source code used to collect the signal from the analog-to-digital converter.

6. Repeat commands four and five for the number of depths specified.

The commands four and five are repeated for the number of times specified in the front panel. In this experiment, the number of times that the commands four and five

were repeated was twenty times because in each profile measurement the microelectrode moved downward twenty steps of 80 μm, taking two readings in each step.

7. Move microelectrode up to initial position.

Once the twenty steps are completed the microelectrode moves up in one step to its initial position. Figure A16 and Figure A17 show the source code that executes this movement. Figure A16 shows the source code that establishes the communication between the computer and the motorized micromanipulator (Travis, 2002b; Travis, 2002d; Travis, 2002e; Travis, 2002g; Travis, 2002i). The numeric values shown in this figure are default values and, therefore, they should not be changed. Figure A17 shows the source code used to execute the 1600 μm upward movement of the motorized micromanipulator to its initial position (Travis, 2002c; Travis, 2002e; Travis, 2002g; Travis, 2002i). When the motorized micromanipulator reaches its initial position, the series of seven commands are then repeated in order to measure the next profile of the 10 × 10 array.

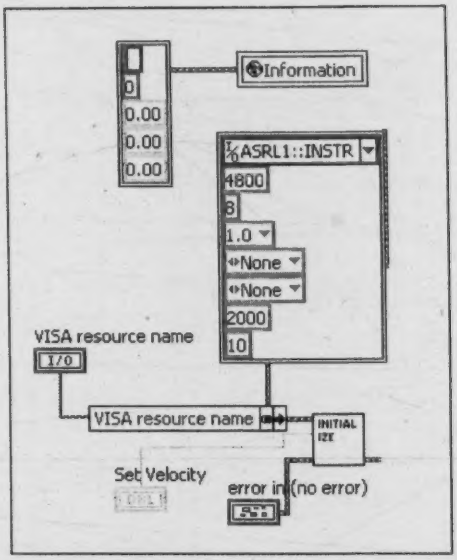

Figure A16. Source code used to establish communication between the computer and the motorized micromanipulator.

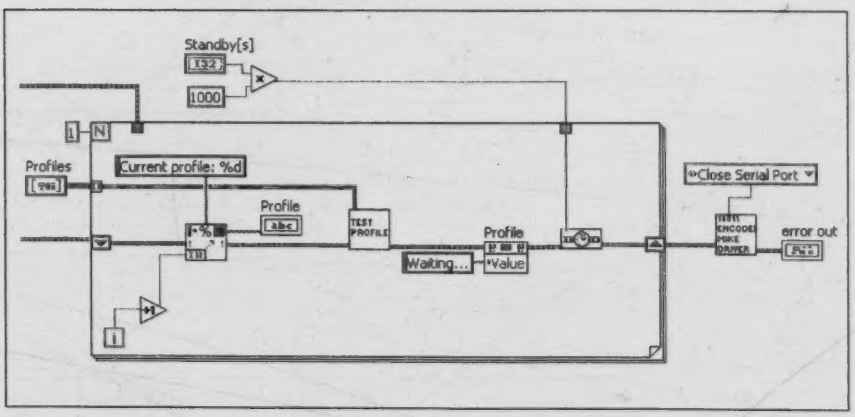

Figure A17. Source code used to control the upward movement of the motorized micromanipulator.

APPENDIX B. OXYGEN DISTRIBUTION FROM THE ARTIFICIAL PLANE

- Dissolved oxygen distribution from the artificial plane in biofilm sample 1.

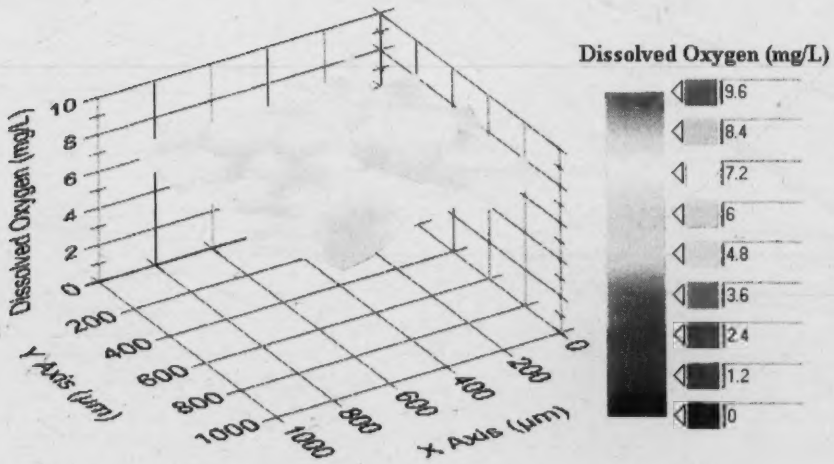

Figure B 1. Dissolved oxygen concentration at the artificial plane in biofilm sample 1, about 920 µm above the biofilm surface.

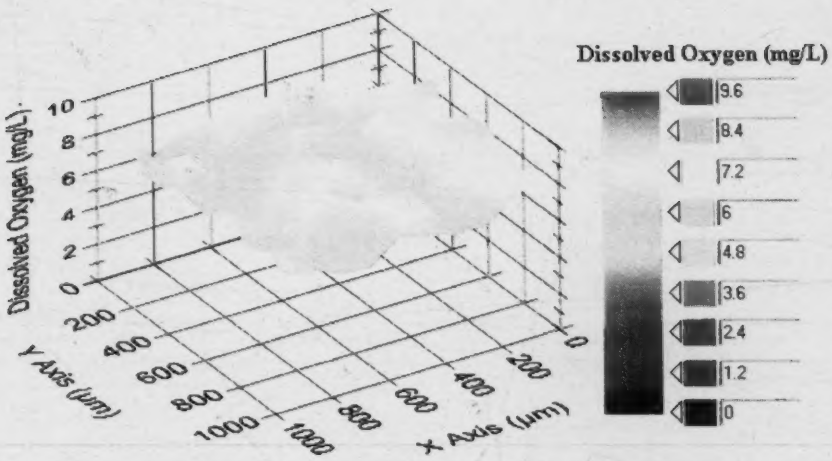

Figure B 2. Dissolved oxygen concentration 80 µm below the artificial plane in biofilm sample 1.

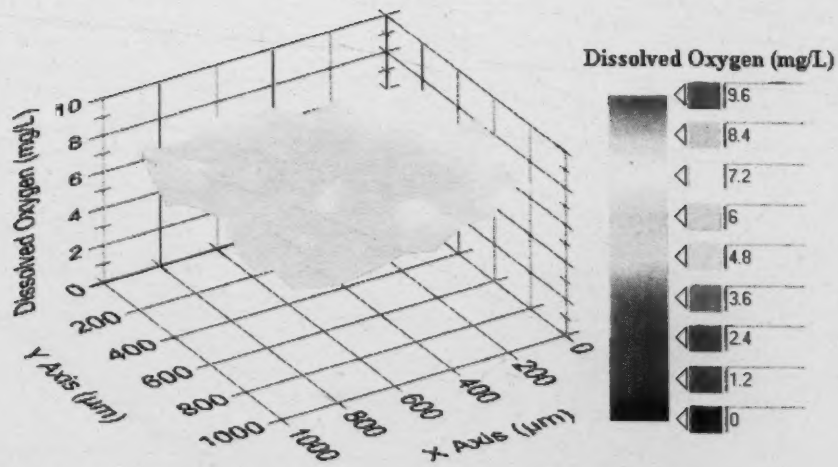

Figure B 3. Dissolved oxygen concentration 160 µm below the artificial plane in biofilm sample 1.

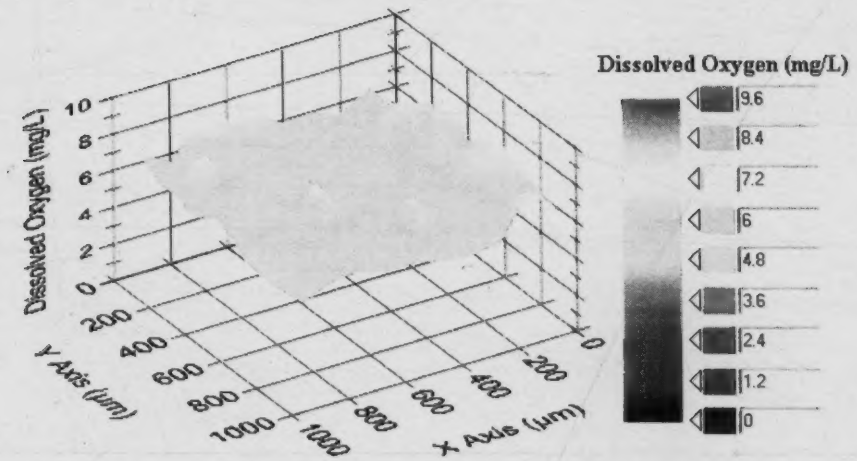

Figure B 4. Dissolved oxygen concentration 240 µm below the artificial plane in biofilm sample 1.

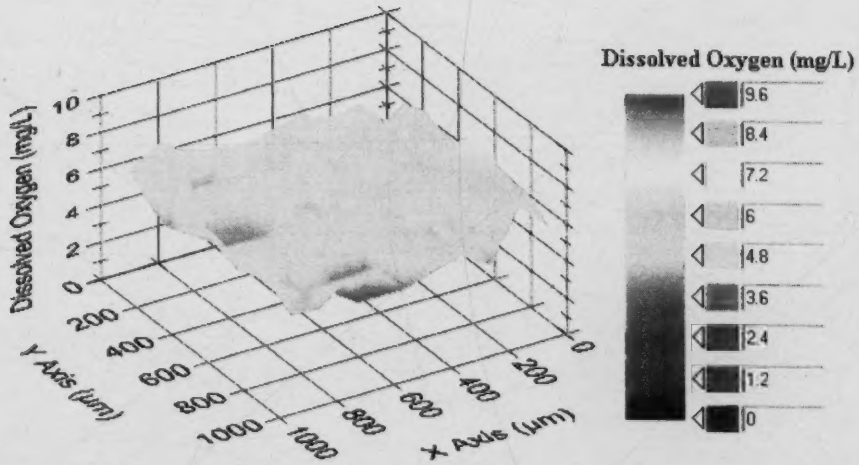

Figure B 5. Dissolved oxygen concentration 320 µm below the artificial plane in biofilm sample 1.

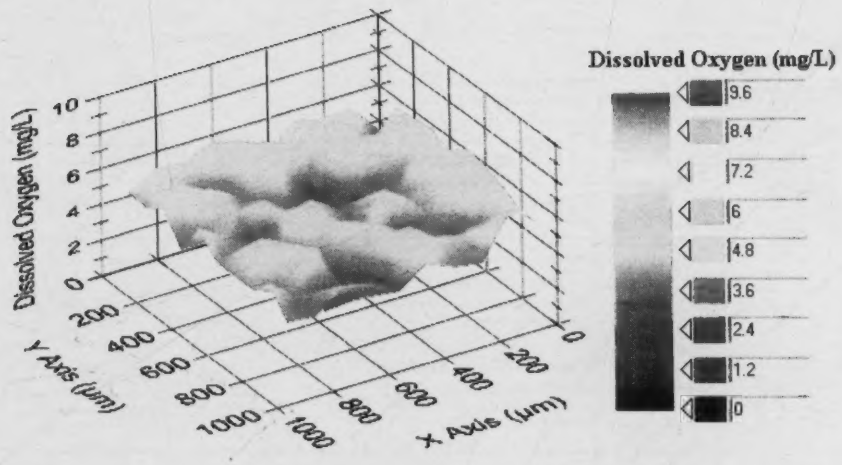

Figure B 6. Dissolved oxygen concentration 400 µm below the artificial plane in biofilm sample 1.

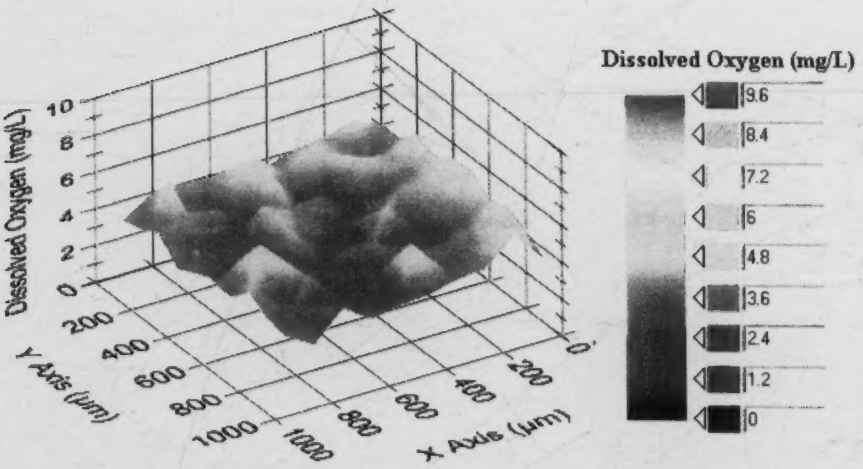

Figure B 7. Dissolved oxygen concentration 480 µm below the artificial plane in biofilm sample 1.

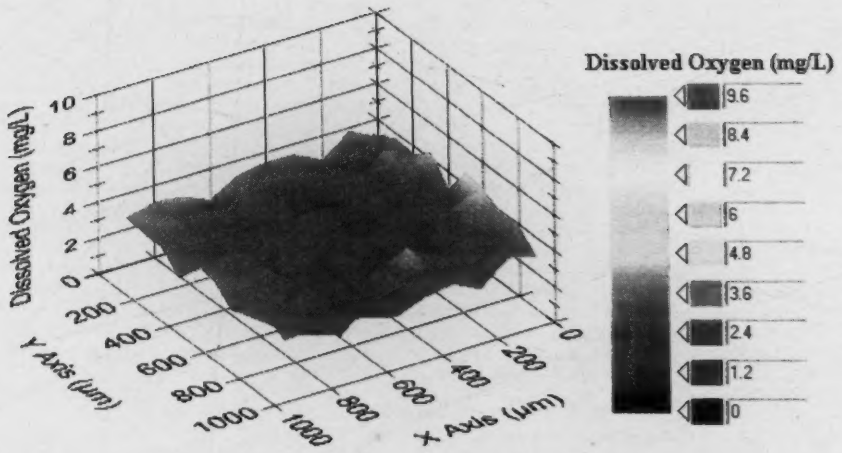

Figure B 8. Dissolved oxygen concentration 560 µm below the artificial plane in biofilm sample 1.

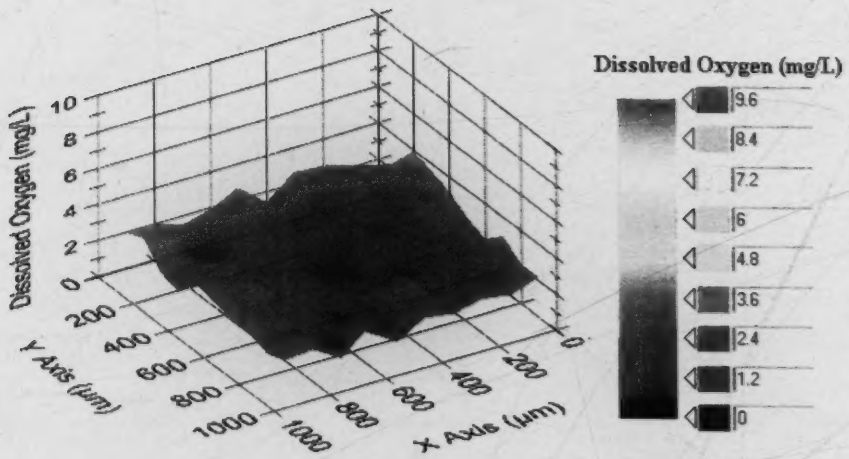

Figure B 9. Dissolved oxygen concentration 640 µm below the artificial plane in biofilm sample 1.

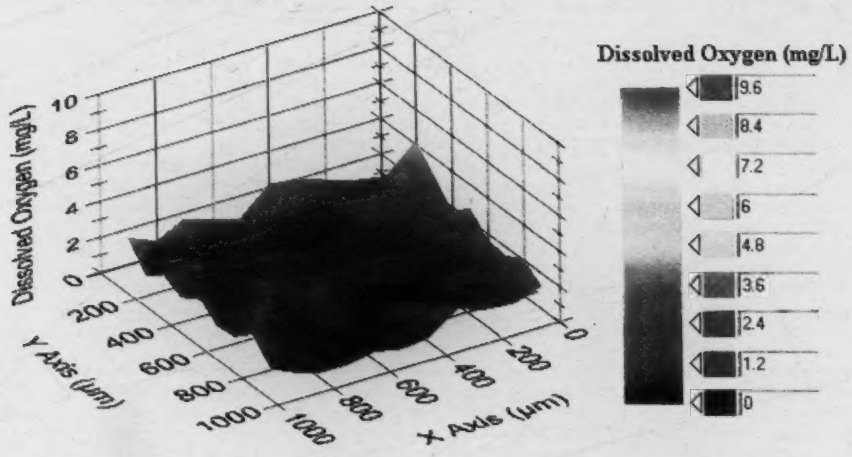

Figure B 10. Dissolved oxygen concentration 720 µm below the artificial plane in biofilm sample 1.

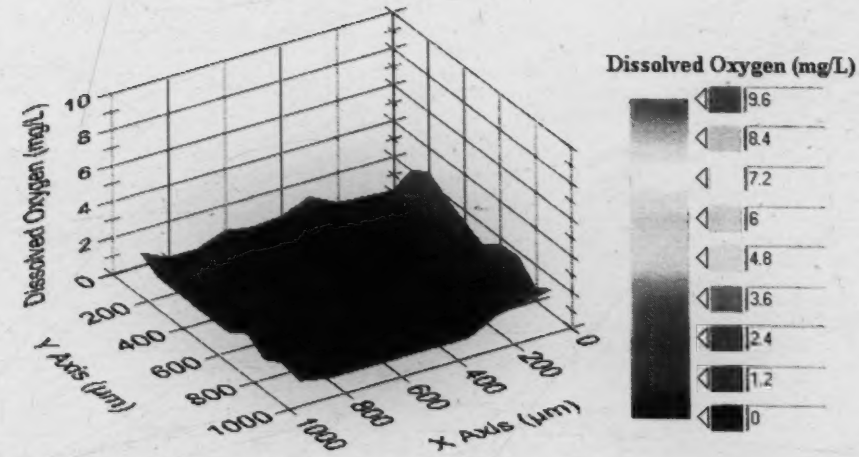

Figure B 11. Dissolved oxygen concentration 800 µm below the artificial plane in biofilm sample 1.

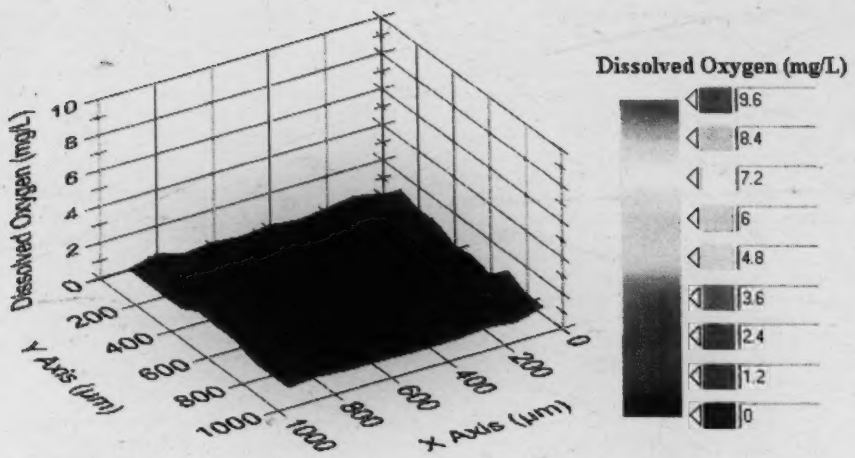

Figure B 12. Dissolved oxygen concentration 880 µm below the artificial plane in biofilm sample 1.

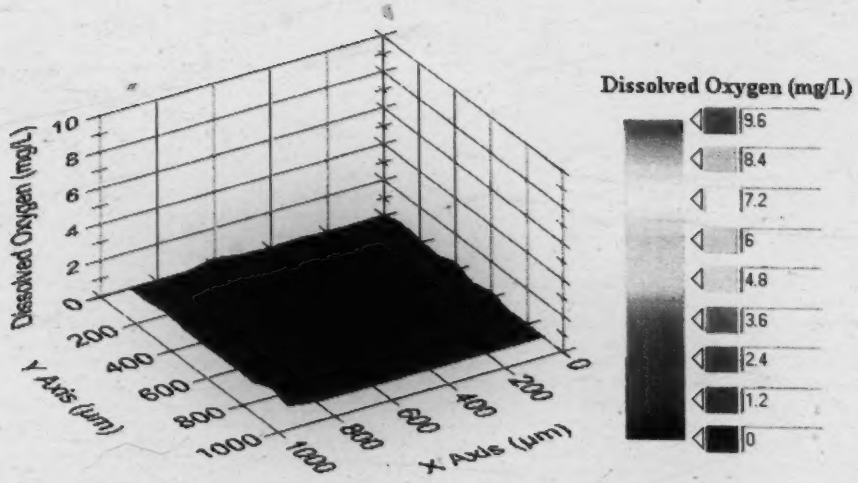

Figure B 13. Dissolved oxygen concentration 960 µm below the artificial plane in biofilm sample 1.

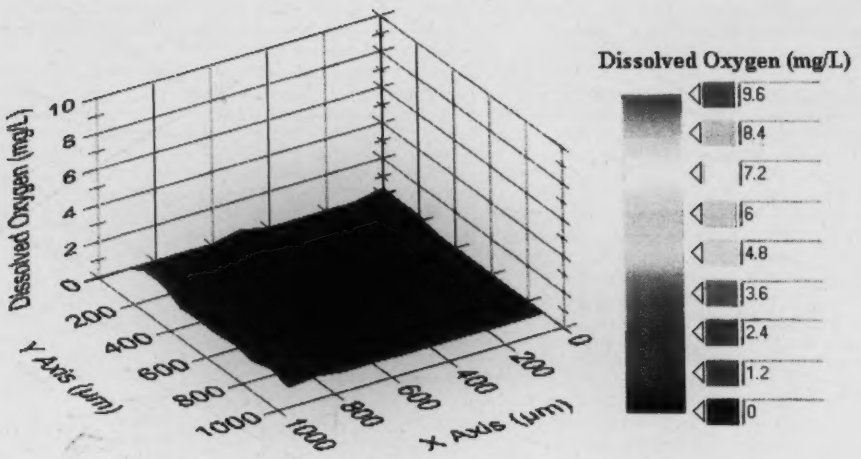

Figure B 14. Dissolved oxygen concentration 1040 µm below the artificial plane in biofilm sample 1.

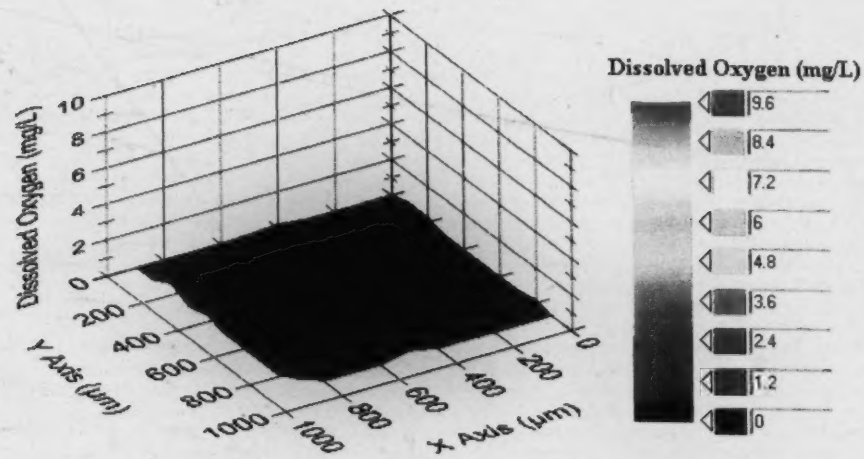

Figure B 15. Dissolved oxygen concentration 1120 µm below the artificial plane in biofilm sample 1.

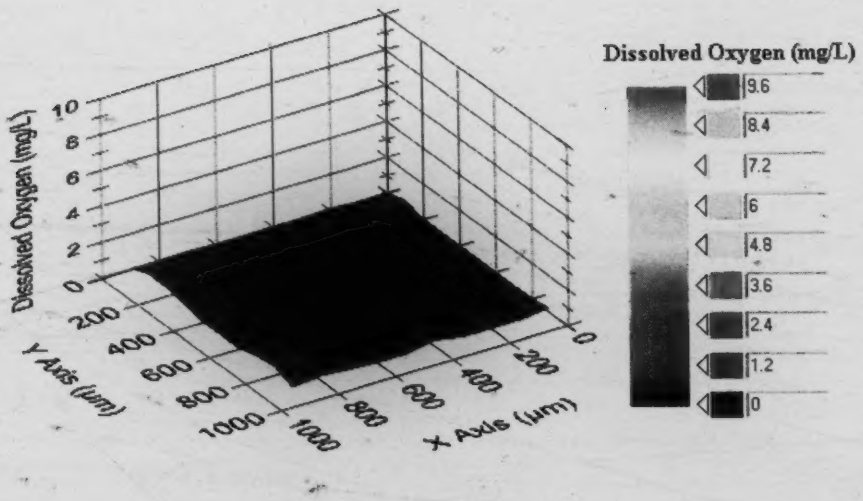

Figure B 16. Dissolved oxygen concentration 1200 µm below the artificial plane in biofilm sample 1.

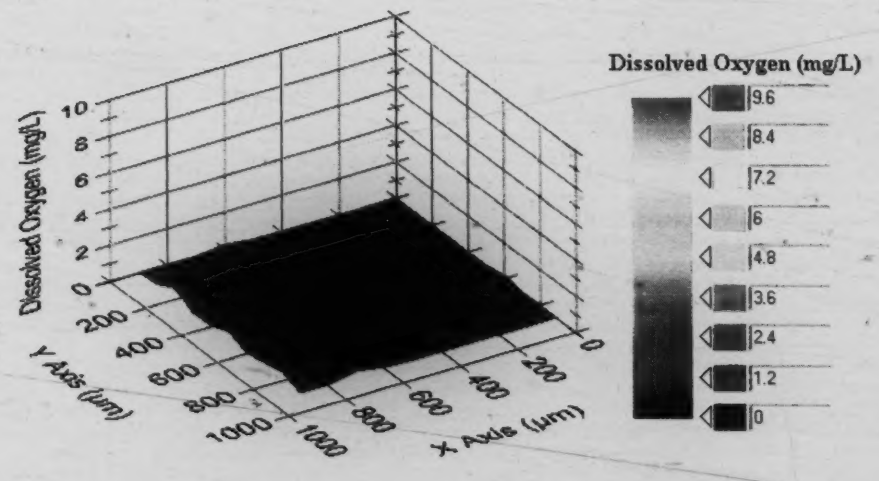

Figure B 17. Dissolved oxygen concentration 1280 µm below the artificial plane in biofilm sample 1.

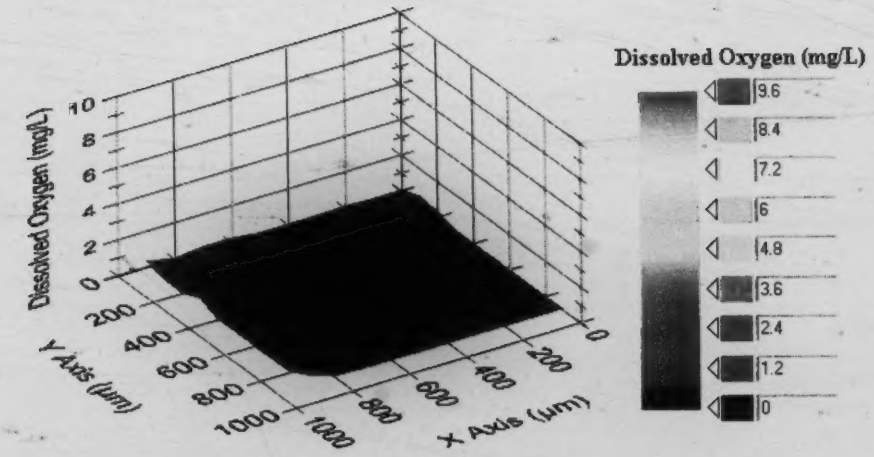

Figure B 18. Dissolved oxygen concentration 1360 µm below the artificial plane in biofilm sample 1.

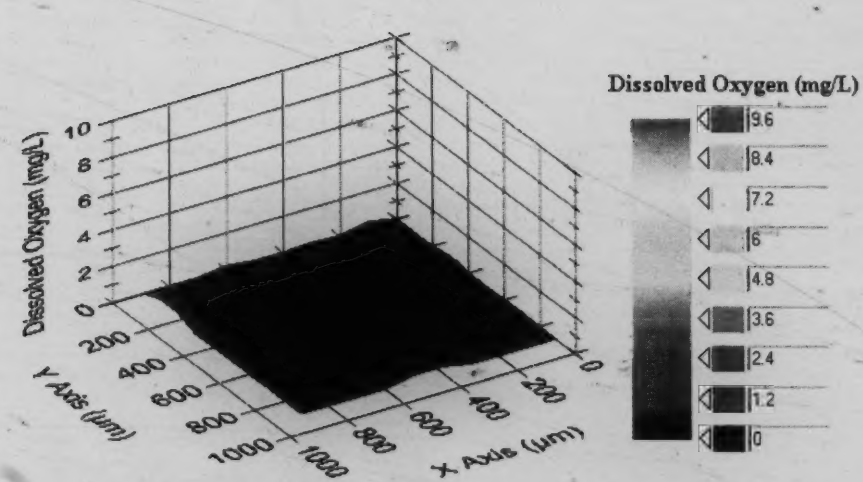

Figure B 19. Dissolved oxygen concentration 1440 µm below the artificial plane in biofilm sample 1.

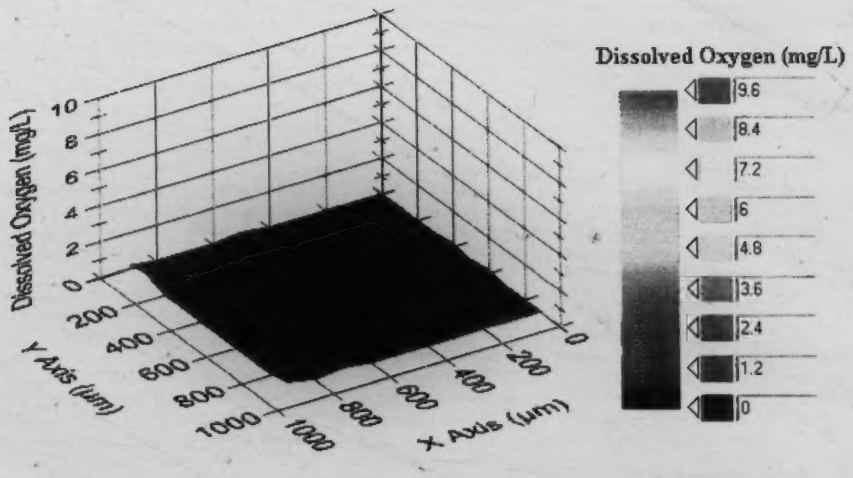

Figure B 20. Dissolved oxygen concentration 1520 µm below the artificial plane in biofilm sample 1.

- Dissolved oxygen distribution from the artificial plane in biofilm sample 2.

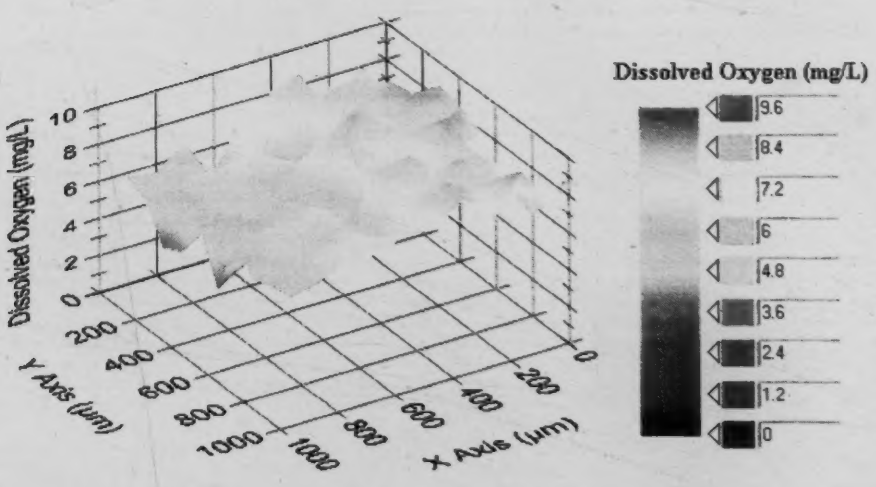

Figure B 21. Dissolved oxygen concentration at the artificial plane in biofilm sample 2, about 920 µm above the biofilm surface.

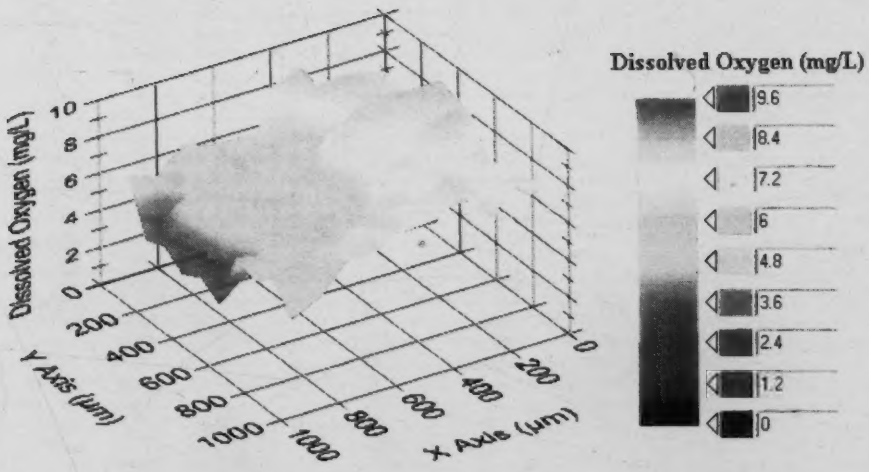

Figure B 22. Dissolved oxygen concentration 80 µm below the artificial plane in biofilm sample 2.

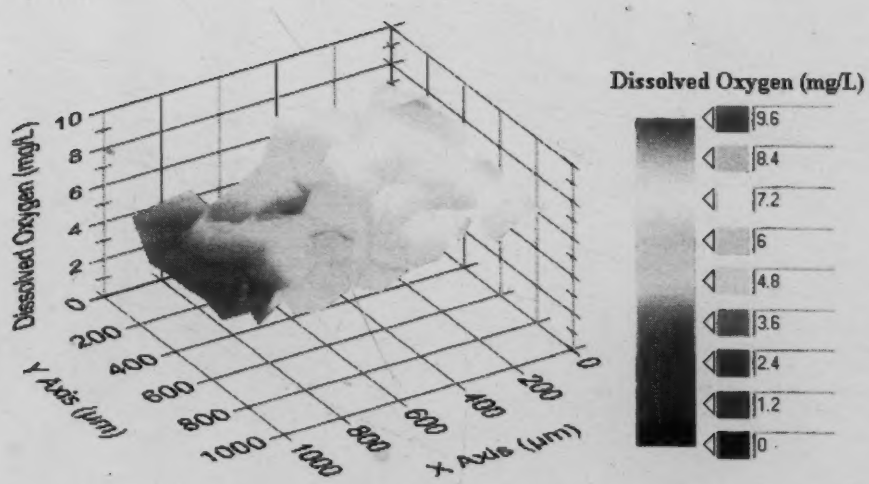

Figure B 23. Dissolved oxygen concentration 160 µm below the artificial plane in biofilm sample 2.

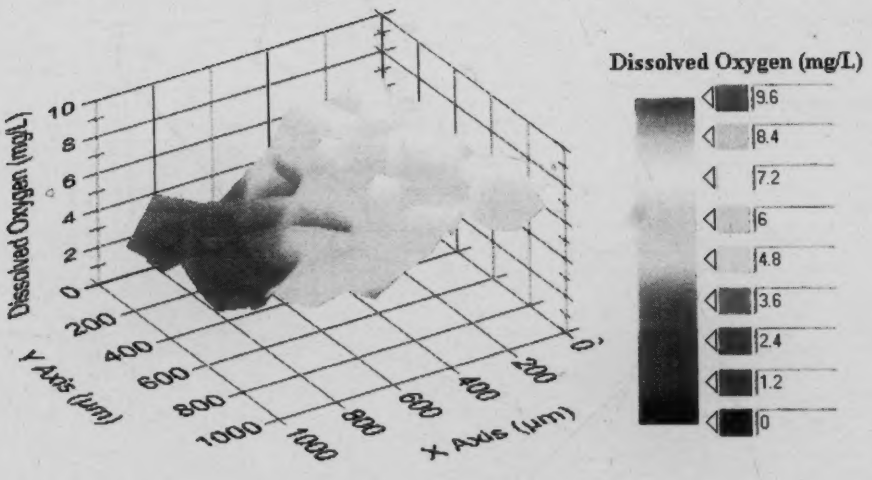

Figure B 24. Dissolved oxygen concentration 240 µm below the artificial plane in biofilm sample 2.

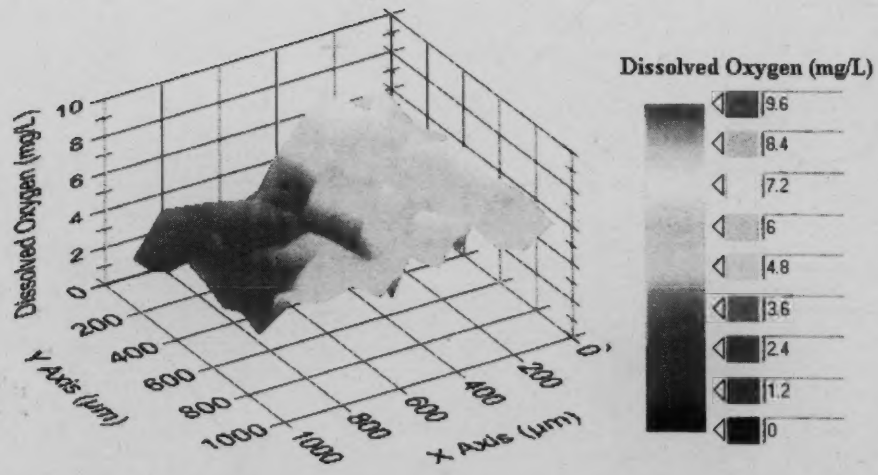

Figure B 25. Dissolved oxygen concentration 320 µm below the artificial plane in biofilm sample 2.

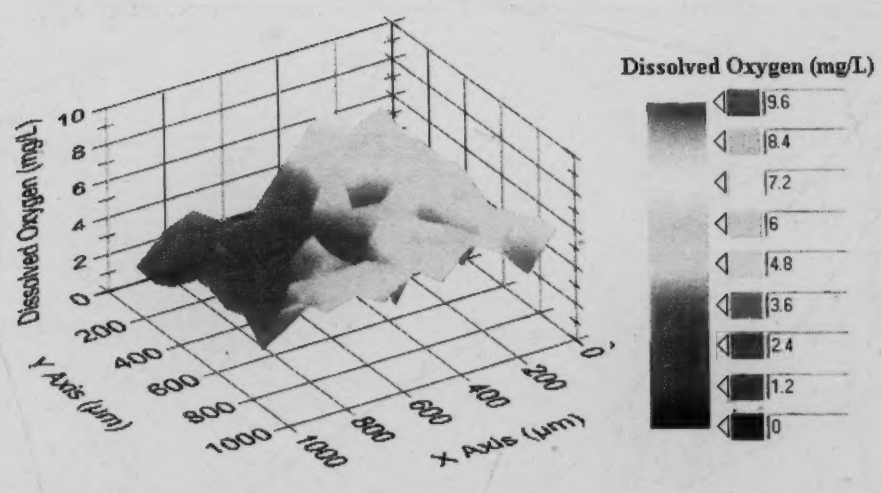

Figure B 26. Dissolved oxygen concentration 400 µm below the artificial plane in biofilm sample 2.

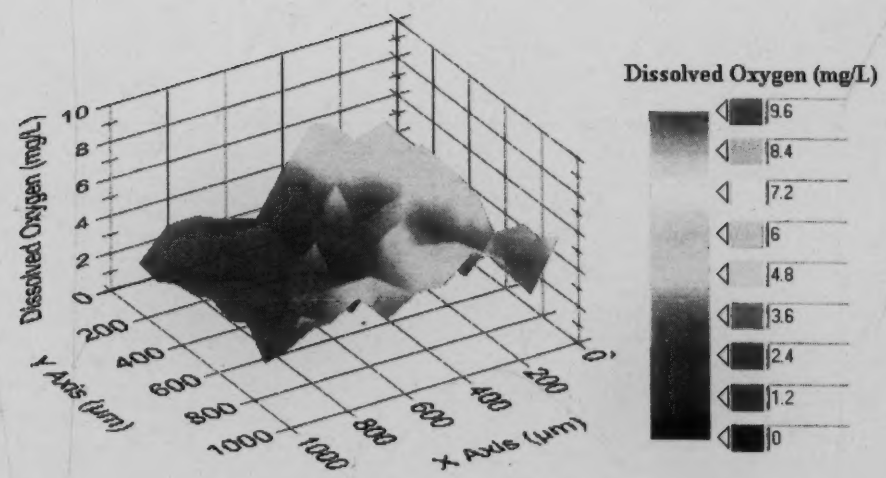

Figure B 27. Dissolved oxygen concentration 480 µm below the artificial plane in biofilm sample 2.

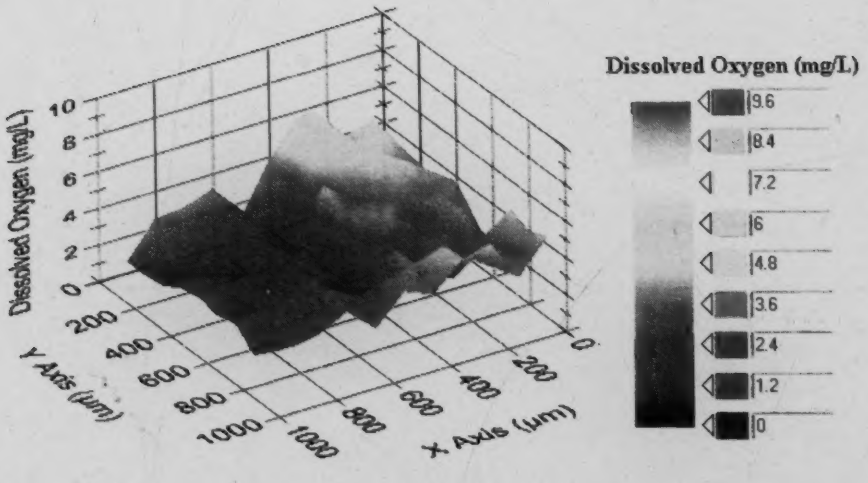

Figure B 28. Dissolved oxygen concentration 560 µm below the artificial plane in biofilm sample 2.

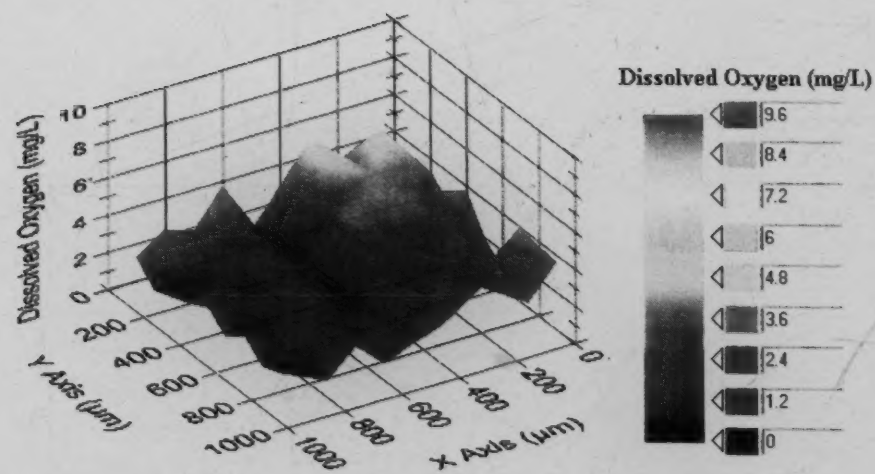

Figure B 29. Dissolved oxygen concentration 640 µm below the artificial plane in biofilm sample 2.

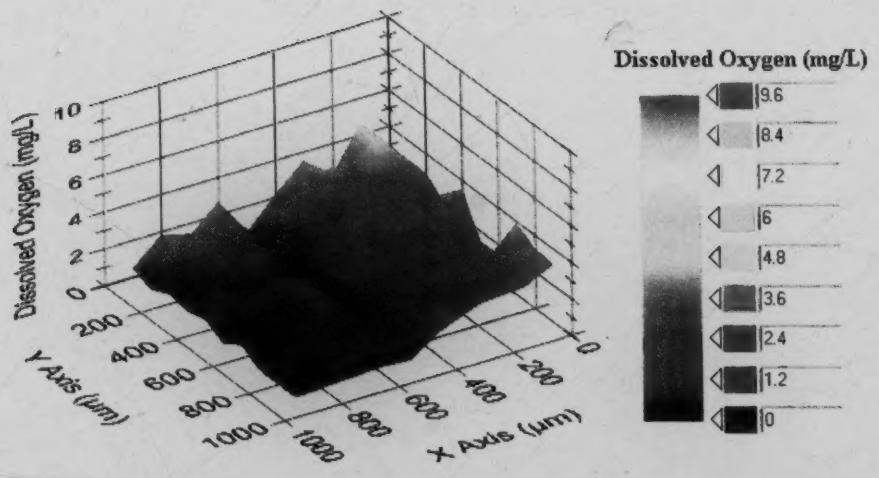

Figure B 30. Dissolved oxygen concentration 720 µm below the artificial plane in biofilm sample 2.

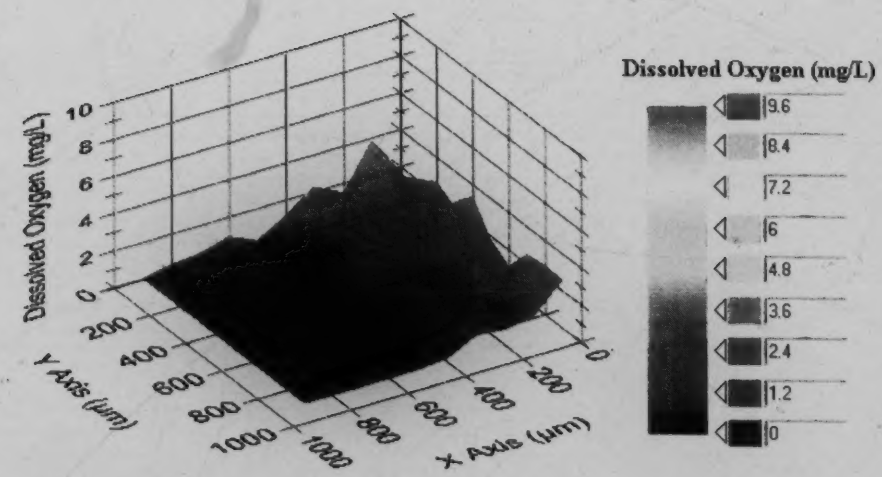

Figure B 31. Dissolved oxygen concentration 800 µm below the artificial plane in biofilm sample 2.

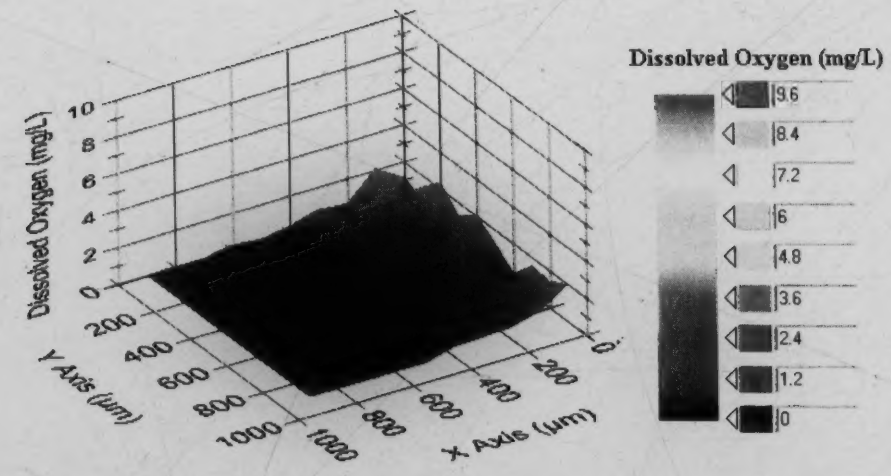

Figure B 32. Dissolved oxygen concentration 880 µm below the artificial plane in biofilm sample 2.

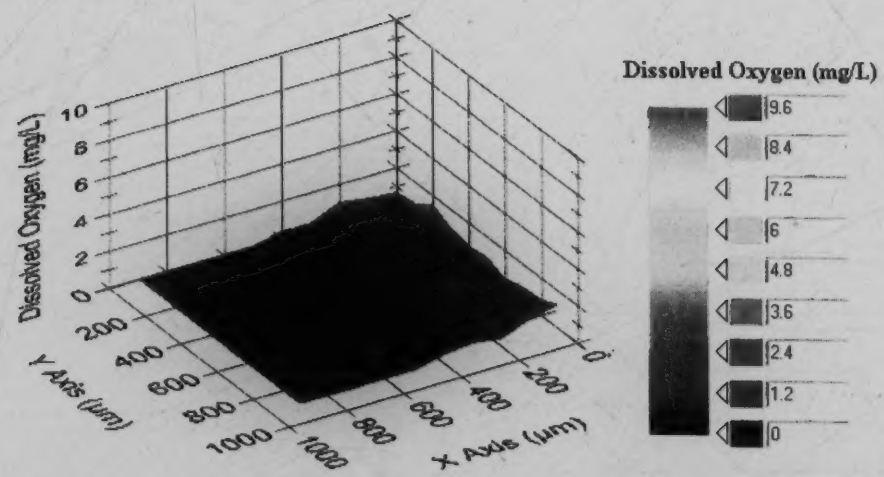

Figure B 33. Dissolved oxygen concentration 960 µm below the artificial plane in biofilm sample 2.

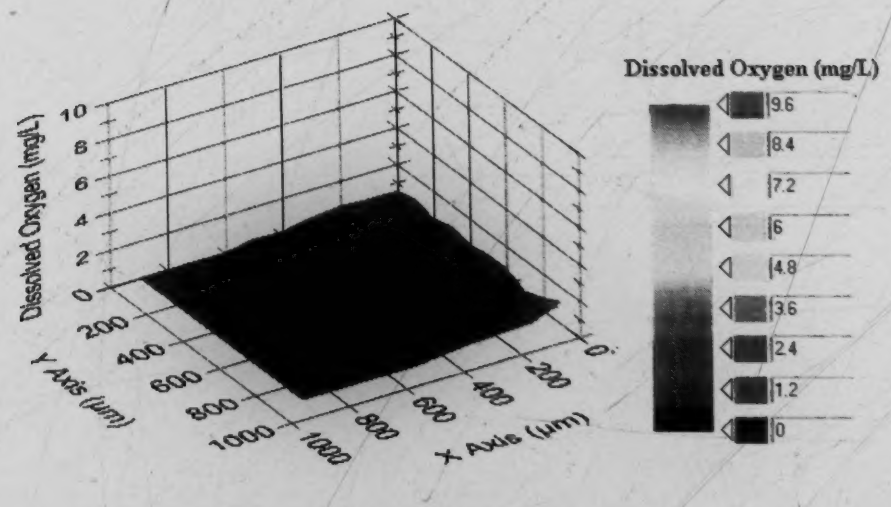

Figure B 34. Dissolved oxygen concentration 1040 µm below the artificial plane in biofilm sample 2.

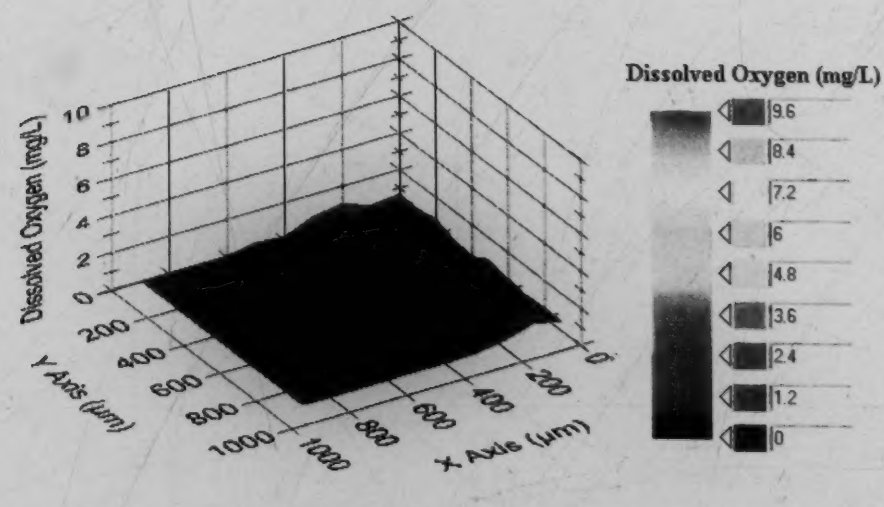

Figure B 35. Dissolved oxygen concentration 1120 µm below the artificial plane in biofilm sample 2.

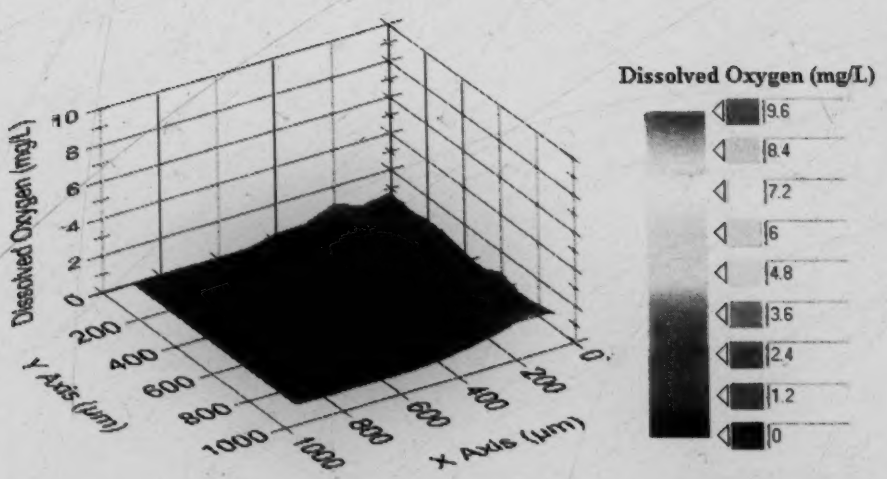

Figure B 36. Dissolved oxygen concentration 1200 µm below the artificial plane in biofilm sample 2.

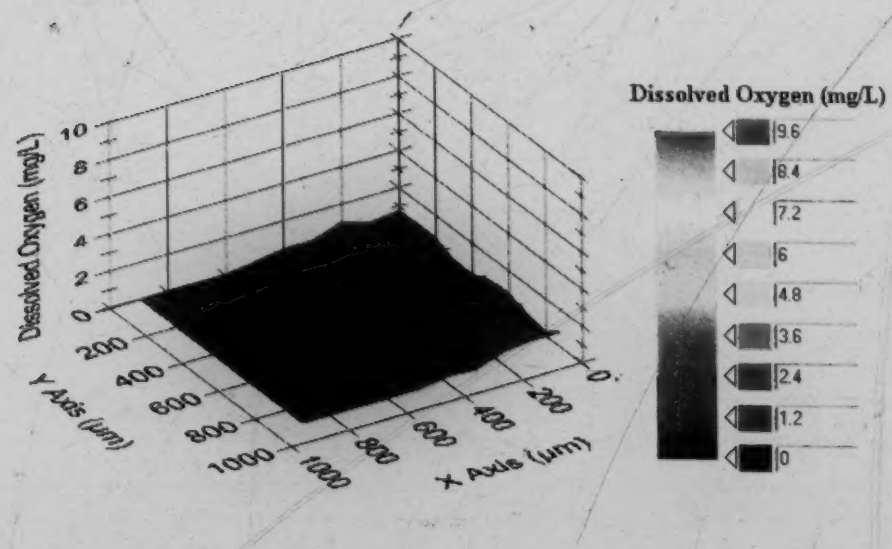

Figure B 37. Dissolved oxygen concentration 1280 µm below the artificial plane in biofilm sample 2.

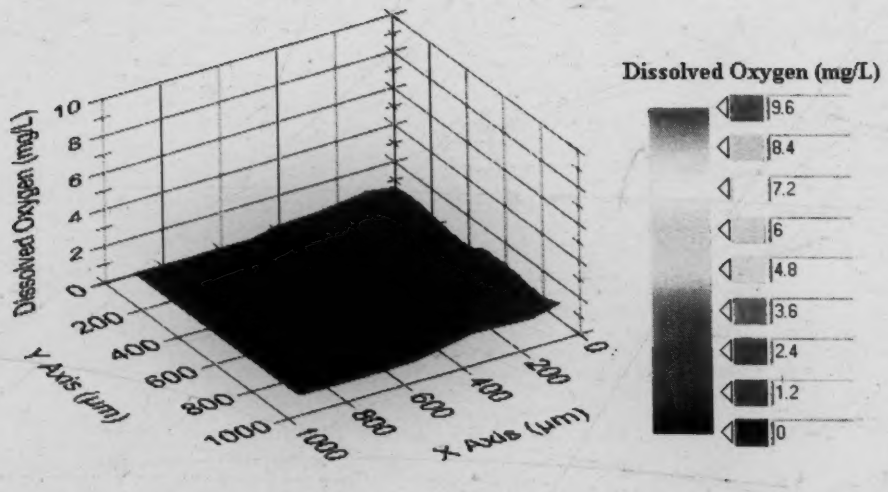

Figure B 38. Dissolved oxygen concentration 1360 µm below the artificial plane in biofilm sample 2.

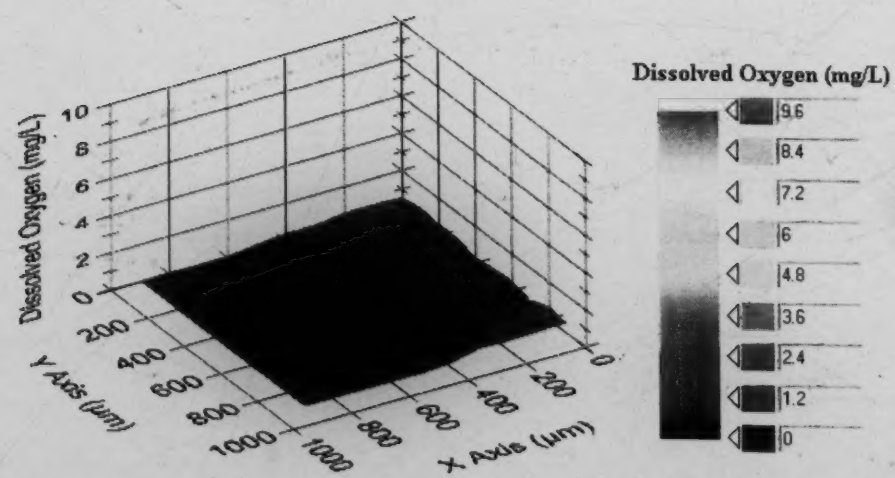

Figure B 39. Dissolved oxygen concentration 1440 µm below the artificial plane in biofilm sample 2.

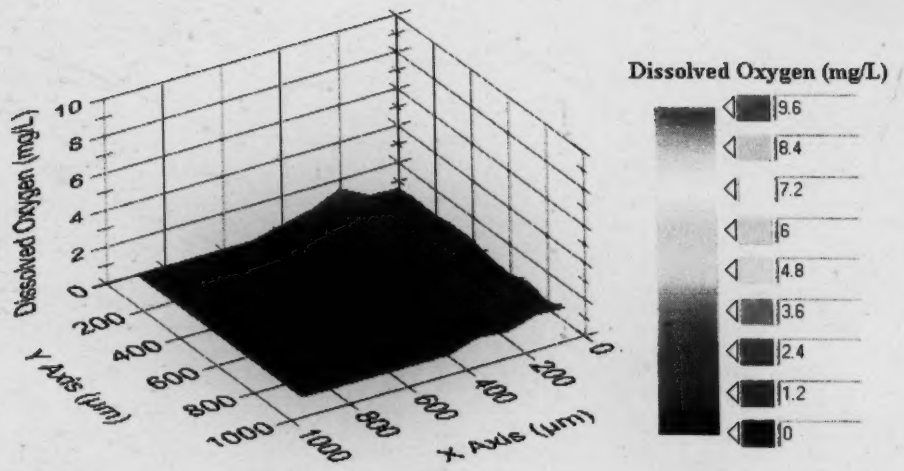

Figure B 40. Dissolved oxygen concentration 1520 µm below the artificial plane in biofilm sample 2.

- Dissolved oxygen distribution from the artificial plane in biofilm sample 3.

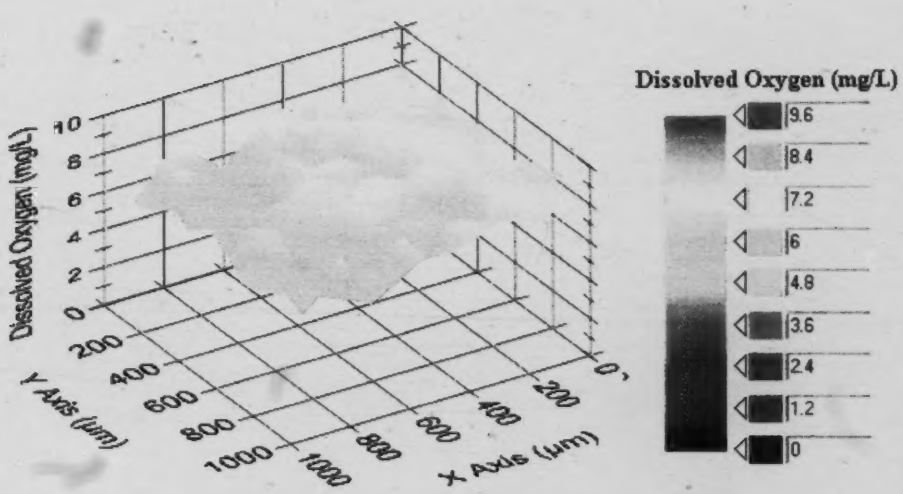

Figure B 41. Dissolved oxygen concentration at the artificial plane in biofilm sample 1, about 920 µm above the biofilm surface.

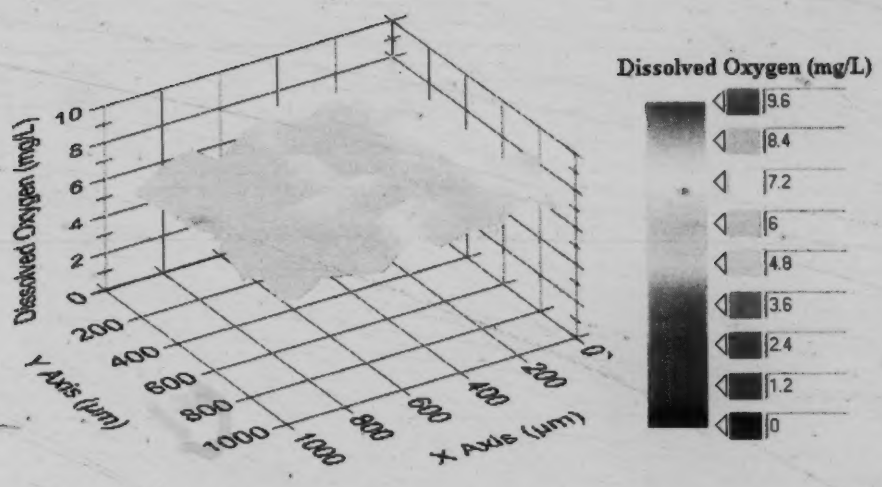

Figure B 42. Dissolved oxygen concentration 80 µm below the artificial plane in biofilm sample 3.

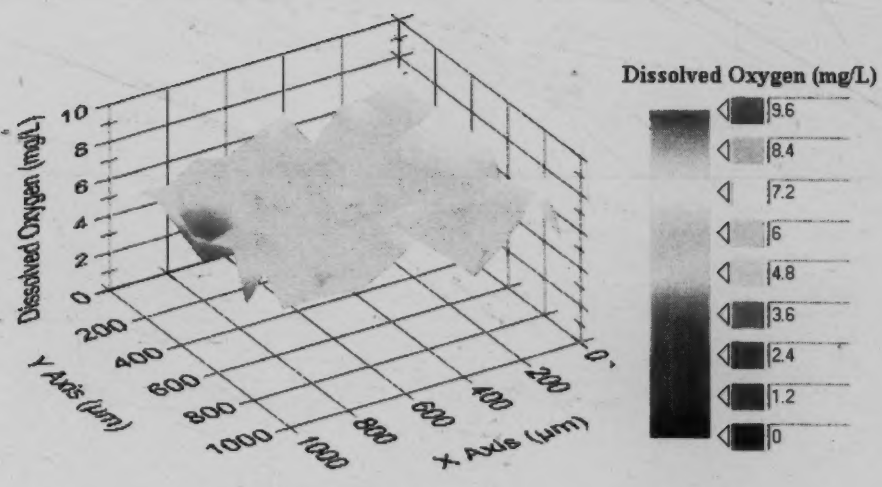

Figure B 43. Dissolved oxygen concentration 160 µm below the artificial plane in biofilm sample 3.

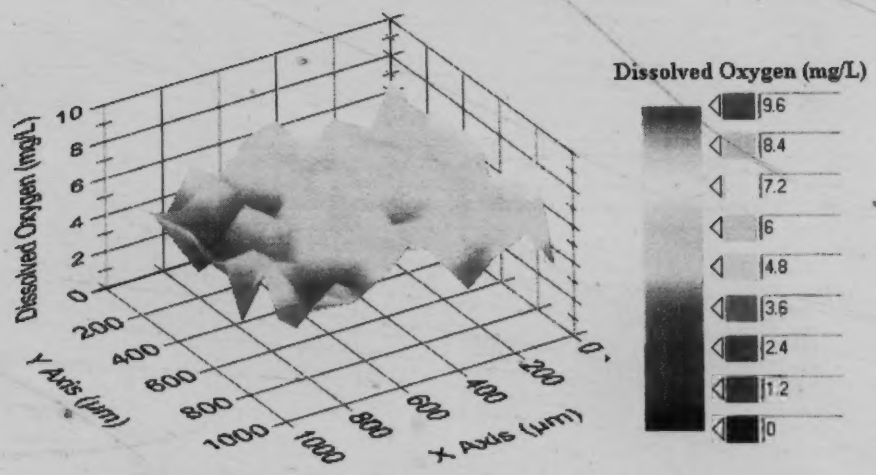

Figure B 44. Dissolved oxygen concentration 240 µm below the artificial plane in biofilm sample 3.

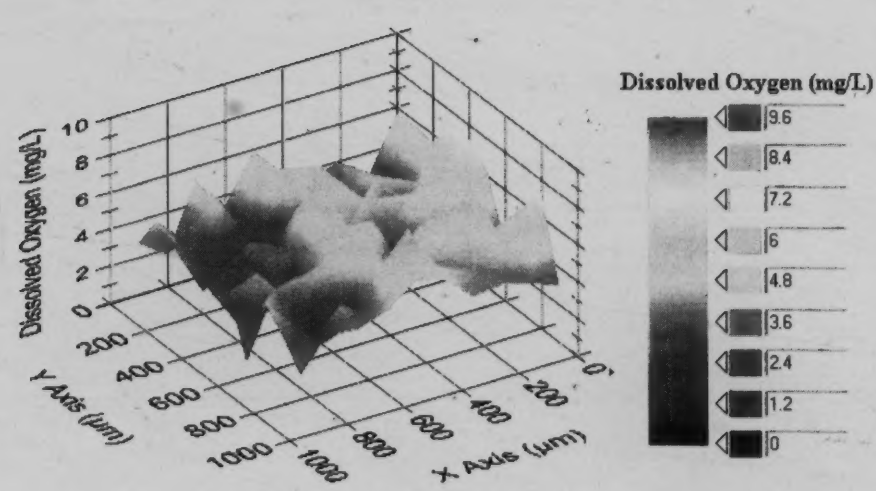

Figure B 45. Dissolved oxygen concentration 320 µm below the artificial plane in biofilm sample 3.

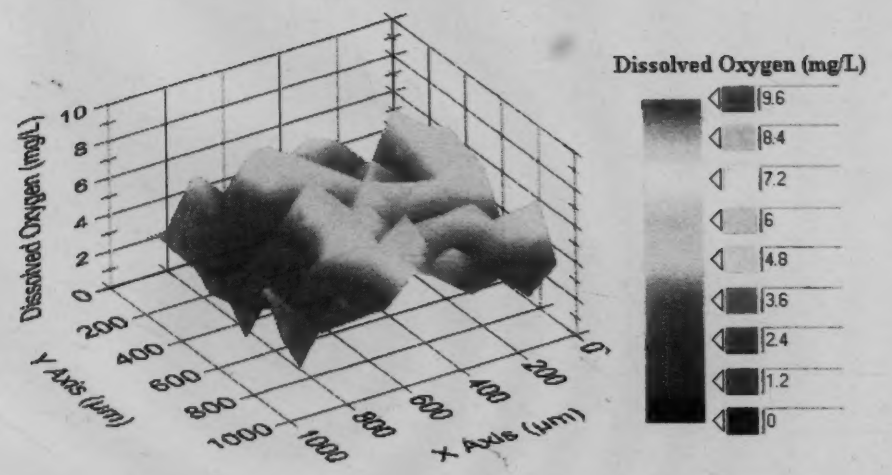

Figure B 46. Dissolved oxygen concentration 400 µm below the artificial plane in biofilm sample 3.

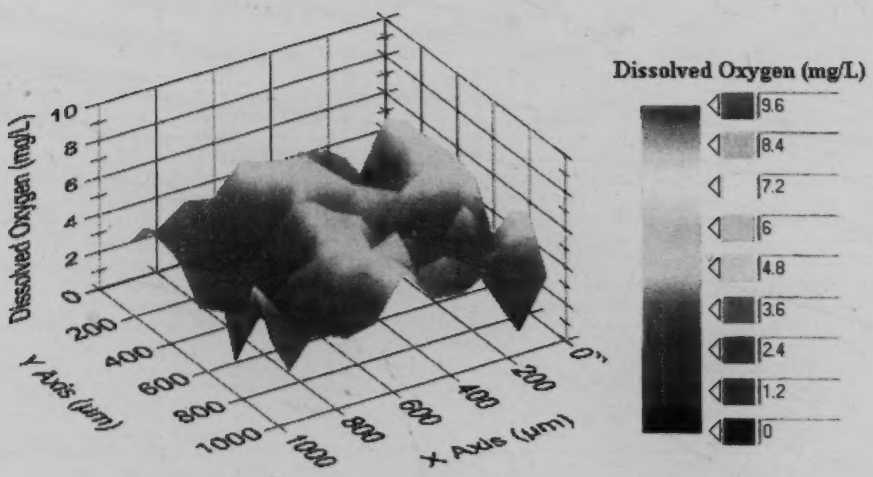

Figure B 47. Dissolved oxygen concentration 480 µm below the artificial plane in biofilm sample 3.

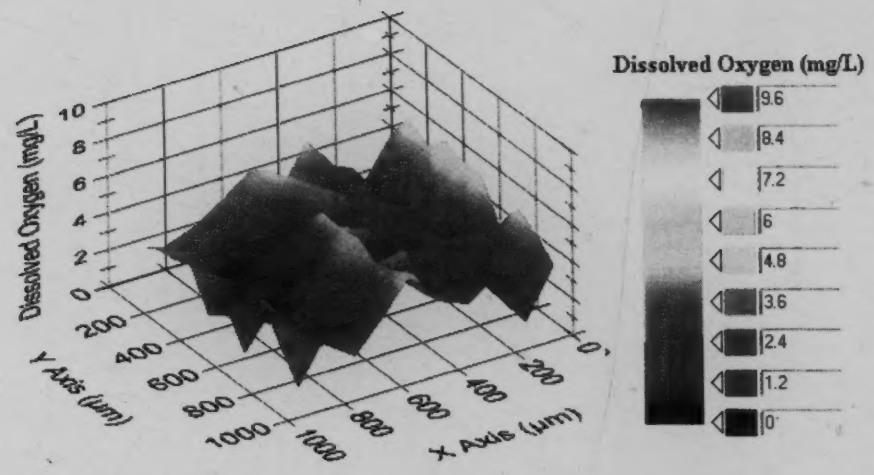

Figure B 48. Dissolved oxygen concentration 560 µm below the artificial plane in biofilm sample 3.

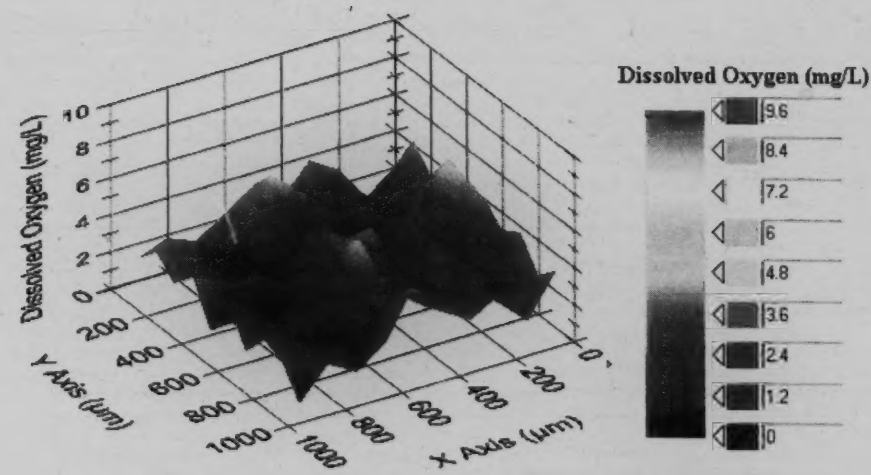

Figure B 49. Dissolved oxygen concentration 640 µm below the artificial plane in biofilm sample 3.

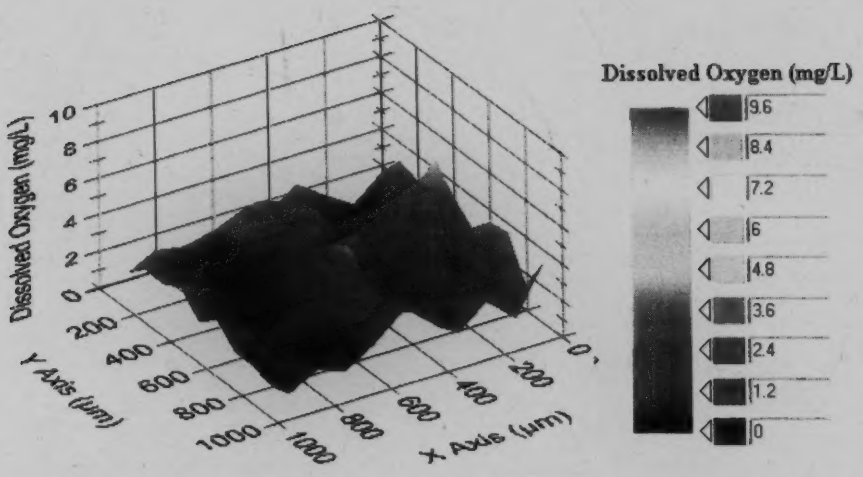

Figure B 50. Dissolved oxygen concentration 720 µm below the artificial plane in biofilm sample 3.

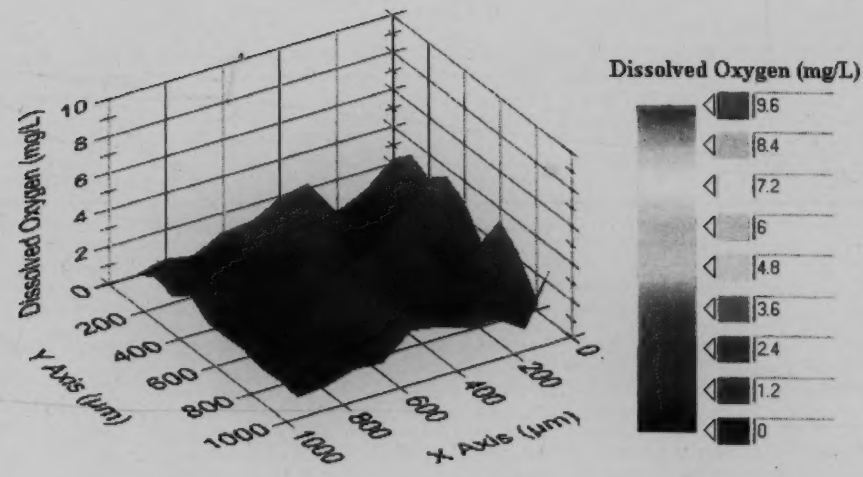

Figure B 51. Dissolved oxygen concentration 800 µm below the artificial plane in biofilm sample 3.

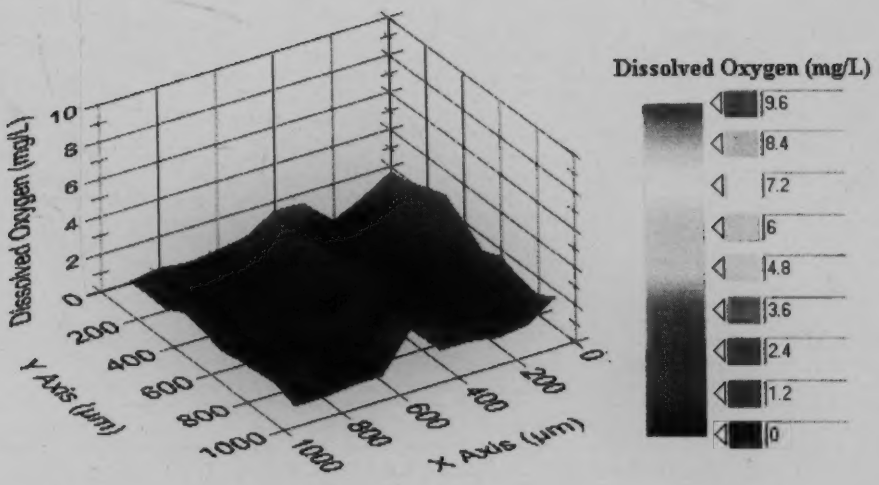

Figure B 52. Dissolved oxygen concentration 880 µm below the artificial plane in biofilm sample 3.

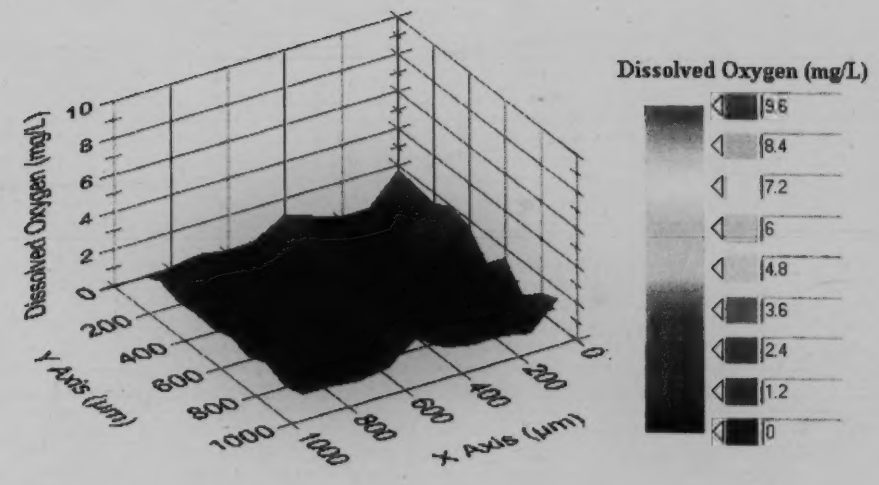

Figure B 53. Dissolved oxygen concentration 960 µm below the artificial plane in biofilm sample 3.

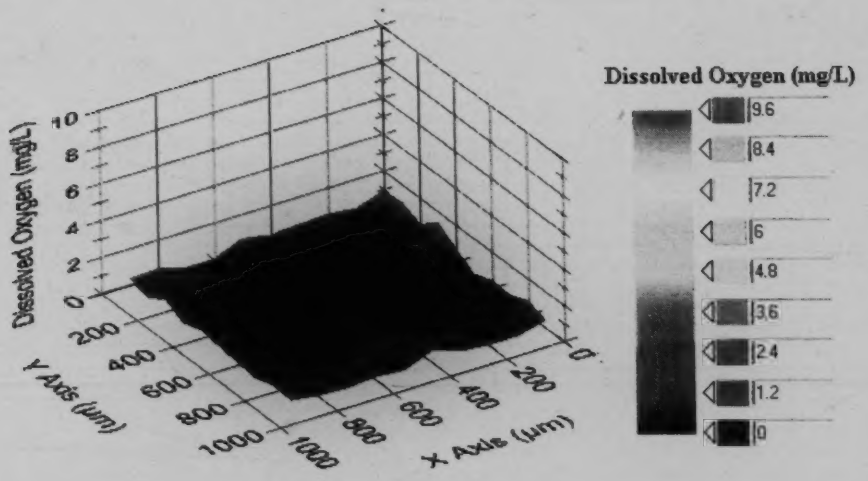

Figure B 54. Dissolved oxygen concentration 1040 µm below the artificial plane in biofilm sample 3.

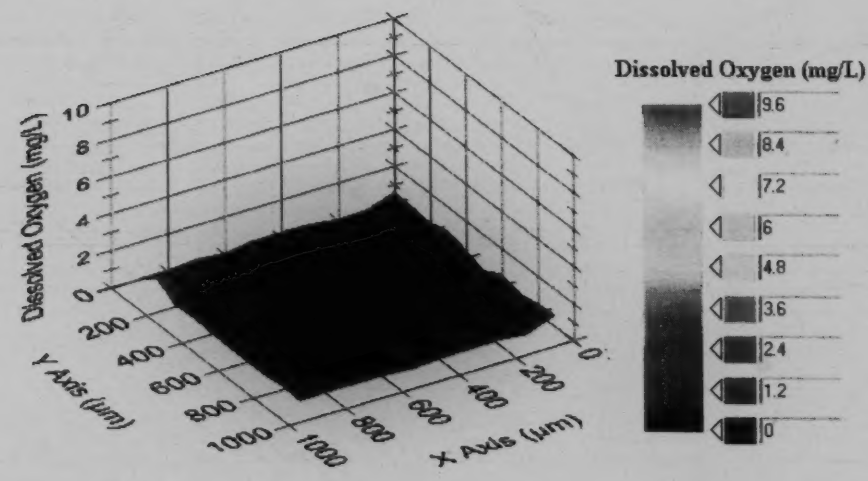

Figure B 55. Dissolved oxygen concentration 1120 µm below the artificial plane in biofilm sample 3.

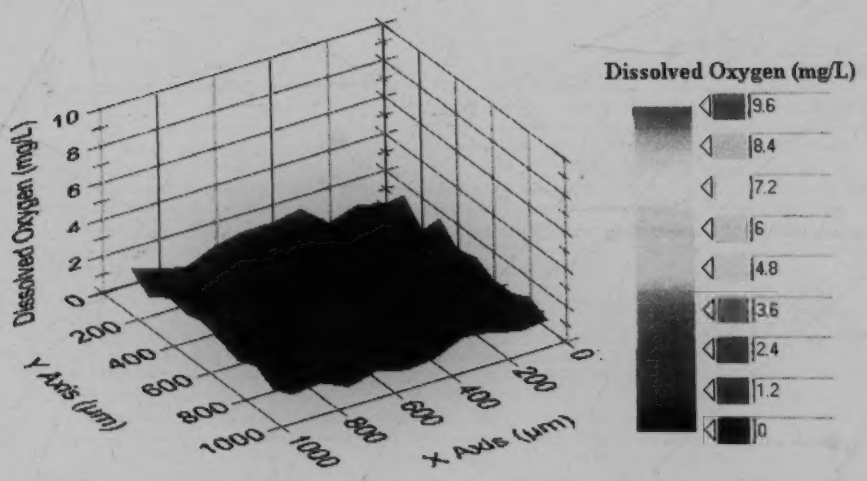

Figure B 56. Dissolved oxygen concentration 1200 µm below the artificial plane in biofilm sample 3.

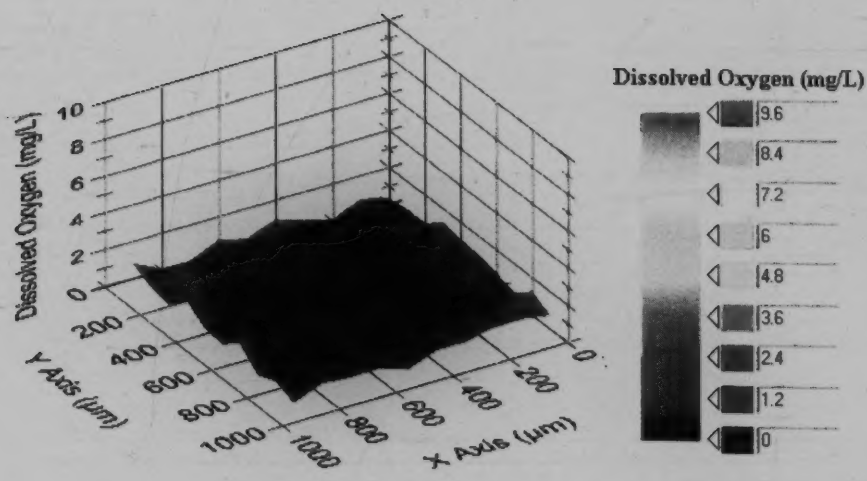

Figure B 57. Dissolved oxygen concentration 1280 µm below the artificial plane in biofilm sample 3.

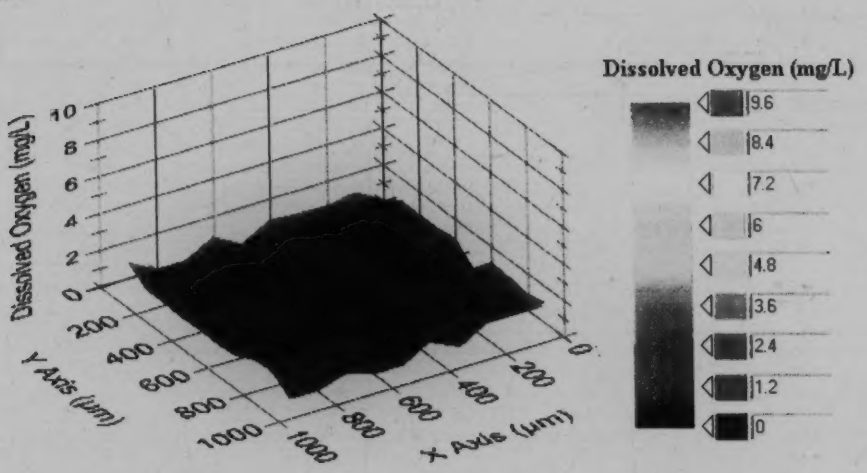

Figure B 58. Dissolved oxygen concentration 1360 µm below the artificial plane in biofilm sample 3.

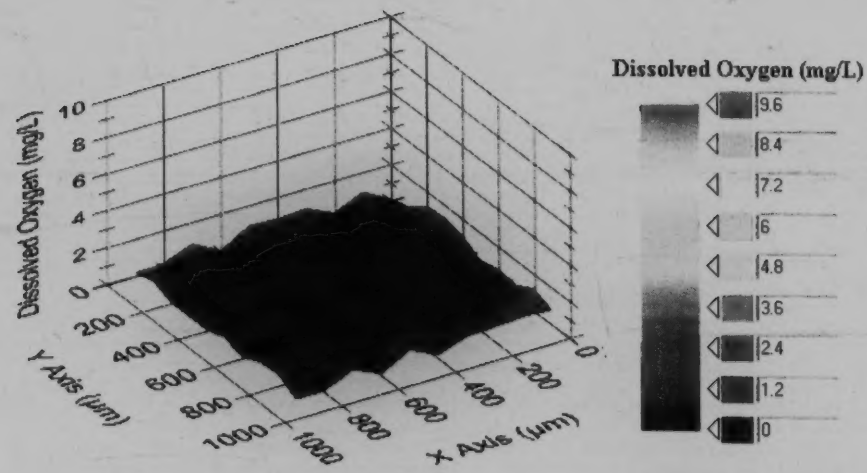

Figure B 59. Dissolved oxygen concentration 1440 µm below the artificial plane in biofilm sample 3.

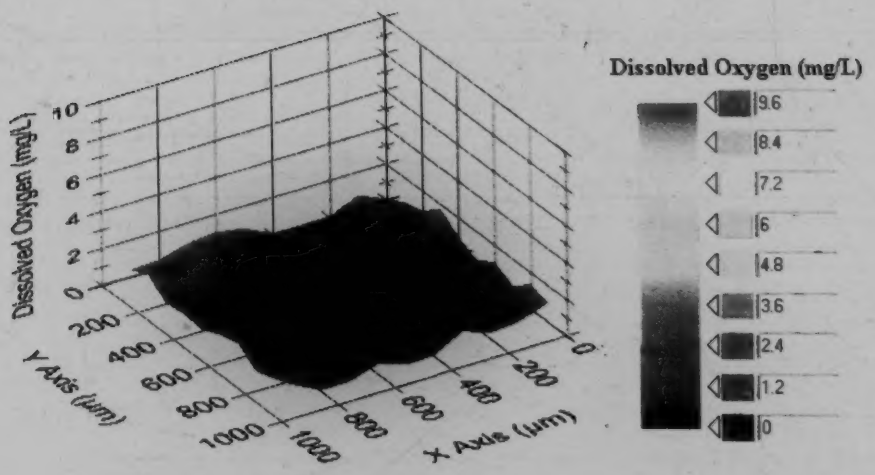

Figure B 60. Dissolved oxygen concentration 1520 µm below the artificial plane in biofilm sample 3.

- Dissolved oxygen distribution from the artificial plane in biofilm sample 4.

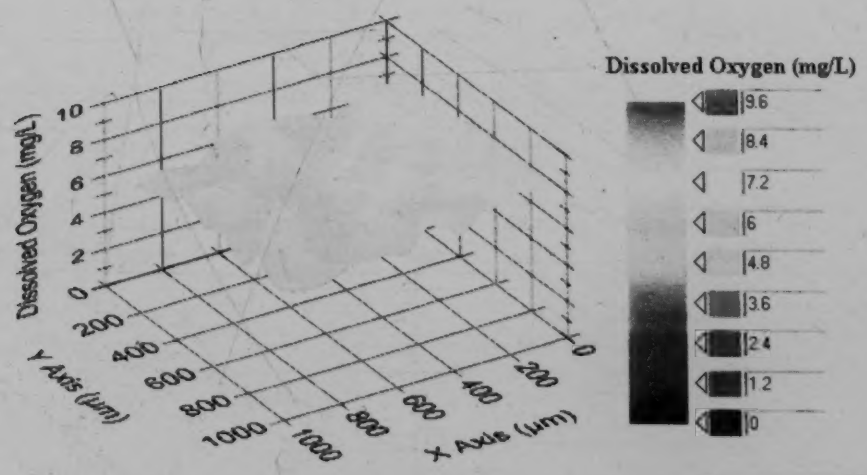

Figure B 61. Dissolved oxygen concentration at the artificial plane in biofilm sample 4, about 920 µm above the biofilm surface.

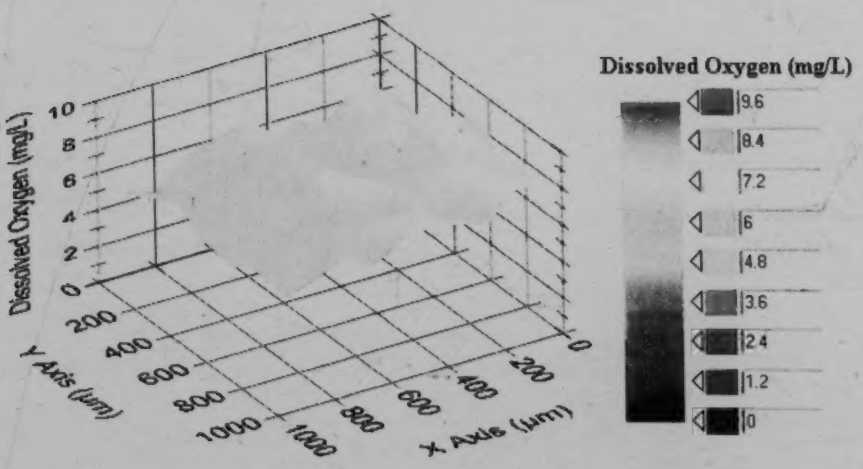

Figure B 62. Dissolved oxygen concentration 80 µm below the artificial plane in biofilm sample 4.

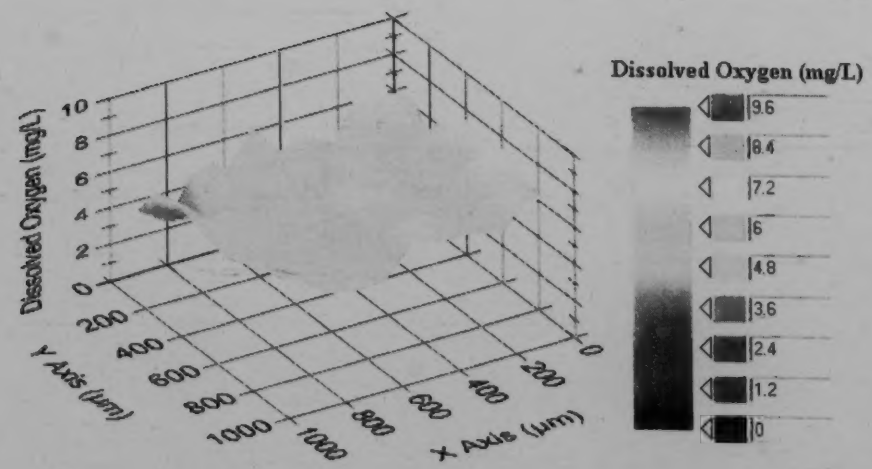

Figure B 63. Dissolved oxygen concentration 160 µm below the artificial plane in biofilm sample 4.

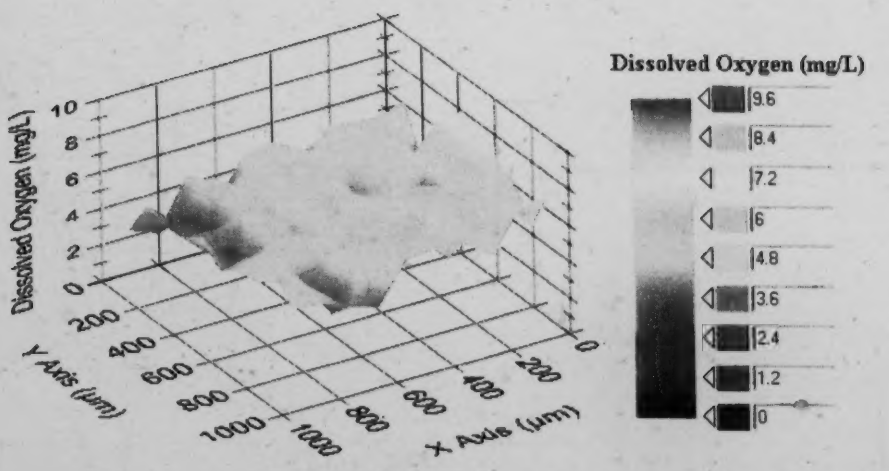

Figure B 64. Dissolved oxygen concentration 240 µm below the artificial plane in biofilm sample 4.

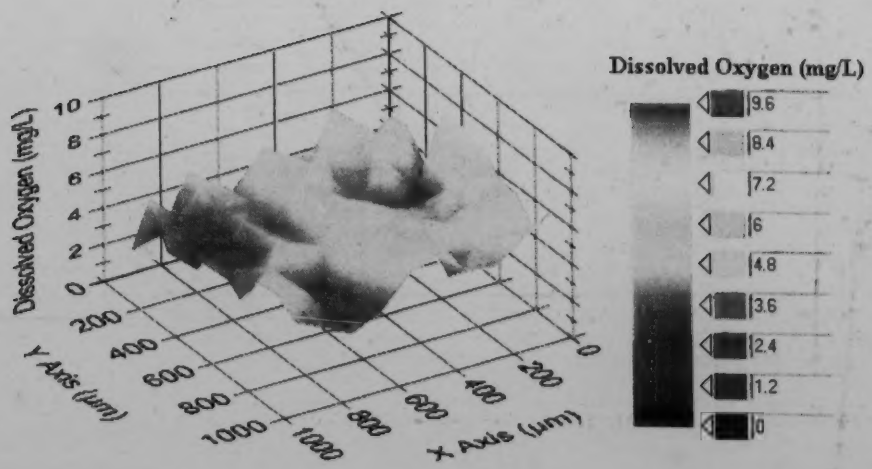

Figure B 65. Dissolved oxygen concentration 320 µm below the artificial plane in biofilm sample 4.

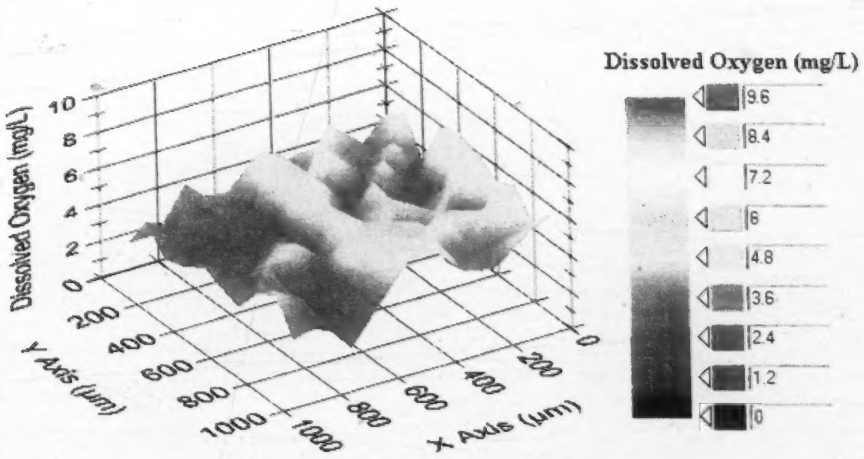

Figure B 66. Dissolved oxygen concentration 400 µm below the artificial plane in biofilm sample 4.

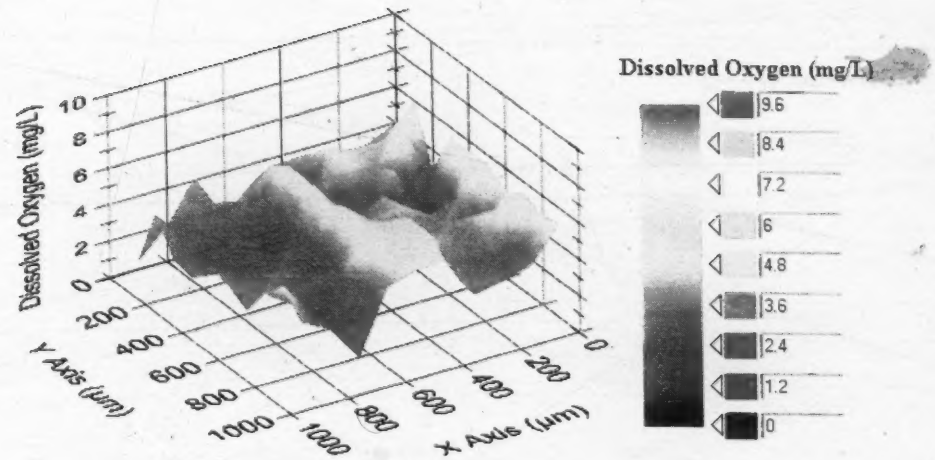

Figure B 67. Dissolved oxygen concentration 480 µm below the artificial plane in biofilm sample 4.

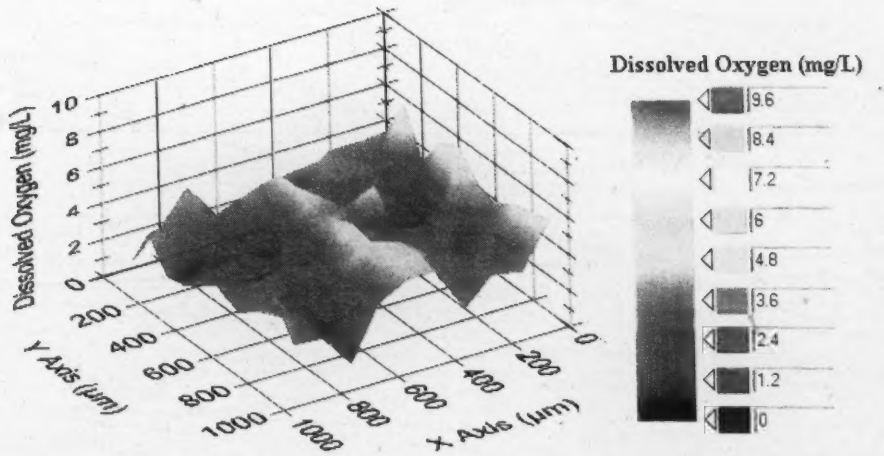

Figure B 68. Dissolved oxygen concentration 560 µm below the artificial plane in biofilm sample 4.

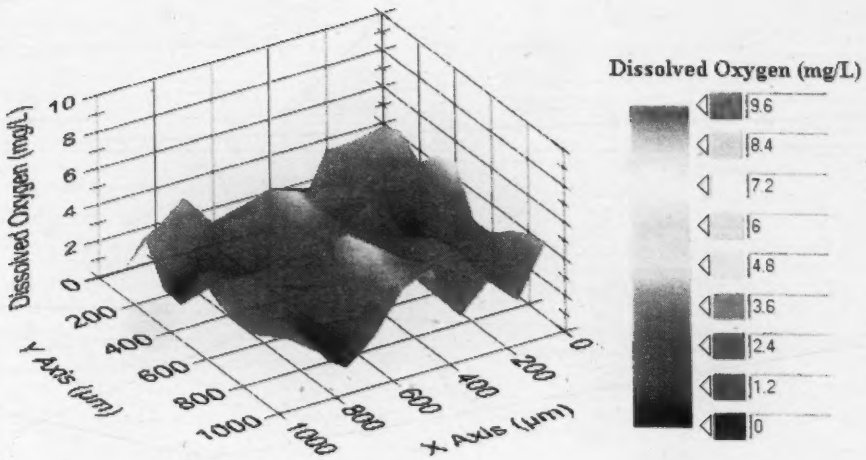

Figure B 69. Dissolved oxygen concentration 640 µm below the artificial plane in biofilm sample 4.

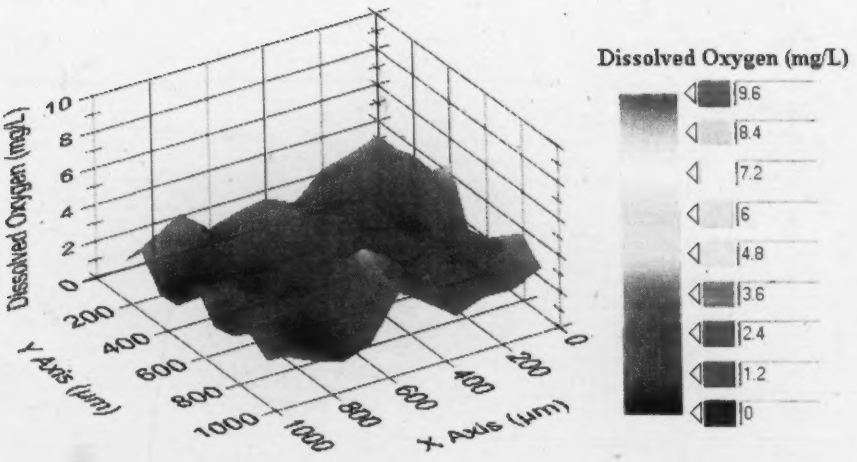

Figure B 70. Dissolved oxygen concentration 720 µm below the artificial plane in biofilm sample 4.

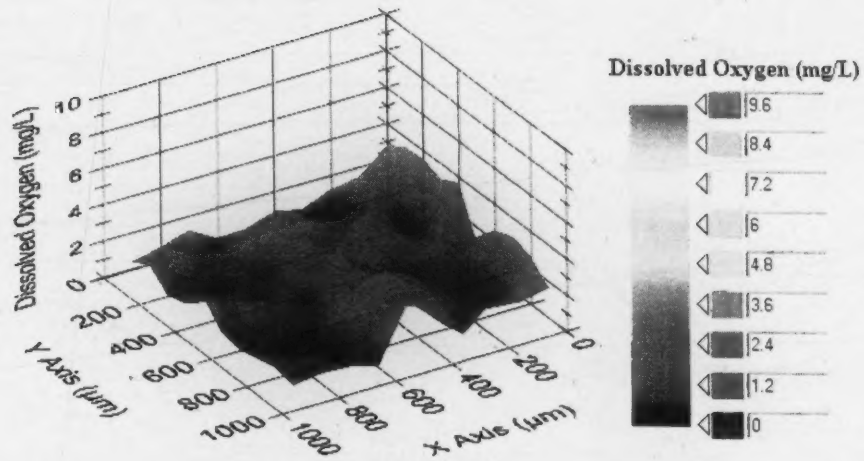

Figure B 71. Dissolved oxygen concentration 800 µm below the artificial plane in biofilm sample 4.

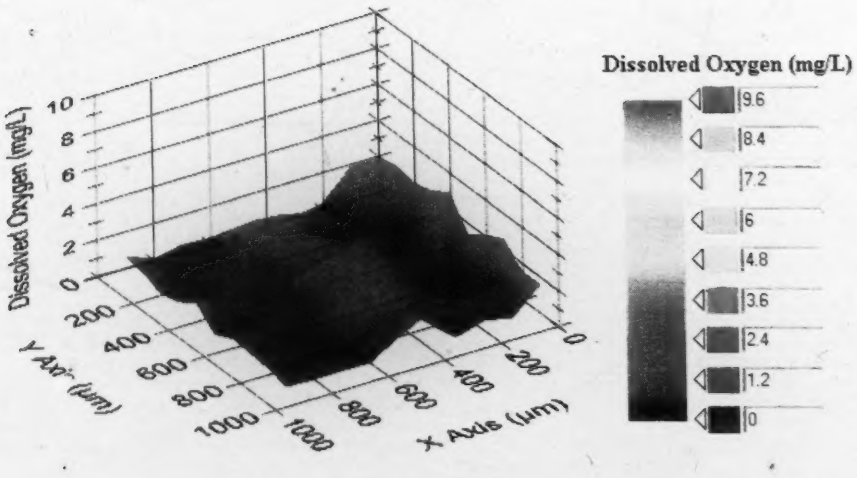

Figure B 72. Dissolved oxygen concentration 880 µm below the artificial plane in biofilm sample 4.

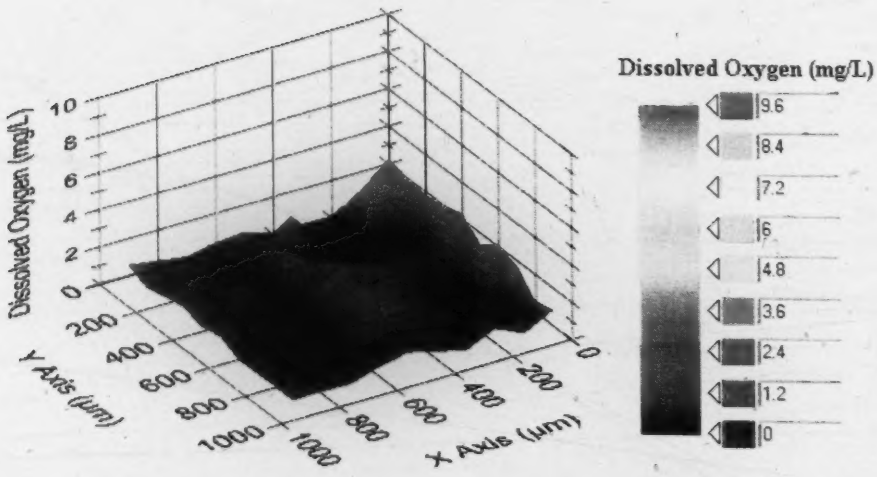

Figure B 73. Dissolved oxygen concentration 960 µm below the artificial plane in biofilm sample 4.

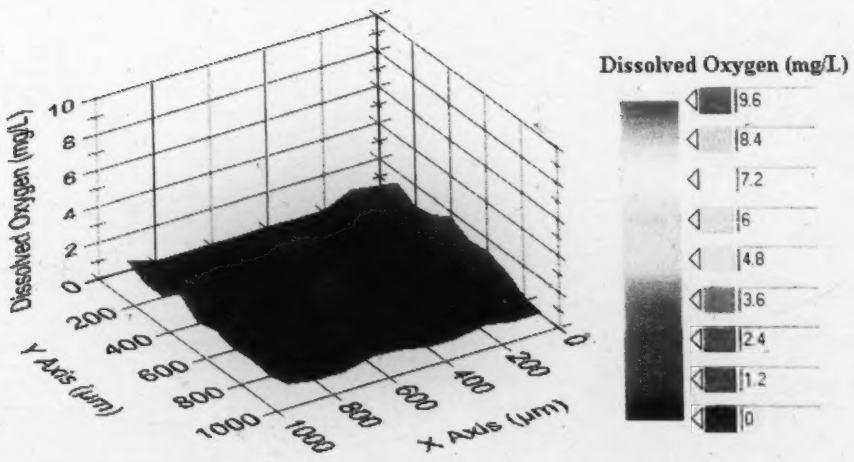

Figure B 74. Dissolved oxygen concentration 1040 µm below the artificial plane in biofilm sample 4.

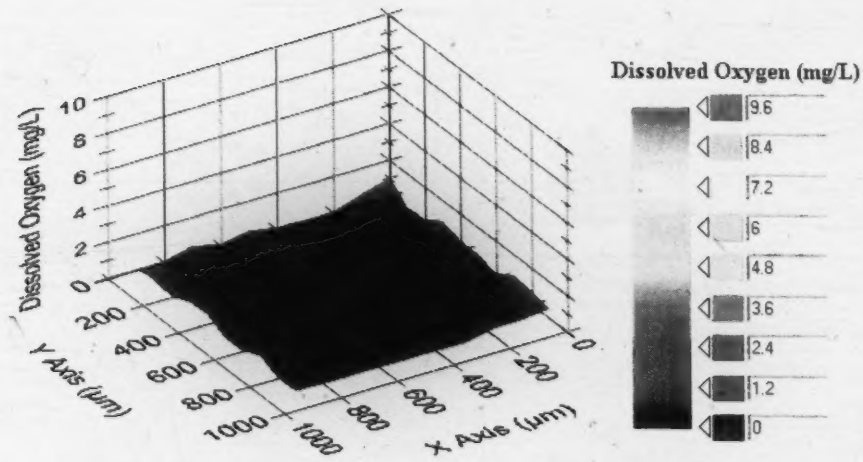

Figure B 75. Dissolved oxygen concentration 1120 µm below the artificial plane in biofilm sample 4.

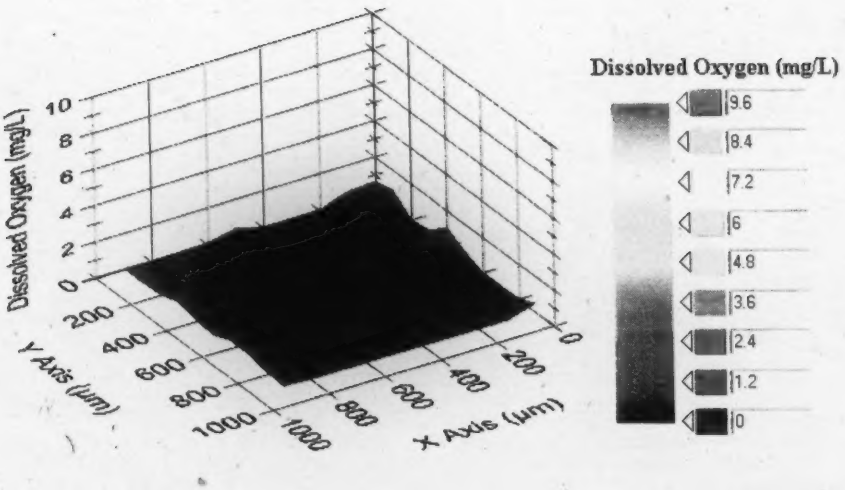

Figure B 76. Dissolved oxygen concentration 1200 µm below the artificial plane in biofilm sample 4.

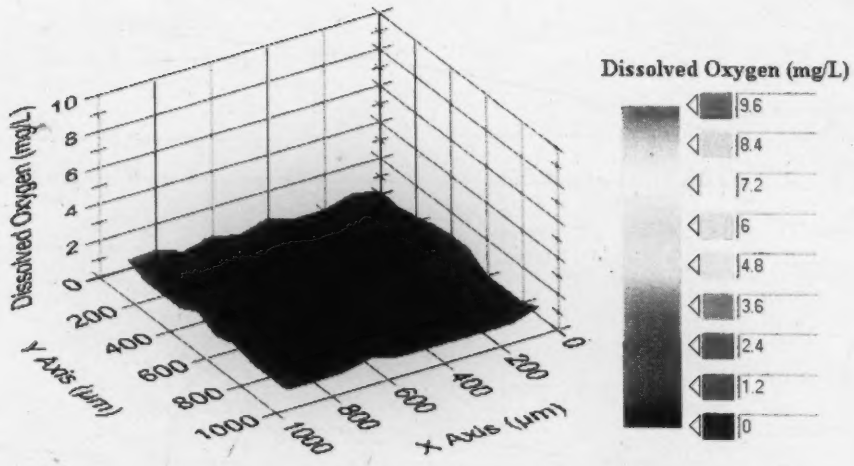

Figure B 77. Dissolved oxygen concentration 1280 µm below the artificial plane in biofilm sample 4.

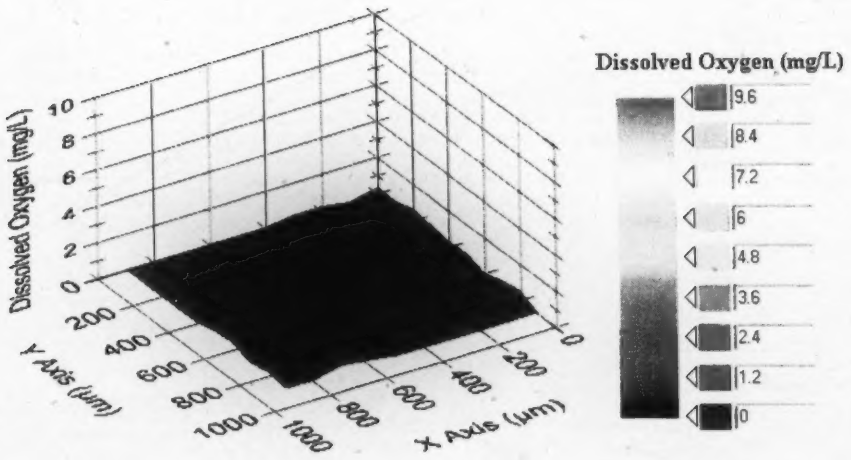

Figure B 78. Dissolved oxygen concentration 1360 µm below the artificial plane in biofilm sample 4.

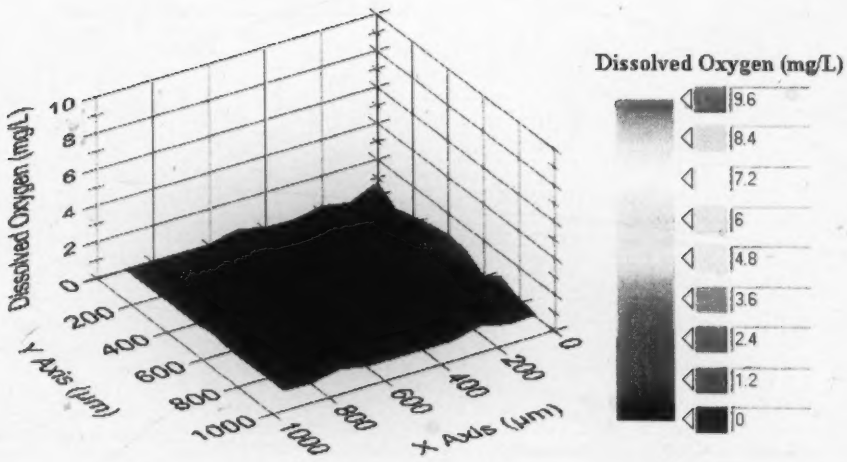

Figure B 79. Dissolved oxygen concentration 1440 µm below the artificial plane in biofilm sample 4.

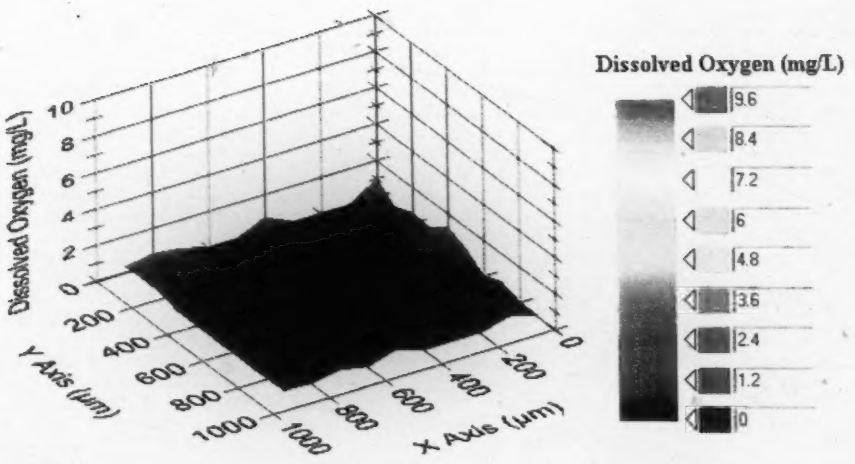

Figure B 80. Dissolved oxygen concentration 1520 µm below the artificial plane in biofilm sample 4.

APPENDIX C. OXYGEN DISTRIBUTION FROM THE BIOFILM SURFACE.

- Dissolved oxygen distribution from the biofilm surface in biofilm sample 1.

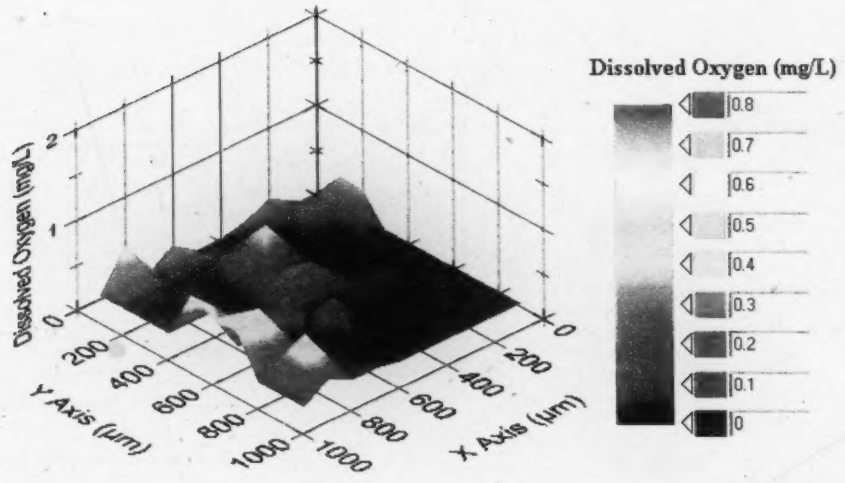

Figure C 1. The dissolved oxygen concentrations 40 µm below the biofilm surface in biofilm sample 1.

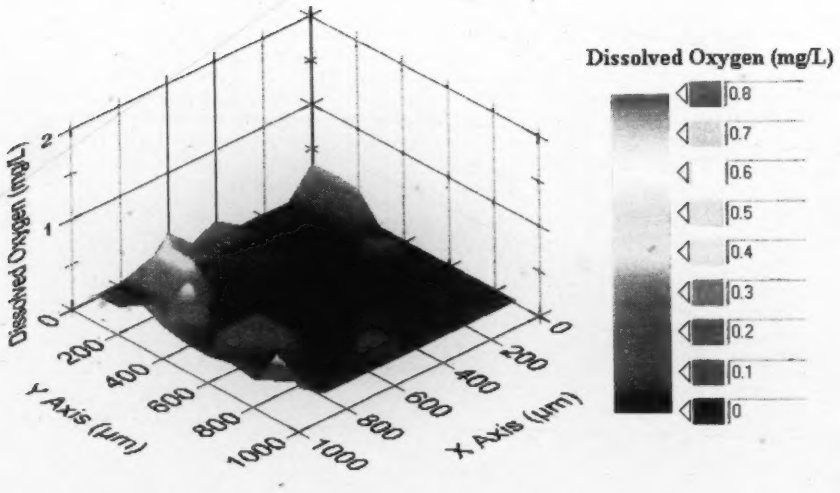

Figure C 2. The dissolved oxygen concentrations 120 µm below the biofilm surface in biofilm sample 1.

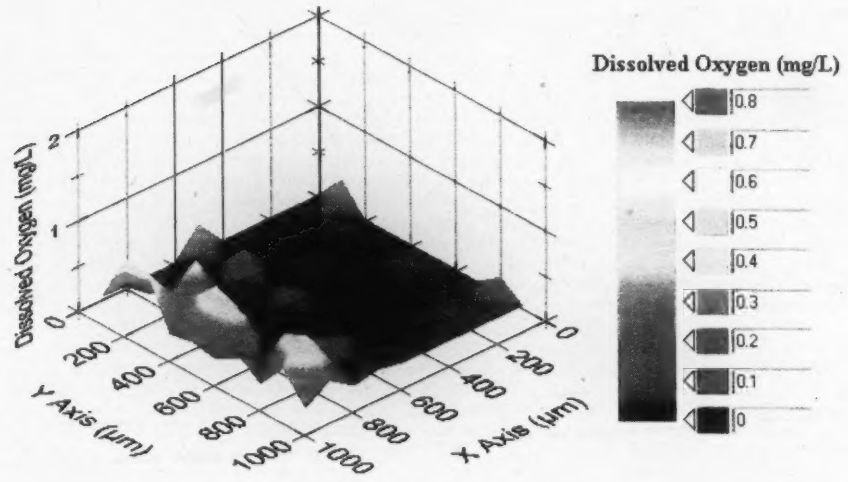

Figure C 3. The dissolved oxygen concentrations 200 µm below the biofilm surface in biofilm sample 1.

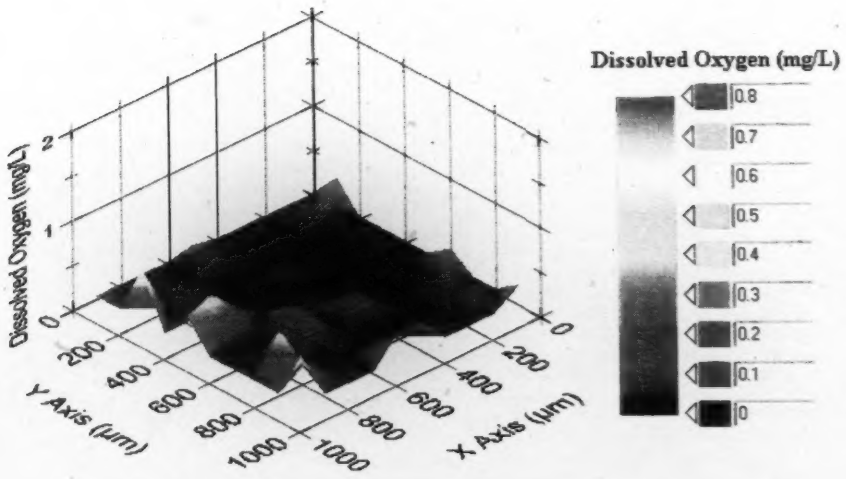

Figure C 4. The dissolved oxygen concentrations 280 µm below the biofilm surface in biofilm sample 1.

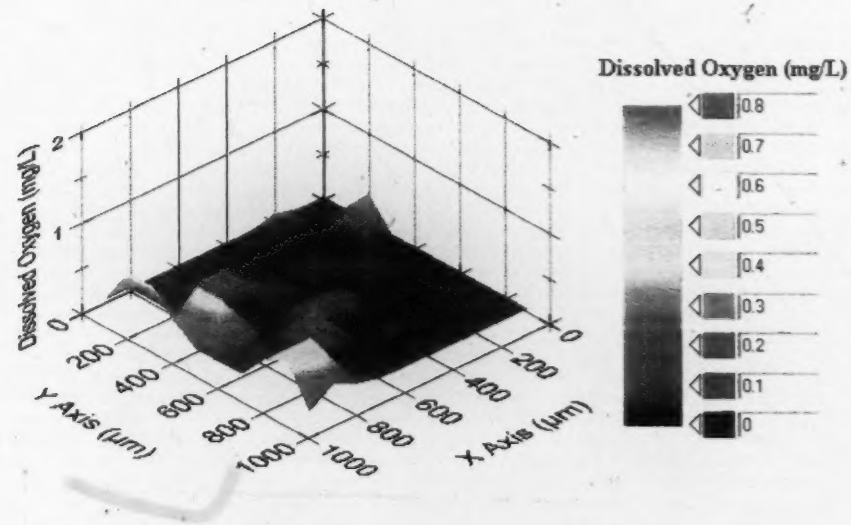

Figure C 5. The dissolved oxygen concentrations 360 µm below the biofilm surface in biofilm sample 1.

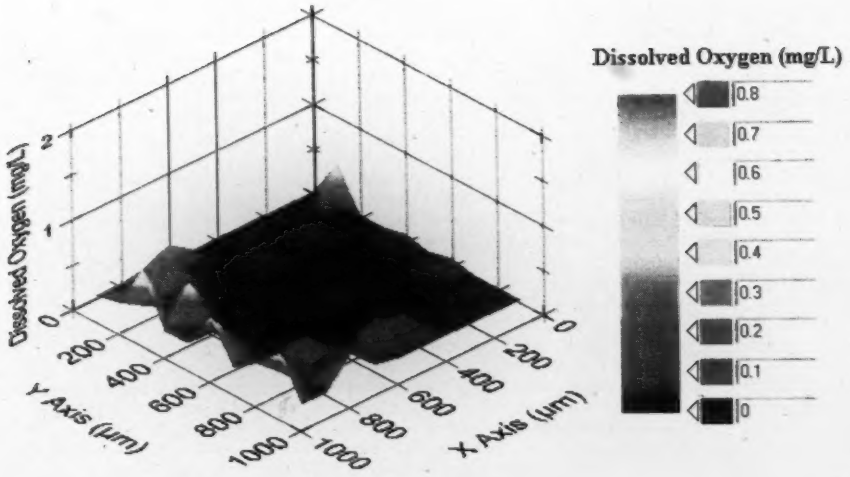

Figure C 6. The dissolved oxygen concentrations 440 µm below the biofilm surface in biofilm sample 1.

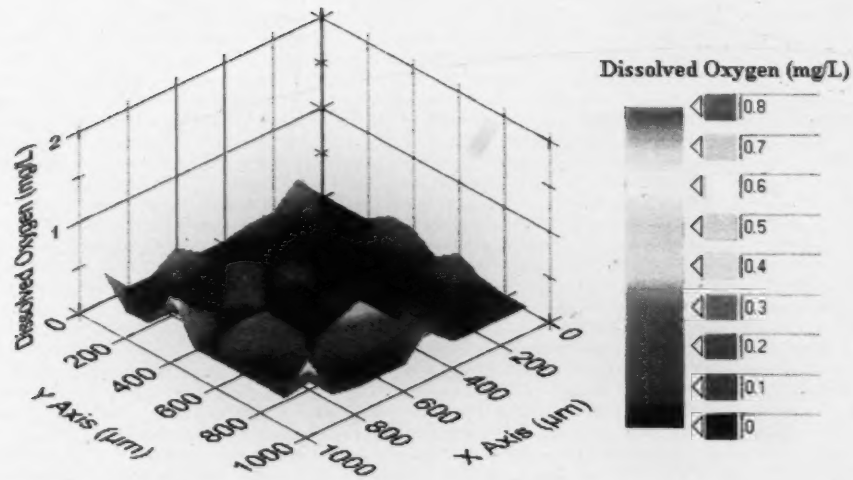

Figure C 7. The dissolved oxygen concentrations 520 µm below the biofilm surface in biofilm sample 1.

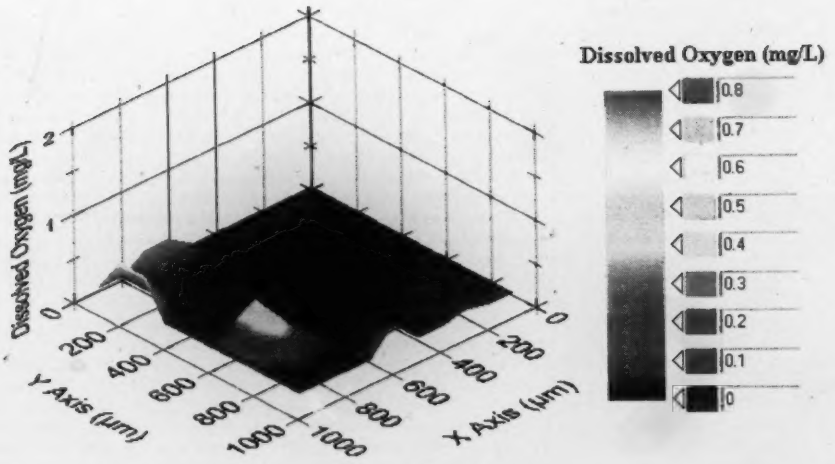

Figure C 8. The dissolved oxygen concentrations 600 µm below the biofilm surface in biofilm sample 1.

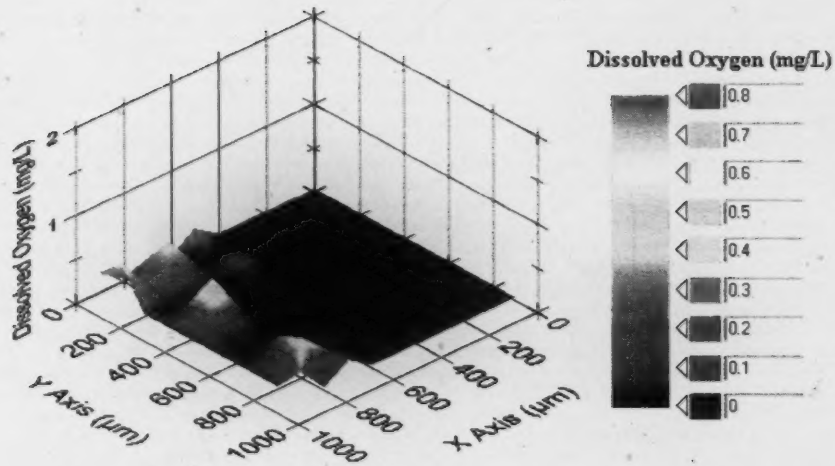

Figure C 9. The dissolved oxygen concentrations 680 µm below the biofilm surface in biofilm sample 1.

- Dissolved oxygen distribution from the biofilm surface in biofilm sample 2.

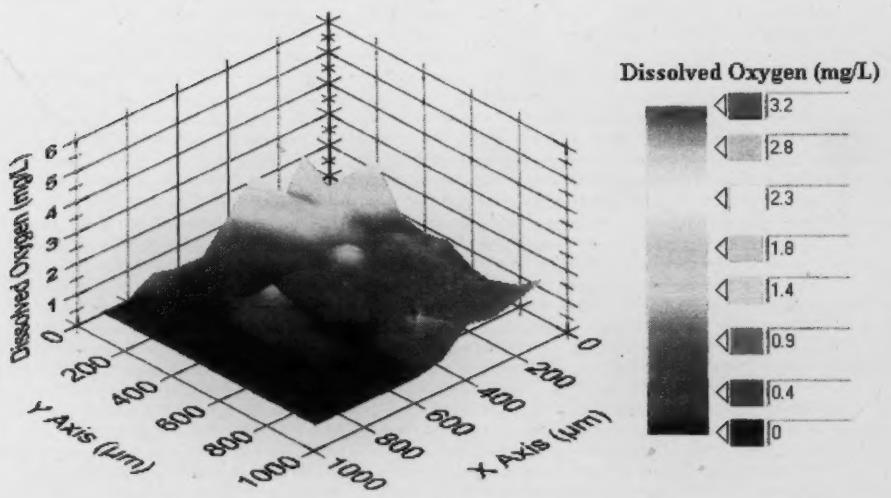

Figure C 10. The dissolved oxygen concentrations 40 µm below the biofilm surface in biofilm sample 2.

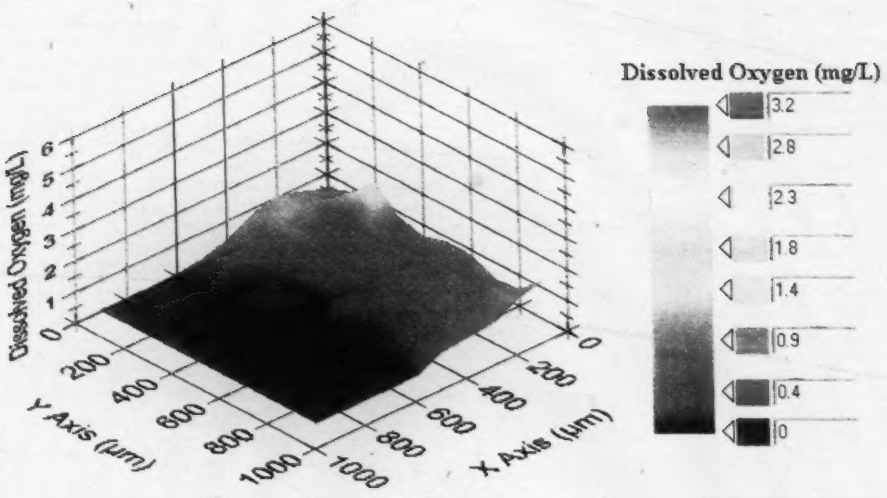

Figure C 11. The dissolved oxygen concentrations 120 µm below the biofilm surface in biofilm sample 2.

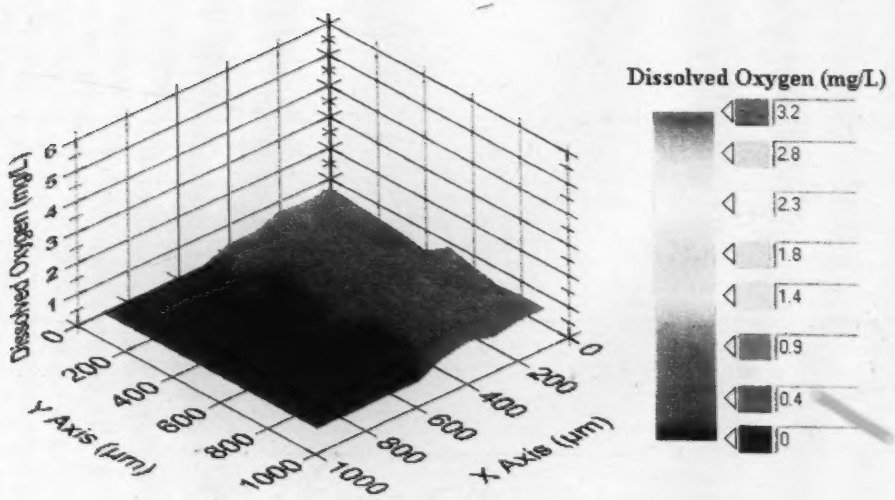

Figure C 12. The dissolved oxygen concentrations 200 µm below the biofilm surface in biofilm sample 2.

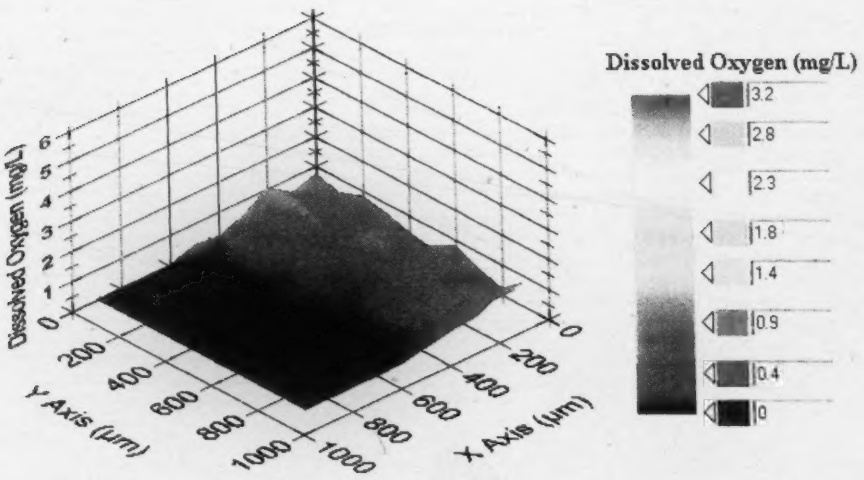

Figure C 13. The dissolved oxygen concentrations 280 µm below the biofilm surface in biofilm sample 2.

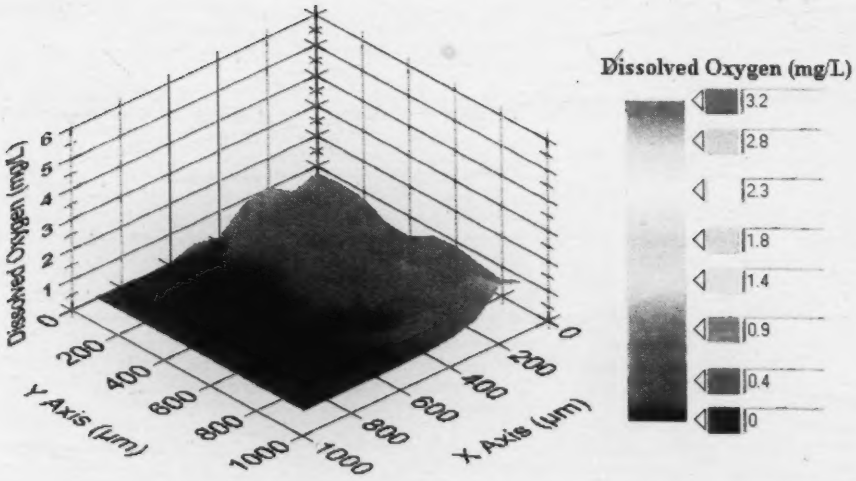

Figure C 14. The dissolved oxygen concentrations 360 µm below the biofilm surface in biofilm sample 2.

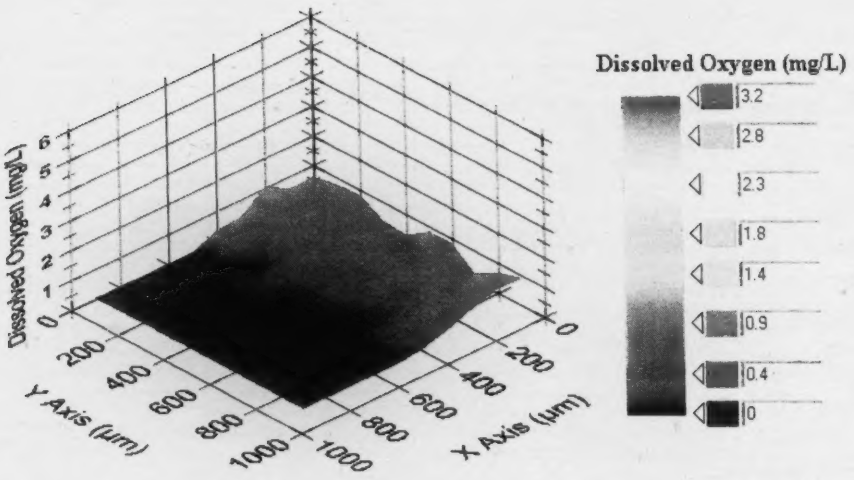

Figure C 15. The dissolved oxygen concentrations 440 µm below the biofilm surface in biofilm sample 2.

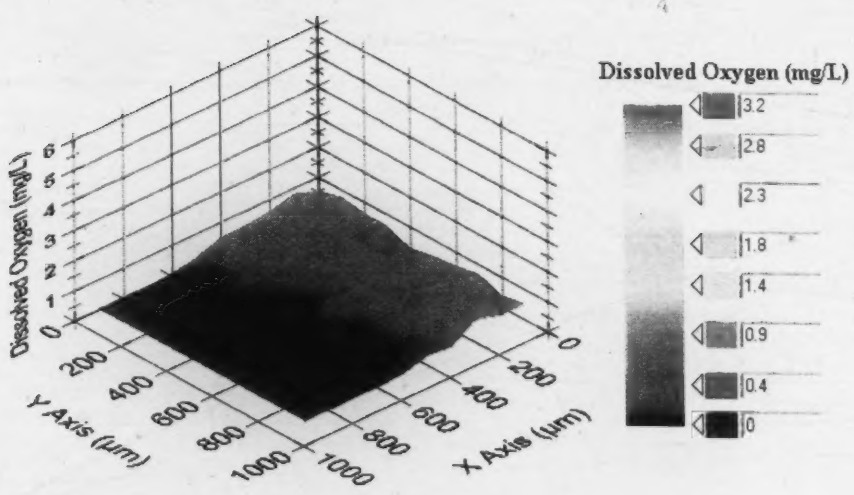

Figure C 16. The dissolved oxygen concentrations 520 µm below the biofilm surface in biofilm sample 2.

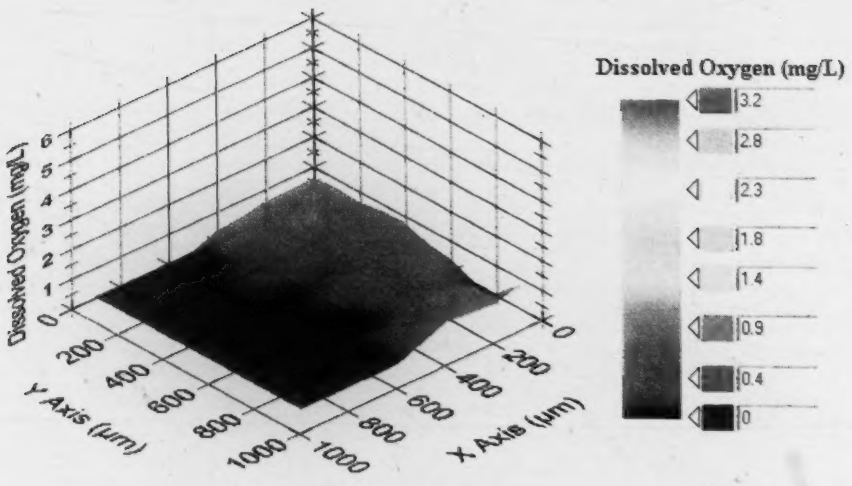

Figure C 17. The dissolved oxygen concentrations 600 µm below the biofilm surface in biofilm sample 2.

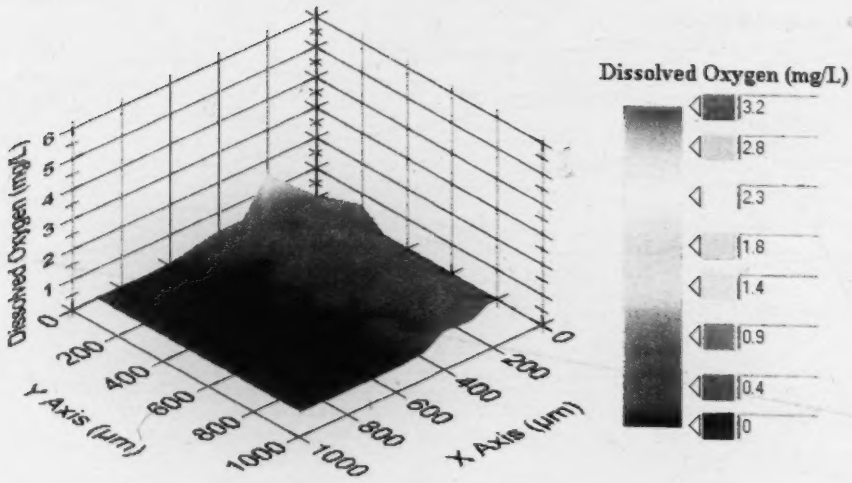

Figure C 18. The dissolved oxygen concentrations 680 µm below the biofilm surface in biofilm sample 2.

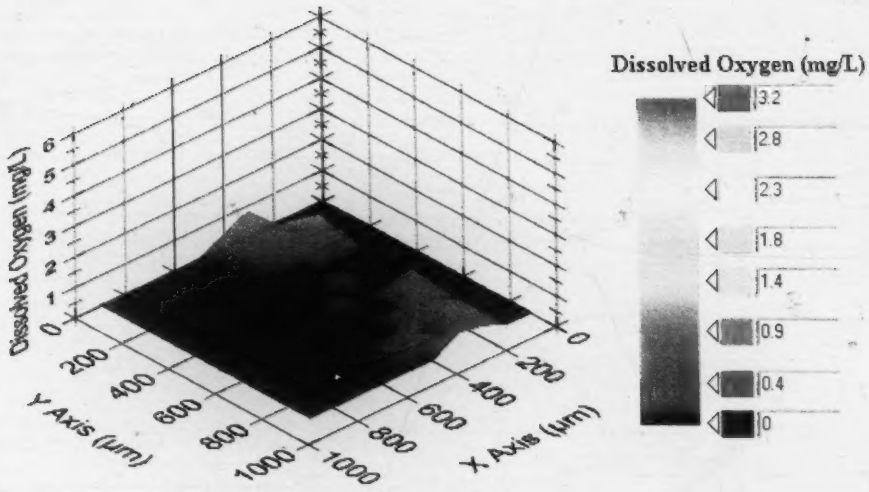

Figure C 19. The dissolved oxygen concentrations 760 µm below the biofilm surface in biofilm sample 2.

- Dissolved oxygen distribution from the biofilm surface in biofilm sample 3.

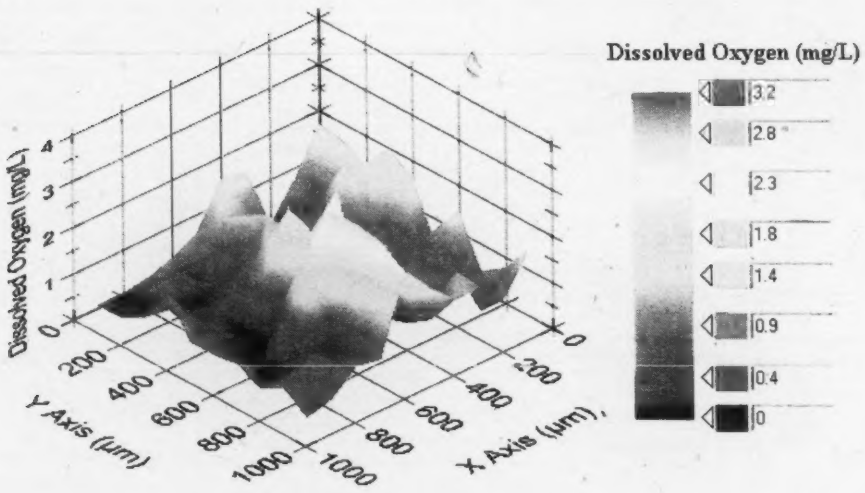

Figure C 20. The dissolved oxygen concentrations 40 µm below the biofilm surface in biofilm sample 3.

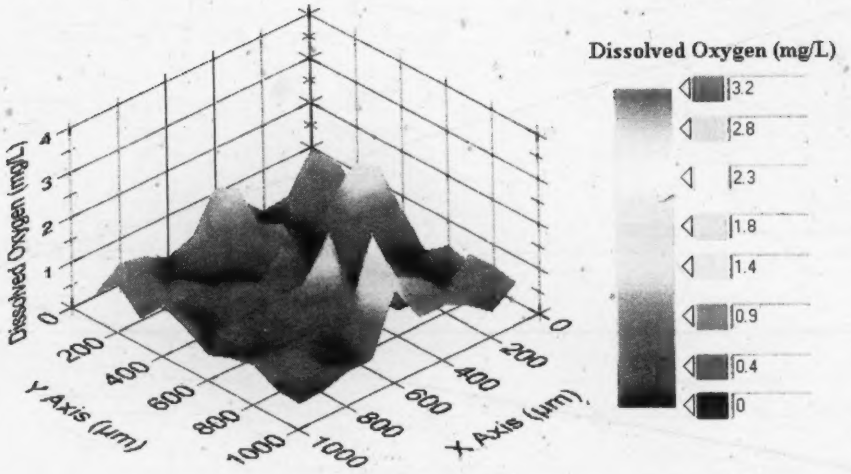

Figure C 21. The dissolved oxygen concentrations 120 µm below the biofilm surface in biofilm sample 3.

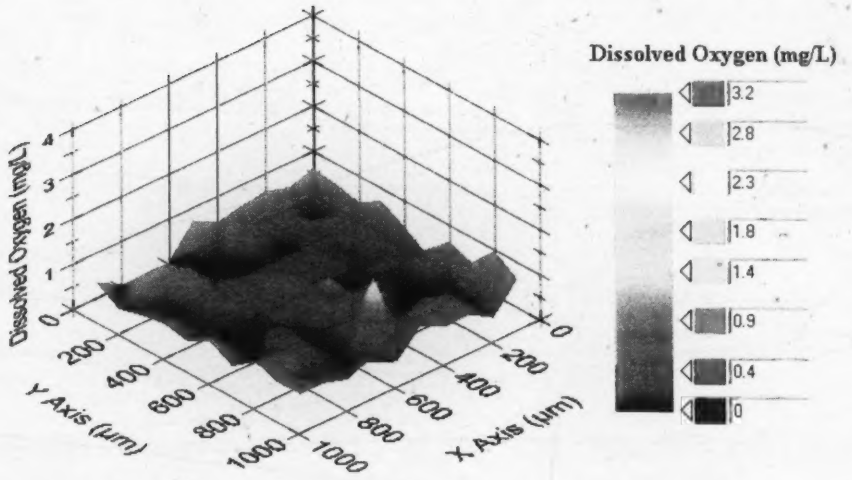

Figure C 22. The dissolved oxygen concentrations 200 µm below the biofilm surface in biofilm sample 3.

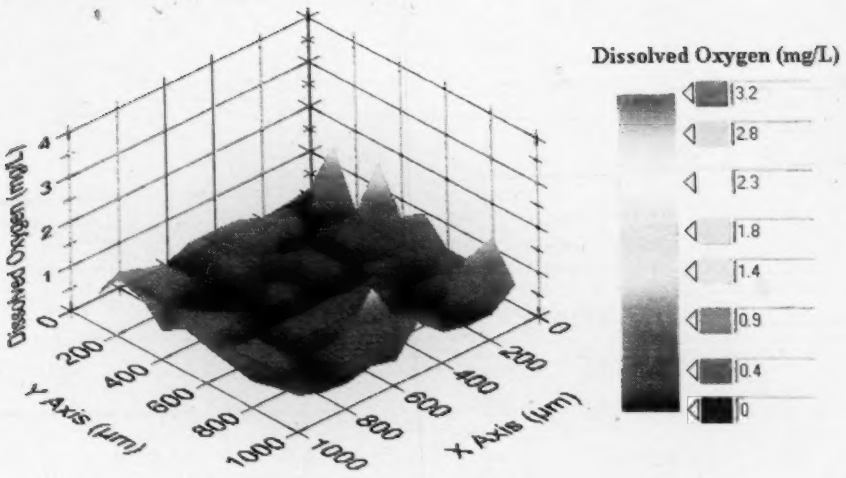

Figure C 23. The dissolved oxygen concentrations 280 µm below the biofilm surface in biofilm sample 3.

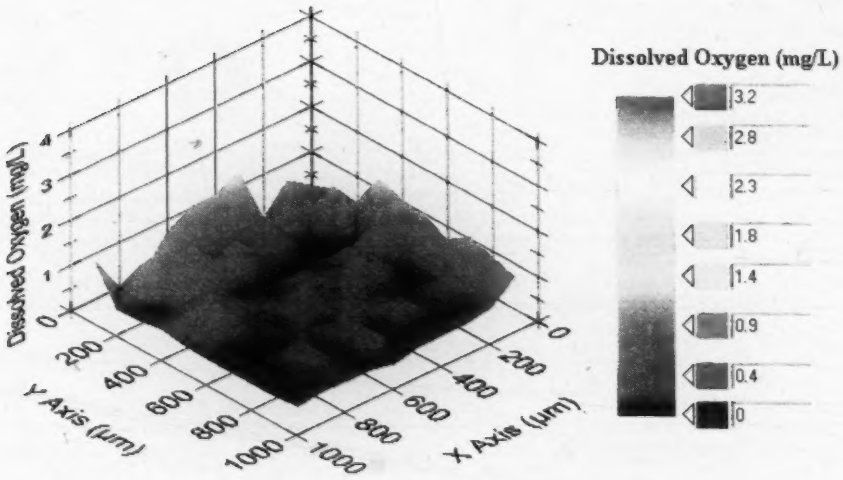

Figure C 24. The dissolved oxygen concentrations 360 µm below the biofilm surface in biofilm sample 3.

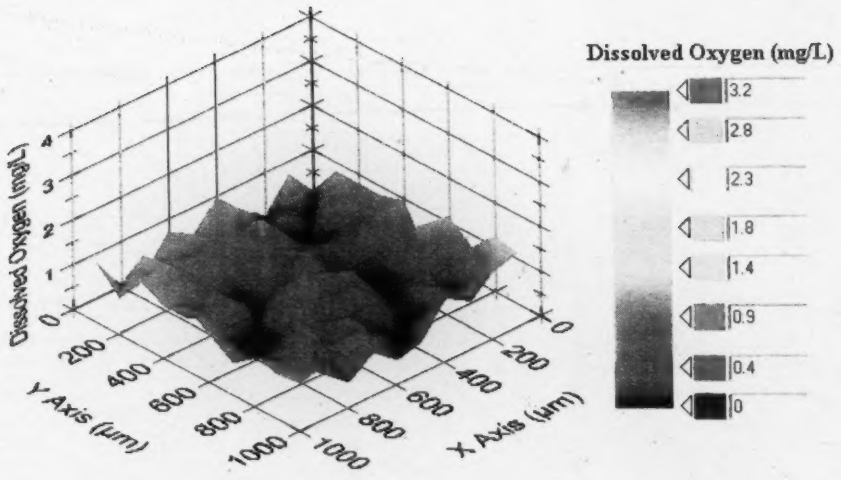

Figure C 25. The dissolved oxygen concentrations 440 µm below the biofilm surface in biofilm sample 3.

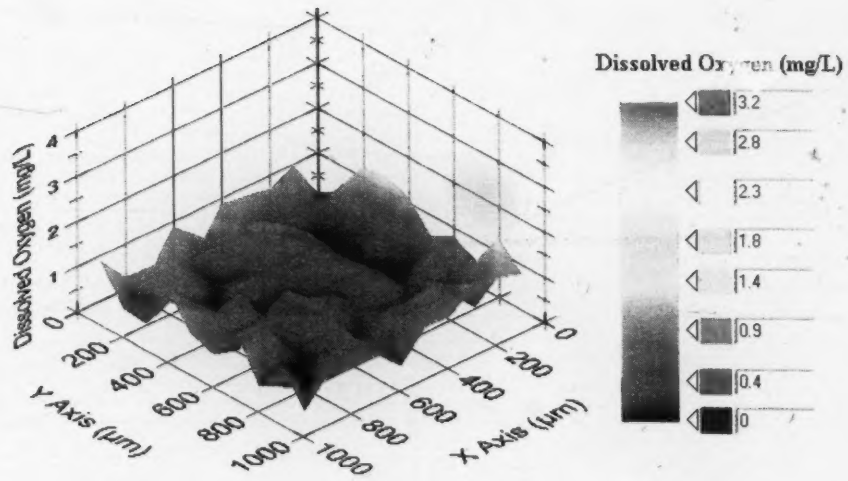

Figure C 26. The dissolved oxygen concentrations 520 µm below the biofilm surface in biofilm sample 3.

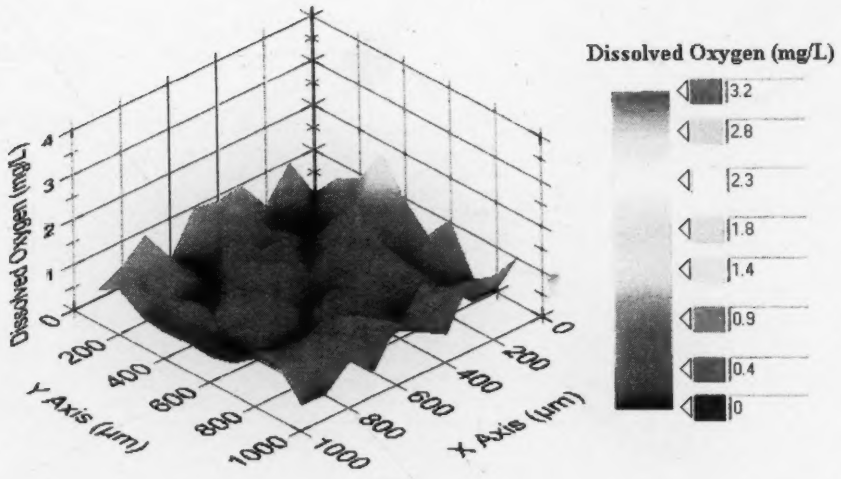

Figure C 27. The dissolved oxygen concentrations 600 µm below the biofilm surface in biofilm sample 3.

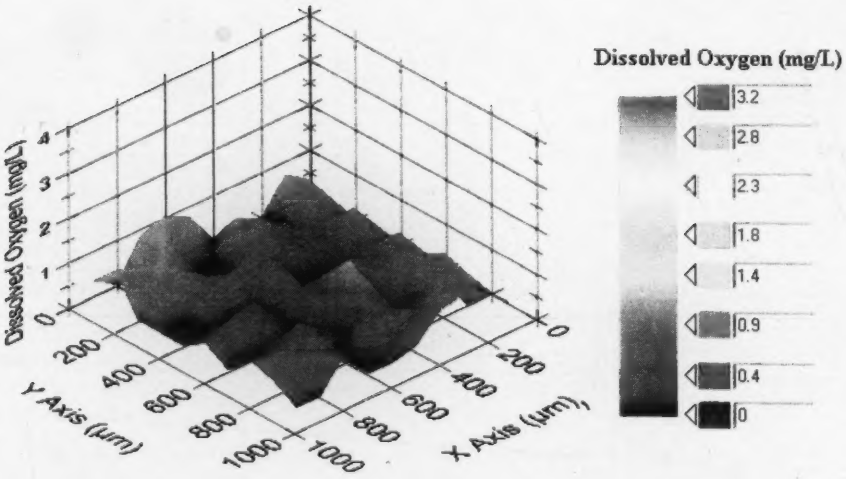

Figure C 28. The dissolved oxygen concentrations 680 µm below the biofilm surface in biofilm sample 3.

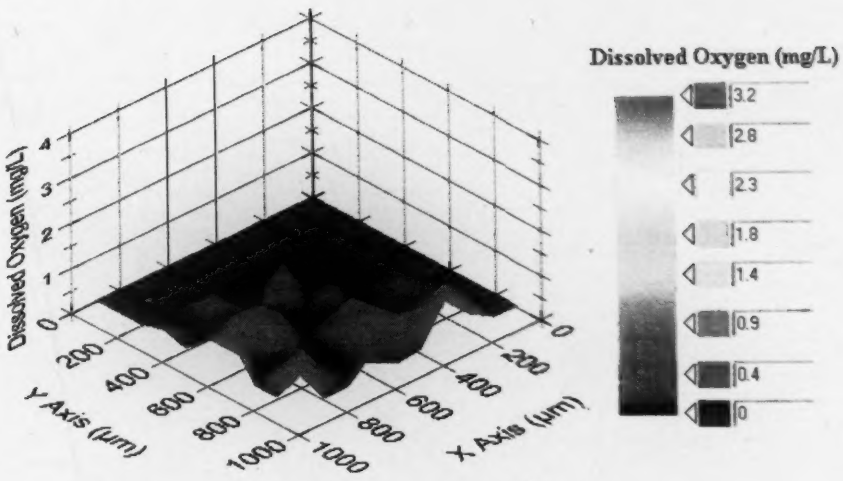

Figure C 29. The dissolved oxygen concentrations 760 µm below the biofilm surface in biofilm sample 3.

- Dissolved oxygen distribution from the biofilm surface in biofilm sample 4.

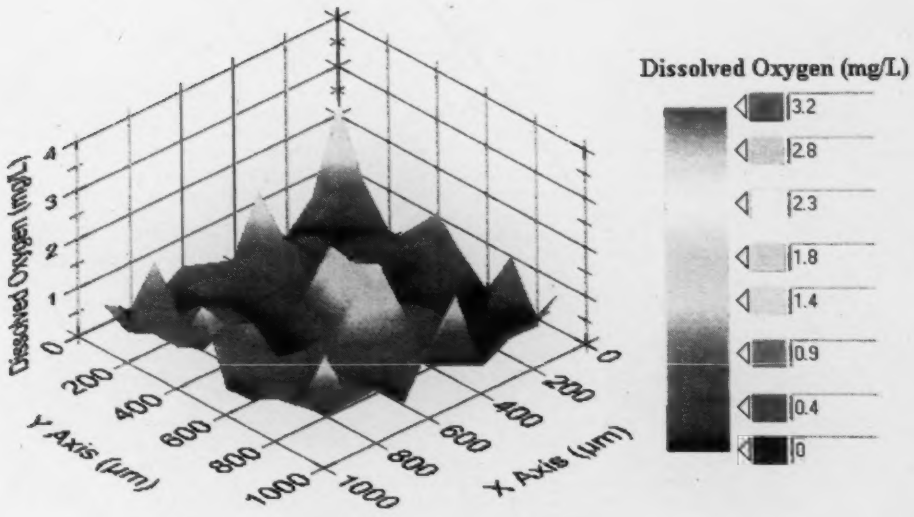

Figure C 30. The dissolved oxygen concentrations 40 µm below the biofilm surface in biofilm sample 4.

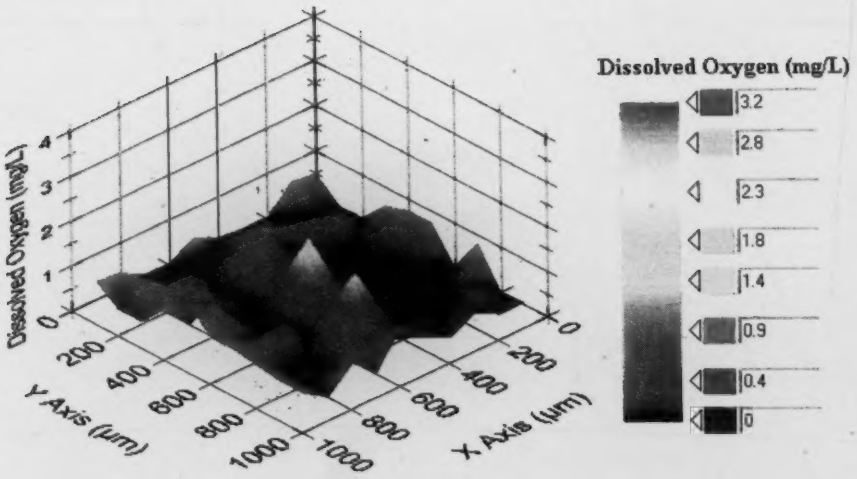

Figure C 31. The dissolved oxygen concentrations 120 µm below the biofilm surface in biofilm sample 4.

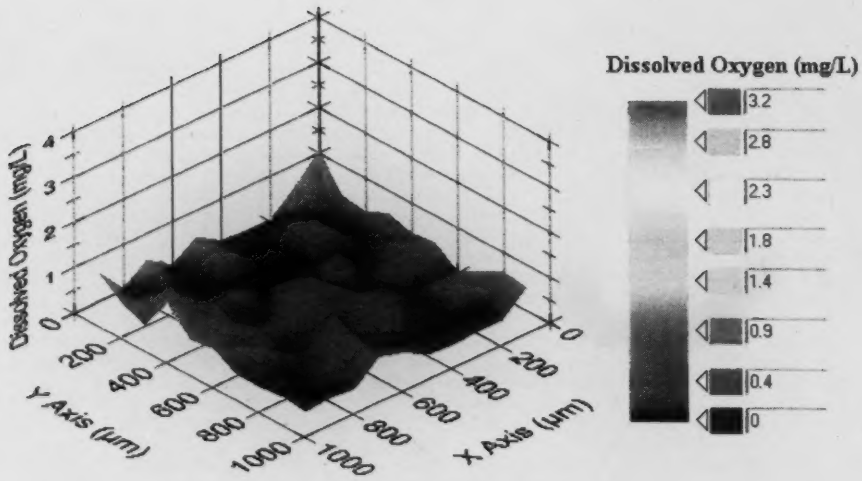

Figure C 32. The dissolved oxygen concentrations 200 µm below the biofilm surface in biofilm sample 4.

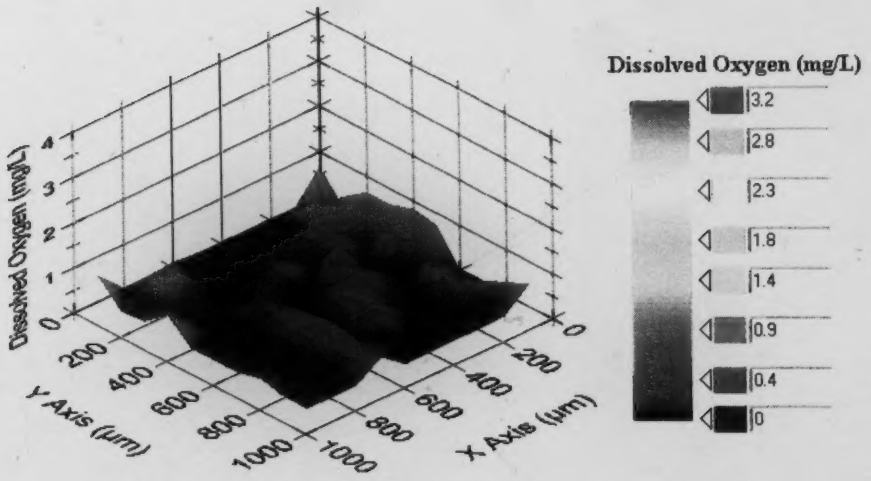

Figure C 33. The dissolved oxygen concentrations 280 µm below the biofilm surface in biofilm sample 4.

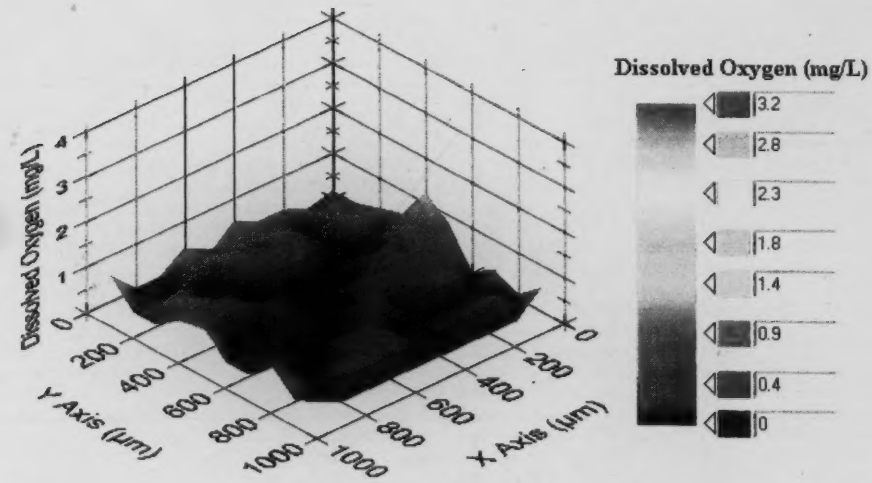

Figure C 34. The dissolved oxygen concentrations 360 µm below the biofilm surface in biofilm sample 4.

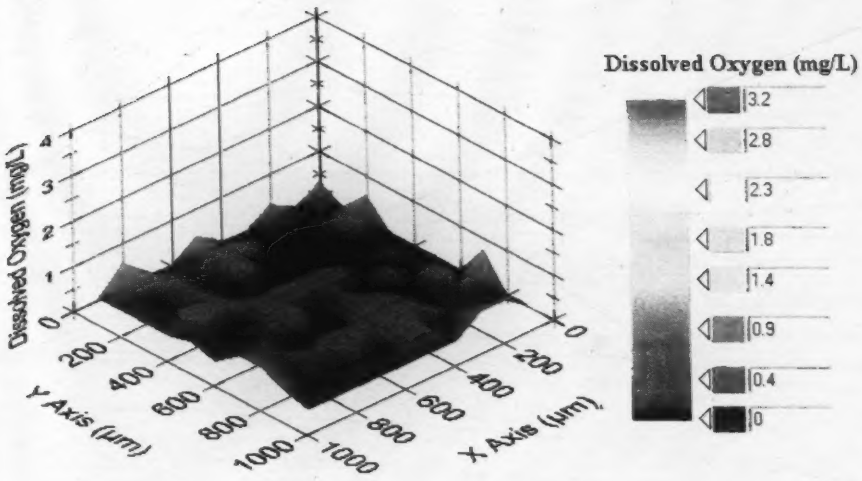

Figure C 35. The dissolved oxygen concentrations 440 µm below the biofilm surface in biofilm sample 4.

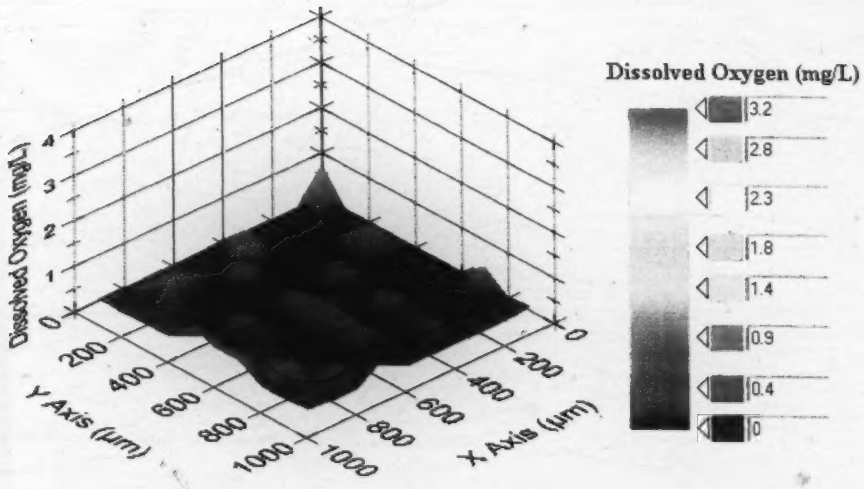

Figure C 36. The dissolved oxygen concentrations 520 µm below the biofilm surface in biofilm sample 4.

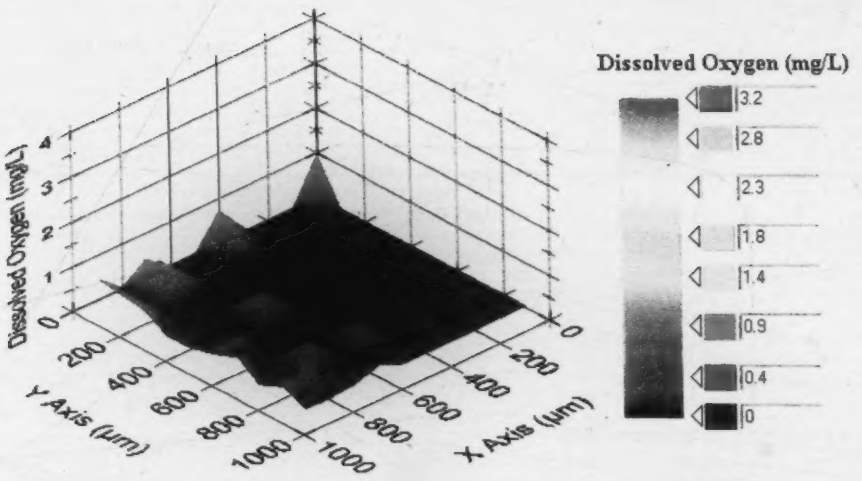

Figure C 37. The dissolved oxygen concentrations 600 µm below the biofilm surface in biofilm sample 4.

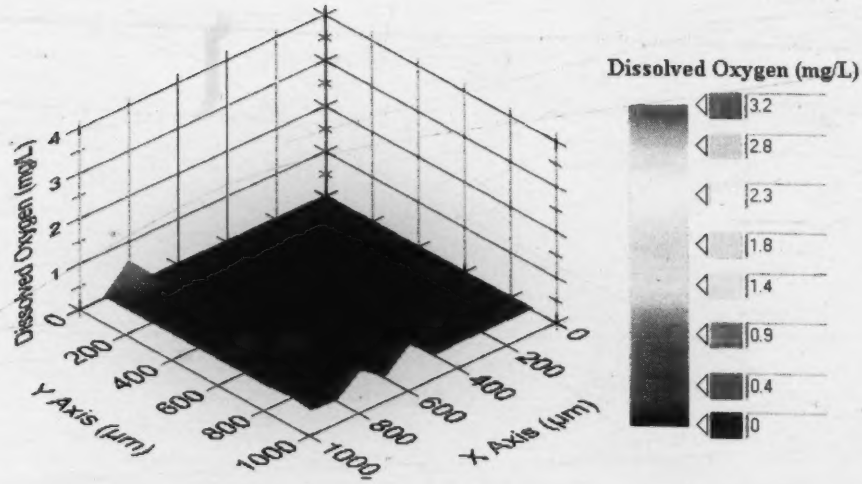

Figure C 38. The dissolved oxygen concentrations 680 µm below the biofilm surface in biofilm sample 4.

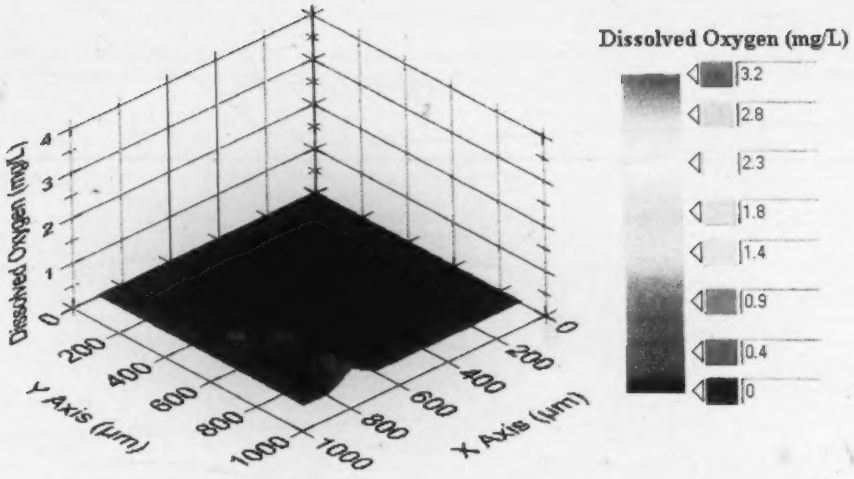

Figure C 39. The dissolved oxygen concentrations 760 µm below the biofilm surface in biofilm sample 4.

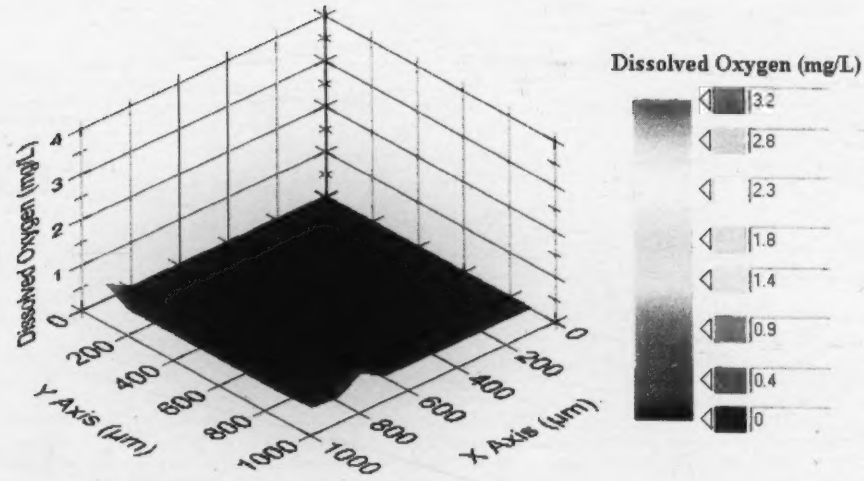

Figure C 40. The dissolved oxygen concentrations 840 µm below the biofilm surface in biofilm sample 4.

APPENDIX D. OXYGEN DISTRIBUTION ABOVE THE BIOFILM SURFACE.

- Dissolved oxygen distribution above the biofilm surface in biofilm sample 1.

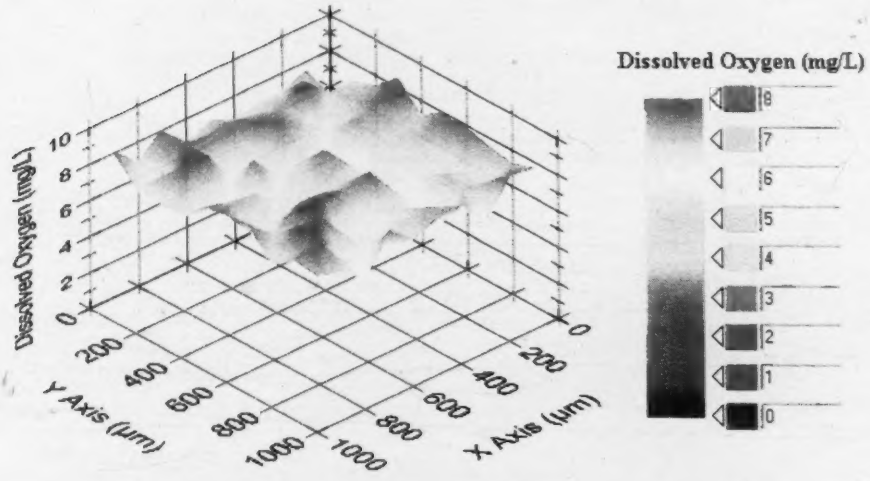

Figure D 1. The dissolved oxygen concentrations 840 µm above the biofilm surface in biofilm sample 1.

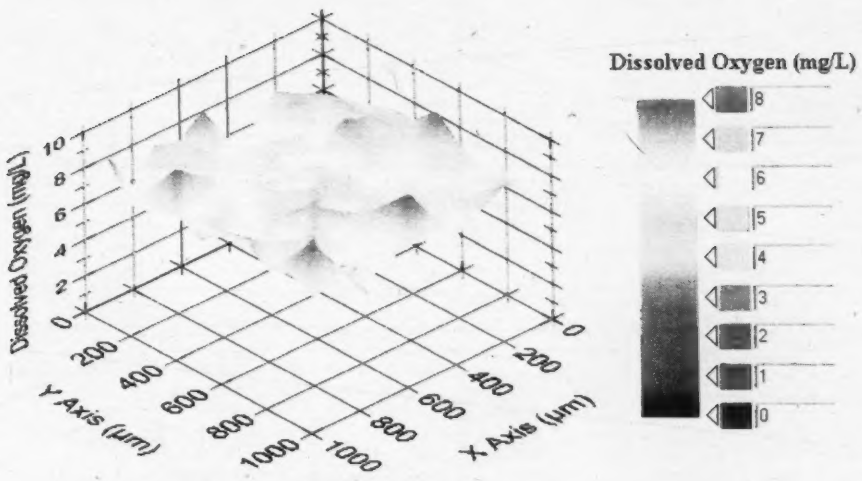

Figure D 2. The dissolved oxygen concentrations 760 µm above the biofilm surface in biofilm sample 1.

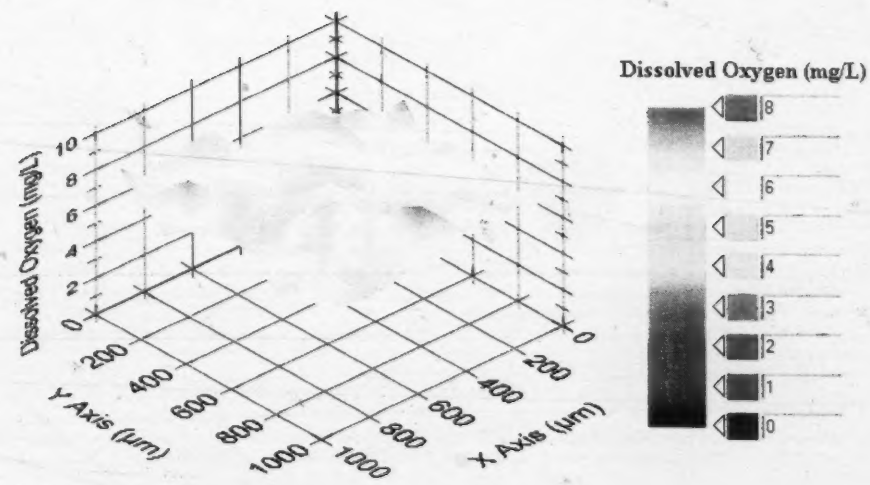

Figure D 3. The dissolved oxygen concentrations 680 µm above the biofilm surface in biofilm sample 1.

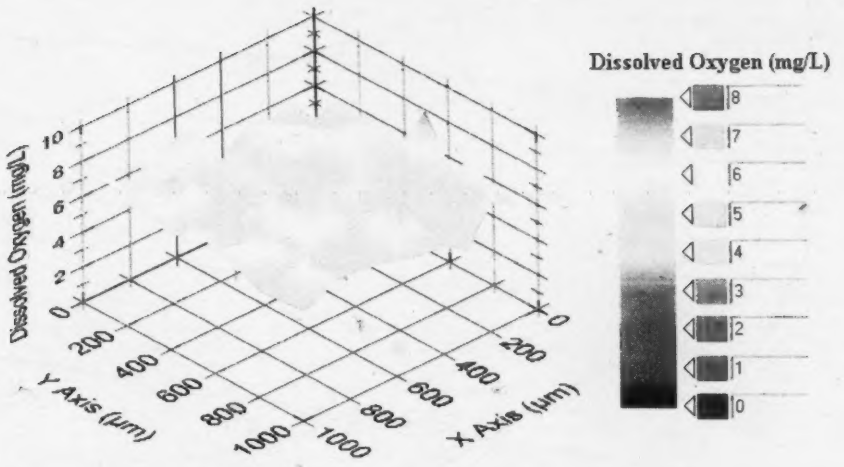

Figure D 4. The dissolved oxygen concentrations 600 µm above the biofilm surface in biofilm sample 1.

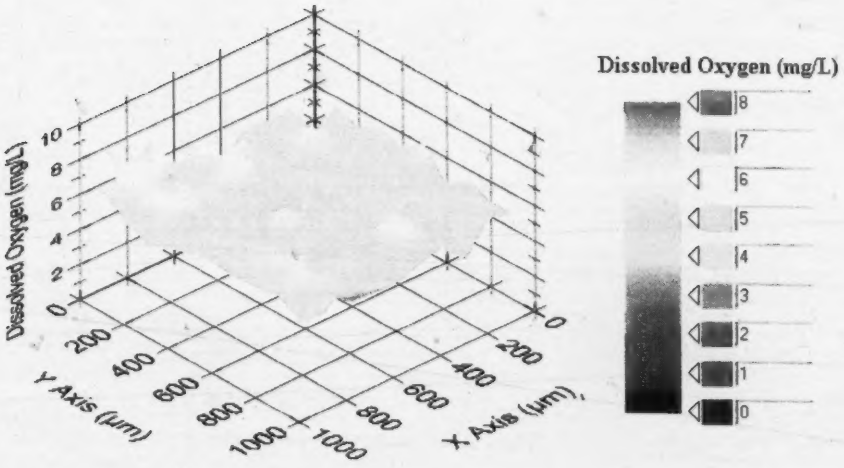

Figure D 5. The dissolved oxygen concentrations 520 µm above the biofilm surface in biofilm sample 1.

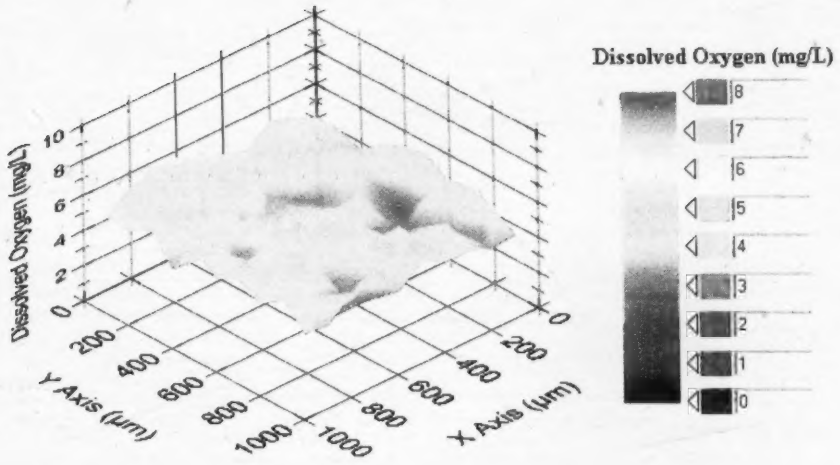

Figure D 6. The dissolved oxygen concentrations 440 µm above the biofilm surface in biofilm sample 1.

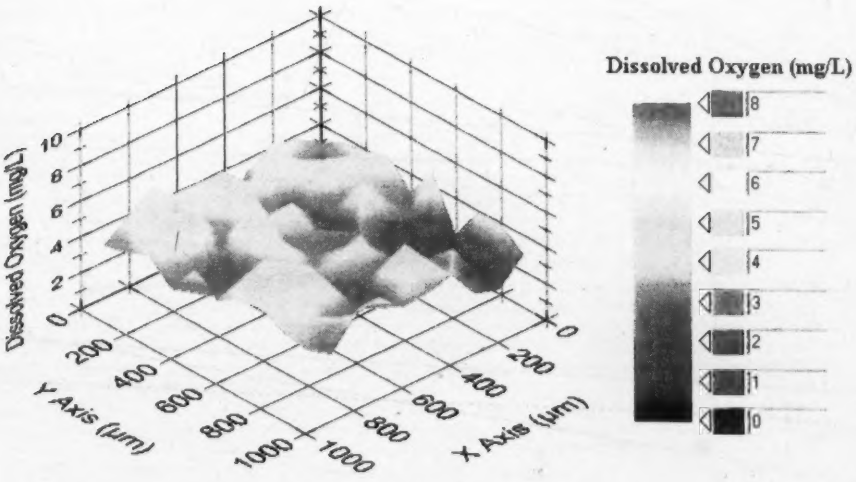

Figure D 7. The dissolved oxygen concentrations 360 µm above the biofilm surface in biofilm sample 1.

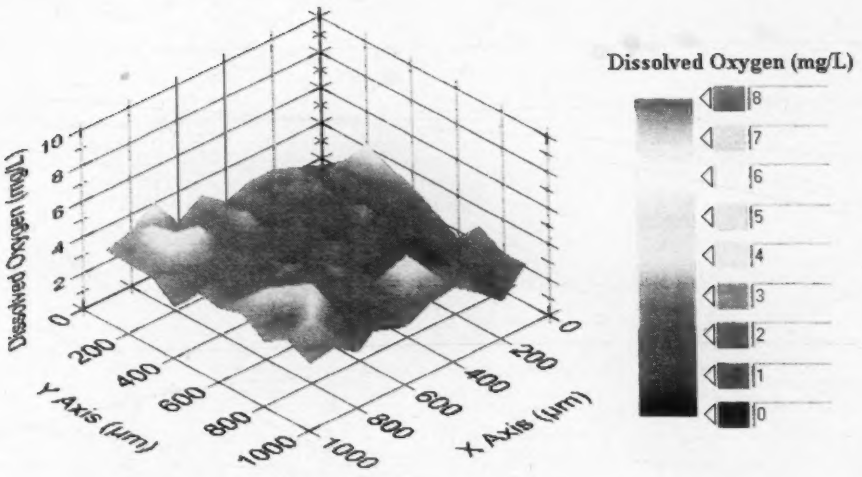

Figure D 8. The dissolved oxygen concentrations 280 µm above the biofilm surface in biofilm sample 1.

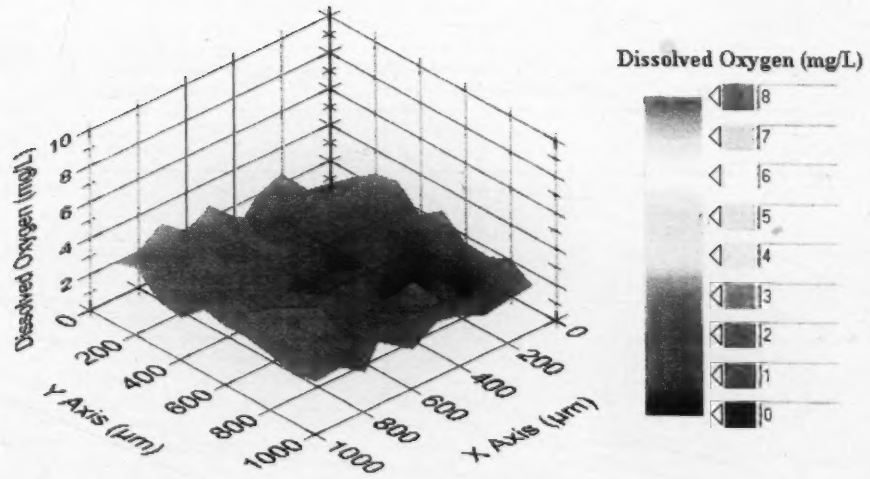

Figure D 9. The dissolved oxygen concentrations 200 µm above the biofilm surface in biofilm sample 1.

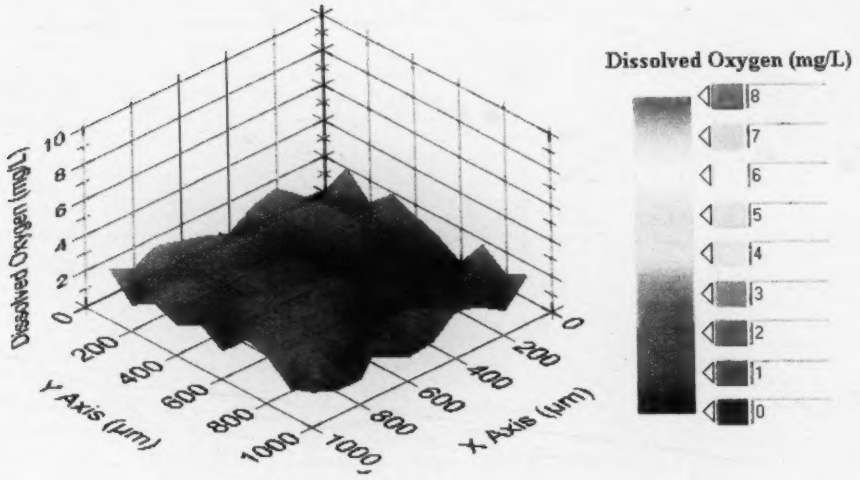

Figure D 10. The dissolved oxygen concentrations 120 µm above the biofilm surface in biofilm sample 1.

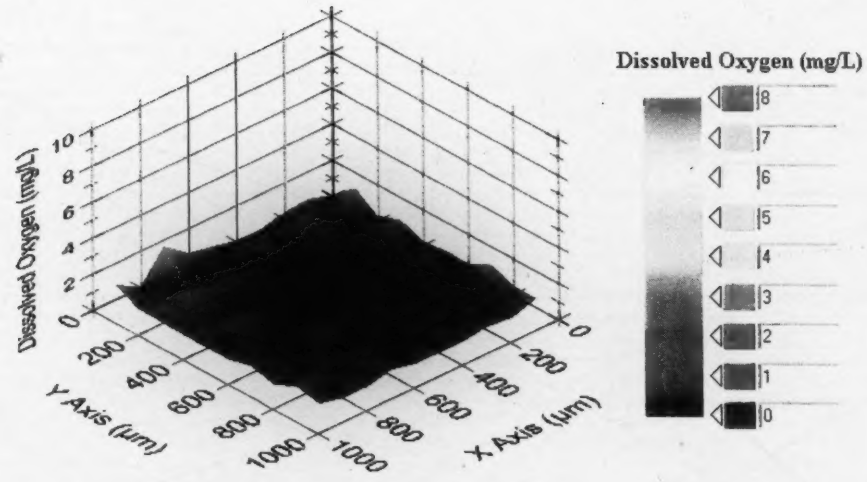

Figure D 11. The dissolved oxygen concentrations 40 µm above the biofilm surface in biofilm sample 1.

- Dissolved oxygen distribution above the biofilm surface in biofilm sample 2.

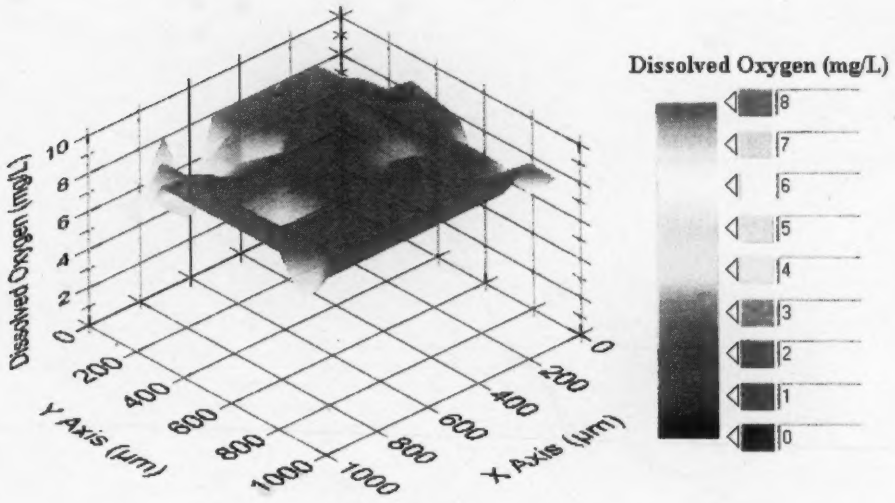

Figure D 12. The dissolved oxygen concentrations 840 µm above the biofilm surface in biofilm sample 2.

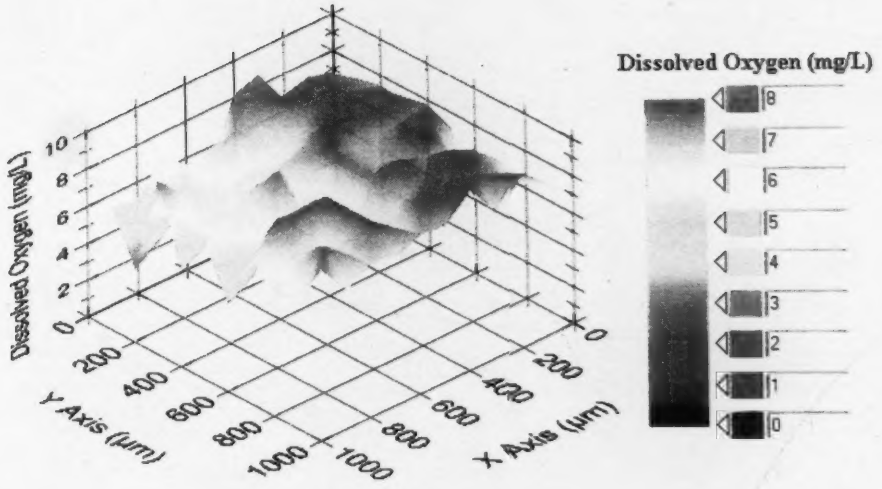

Figure D 13. The dissolved oxygen concentrations 760 µm above the biofilm surface in biofilm samplle 2.

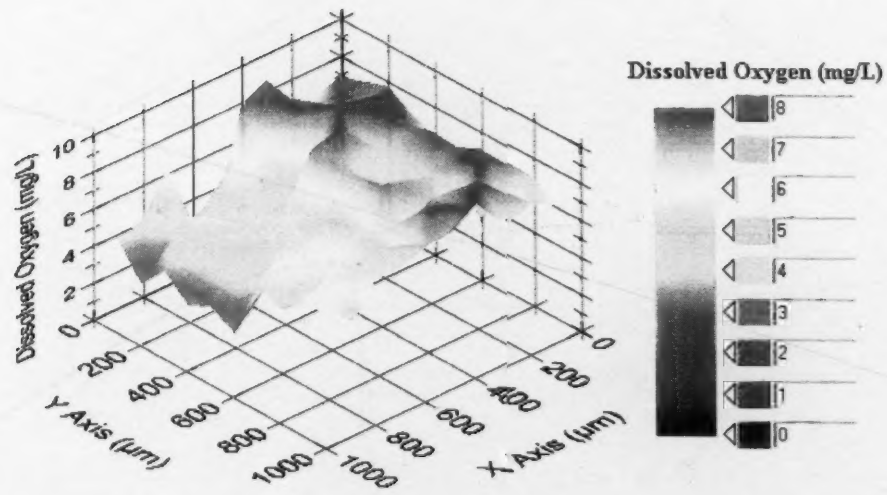

Figure D 14. The dissolved oxygen concenttrations 680 µm above the biofilm surface in biofilm sample 2.

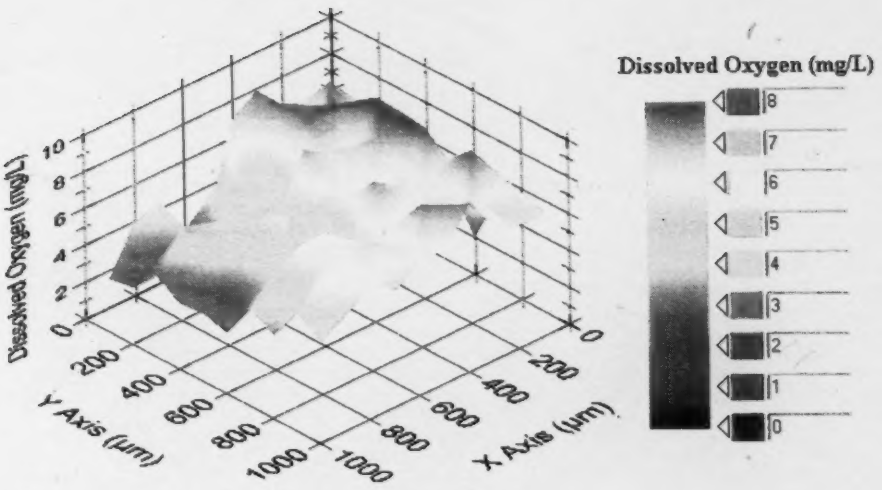

Figure D 15. The dissolved oxygen concentrations 600 µm above the biofilm surface in biofilm sample 2.

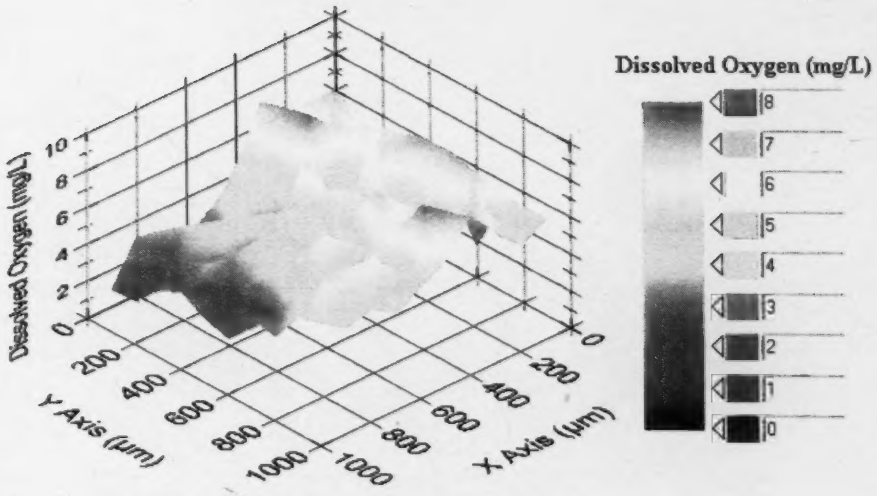

Figure D 16. The dissolved oxygen concentrations 520 µm above the biofilm surface in biofilm sample 2.

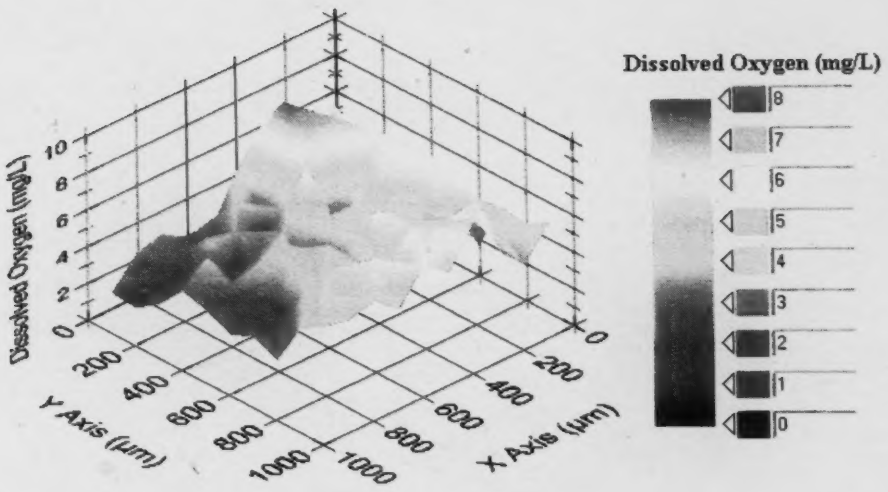

Figure D 17. The dissolved oxygen concentrations 440 µm above the biofilm surface in biofilm sample 2.

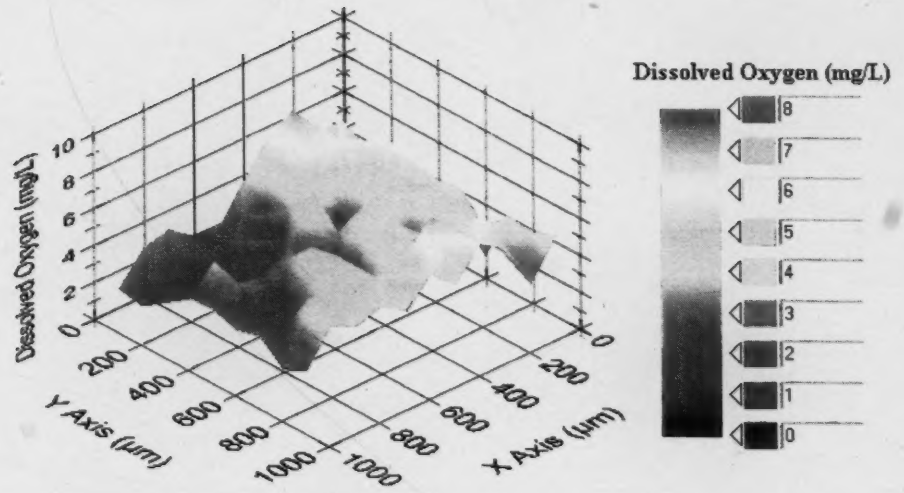

Figure D 18. The dissolved oxygen concentrations 360 µm above the biofilm surface in biofilm sample 2.

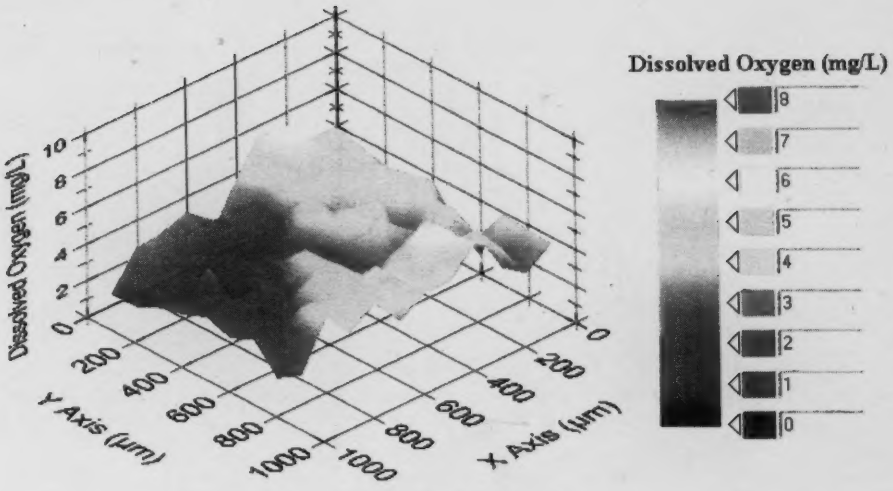

Figure D 19. The dissolved oxygen concentrations 280 µm above the biofilm surface in biofilm sample 2.

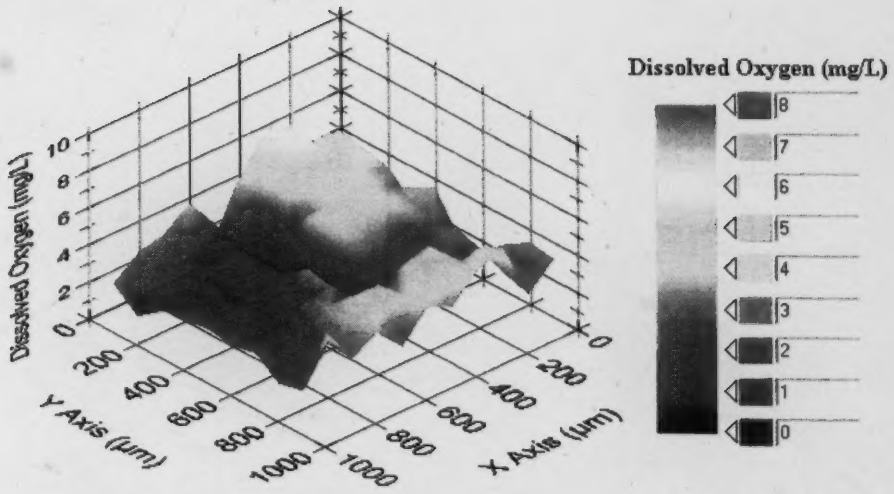

Figure D 20. The dissolved oxygen concentrations 200 µm above the biofilm surface in biofilm sample 2.

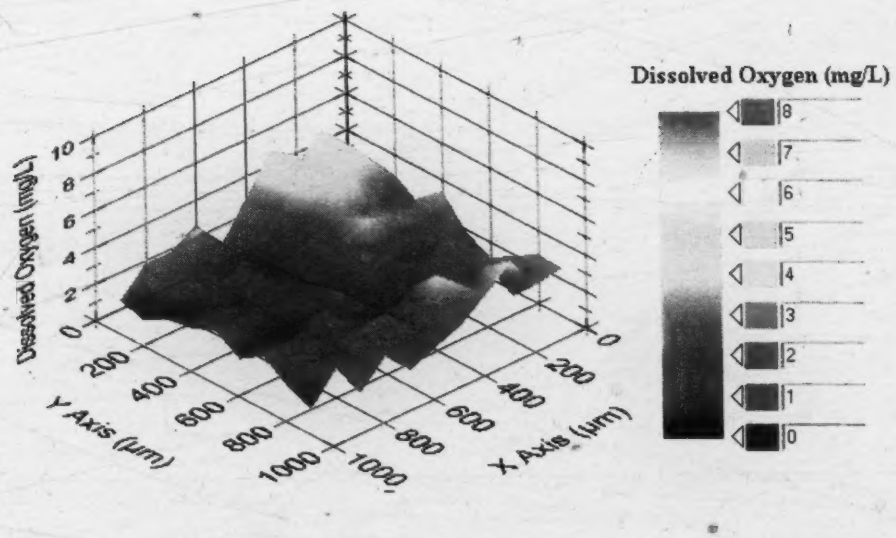

Figure D 21. The dissolved oxygen concentrations 120 µm above the biofilm surface in biofilm sample 2.

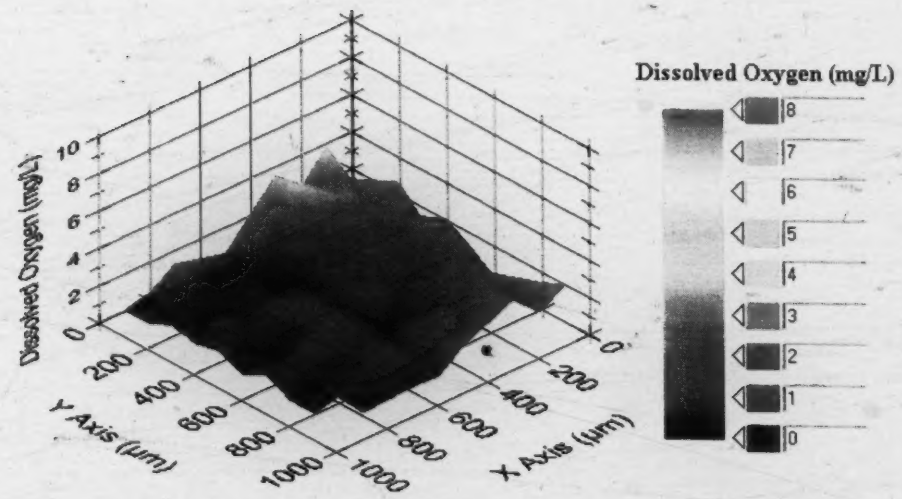

Figure D 22. The dissolved oxygen concentrations 40 µm above the biofilm surface in biofilm sample 2.

- Dissolved oxygen distribution above the biofilm surface in biofilm sample 3.

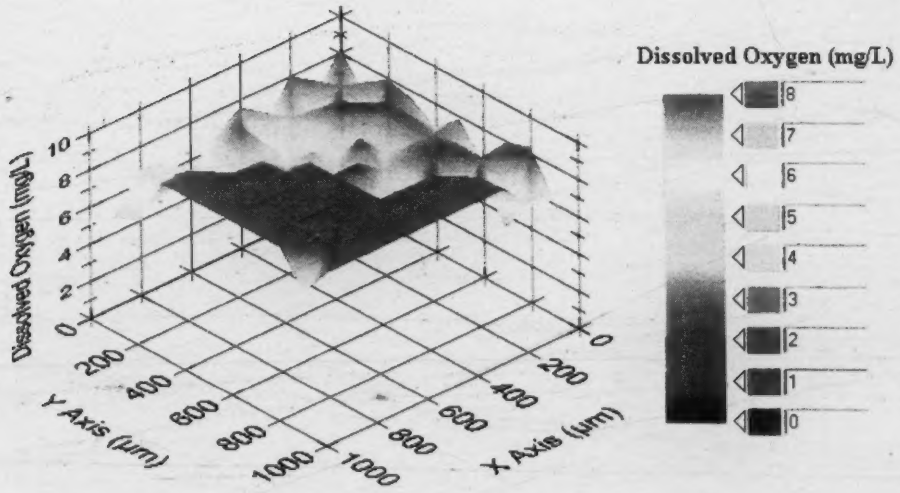

Figure D 23. The dissolved oxygen concentrations 840 µm above the biofilm surface in biofilm sample 3.

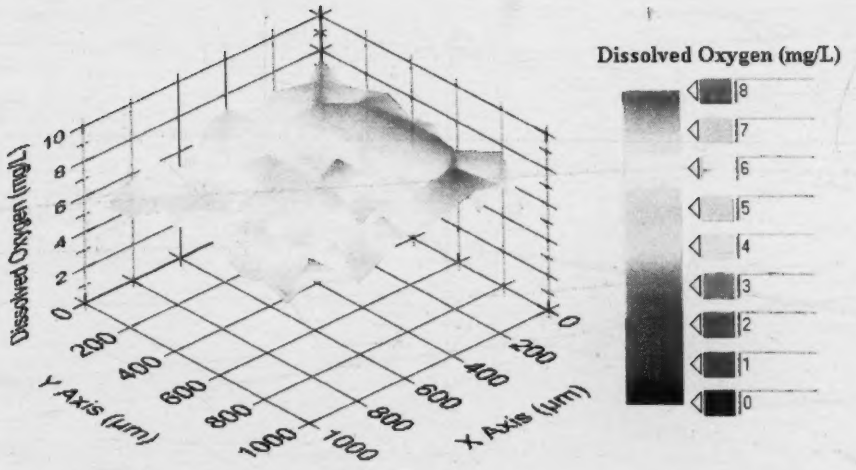

Figure D 24. The dissolved oxygen concentrations 760 µm above the biofilm surface in biofilm sample 3.

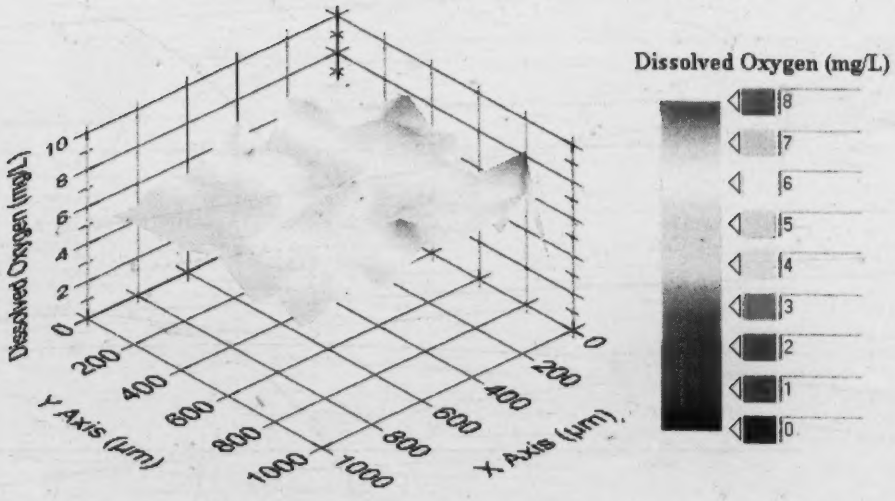

Figure D 25. The dissolved oxygen concentrations 680 µm above the biofilm surface in biofilm sample 3.

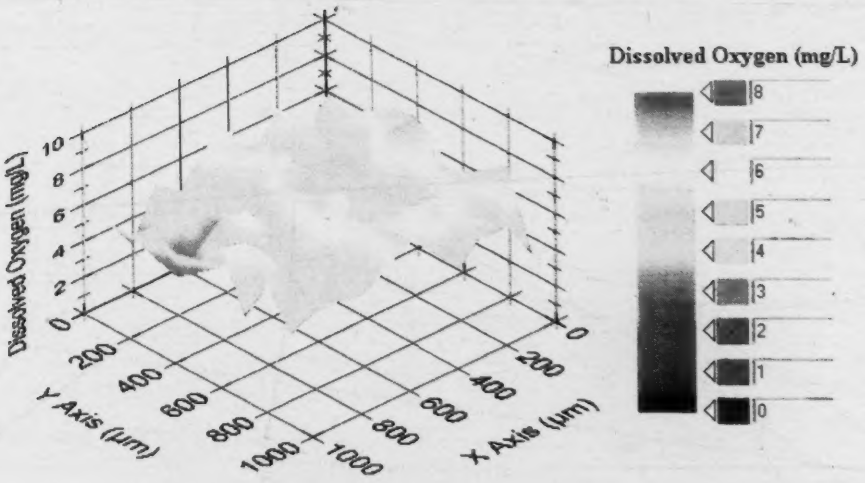

Figure D 26. The dissolved oxygen concentrations 600 µm above the biofilm surface in biofilm sample 3.

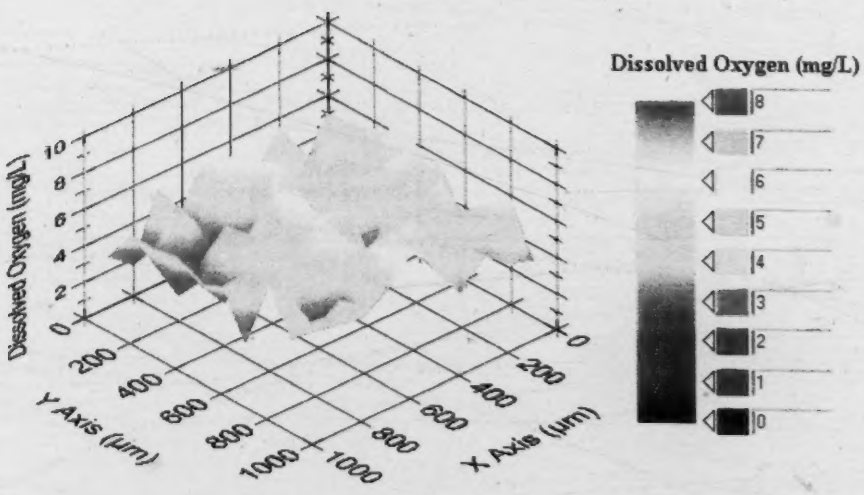

Figure D 27. The dissolved oxygen concentrations 520 µm above the biofilm surface in biofilm sample 3.

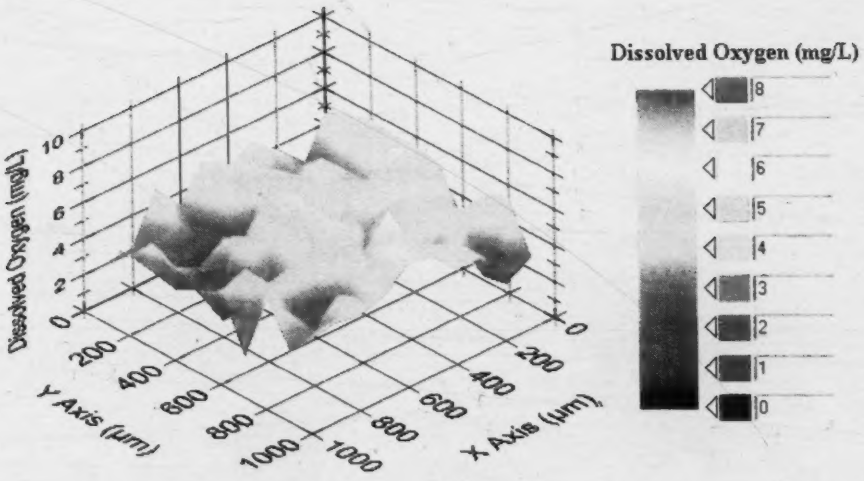

Figure D 28. The dissolved oxygen concentrations 440 µm above the biofilm surface in biofilm sample 3.

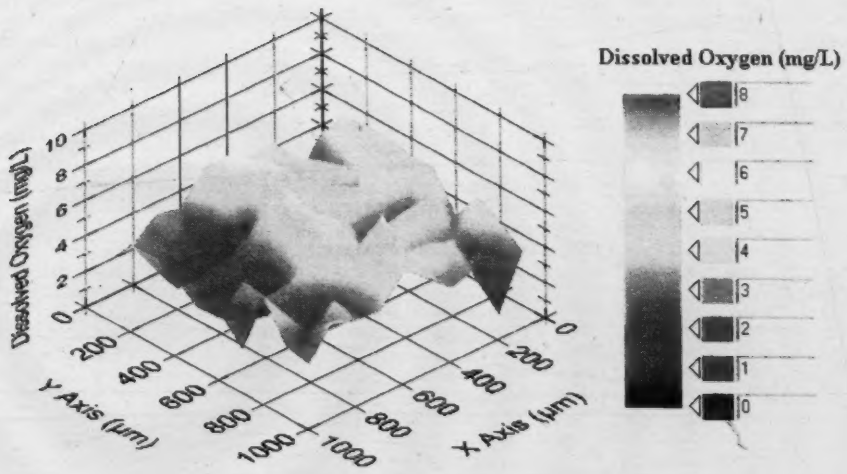

Figure D 29. The dissolved oxygen concentrations 360 µm above the biofilm surface in biofilm sample 3.

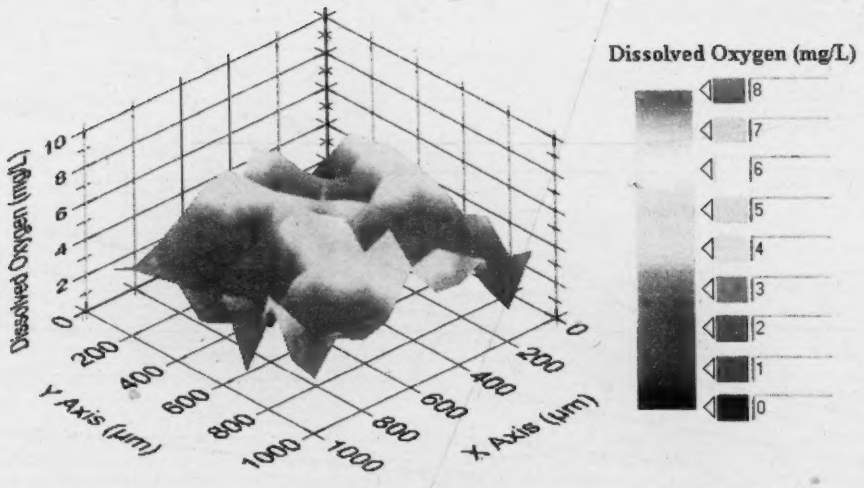

Figure D 30. The dissolved oxygen concentrations 280 µm above the biofilm surface in biofilm sample 3.

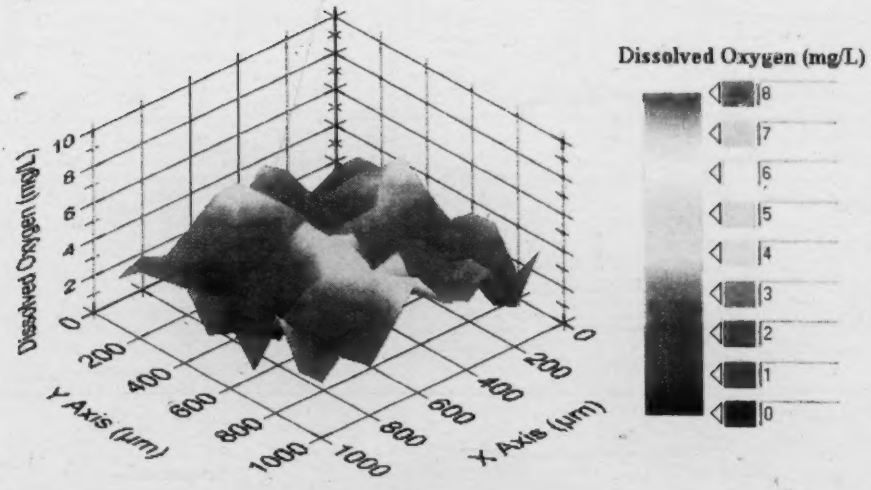

Figure D 31. The dissolved oxygen concentrations 200 µm above the biofilm surface in biofilm sample 3.

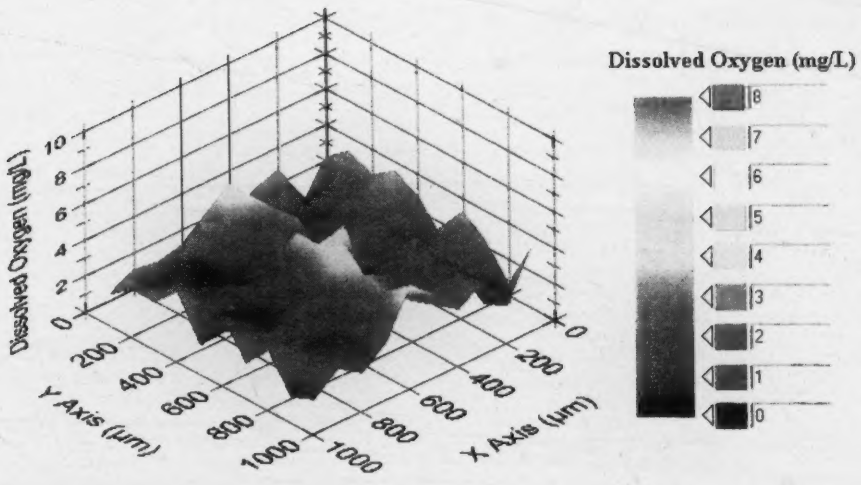

Figure D 32. The dissolved oxygen concentrations 120 µm above the biofilm surface in biofilm sample 3.

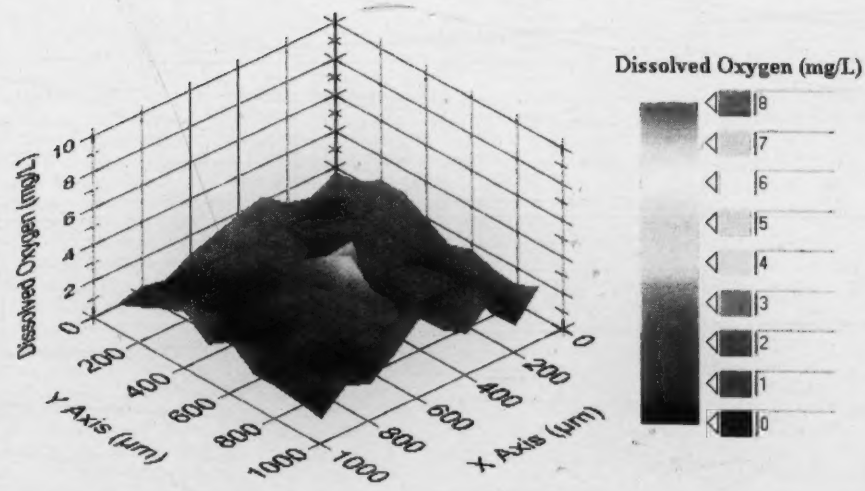

Figure D 33. The dissolved oxygen concentrations 40 µm above the biofilm surface in biofilm sample 3.

- Dissolved oxygen distribution above the biofilm surface in biofilm sample 4.

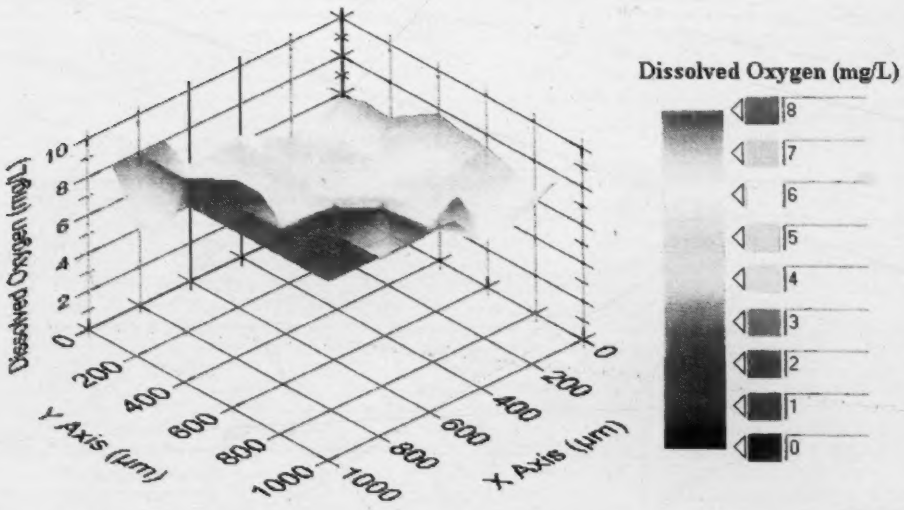

Figure D 34. The dissolved oxygen concentrations 920 µm above the biofilm surface in biofilm sample 4.

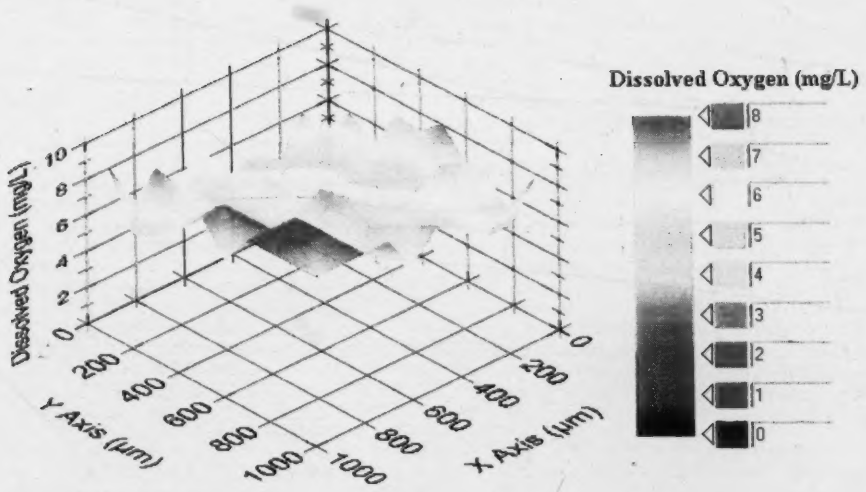

Figure D 35. The dissolved oxygen concentrations 840 µm above the biofilm surface in biofilm sample 4.

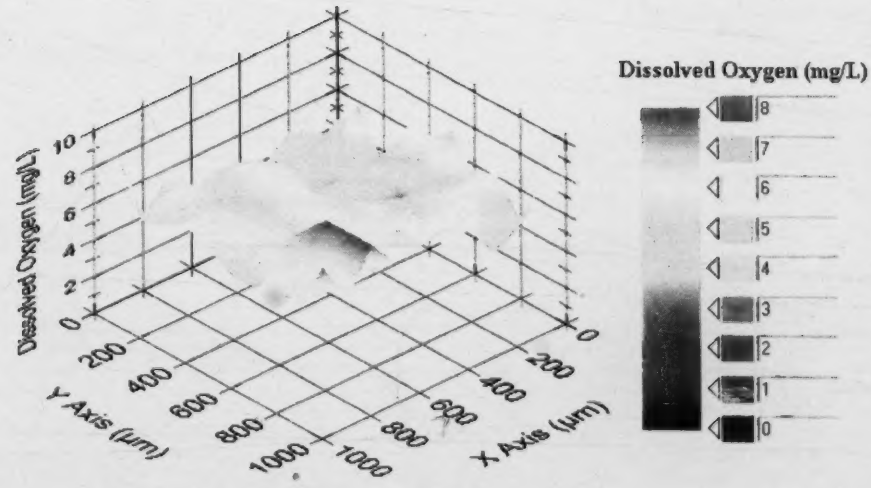

Figure D 36. The dissolved oxygen concentrations 760 µm above the biofilm surface in biofilm sample 4.

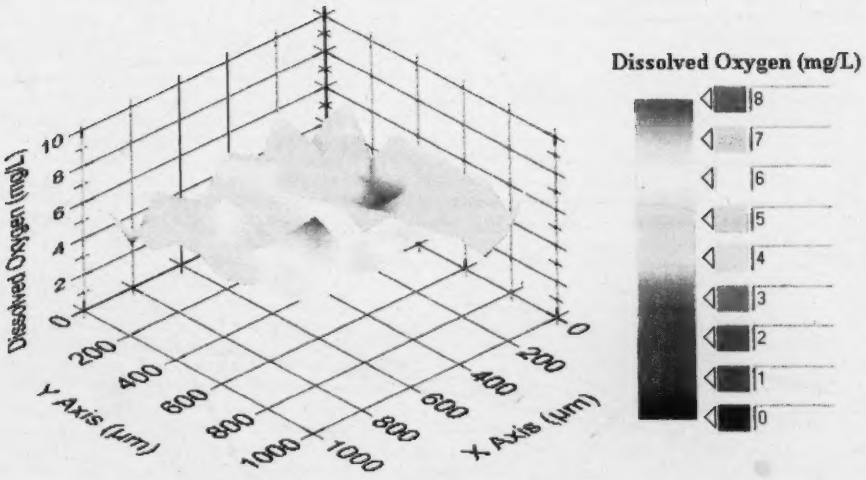

Figure D 37. The dissolved oxygen concentrations 680 µm above the biofilm surface in biofilm sample 4.

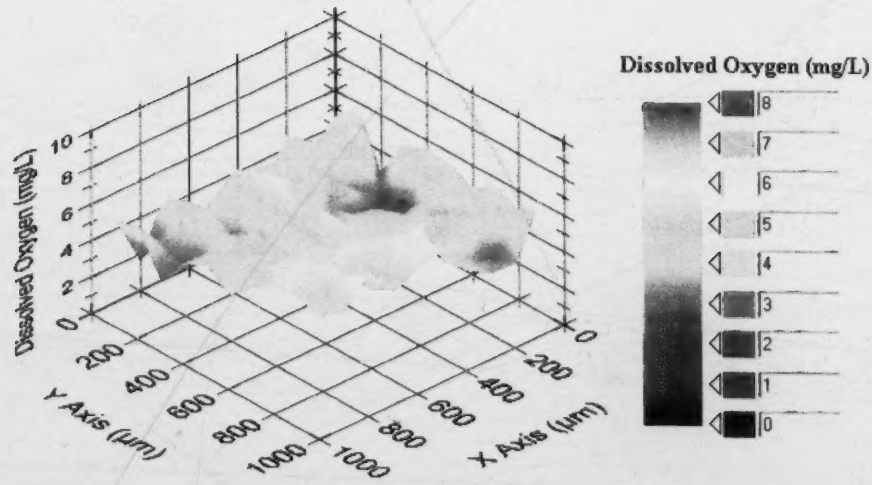

Figure D 38. The dissolved oxygen concentrations 600 µm above the biofilm surface in biofilm sample 4.

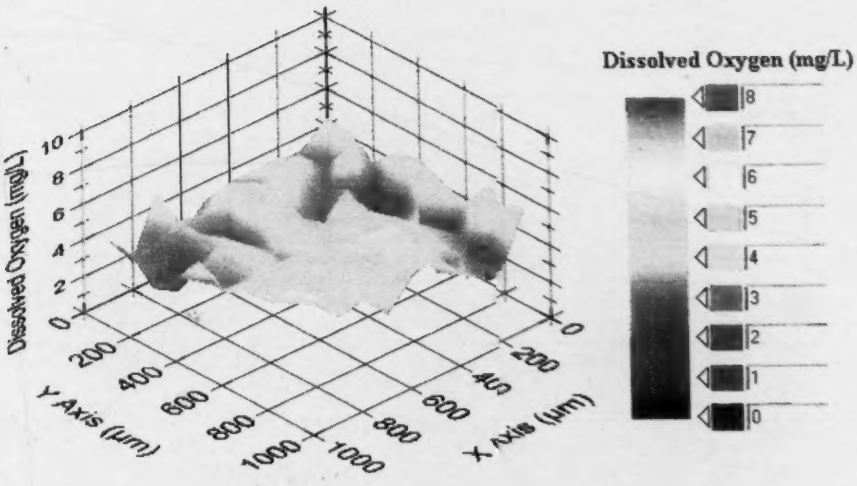

Figure D 39. The dissolved oxygen concentrations 520 µm above the biofilm surface in biofilm sampe 4.

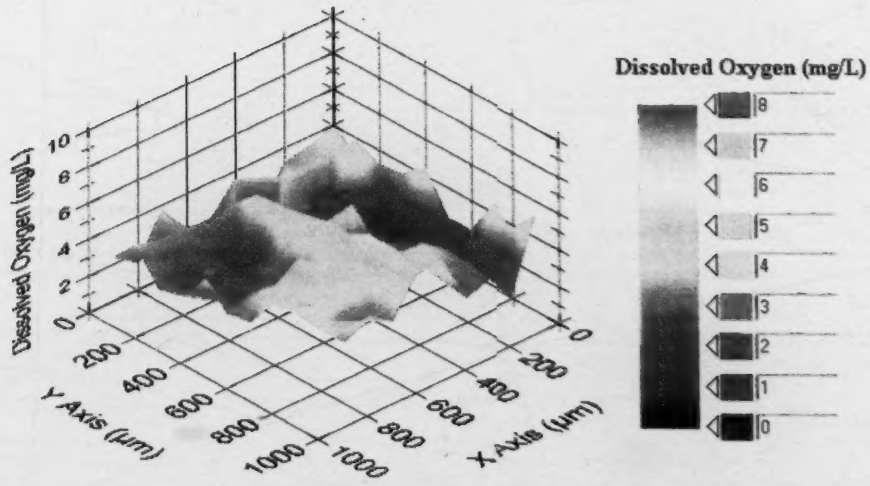

Figure D 40. The dissolved oxygen concentrations 440 µm above the biofilm surface in biofilm sample 4.

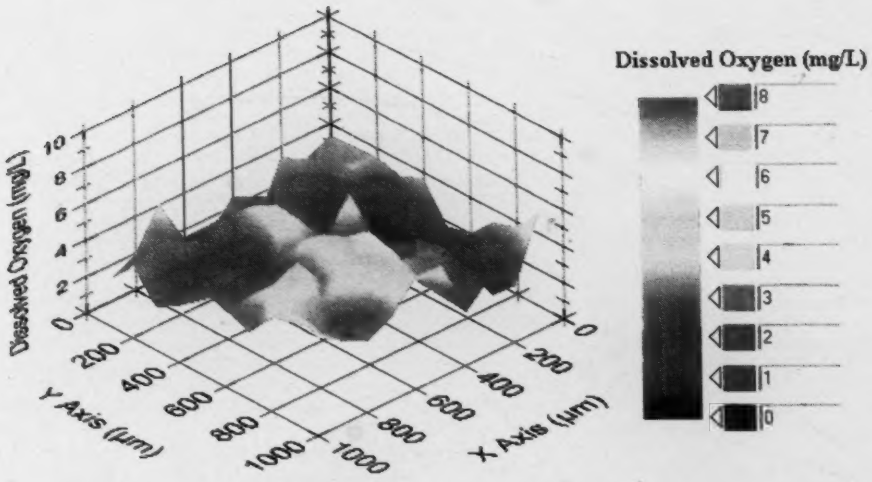

Figure D 41. The dissolved oxygen concentrations 360 µm above the biofilm surface in biofilm sample 4.

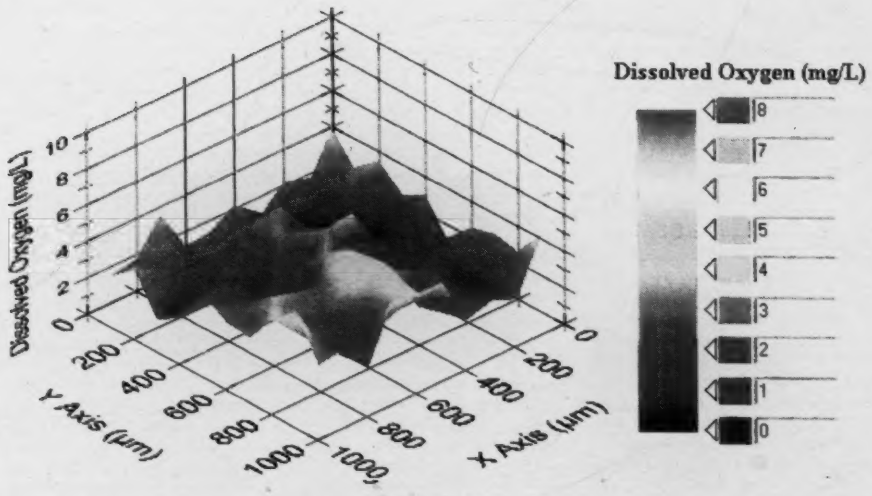

Figure D 42. The dissolved oxygen concentrations 280 µm above the biofilm surface in biofilm sample 4.

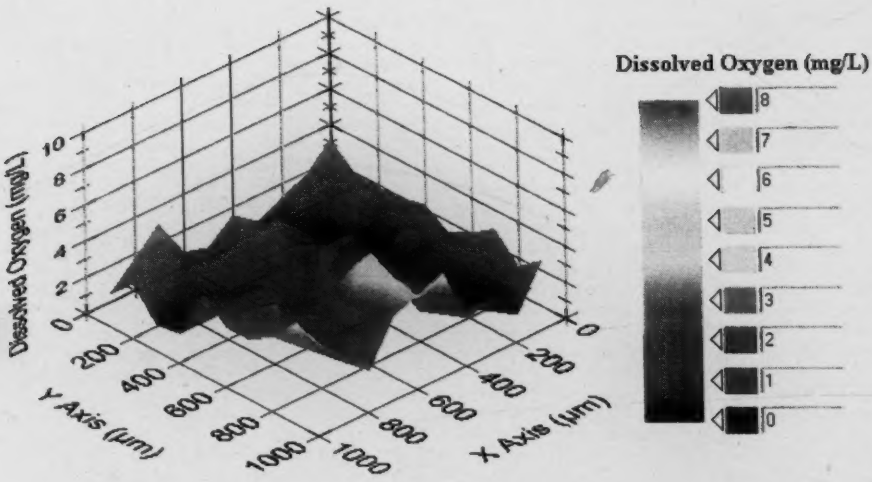

Figure D 43. The dissolved oxygen concentrations 200 µm above the biofilm surface in biofilm sample 4.

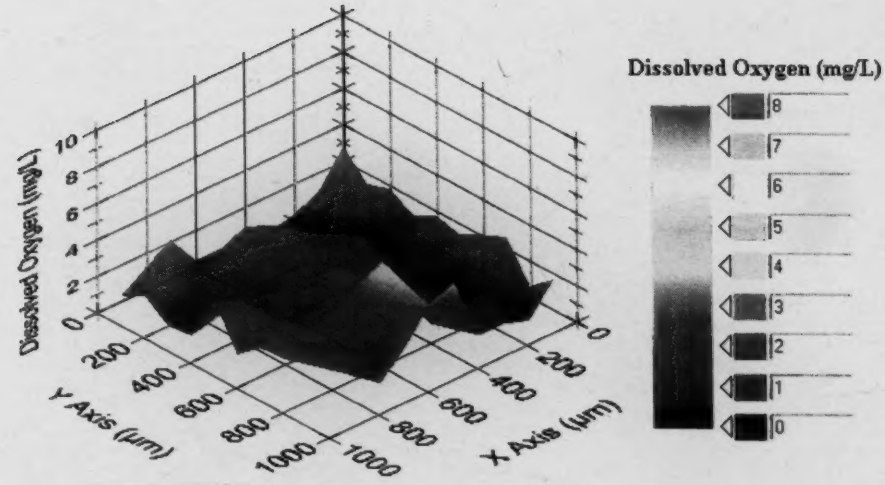

Figure D 44. The dissolved oxygen concentrations 120 µm above the biofilm surface in biofilm sample 4.

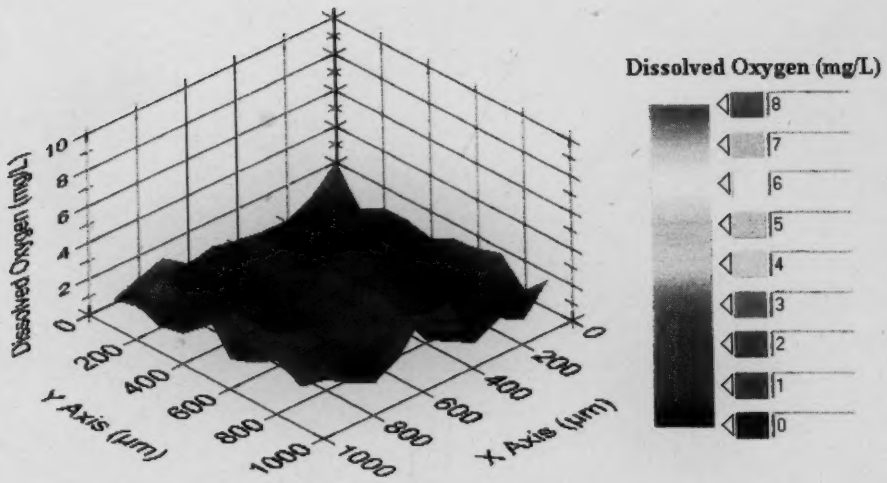

Figure D 45. The dissolved oxygen concentrations 40 µm above the biofilm surface in biofilm sample 4.

For those who are interested in the original data, please contact the author,

Carlos de la Rosa

E-mail :

and the Advisor,

Tong Yu

mental Engineering